GaPN-on-Si(100) and buried interfaces: *In situ* spectroscopy during MOVPE growth

Dissertation
zur Erlangung des akademischen Grades
doctor rerum naturalium
(Dr. rer. nat.)
im Fach Physik
Spezialisierung: Experimentalphysik

eingereicht an der
Mathematisch-Naturwissenschaftlichen Fakultät
der Humboldt-Universität zu Berlin

von
Dipl. Phys. Oliver Supplie

Präsident der Humboldt-Universität zu Berlin:
Prof. Dr. Jan-Hendrik Olbertz

Dekan der Mathematisch-Naturwissenschaftlichen Fakultät:
Prof. Dr. Elmar Kulke

Gutachter:
1. Prof. Dr. Recardo Manzke
2. Prof. Dr. Thomas Hannappel
3. Prof. David E. Aspnes, PhD

Tag der mündlichen Prüfung: 03.09.2015

Zusammenfassung

Effiziente und erneuerbare Wasserstofferzeugung ist eine der entscheidenden Herausforderungen für eine nachhaltige, von fossilen Brennstoffen unabhängige Gesellschaft. Tandem-Absorber-Strukturen, die auf verdünnt Stickstoff-haltigem GaPN/Si(100) basieren, sind vielversprechend für die Wasserstoffproduktion mittels direkter solarer Wasserspaltung. Die Herstellung im industriellen Maßstab ist anspruchsvoll, sowohl wegen der komplexen Wachstumsprozesse in der metallorganischen Gasphasenepitaxie (MOVPE) als auch wegen des Materialsystems an sich, insbesondere bezüglich gezielter Präparation der Grenzflächen. Einen Grund dafür stellen die unterschiedlichen Kristallstrukturen der III-V Halbleiter und des Si dar. Wegen der geringen Gitterfehlanpassung eignen sich pseudomorphe GaP/Si(100) Strukturen als Quasisubstrate. Können diese mit hoher Kristallqualität hergestellt werden, vereinfacht dies die weitere Integration anderer III-V Halbleiter erheblich. In der vorliegenden Arbeit wird die atomare Ordnung von Si(100) und GaP(N)/Si(100) Oberflächen, sowie der vergrabenen GaP/Si(100) Heterogrenzfläche *in situ* mit Reflexions-Anisotropie-Spektroskopie (RAS) untersucht. Der Einfluss von Hintergrundverunreinigungen von vorhergehenden III-V Wachstumsprozessen auf die Ausbildung der Ober- und Grenzflächen wird hinsichtlich der Prozessbedingungen analysiert. RAS Ergebnisse werden dabei mit Ergebnissen komplementärer Methoden der Oberflächenanalytik im Ultrahochvakuum (UHV) verglichen, beispielsweise mit niederenergetischer Elektronenbeugung (LEED) und Röntgenphotoelektronenspektroskopie (XPS).

Ein detailliertes Verständnis der RA Spektren ermöglicht *in situ* Kontrolle über die Ausbildung atomar unterschiedlich geordneter Si(100) Oberflächen und damit über die Struktur des GaP Films. Die Präparation nahezu eindomäniger, dimerisierter Si(100) Oberflächen gelingt erfolgreich in MOVPE Atmosphäre mit Hintergrundverunreinigungen von (Ga, P, As). Antiphasenunordnung in III-V Filmen kann somit zuverlässig vermieden werden. Ladungskompensation an der GaP/Si(100) Grenzfläche kann durch atomare Durchmischung mit identischer Anzahl von Si–P und Si–Ga Bindungen ermöglicht werden. Für diese kompensierten Grenzflächen sagen Dichtefunktionaltheorie-Rechnungen eine geringere Formationsenergie als für abrupte Grenzflächen vorher. XPS Messungen weisen jedoch auf eine kinetisch limitierte Bildung einer eher abrupten Grenzfläche bestehend aus ungefähr einer Monolage Si–P Bindungen hin. Eine abrupte Si–P Grenzfläche kann auch die beobachtete Untergitterorientierung des GaP Films erklären. Prozessbedingungen für exakt orientierte Si(100) Substrate begünstigen die Diffusion von Hintergrundverunreinigungen auf die Oberfläche. Die Menge der sub-Monolagen-Bedeckung des Substrats vor der GaP Nukleation beeinflusst dabei stark die Ausprägung der Grenzfläche und die Struktur des GaP Films. Mittels As-Modifikation der zuvor Monohydrid-terminierten Si(100) Oberfläche kann die GaP Untergitterorientierung invertiert werden. Die entsprechenden GaP/Si(100) Oberflächen sind ebenfalls frei von Antiphasenunordnung. Die Untersuchungen zeigen außerdem, dass die Ausbildung atomar wohl geordneter GaP/Si(100) Oberflächen bereits durch die gepulste GaP Nukleation auf Si(100) und anschießendes Heizen mit Phosphorstabilisierung eingeleitet werden kann. Wachstum von zu Si(100) gitterangepasstem GaPN gelingt sowohl auf diesen nukleierten Substraten als auch auf pseudomorphen GaP/Si(100) Quasisubstraten. Die $GaP_{0.98}N_{0.02}$/Si(100) Oberfläche rekonstruiert analog zur GaP/Si(100) Oberfläche, wenn überschüssiger N vermieden wird. Die RA Spektren enthalten einen zusätzlichen Beitrag am E_1 Interbandübergang von GaP, welche dem Stickstoffeinbau zugeordnet wird. RAS eignet sich demnach hervorragend zur präzisen *in situ* Überwachung des gesamtem GaPN/Si(100) MOVPE Prozesses, von Si(100) Substratpräparation über GaP Nukleation bis zur finalen GaPN/Si(100) Oberflächenpräparation.

Abstract

Renewable and efficient generation of hydrogen is one of the key challenges towards a sustainable society being independent from fossil fuels. Tandem absorber structures based on dilute nitride GaPN/Si(100) are promising candidates regarding hydrogen evolution by direct solar water splitting. Challenges of industrially scalable device fabrication are inherently rooted in the complexity of growth processes in metalorganic vapor phase epitaxy (MOVPE) ambient and in the material system itself, particularly regarding specific preparation of the heterointerface. One reason is the different crystal structure of III-V semiconductors and of Si. Due to the small lattice mismatch, GaP/Si(100) structures are suitable as quasisubstrates. If these can be prepared with high crystal quality, subsequent integration of further III-V semiconductors will succeed more easily. In the present work, the atomic order of Si(100) and GaP(N)/Si(100) surfaces, as well as of the buried GaP/Si(100) heterointerface is studied *in situ* with reflection anisotropy spectroscopy (RAS). The influence of reactor residuals from previous III-V growth processes on the surface and interface formation is analyzed in dependence on the involved process conditions. RAS results are benchmarked to results from complementary surface science techniques in ultrahigh vacuum (UHV), such as low energy electron diffraction (LEED) and X-ray photoelectron spectroscopy (XPS).

A detailed understanding of the RA spectra enables *in situ* control of the formation of atomically differently ordered Si(100) surfaces and thereby of the desired structure of the GaP epilayer. Preparation of almost single-domain dimerized Si(100) surfaces succeeds in MOVPE ambient containing (Ga, P, As) background residuals. Antiphase disorder in III-V epilayers thus can be reliably suppressed. Charge compensation at the GaP/Si(100) heterointerface can be achieved by atomic intermixture with an equal number of Si–P and Si–Ga bonds. The formation energy for such compensated interfaces is predicted to be lower than for abrupt interfaces by density functional theory calculations. However, XPS measurements suggest a kinetically limited formation of a rather abrupt interface consisting of about one monolayer of Si–P bonds. An abrupt Si–P interface agrees also with the observed sublattice orientation of the GaP epilayer. Process conditions required for exactly oriented Si(100) surfaces promote diffusion of background residuals on the surface. The amount of sub-monolayer coverage of the substrate prior to nucleation strongly affects the formation of the interface and the structure of the GaP epilayer. Modification of the formerly monohydride-terminated Si(100) surface with As enables inversion of the GaP sublattice orientation. The corresponding GaP/Si(100) surfaces are also free of antiphase disorder. Moreover, the investigations reveal that the formation of atomically ordered GaP/Si(100) surfaces can already be initiated by pulsed GaP nucleation on Si(100) and subsequent annealing with phosphorus stabilization. Lattice-matched GaPN growth on these nucleated substrates succeeds as well as on pseudomorphically grown GaP/Si(100) quasisubstrates. $GaP_{0.98}N_{0.02}$/Si(100) surfaces reconstruct analogously to GaP/Si(100) surfaces, when excess N at the surface is avoided. The RA spectra contain an additional contribution at the E_1 interband transition of GaP, which is attributed to N incorporation. RAS thus is eminently suitable for precise *in situ* monitoring of the entire GaPN/Si(100) MOVPE processing from Si(100) substrate preparation over GaP nucleation to final GaPN/Si(100) surface preparation.

Preface

This work is part of a project with the long-term objective of renewable solar hydrogen generation with dilute nitride III-V/Si tandem absorber structures. Within that project, I closely collaborated with M. M. May, who mainly focused on the III-V:liquid interface and electrochemistry, as discussed in his thesis [181]. My work comprises *in situ* studies during Si(100) preparation in metalorganic vapor phase epitaxy (MOVPE) processing ambient, which contains III-V residuals, as well as on subsequent heterointerface preparation and GaP(N) growth. Our preliminary joint work on Si(100) and Ge(100) surfaces in III-V free ambient is discussed in detail in S. Brückner's thesis [41]. These results regarding "clean" Si(100), as well as related results obtained during my diploma thesis, will be summarized before the actual results and discussion chapters of this work. The structure of this work is as follows:

Chapter 1 contains the motivation for the following studies, introduces challenges and presents our experimental approach.

Chapter 2 comprises the theoretical background as well as a concise introduction to the main experimental techniques used for this work. The state of the art regarding MOVPE preparation of Si(100), GaP(100) and GaP/Si(100) surfaces applying *in situ* RAS is presented.

Chapter 3 opens the main part discussing GaP(100) reference surfaces. The focus is then on the atomic structure of GaP/Si(100) heterointerfaces and growth of GaP/Si(100) quasisubstrates, as well as the influence of residual (Ga, P) species and GaP growth on As-modified Si(100) surfaces.

Chapter 4 continues studying lattice-matched GaPN growth on Si(100) both *in situ* and *ex situ*.

Chapter 5 concludes on the main results and gives an outlook to future studies.

This work was supervised by Prof. Dr. R. Manzke at Humboldt-Universität zu Berlin and by Prof. Dr. T. Hannappel at Helmholtz-Zentrum Berlin for Materials and Energy (HZB) respectively Technische Universität (TU) Ilmenau, Germany. Experiments were first performed at HZB. During this work, the group and essential parts of the experimental setup, such as the MOVPE reactor, moved from HZB to TU Ilmenau. Additionally, we put a second MOVPE reactor and a ultrahigh vacuum-based surface science cluster in operation at TU Ilmenau.

Publications

Peer-reviewed journal articles:

1. Supplie, O.; May, M. M.; Höhn, C.; Stange, H.; Müller, A.; Kleinschmidt, P.; Brückner, S.; Hannappel, T.: *Formation of GaP/Si(100) heterointerfaces in presence of inherent reactor residuals.*
   submitted, 2015.
2. Supplie, O.; May, M. M.; Steinbach, G.; Romanyuk, O.; Grosse, F.; Nägelein, A.; Kleinschmidt, P.; Brückner, S.; Hannappel, T.: *Time-resolved in situ spectroscopy during formation of the GaP/Si(100) heterointerface.*
   Journal of Physical Chemistry Letters, **6**:464, 2015.
3. Supplie, O.; Brückner, S.; Romanyuk, O.; Döscher, H.; Höhn, C.; May, M. M.; Kleinschmidt, P.; Grosse, F.; Hannappel, T.: *Atomic scale analysis of the GaP/Si(100) heterointerface by in situ reflection anisotropy spectroscopy and ab initio density functional theory.*
   Physical Review B, **90**:235301, 2014.
4. Supplie, O.; May, M. M.; Stange, H.; Höhn, C.; Lewerenz, H.-J.; Hannappel, T.: *Materials for light-induced water splitting: In situ controlled surface preparation of GaPN epilayers grown lattice-matched on Si(100).*
   Journal of Applied Physics, **115**:113509, 2014.
5. Supplie, O.; Hannappel, T.; Pristovsek, M; Döscher, H.: *In situ access to the dielectric anisotropy of buried III-V/Si(100) heterointerfaces.*
   Physical Review B, **86**:035308, 2012.
6. Sippel P.; Supplie, O.; May, M. M.; Eichberger, R.; Hannappel, T.: *Electronic structures of GaP(100) surface reconstructions probed with two-photon photoemission spectroscopy.*
   Physical Review B, **89**:165312, 2014.
7. May, M. M.; Supplie, O.; Höhn, C.; van de Krol, R.; Lewerenz, H.-J.; Hannappel, T.: *The interface of GaP(100) and H_2O studied by photoemission and reflection anisotropy spectroscopy.*
   New Journal of Physics, **15**:103003, 2013.

8. Döscher, H.; Supplie, O.; May, M. M.; Sippel, P.; Heine, C.; Muñoz, A. G.; Eichberger, R.; Lewerenz, H.-J.; Hannappel, T.: *Epitaxial III-V Films and Surfaces for Photoelectrocatalysis.*
ChemPhysChem, **13**:2899, 2012.

9. Brückner, S.; Supplie, O.; Barrigón, E.; J. Luczak, Kleinschmidt, P.; Rey-Stolle, I; Döscher, H.; Hannappel, T.: *In situ control of As dimer orientation on Ge(100) surfaces.*
Applied Physics Letters, **101**:121602, 2012.

10. Brückner, S.; Döscher, H.; Kleinschmidt, P.; Supplie, O.; Dobrich, A.; Hannappel, T.: *Anomalous double-layer step formation on Si(100) in hydrogen process ambient.*
Physical Review B, **86**:195310, 2012.

11. Brückner, S.; Kleinschmidt, P.; Supplie, O.; Döscher, H.; Hannappel, T.: *Domain-sensitive in situ observation of layer-by-layer removal at Si(100) in H_2 ambient.*
New Journal of Physics, **15**:113049, 2013.

12. Barrigón, E.; Brückner, S.; Supplie, O.; Kleinschmidt, P.; Rey-Stolle, I.; Hannappel, T.: *Optical in situ monitoring of hydrogen desorption from Ge(100) surfaces.*
Applied Physics Letters, **102**:111608, 2013.

13. Brückner, S.; Barrigón, E.; Supplie, O.; Kleinschmidt, P.; Dobrich, A.; C. Löbbel, I. Rey-Stolle, Döscher, H.; Hannappel, T.: *Ge(100) surfaces prepared in vapor phase epitaxy process ambient.*
Physica Status Solidi—Rapid Research Letters, **6**:178, 2012.

14. Barrigón, E.; Brückner, S.; Supplie, O.; Döscher, H.; Rey-Stolle, I; Hannappel, T.: *In situ study of Ge(100) surfaces with tertiarybutylphosphine supply in vapor phase epitaxy ambient.*
Journal of Crystal Growth, **370**:173, 2013.

15. Paszuk, A.; Brückner, S.; Steidl, M.; Zhao, W.; Dobrich, A.; Supplie, O.; Kleinschmidt, P.; Prost, W.; Hannappel, T.: *Controlling the polarity of MOVPE-grown GaP on Si(111) for subsequent III-V nanowire growth.*
submitted, 2015.

Other publications:

16. Supplie, O.; Brückner, S.; May, M. M.; Dobrich, A.; Kleinschmidt, P.; Hannappel, T.: *Watching growth—In situ control of III-V/Si(100) heteroepitaxy on the atomic level.*
Compound Semiconductor Magazine, accepted, 2015.

17. Brückner, S.; Döscher, H.; Hannappel, T; Kleinschmidt, P.; Dobrich, A.; Supplie, O.: *Verfahren zur Oberflächenpräparation von Si(100)-Substraten.* DE/30.12.11/DEA102011122749, (pub. 03.07.2013, reg. 21.12.2012, priority 30.12.2011). European Patent 12008516.2 - 1362.

Contributions to international conferences:

(a) Selected conference proceeding articles

18. Supplie, O.; Brückner, S.; Romanyuk, O.; May, M. M.; Döscher, H.; Kleinschmidt, P.; Stange, H.; Dobrich, A.; Höhn, C.; Lewerenz, H.-J.; Grosse, F.; Hannappel, T.: *An experimental-theoretical atomic-scale study–In situ analysis of III-V on Si(100) growth for hybrid solar cells.* IEEE Photovoltaic Specialists Conference, **40**:2707, 2014. *40th IEEE Photovoltaic Specialists Conference (PVSC-40), Denver (USA), 2014.*
19. Supplie, O.; Brückner, S.; Döscher, H.; Kleinschmidt, P.; Hannappel, T.: *III-V/Si(100) heterointerfaces studied in VPE ambient via surface dimers by in situ reflection anisotropy spectroscopy.* IEEE Photovoltaic Specialists Conference, **39**:879, 2013. *39th IEEE Photovoltaic Specialists Conference (PVSC-39), Tampa (USA), 2013.*
20. Supplie, O.; Döscher, H.; May, M. M.; Hannappel, T.: *Heteroepitaxial III-V on Si(100) tandem absorber structures for photoelectrolysis.* AIP Conference Proceedings, **1568**:20, 2013. *1st International Workshop on Solar Chemical Energy Storage (SolChES-1), Sendai (Japan), 2012.*

(b) Selected oral presentations

- *E-MRS—Fall Meeting 2014 of the European Materials Research Society, Symposium J.* Warsaw, Poland (09/15/2014 – 09/18/2014).
  Supplie, O.; Brückner, S.; Kleinschmidt, P.; Romanyuk, O.; Döscher, H.; May, M. M.; C. Höhn, Grosse, F.; Hannappel, T.: *The atomic structure of GaP/Si(100) heterointerfaces studied with ab initio DFT and in situ RAS.*
  Awarded the *Best student oral presentation* of the symposium.

- *IPS 20—International Conference on Conversion and Storage of Solar Energy.* Berlin, Germany (07/27/2014 – 08/01/2014).
  Supplie, O.; May, M. M.; Stange, H.; Brückner, S.; Höhn, C.; Lewerenz, H.-J.; Hannappel, T.: *Growth and surface preparation of single-domain GaPN epilayers on Si(100) studied in situ with optical spectroscopy during vapor phase epitaxy.*
- *OSI 10—International Conference on Optics of Surfaces and Interfaces.* Chemnitz, Germany (09/08/2013 – 09/13/2013).
  Supplie, O.; Brückner, S.; Döscher, H.; Kleinschmidt, P.; Hannappel, T.: *Correlating in situ RA spectra of surface dimers to study bonds at III-V/Si(100) heterointerfaces.*
- *ECOSS 29—European Conference on Surface Science.* Edinburgh, Scotland (09/03/2012 – 09/07/2012).
  Supplie, O.; Brückner, S.; Barrigón, E.; Luczak, J.; Kleinschmidt, P.; Rey-Stolle, I.; Döscher, H.; Hannappel, T.: *Directing arsenic dimers on vicinal Ge(100).*

(c) Selected poster presentations

- *ICMOVPE 17—International Conference on Metalorganic Vapor Phase Epitaxy.* Lausanne, Switzerland (07/13/2014 – 07/18/2014).
  Supplie, O.; May, M. M.; Brückner, S.; Romanyuk, O.; Stange, H.; Kleinschmidt, P.; C. Höhn, Döscher, H.; Grosse, F.; Lewerenz, H.-J.; Hannappel, T.: *Dilute nitride GaPN growth on Si(100) studied in situ with RAS.*
- *EUPVSEC 27—European PV Solar Energy Conference.* Frankfurt, Germany (09/25/2012 – 09/28/2012).
  Supplie, O.; Brückner, S.; Barrigón, E.; Kleinschmidt, P.; Luczak, J.; Löbbel, C.; Dobrich, A.; Rey-Stolle, I.; Döscher, H.; Hannappel, T.: *Monohydride and arsenic terminated Ge(100): In situ control over the surface preparation in vapor phase epitaxy ambient.*
- *5th Gerischer Symposium—Photoelectrochemistry: From Fundamentals to Solar Applications.* Berlin, Germany (06/22/2011 – 06/24/2011).
  Supplie, O.; May, M. M.; Bischler, R.; Fiechter, S.; Lewerenz, H.-J.; Döscher, H.; Hannappel, T.: *In situ investigation of MOVPE prepared GaP/Si(100) for photoelectrocatalysis.*
- *EWMOVPE 14—European Workshop on Metalorganic Vapor Phase Epitaxy.* Wroclaw, Poland (06/05/2011 – 06/08/2011).
  Supplie, O.; Döscher, H.; Brückner, S.; Dobrich, A.; Kleinschmidt, P.; Hannappel, T.: *Modeling in situ Reflectance Anisotropy Spectra of MOVPE-prepared GaP/Si(100).*

Contents

1

Introduction

Photovoltaics today has become a competitive, renewable source of electric power. Single-junction solar cell modules with solar conversion efficiencies beyond 20 % are commercially available for rooftop power plants, and high-efficiency, concentrating photovoltaics has entered the market for terrestrial applications [207]. The levelized cost of electricity for solar power generation in many European countries has already reached grid parity or will reach it within this decennium [36]. Towards a renewable economy, which is liberated of the dependence on fossil fuels, however, it is essential to become independent of the intermittence of solar irradiance. Moreover, heating and mobility applications, which even have a higher share in burning fossil fuels compared to generation of electric power, must be considered to effectively curtail climate change. Photoelectrolysis may be the key to solve both issues: The energy which is stored in molecular hydrogen bonds can be converted on demand by fuel cells generating electricity. Furthermore, hydrogen can be converted into methanol or synthetic hydrocarbons, which may be burned instead of fossil fuels, ideally within a sustainable anthropogenic carbon cycle [200].

Splitting water into hydrogen and oxygen requires to overcome the redox potential of water. In principle, any power source, be it solar, wind, water, nuclear or fossil, may be connected to electrodes, as done in large-scale electrolyzers, which currently are tested in the field. Directly utilizing the photovoltage generated by a solar cell immersed into water, however, could reduce cost as well as the need for huge amounts of noble metals. This approach would also facilitate decentralized application. Besides stability and adequate electronic band alignment in such a wireless water splitting device, sufficient solar-to-hydrogen conversion efficiency is a big issue for reasonable cost, which is targeted 5.50 € / kg H_2 in 2025 by the European Union. Already the photovoltaic solar energy conversion of a single-junction solar cell is limited to about 30 % for ideal bandgaps roughly ranging between Si and GaAs with 1.12 and 1.42 eV, respectively, within the detailed balance-limit by Shockley and Queisser at room temperature [237]. Including overpotentials, which are required to drive the chemical reaction, a photovoltage of about 1.8 V must be generated to split water [136]. To obtain this with a realistic single junction absorber, the required bandgap will be larger than 2 eV. Consequently, transmission losses will limit conversion efficiency as photons with energies below the bandgap will not be absorbed generating electron-hole pairs. Multi-junction absorbers, where subcells with different bandgaps are stacked on top of each other, enable efficiencies beyond the single-junction Shockley-Queisser limit: Light that is transmitted by a preceding subcell can be absorbed by the subsequent one. Combining three and more junctions, photovoltaic conversion efficiencies above 44 % at concentrated sunlight have already been certified [68, 112]. In ideal serious connection of the subcells, for example via a tunnel diode, the current is limited by the subcell generating the least photocurrent while generated photovoltages add. Tandem absorber structures thus are highly feasible for photoelectrolysis to obtain both the minimum voltage and a high absorption efficiency.

High-efficiency multi-junction solar cells today are based on III-V semiconductors. Precise control of the stoichiometry of multinary III-V compounds enables to tune their bandgap and lattice constant over a wide range. Many of these III-V compounds are direct semiconductors with high carrier mobilities and excellent optoelectronic properties. Epitaxial growth on a substrate with identical lattice constant is very beneficial for high quality material, which accounts for GaInP/GaAs/Ge(100) triple junction solar cells as industry standard. Germanium, however, is a rather expensive substrate and the conversion efficiency would greatly benefit from a 1 eV bandgap bottom cell. A substrate with such a bandgap would be also the optimum choice for a tandem absorber for direct solar water splitting [126]. Silicon promises an almost ideal bandgap, exhibits suitable material properties, is very abundant, about ten times cheaper than Germanium and benefits from a mature technology. Alongside photovoltaics, the combination of III-V and Si(100) is highly desired also in opto- and microelectronics [3]. The transition from the non-polar Si(100) substrate to polar III-V epilayers, however, proved to be challenging [156]. It is complicated by lattice mismatch and different thermal expansion coefficients. Of all classical III-V compounds, Galliumphosphide features the smallest lattice mismatch to Si and can be grown pseudomorphic up to a thickness of a few tens of nanometers. Defect-free GaP/Si(100) quasisubstrates, where the non-polar to polar transition was successfully overcome, thus are suitable for further generic III-V integration. This may involve either grading towards higher lattice constants or lattice-matched growth of nitrogen-diluted III-V compounds, depending on the device of interest. The desired bandgap of 1.6 to 1.9 eV for the top cell of a Si-based tandem absorber for photoelectrolysis, for example, can be reached lattice-matched by GaPNAs compounds.

The GaP/Si(100) quasisubstrates are in focus of the present work. An adequate preparation of the GaP/Si(100) heterointerface is crucial to minimize defect formation during subsequent growth. The atomic structure of the heterointerface and the dependence of its formation on processing parameters is an open question that will be tackled here. In principle, metalorganic vapor phase epitaxy (MOVPE) enables growth of high-quality III-V epilayers at industrially relevant scale. The involved processes are highly complex due to the presence of a process gas and precursors interacting with the growth surfaces. Kinetically or energetically driven reactions may counteract each other and residual III-V species from previous processes impact the growth process. Electron-based *in situ* techniques, which are established in ultrahigh vacuum (UHV), cannot be applied in MOVPE ambient due to the comparably high pressures ranging from 50 to 950 mbar. For cubic crystals, which are investigated here, reflection anisotropy spectroscopy (RAS) is a very surface sensitive optical probe [15]. RA spectra can contain rich information about the probed samples. The lineshape, however, is often complex and a detailed understanding of the spectral features requires benchmarking to complementary techniques. In this work, a dedicated MOVPE-to-UHV transfer system [119] enables contamination-free transfer of the MOVPE-prepared surfaces to UHV, where electron-based surface science techniques can be applied for benchmarking the *in situ* spectra. As RAS is

applicable also in UHV, the state of the surface can be checked during further *in vacuo* analysis.

The MOVPE preparation of the GaP/Si(100) heterointerface and its atomic structure will be studied for different conditions in realistic processing ambient. *In situ* RAS, in combination with X-ray photoelectron spectroscopy (XPS) for chemical analysis and low energy electron diffraction (LEED) for the atomic order at the prepared surfaces, will be correlated to theoretical modeling. Depending on the misorientation of the substrate and its atomic termination, single-domain GaP epilayers with both types of sublattice orientation can be prepared. The structure of the heterointerface is found to depend on the kinetics and chemical ambient during nucleation. Regarding consecutive GaPNAs growth, incorporation of nitrogen into GaP is known to drastically deteriorate material quality. *In situ* signals of GaPN/Si(100) surfaces will therefore be established focusing on the influence of N on the GaP/Si(100) surface preparation.

2

Theoretical and experimental background

In the following, the principles of the two applications, which are the main motivation for studying GaP/Si(100) growth in this work, will be briefly discussed: High-efficiency multi-junction solar cells and their application for direct solar water splitting. Basics regarding III-V/Si(100) heteroepitaxy, the involved crystal structures and surfaces will be summarized. Properties of dilute nitride GaPN and previous work on GaP nucleation on Si(100) will be succinctly reviewed. Afterwards, the main experimental techniques are introduced with focus on metalorganic vapor phase epitaxy and reflection anisotropy spectroscopy. Subsequently, preliminary work on in situ controlled preparation of Si(100), GaP(100), and GaP/Si(100) surfaces in MOVPE ambient will be summarized as the basis where this work follows up on.

2.1 III-V/Si(100) heteroepitaxy—Advantages and challenges

Advantages

Combining III-V semiconductors to ternary or multinary compounds allows for tuning both bandgaps, E_g, and lattice constants, a, of III-V semiconductors over a wide range, as shown in Fig. 2.1. Many III-V semiconductors are direct materials and exhibit excellent optoelectronic properties, such as high carrier mobilities. Today's world record solar cells are based on III-V semiconductors [68, 296], as well as light emitting diodes (LEDs) [155], lasers [154, 170, 196] or integrated waveguides. Also future nanometer-scaled electronics may rely on III-V semiconductors [3]. Silicon, on the other hand, is probably the most established material in semiconductor industry, it is abundant, mechanically stable, and cheap.

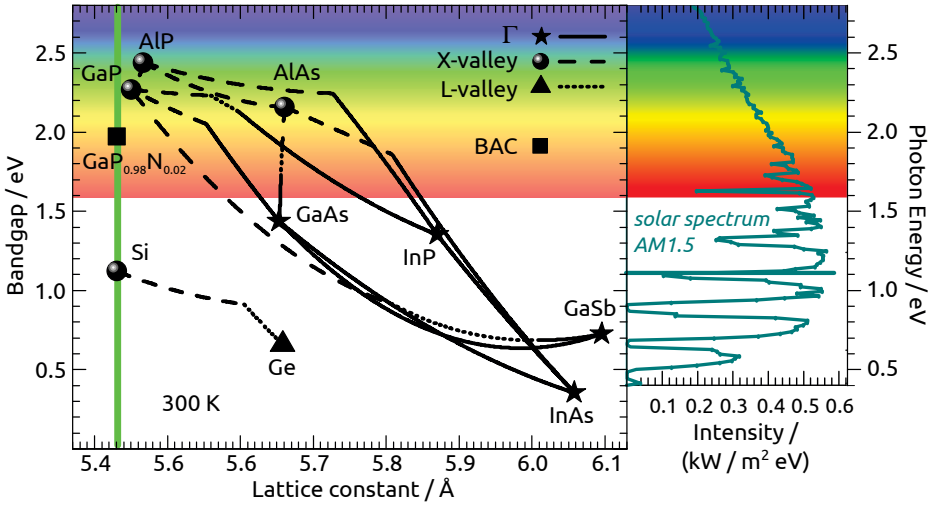

Fig. 2.1 – Bandgap of binary (symbols) and ternary (lines) III-V compounds, as well as Si and Ge, as a function of lattice constant at room temperature ("world map"). Direct and indirect bandgaps are indicated by the style of the line resp. symbol (see legend). Bandgaps and bowing parameters are taken from Vurgaftman et al.[281, 282] assuming Vegard's law [277] for the lattice constants. The curve on the right shows the standard AM1.5 ASTM-G-173-03 solar spectrum [5]. The vertical green line indicates lattice-matching to Si.

Regarding photovoltaics (PV), the maximum efficiency for a single-junction solar cell of about 30 % under non-concentrated sunlight in the detailed balance limit [237] depends particularly on balancing transmission and thermalization losses. Photons with energies lower than E_g are not absorbed, while photo-generated electron-hole-pairs relax to the band edges at picosecond timescale due to electron-phonon-

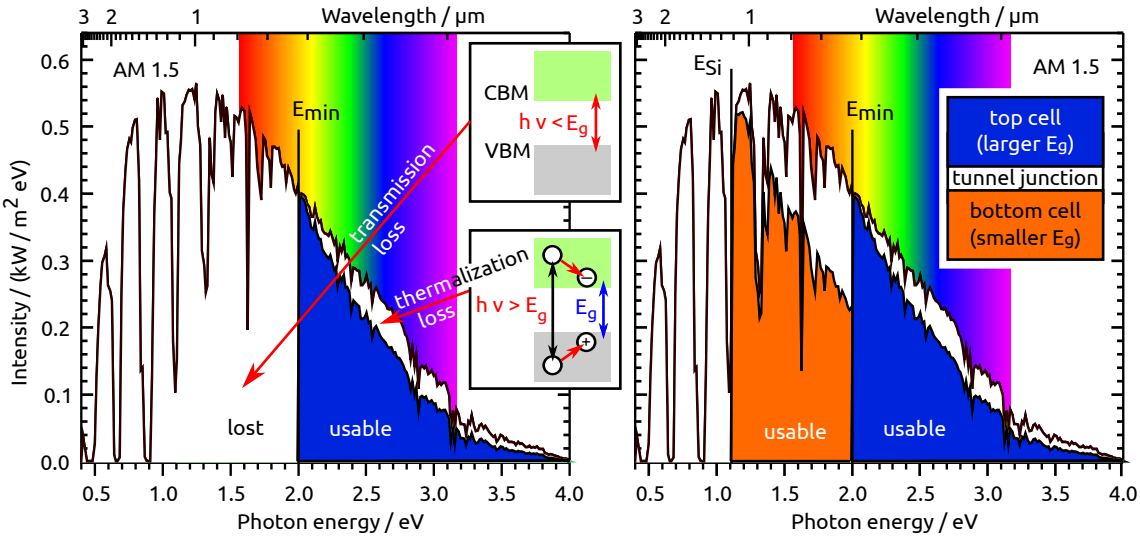

Fig. 2.2 – (left) Solar spectrum (black line) and convertible energy (blue area) upon absorption for a single absorber with $E_g = 2\,\text{eV}$. Transmission and thermalization losses (see insets) occur in the white areas. *(right)* Both loss mechanisms can be reduced in a tandem absorber structure. The solar spectrum refers to the AM1.5 ASTM-G-173-03 standard [5].

interaction [110]. Figure 2.2(a) exemplifies the losses for a 2 eV absorber (which would be of interest for a single-junction photochemical diode for direct photolysis, see section 2.8) and the ASTM-G-173-03 reference solar spectrum at air mass (AM) 1.5 [5]. While reducing the bandgap decreases the transmission loss, thermalization loss will increase. Serious connection of multiple solar cells with different bandgaps to multi-junction solar cells, in contrast, leads to reduced losses, since the light transmitted by the top cell can be absorbed by the subjacent cell (see Fig. 2.2(b)). Triple- and quadruple-junction III-V solar cells, interconnected with tunnel-junctions, currently reach solar conversion efficiencies beyond 40 % at concentrated sunlight [68, 112]. An infinite number of absorbers theoretically enables the thermodynamic efficiency limit of 85 % at AM 1.5 [61, 177]. Multi-junction solar cells are more expensive and were applied mostly in space applications for a long time. Concentrating photovoltaics (CPV), however, enables reduced costs per kWh by both increased solar conversion efficiencies and large decrease in material consumption. Advances in cheap focusing lenses and trackers make terrestrial CPV with multi-junction solar cells today feasible [207].

Figure 2.3 on the next page shows limiting efficiencies, which were calculated within the current-matched detailed balance limit (using the software *EtaOpt* [168]), as a function of the involved bandgap energies [84]. A material with a bandgap of about 1 eV promises optimum efficiencies for tandem solar cells. The desired top absorber with a bandgap of about 1.7 eV could be based on dilute nitride III-V semiconductors lattice-matched to Si, or other III-V compounds involving graded buffer layers to reach higher lattice constants. GaPN/Si tandem absorber structures

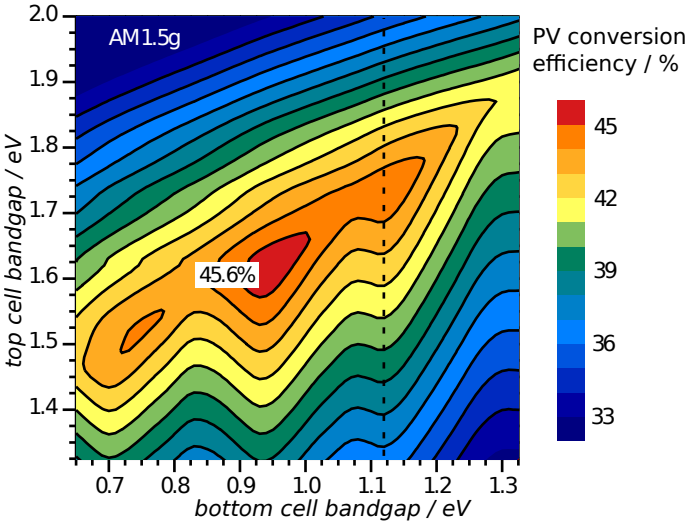

Fig. 2.3 – Tandem absorber solar conversion efficiencies (color coded) as function of the top and bototm cell bandgap energies, calculated with [168] in the current matched detailed balance limit for solar AM1.5g irradiation at room temperature. The dashed black line indicates E_g of Si.

are also promising for direct solar water splitting, as will be discussed in section 2.8. In triple-junction GaInP/GaInAs/Ge solar cells, such a 1 eV absorber would yield a better current matching. InGaNAs is promising [100, 161] as additional subcell, but no such 1 eV substrate exists on the lattice constant of GaAs (cf. Fig. 2.1 on page 6). Silicon and InP, in contrast, would be suitable. InP, however, is expensive compared to Ge. Si, in contrast, is about ten times cheaper than Ge. Further advantages of Si are its abundance and the mature technology.

Challenges

As obvious from Fig. 2.1 on page 6, none of the "classic" III-V compounds (i.e. excluding nitrides) is lattice-matched to Si. Strain thus accumulates during growth and misfit dislocations form after reaching a critical thickness [179, 187]. Threading dislocations [178] deteriorate device efficiency and must be avoided in active materials. The lattice constant of Si at room temperature is 5.43 Å [269] and that of GaP 5.45 Å [282]. Consequently, the lattice mismatch at room temperature is 0.37 %. GaP can therefore be grown pseudomorphic up to a critical thickness of about $70 - 80$ nm, which makes GaP/Si(100) a promising quasisubstrate. Further III-V integration may be achieved with lattice-matched growth of dilute nitride III-V compounds, such as GaPNAs [103, 170] (see section 2.7), or stepwise grading towards higher lattice constants [101, 216].

Other challenges include different thermal expansion coefficients, which can lead to cracks during cooling from growth temperature [260, 297]. Atomic interdiffusion between silicon and the III-V epilayer can cause cross-doping in both direction across the heterointerface. The heterointerface may introduce defects such as stacking faults or twins.

Basic problems are related to the different crystal structures, as polar III-V compounds are grown on nonpolar Si(100) substrates. In polar-on-nonpolar epitaxy,

charge compensation at the interface is an issue. Moreover, steps at zincblende(100) surfaces exhibit heights of even multiples of a biatomic layer, while diamond(100) surfaces can also show steps of monatomic height. In consequence, monatomic steps (or odd multiples) induce antiphase disorder in the III-V epilayers [88, 156]. Antiphase disorder, which needs to be avoided since antiphase boundaries may act as non-radiative recombination centers degrading device efficiency, will be discussed in section 2.4.

This works aims at resolving the atomic structure of the crucial heterointerface between GaP and Si(100) and its formation in MOVPE ambient. Also, RA spectra of GaPN/Si(100) surfaces grown lattice-matched on Si(100), which are required for *in situ* control, will be established.

2.2 Crystal and band structures of GaP and Si

Figure 2.4 on page 11 shows the crystal structures of silicon (diamond lattice[1]) and the zincblende lattice[2], which is typical for III-V compounds studied in this work. The diamond lattice corresponds to an fcc lattice with a biatomic base, where the second atom is moved 1/4 along the space diagonal of the unit cell (i.e. two interpenetrating fcc sublattices, whereof one is displaced 1/4 along the space diagonal). In a III-V zincblende structure, one of the two fcc sublattices is occupied by group-III atoms and the other one by group V-atoms. Every group-III atom is covalently bond to four group-V atoms in tetrahedral coordination.

The band structures of GaP and Si are shown in Fig. 2.5 on page 11 according to [208, 214, 302]. GaP and Si are both indirect semiconductors with band gap energies of 2.26 eV and 1.12 eV, respectively, at room temperature. The optical *in situ* signals, which will be discussed in this work, often show characteristic features at the critical point energies (CPE), which are marked in Fig. 2.5. The density of states (DOS) may be expressed as surface integral over a sphere S of constant energy in reciprocal $\vec{k}$ space [186],

$$\mathrm{DOS} = \frac{1}{(2\pi)^3} \int\limits_{E=\mathrm{const}} \frac{1}{\left|\nabla_{\vec{k}} E(\vec{k})\right|} \,\mathrm{d}S \quad , \tag{2.1}$$

which is large at local extrema in the band structure, where $|\nabla_{\vec{k}} E(\vec{k})|$ is small (van-Hove singularities). CPEs are electronic interband transitions, where $|\nabla_{\vec{k}} E(\vec{k})|$ is small both for valence and conduction bands, which yields a high joint density of states (JDOS). The indices 0, 1, 2 denote transitions at Γ, along Λ, and along Δ,

[1] Space group $Fd\bar{3}m$, hexakisoctahedral (cubic).
[2] Space group $F\bar{4}3m$, hexakistetrahedral (cubic).

respectively (cf. Brillouin zone in Fig. 2.5(c)). For silicon, the E_2 transition along Σ direction is about 250 meV larger than $E_2(X)$ (at room temperature). Transition into upper bands are assigned $^{|}$ and $+\Delta$ corresponds to the spin-orbit offset. The dependence of the CPEs for GaP [310] and Si [165] on absolute temperature T were published by Cardona et al.

2.3 Si(100) surfaces

Monohydride-terminated Si(100) surfaces

The step structure and atomic structure of the Si(100) surface is highly important for subsequent III-V heteroepitaxy. Silicon crystallizes in diamond lattice structure, where (100) surface cuts would lead to two dangling bonds per Si atom. In UHV, the Si(100) surface reconstructs forming dimers to reduce the number of dangling bonds [223] and buckling of the dimers further reduces the surface energy [272, 291]. Exposure to atomic hydrogen in UHV passivates the surface, where both monohydride, dihydride and mixed phases form dependent on temperature and chemical potential of hydrogen [31, 50, 198]. Significant adsorption of molecular hydrogen requires higher temperatures due to the small sticking coefficient at room temperature [152]. Symmetric monohydride-terminated Si dimers, where each Si atom is bond to one H atom, form upon thermal annealing in H_2 ambient [6, 25, 153]. The coverage of H depends on the adsorption and desorption rates and thus on the partial pressure of H_2 and temperature [46, 153].

Figure 2.6 on page 12 depicts different monohydride-terminated Si(100) surfaces, which differ in dimer orientation with reference to the step edges. Due to the tetrahedral coordination in the diamond lattice structure, the Si bond orientation in (100) projection is rotating by 90° for every subjacent layer along [100] direction. This causes domains of mutually perpendicular dimer orientations on adjacent terraces separated by single-layer steps of atomic step height, while all dimers at the terraces are aligned in parallel at double-layer stepped surfaces.[3] Sticking to the notation of Chadi [52], (1×2) domains with dimers oriented perpendicularly to the step edge (i.e. with dimer rows parallel to the step edge) will be denoted A-type respectively T_A terraces throughout this work.[4] (2×1) domains consist of dimers oriented in parallel to the step edge (i.e. dimer rows perpendicular to the step edge) and are denoted B-type respectively T_B terraces. The notation for single-layer steps, $S_{A,B}$, and double-layer steps, $D_{A,B}$, refers to the upper terrace. Figure 2.6 on page 12 sketches this for S_A (upper left box), S_B (bottom left box), D_A (upper right

[3] More generally, this is true for odd respectively even numbered atomic step heights.

[4] The notation in this work always refers the terrace types to the step edges along $[0\bar{1}1]$ given by a well-defined misorientation of $X°$ towards [011] direction.

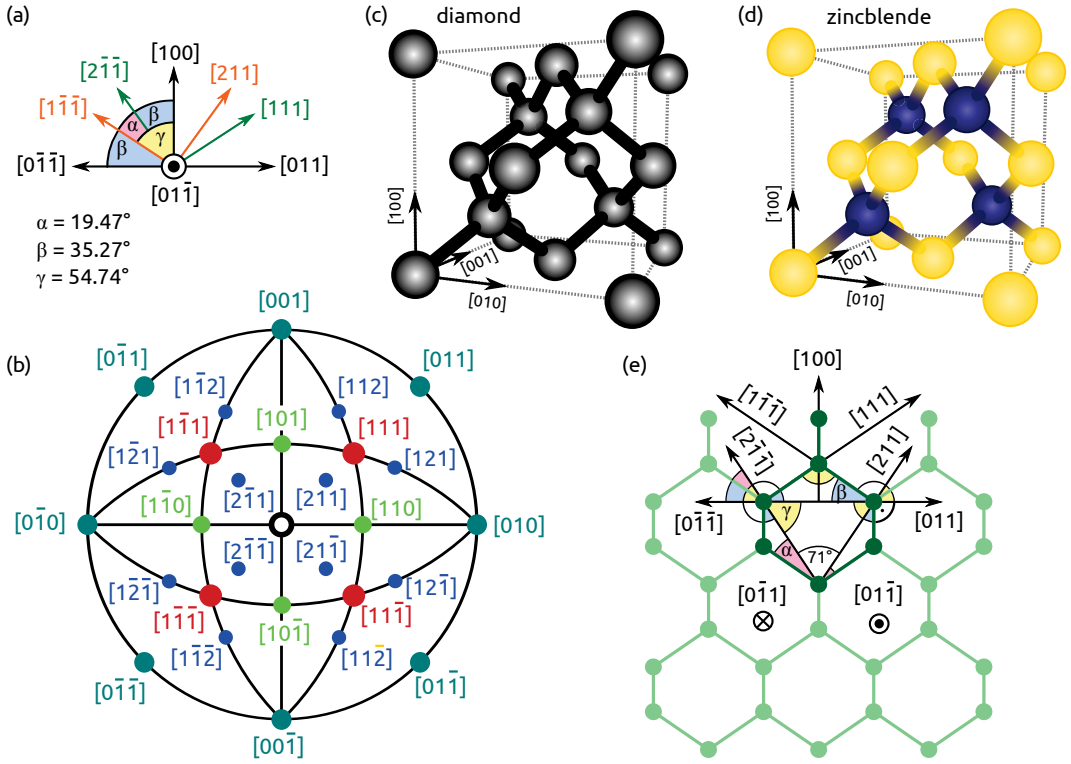

Fig. 2.4 – (a) Crystal directions and their angles. (b) Stereographic Wulff projection in [100] direction. (c) Unit cell of a diamond lattice. (d) Unit cell of a zincblende lattice. (e) Side view of the diamond lattice.

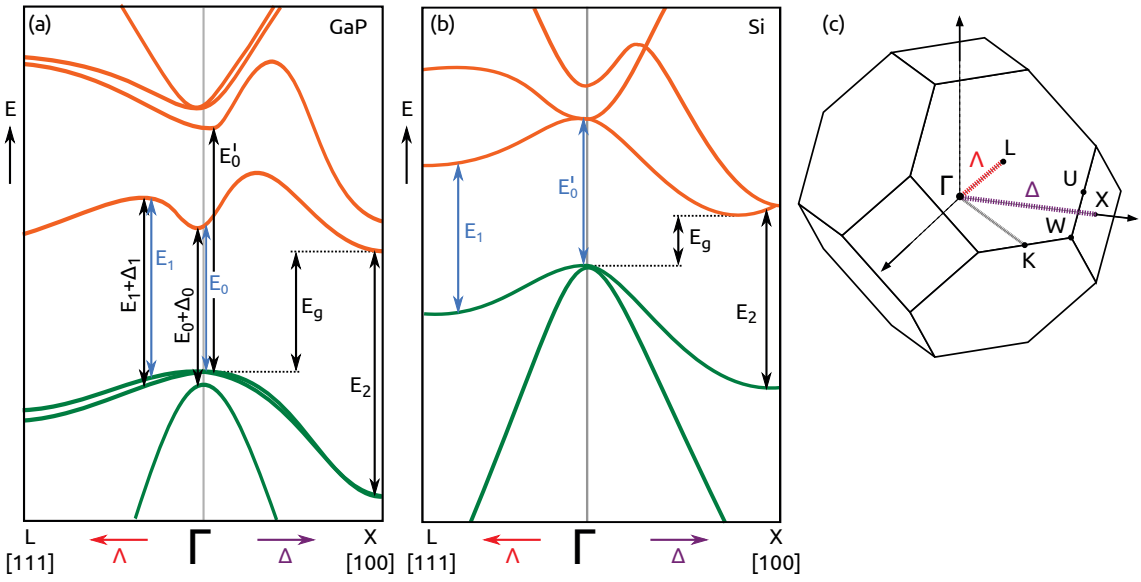

Fig. 2.5 – (a) Conduction (orange) and valence band (green) structure of GaP (after [302] resp. [208]). (b) Conduction band (orange) and valence band (green) structure of Si (after [214]). Note that a spin-orbit offset of 44 meV for Si is included but too small to be resolved [214]. (c) First Brillouin zone of the fcc lattice (after [129]).

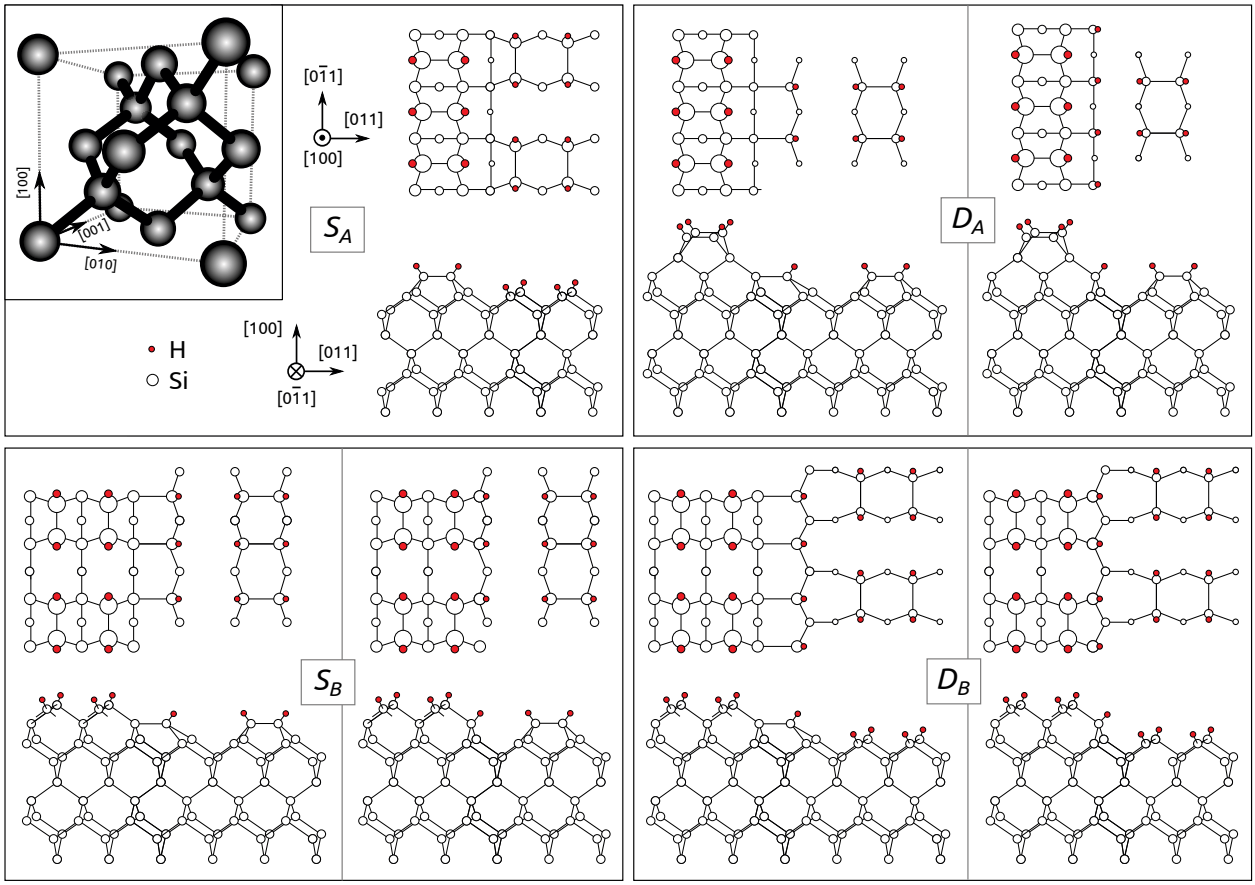

Fig. 2.6 – Step and terrace types at monohydride-terminated Si(100) surfaces misoriented towards [011] (modified after Chadi [52]). *(upper left box)* S_A step structure. *(bottom left box)* S_B step structure. *(upper right box)* D_A step structure. *(bottom right box)* D_B step structure. Within the boxes, left and right columns depict the rebonded and non-rebonded configuration, respectively. Top and bottom rows within the boxes show the top and side views, respectively. Si atoms are drawn empty and H in red. The unit cell of the diamond lattice is shown in the inset of the upper left box.

box), and D_B (bottom right box) steps, where the top view is always shown on top of the side view. Structures shown left within the boxes depict rebonded step edges and structures shown right non-rebonded step edges.

In UHV, biatomic B-type steps were observed at Si(100) misoriented towards [011] upon annealing in agreement with theory, where they were predicted to be energetically favored [13, 50, 52, 209, 259]. D_A steps are energetically least favored in UHV [52], but have been prepared by applying additional driving forces such as electric currents [72], external stress [185] or ion bombardment [23, 258].

The Si(100) surfaces prepared in H_2-based MOVPE ambient for this work exhibit monohydride termination: After contamination-free transfer [119] of our samples from MOVPE to UHV, Dobrich et al.[70, 71, 77] confirmed the existence of

absorption bands related to coupled stretch modes of monohydride Si-H [49, 51] with Fourier-transform infrared spectroscopy (FTIR) in total attenuation reflection (ATR) mode. Tip-induced H desorption by scanning tunneling microscopy (STM) [31] proofed complete hydrogen coverage [77]. On vicinal Si(100), *in situ* reflection anisotropy spectroscopy showed that Si(100) is terminated by monohydrides at temperatures $\lesssim 800\,^{\circ}\mathrm{C}$ during cooling from $1000\,^{\circ}\mathrm{C}$ in 950 mbar H_2 [41, 43].

Hydrogen highly impacts the step formation: Non-rebonded single-layer steps at monohydride-terminated Si(100), which lead to two-domain surfaces, were predicted to be energetically favored [135, 212]. STM studies of Si(100) surfaces prepared in UHV in presence of atomic H confirmed this prediction for nominal and vicinal Si(100) surfaces with misorientations up to 7° towards [011] direction [163]. Annealing in H_2 ambient, in contrast, was found to promote biatomic steps by a retreat of S_A steps [148]. Early experiments by Olson et al.[201] report on APD-free GaP growth on Si(100) with 2° misorientation in hydrogen-based MOVPE ambient. Such a preference for double-layer steps of unspecified type was also observed for nominal Si(100) surfaces [28, 159]. Though first studies at our labs indicated two-domain Si(100) surfaces after preparation in MOVPE ambient with H_2 as process gas [80], quantitative Fourier-transformed infrared spectroscopy (FTIR) studies revealed a domain imbalance towards T_A after slow cooling in H_2 [71], i.e. the energetically least favored case. These results suggest that kinetic processes, and therefore process routes, highly impact the Si(100) surface formation in hydrogen ambient, which in turn cannot be sufficiently described by energetic considerations alone. Indeed, a dynamic equilibrium of continuous adsorption and desorption of H takes place at relevant processing temperatures above about $700\,^{\circ}\mathrm{C}$ [43, 77, 153]. The implications for Si(100) surface preparation in MOVPE ambient will be discussed in section 2.10.1.

As-terminated Si(100) surfaces

In UHV, it is known that As_4 highly impacts the atomic order at clean Si(100) surfaces which, in turn, influences subsequent GaAs heteroepitaxy [38]. Depending on processing routes, As dimers were found either additive or replacive with respect to the Si dimers of the As-free surfaces. Both predominantly (1×2) and (2×1) reconstructed surfaces could be achieved [147]. As consequence, the sublattice orientation of subsequently grown GaAs can be inverted [38]. In contrast to background As_x, both arsine (AsH_3) and tertiarybutylarsine (TBAs) were found to etch Si(100) surfaces in MOVPE ambient [32, 118, 184]. Supply of TBAs or AsH_3 during thermal deoxidation of the Si substrate, was found to decrease the required temperatures below $900\,^{\circ}\mathrm{C}$ [32, 118, 184]. TBAs annealed Si(100) in MOVPE ambient showed a two-domain surface structure [32].

2.4 Antiphase disorder

Single-layer steps at the Si(100) substrate inherently introduce antiphase disorder in III-V epilayers [88, 156], as illustrated in Fig. 2.7. The antiphase domains (APDs) exhibit an inverted sublattice and are separated by antiphase boundaries (APBs). APBs, which are characterized by homopolar bonds between Ga–Ga or P–P atoms, may either propagate in growth direction or kink. If two kinked APBs meet, they can annihilate [139, 194, 261]. Németh et al.[194] showed that the growth temperature highly influences the kinking of the ABPs in MOVPE ambient and that temperatures in the range of 575 °C are beneficial for a kinking from {011} planes towards {111} planes and subsequent self-annihilation. Single-domain Si(100) substrates, however, avoid antiphase disorder from the beginning: At step edges of even numbered atomic height, the GaP bilayer can grow with one single domain as shown for a D_A step in Fig. 2.7. Si surface preparation in hydrogen-based MOVPE ambient will be discussed in section 2.10.1.

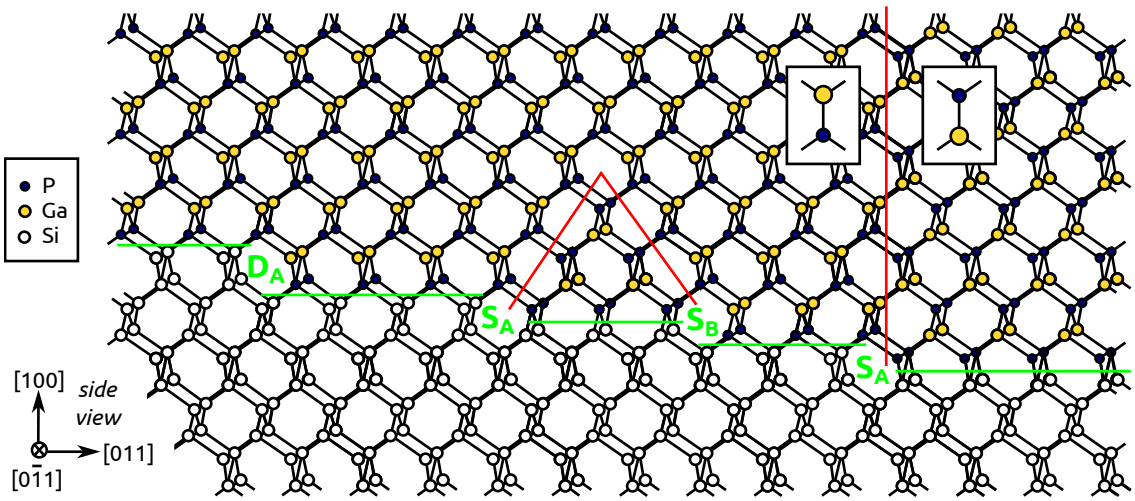

Fig. 2.7 – Antiphase disorder emerges at single-layer steps at the Si(100) substrate (the interface is marked by the green line). Antiphase boundaries (red lines) may propagate straight in growth direction or kink and annihilate [139, 194]. Note that the terrace width is drawn arbitrarily here and Si-P bonds are assumed at the interface (modified after [194]).

Quantification of APDs was achieved, for example, by high-resolution transmission electron microscopy (TEM) [27, 108, 309], X-ray scattering [88] and synchrotron-based XRD [265], as well as Raman spectroscopy [90]. The decreased binding energy of the APBs also enables preferential etching, either chemical [275] or by thermal annealing [79, 193], so that they can be measured via a height contrast by AFM. Re-

cently, also low energy electron microscopy (LEEM) was applied to visualize APDs [33, 74]. Reflection anisotropy spectroscopy enables *in situ* quantification of antiphase disorder at the GaP/Si(100) surface in MOVPE ambient [79], as will be discussed in section 2.10.2.

2.5 Heterovalent interfaces

According to Harrisson et al.[123], a valence mismatch occurs at ideally abrupt III-V/IV(100) interfaces: One group V (group III) atom has five (three) valence electrons, which is 5/4 (3/4) partial electronic charge per bond. Two electrons are required for each IV–V/III bond. In consequence, there is 1/4 excess (deficit) of electronic charge per (1×1) interface cell formed by a IV–V (IV–III) bond at abrupt interfaces. Such a heterovalent interface can be compensated by atomic intermixture [123, 192] during the initial stage of growth. Atomic intermixture within the interface layer is associated with an electron charge redistribution among the (III-V)–IV bonds so that the electron-counting rule model (ECM) [203] is fulfilled within the interface.

For many semiconductor heterostructures, it was found that such an atomic intermixture at the interface lowers the interface formation energy compared to abrupt interfaces [54, 55, 150, 162, 206]. Romanyuk et al. investigated GaP/Si(111) heterointerface structures by *ab initio* DFT calculations [218]. They found that the interface energy decreases for the majority of charge compensated interfaces with Si/P (Si/Ga) atomic intermixture in the interfacial layer, with the exception of the P-rich GaP(111)A/Si(111) interface.

Kroemer argues, that occurence of a locally equal number of IV–III and IV–V bonds will be hindered during epitaxy due to chemical bonding preferences [157]. This is observed by Bringans et al.[39] for GaAs/Si(100), where it is shown with XPS that the majority of the bonds at the interface are Si–As bonds. For GaP/Si(100), the binding situation at the heterointerface will be studied in this work.

2.6 GaP nucleation on Si(100)

An adequate nucleation procedure is of utmost importance to minimize defect formation at the GaP/Si(100) heterointerface. In UHV, low-temperature migration enhanced epitaxy (MEE) is known to promote two-dimensional GaP growth on Si(100) with 4° and 6° misorientation towards [011] direction [109, 261]. *In situ* studies during pulsed GaP nucleation by chemical beam epitaxy (CBE) [18, 219] revealed that contiguous GaP film growth with minimum roughening requires a precisely balanced

amount of gallium being present to avoid three-dimensional nucleation respectively Ga droplet formation. During low-temperature nucleation, the P precursor tertiarybutylphosphine (TBP) was found to react immediately when reaching the surface [219]. Decomposition of the Ga precursor triethylgallium (TEGa) was identified as rate limiting step [18].

Also early MOVPE studies by Olson et al.[201] report on reduced defect densities by performing GaP nucleation at 500 °C followed by growth at 750 °C. However, high densities of structural defects occurred at the interface, which was attributed to SiO_2 or SiC. High V:III ratios were found to reduce island growth [241, 257], but the high growth temperature of 900 °C increased interface roughening [242]. *In situ* spectroscopic ellipsometry (SE) revealed intermixing at the GaP/Si(100) interface during GaP growth at about 600 °C [24]. Nanoscopically roughened Si(100) was found to promote continuous GaP film growth, but care must be taken to avoid generation of metallic Ga [172]. Low temperature nucleation at 425 °C in a two-step growth process was shown to reduce Si interdiffusion in the GaP epilayer [69]. All these studies were performed with the precursors trimethylgallium (TMGa) and phosphine (PH_3).

As recently reviewed by Volz et al.[279], a two step growth sequence successfully suppresses defects in MOVPE ambient using the precursors triethylgallium (TEGa) and tertiarybutylphosphine (TBP): Pulses of TBP and TEGa (1s each with 1s pause in between) are applied at low temperature in the range of 400 °C prior to GaP growth above 570 °C. This so-called "flow modulated epitaxy" (FME) nucleation at low T leads to GaP epilayers free of islands, twin defects and stacking faults, as long as the Ga amount is low enough to avoid Ga droplet formation. Though it is suggested in Ref.[279] that equal amounts of Si–P and Si–Ga bonds form during this pulsed nucleation, the atomic structure of the GaP/Si(100) interface could not be directly resolved yet.

2.7 Dilute nitride GaPN

According to Vegard's law, $GaP_{0.92}N_{0.02}$ may be grown lattice-matched on Si(100). Already such little incorporation of N in III-V compounds (dilute nitrides), strongly affects the electronic structure of the compound. Weyers et al.[289] observed an systematic decrease of the photoluminescence (PL) energy of GaAsN for increasing N concentrations up to 1.5 %. This behavior can be reproduced quantitatively correct by the band anticrossing model (BAC) [234]: Localized N atoms are considered to show no dispersion in the band structure. The interaction between the conduction band of the host material, E_C, and the N level, E_N, is described in terms of an interaction potential, i.e. a non-diagonal perturbation of the energy eigenvalue determinant. Consequently, dependent on the N concentration, x, the conduction

band splits into $E_{\pm}$,

$$E_{\pm}(k) = \frac{1}{2}\left(E_C(k) - E_N \pm \sqrt{(E_C(k) - E_N)^2 + 4\,x\,C_N^2}\right) \quad , \tag{2.2}$$

where the parameter C_N is fitted to experimental data. A large bandgap bowing was also observed for GaPN [19, 29, 188], and N incorporation in GaPN leads to a "direct-like" bandgap already for concentration below 0.5 % [235, 295]. Though the PL peak shows a redshift, a blueshift of E_Γ and E_1 was found, while $E_0^|$, $E_1^|$, $E_1(2)$, and $E_2(2)$ remained almost constant [167]. As for GaAsN, the bandgap bowing was described by the BAC model [294]. The repulsion of N-related levels with increasing N concentration, however, was experimentally disproved [47, 306]. Excitons bound to single N atoms, pairs or clusters in GaPN cause states within the bandgap and were detected by their absorption bands [305]. Kent and Zunger [141, 142] include N clustering in their theoretical model. They find that there is no sharp transition to a direct bandgap, but that "adding any amount of nitrogen impurities in GaP can be considered as adding 'direct gap' (Γ) character to the material". They predict that cluster states get energetically pinned, while the dependence of the bandgap on the N concentration is caused by host states, which are perturbed by substitutional N incorporation. PL experiments seem to agree with that model [47], but the results are questioned by Mascarenhas et al.[92, 93], who argue that the redshift of the absorption edge is rather caused by the formation of an impurity band and not by interaction with the conduction band [93, 301, 306, 307]. They also conclude that finding a universal model describing both GaAsN and GaPN is "unrealistic". Time-resolved PL of GaPN was explained by N cluster states in terms of exciton hopping between localized states and recombination of localized excitons [89, 195].

Adding As to GaPN may be beneficial regarding the electronic structure and will increase absorption, but it also requires an increased N content to maintain the lattice match to Si. Geisz et al.[103] demonstrated a lattice-matched GaPNAs/Si(100) tandem solar cell. The solar conversion efficiency of 5.2 % at the AM1.5g solar spectrum was mainly limited by low current in the top cell. The diffusion length in the GaPNAs top cell needs to be improved [103] and carbon as well as hydrogen incorporation need to be avoided [102]. A general proof for the ability of reaching high efficiencies with dilute nitride III-V solar cells was recently demonstrated: MBE-grown GaInNAs subcells reached conversion efficiencies of 44 % in a triple-junction configuration under concentrated sunlight [111]. Antimony is considered to act as surfactant suppressing defects during MBE growth [280]. Regarding MOVPE, the role of the Sb precursor itself is still under debate, as different results were obtained with triethylantimony (TESb) and trimethylantimony (TMSb) [67, 99, 146]. In general, a better understanding of the formation of N clusters or line defects in dependence on the actual processing is required.

Due to the higher stability of GaPN compared to GaPNAs in electrolyte solution [64] and the higher bandgap desired for photoelectrolysis (cf. section 2.8), this work

will focus on GaPN/Si heteroepitaxy. Based on these results, future work may consider *in situ* studies of GaPNAs growth on Si(100).

2.8 GaPN/Si-based photochemical diode

The following considerations have partly been published [255]. Photoelectrolysis of water converts sunlight into chemical energy, stored in bonds of molecular hydrogen. H_2 can subsequently be further converted into renewable fuels, such as methanol or synthetic hydrocarbons [200]. State of the art electrolyzers, which are currently tested in the field, are mostly dark electrolyzers which are powered by external power supply, efficient only at large scale, and involve non-abundant metals and catalysts. Multi-junction approaches for direct, "wireless" photoelectrolysis, in contrast, aim at combining absorption of sunlight and unbiased water splitting into one single device, as pioneered already in the 1980's [16] and demonstrated for Si triple junction cells [213, 215]. Such a device differs from "standard" solar cells:

(1) The redox potential of water is 1.23 eV. Including required overpotentials, generation of a minimum photovoltage of about 1.8 V is necessary to split water [136]. Figure 2.2 on page 7 visualizes the absorption loss for a material with $E_g = 2\,\text{eV}$, which is (optimistically) about the minimum bandgap required for a single-junction material in order to generate sufficient photovoltage. Tandem devices thus are more feasible to achieve both high absorption and necessary voltage.

(2) Water is not necessarily split at the maximum power point of a solar cell. Stacking more junctions to increase the photovoltage far above 1.8 V is therefore not instructive. Further increasing the conversion efficiency requires to increase the photocurrent.

(3) At the semiconductor-liquid interface, conduction and valence bands need to be aligned in a way that the redox potential is located within the band gap and carrier transport into the electrolyte is promoted. The semiconductor-liquid interface may serve as Schottky-like contact to separate generated charge carriers [199].

(4) (Photo-)Corrosion in the liquid must be minimized. The $GaInP_2$/GaAs tandem, for example, which currently holds the record solar-to-hydrogen efficiency [144], was not stable [145].

GaPN/Si(100)-based tandem absorber structures are promising regarding these criteria: While the band alignment of GaP(100) is suitable for direct hydrogen evolution [137], its indirect large bandgap reduces the absorption efficiency. Already

incorporation of only 2 % of nitrogen, however, enables lattice-matched growth of $GaP_{0.98}N_{0.02}$ on Si(100). Recently, Hu et al. calculated solar-to-hydrogen efficiencies for tandem absorbers in different chemical environments [126]. Similar to Fig. 2.3 on page 8 for photovoltaic application, their results also favor Si as a substrate in combination with a top absorber between 1.6 and 1.8 eV. Si as a bottom cell and $GaP_{0.98}N_{0.02}$ as a lattice-matched top cell, with bandgap energies of 1.12 and 1.95 eV, respectively, are relatively close to optimum. While adding As into a quaternary GaPNAs material would further decrease the bandgap of the top cell and thereby increase absorption efficiency, realistic losses in the photovoltage of a tandem device must also be considered additionally. $GaP_{0.98}N_{0.02}$/Si(100) with a sum of bandgaps of about 3 eV seems feasible for direct photochemical water splitting operation regarding sufficient voltage supply. Additionally, nitrogen incorporation in III-V semiconductors can increase the stability towards the electrolyte [63] and GaPN was shown to be more stable than GaAsPN [64].

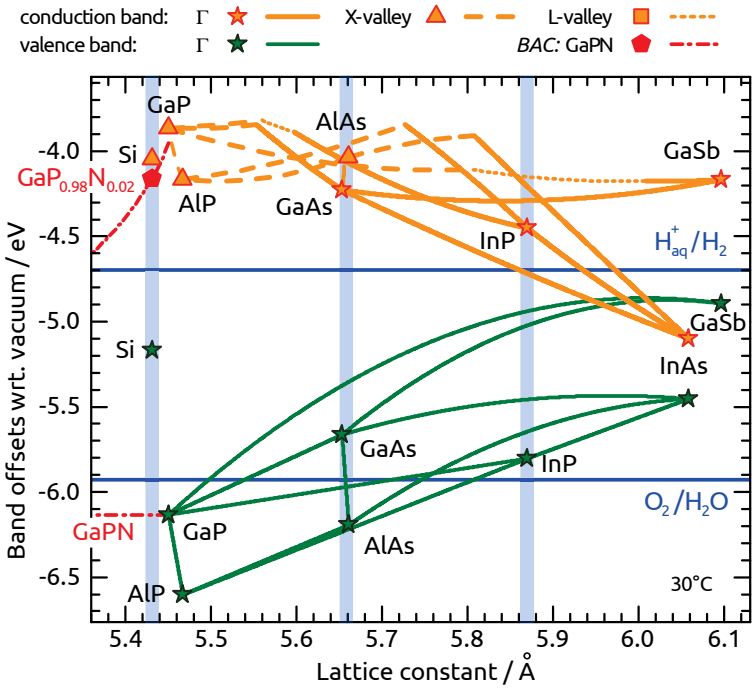

Fig. 2.8 – Alignment of valence band maxima (green) and conduction band minima (orange) of various III-V compound semiconductors, their ternary compounds, and Si relative to vacuum as a function of lattice constant. The line resp. symbol style indicates the type of the bandgap (see legend). Blue horizontal lines indicate the redox potential of water. Light blue vertical lines highlight the lattice constants of the common substrates Si, Ge/GaAs and InP. Data for 30 °C from Refs [91, 120, 130, 269, 281, 282].

Regarding point (3), the band offsets of various III-V semiconductors and Si as well as their ternary compounds are estimated in Fig. 2.8 as an update of the work

by Tiwari and Frank [269]. The values are a compilation of the lattice constants, bandgaps, valence band offsets (VBO) and bowing parameters given by Vurgaftman et al.[282] for the III-V compounds, and Tiwari and Frank [269] for Si. It is assumed that the lattice constants of ternary III-V's follow Vegard's law [277]. For the bandgap E_g and VBO of a compound, bowing according to Ref.[276] was considered. The conduction band offset (CBO) is then given by CBO $= E_g +$ VBO. To include the redox potential of water, the band offsets were transformed relative to vacuum scale using the electron affinity of InP of 4.38 eV given in Ref.[91] and 4.05 eV for Si [130]. It must be noted that Fig. 2.8 can only give a rough idea of the relative band alignment since doping, band bending, strain and different interface formations are not taken into account here.[5] The work function of the H_2/H_2O potential against vacuum scale is assumed to be about -4.7 eV [120] with the O_2/H_2O potential 1.23 eV below that value. For nitrogen-diluted III-V alloys, E_g is highly reduced already by small nitrogen incorporation [289], as can be described by the band anticrossing (BAC) model [234, 294] (see section 2.7 for more details). The BAC model assumes changes only in the conduction band, so that the values tabulated by Vurgaftman and Meyer [281] are applied to the CBO of GaPN only. For $GaP_{0.98}N_{0.02}$, Umeno et al.[274] predict a decrease of the VBO of about 40 meV with reference to GaP.

To promote efficient transport to the liquid via band bending at the semiconductor-liquid interface, where the charge carriers are separated, hydrogen should be evolved at the p-doped semiconductor side and oxygen at the n-doped side. The need for charge separation at pn-junctions is omitted in such a so-called photochemical diode [199], where the subdiodes are interconnected by a tunnnel-junction. With all the given uncertainties, Fig. 2.8 on the previous page suggests that both oxygen and hydrogen evolution could be possible with GaP(N), while uncoated Si could only evolve hydrogen. In consequence, hydrogen evolution would be considered at the p-Si subdiode and oxygen evolution at the n-GaPN subdiode. Hydrogen evolution with p-GaPN, in contrast, could be achieved with either an oxidation catalyst that also protects the n-Si subdiode [140] or a Si photovoltaic bottom cell, which could be covered with an intransparent ohmic contact and a metal electrode, similar to Khaselev and Turner's approach [144].

[5] If an average Ge/GaAs offset from Ref.[95] was assumed, for example, keeping the alignment of Si referred to Ge from Ref.[269] would shift the Si band edges about 300 meV downwards.

2.9 Experimental techniques

2.9.1 Metalorganic vapor phase epitaxy (MOVPE)

The application of metalorganic vapor phase epitaxy (MOVPE) (also known as metalorganic chemical vapor deposition (MOCVD) and organometallic vapor phase epitaxy (OMVPE)) dates back to GaAs growth in the late 1960's [174]. MOVPE established soon as growth technique for III-V heterostructures and devices [85]. Monocrystalline epitaxial layers, ranging from nanometer thin to micrometer thick layers, can be produced with high reproducibility and industrially scalable throughput. Given the broad variety of III-V compounds, entire device structures can be grown monolithically. As the name tells, the growth principle is based on metalorganic precursors, which contain the chemical elements to be grown. These molecules are transported with an ultrapure carrier gas in laminar flow over the heated substrate, where they decompose by thermal activation and surface chemistry. The desired materials are incorporated, while precursor residuals leave the reactor with the carrier gas. Processes usually take place at pressures from 10 to 1000 mbar and temperatures commonly range from 300 °C to 1200 °C. Growth processes in MOVPE ambient are complex, as chemical reactions of the precursors and their components may occur in the gas phase, on the surface of the substrate as well as with reactor walls, which may be coated from previous processes. Often, H_2 is used as carrier gas and can interact with the other species involved. Also, energetically and kinetically driven processes compete. In general, growth can be categorized in three different growth modes:

(1) *Vollmer-Weber* mode: The specific surface enthalpy of the substrate is smaller than that of the epilayer. The consequence is island-like growth.

(2) *Frank-van der Merwe* mode: The specific surface enthalpy of the substrate is larger than that of the epilayer, which ideally results in layer-by-layer growth. This is the preferred growth mode for planar epilayers.

(3) *Stranski–Krastanov* mode: Beyond a critical thickness, the mode changes from initial Frank-van der Merwe mode to Vollmer-Weber mode.

III-V growth usually takes place with excess supply of the group V precursor for stabilization. Commonly, the partial pressures of the group-III species then govern the growth rates. Depending on temperature, growth rates may be divided into three regimes (assuming the other parameters constant) [247]:

(a) At low temperatures, the growth rate increases exponentially with increasing temperature, since chemical precursor reactions at the surface are the limiting factor (*kinetically limited*).

(b) At temperatures, where the chemical reactions are faster, the growth rate becomes limited by diffusion of the species to the growth surface (*mass transport limited*) and the growth rate is almost constant. This is the commonly desired growth regime.

(c) At further increased temperatures, desorption is limiting and the growth rate decreases (*thermodynamically limited*).

Setup and MOVPE-to-UHV transfer

Application of *in situ* techniques is highly desired to understand and control the complex processes in MOVPE ambient [11, 303]. The presence of a process gas hinders application of electron-based *in situ* techniques, which are established in ultra-high vacuum (UHV). A common general approach therefore is application of optical techniques [8]. Reflection anisotropy spectroscopy (RAS) is a versatile surface sensitive optical technique (see section 2.9.2 for details), but the obtained spectra are complex as well. Our approach therefore is to combine RAS-monitored MOVPE growth with UHV-based surface science techniques in order to gain a deeper understanding of the *in situ* spectra, and thereby of the involved processes, aiming at *in situ* control. Figure 2.9 on the facing page gives a simplified sketch of this setup. The basis is a commercially available, horizontal flow MOVPE reactor (AIX-200 from Aixtron), which is modified with a custom designed, contamination-free MOVPE-to-UHV transfer system [119].[6] Growth processes may be interrupted at interesting stages to transfer the samples to a mobile UHV shuttle and study the surfaces with established surface science techniques, such as scanning tunneling microscopy (STM), photoelectron spectroscopy (PES), low energy electron diffraction (LEED) or Fourier-transform infrared spectroscopy (FTIR). Also remote locations, such as the synchrotron facility BESSY II, or laboratories of collaborators can be addressed. While interrupting the process, care must be taken that the surfaces remain unchanged. *In situ* monitoring is feasible until the surface leaves the MOVPE reactor and can later be applied also in UHV to verify that the signals did not change. As sketched in Fig. 2.9 on the next page, the UHV part consists of a main chamber with a base pressure of about $2 \cdot 10^{-10}$ mbar (pumped by a turbo molecular pump), which is connected via a valve to an interim chamber (which can be separately pumped by the rough pump of the main chamber). The interim chamber is connected to the MOVPE reactor with another valve and also serves for loading the reactor. The mobile UHV shuttle is pumped by a battery powered ion getter pump and can be connected to the interim chamber. Prior to the transfer, the entire UHV system is baked at 120 °C for $5-10$ h while the system is pumped via the main chamber. This yields a pressure in

[6] During this work, the MOVPE was moved from HZB to TU Ilmenau. At TU Ilmenau, we also put a second MOVPE in operation, which consists of two horizontal flow reactors connected to one single gas-mixing cabinet and control electronics. One side corresponds to the former HZB MOVPE and is equipped with the MOVPE-to-UHV transfer setup instead of a glovebox. On the other reactor side, 2 inch wafers may be processed (with rotation). Samples for this work were only grown on the two reactors enabling transfer to UHV.

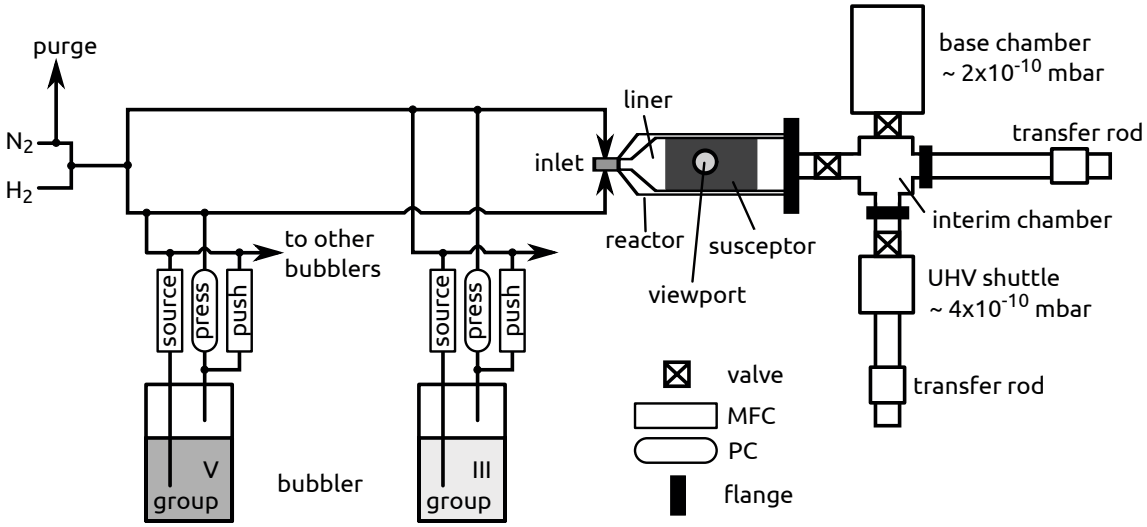

Fig. 2.9 – Simplified schematic drawing of the MOVPE and UHV transfer system.

the low 10^{-10} mbar regime. Upon sample transfer, both shuttle and main chamber valves are closed and the reactor is pumped down. A cold trap in the main chamber is cooled with liquid nitrogen. The valve to the reactor is opened and the sample transferred into the interim chamber. The valve to the reactor closes automatically upon contact of the transfer rod with a sensor and the valve to the main chamber is opened. Within 30 s, a pressure below $2 \cdot 10^{-9}$ mbar can be reached and a pressure below $5 \cdot 10^{-10}$ mbar typically is reached after 5 min. At that pressure, the sample is transferred to the UHV shuttle with a comparable pressure.

The reactor itself consists of an outer quartz-tube (reactor tube) and an inner quartz-tube (liner). An optical viewport at the reactor tube and a hole in the liner enable optical *in situ* monitoring of the processes. The liner is connected to the gas inlet. To avoid contamination of the reactor tube, the volume between reactor tube and liner is purged. Within the liner, a graphite susceptor is heated by six halogen IR lamps with a power of 1.6 kW each, enabling maximum temperatures of about $1020 - 1050\,^{\circ}\mathrm{C}$. Temperatures given in this work are measured with a thermocouple in the susceptor.[7] Liner and susceptor can be changed easily to separate different material systems. The liner may be cleaned in nitro-hydrochloric acid (aqua regia). The susceptor holds a molybdenum sample carrier, about $3 \times 3\,\mathrm{cm}^2$ in size, on which samples with edge lengths up to about 2.5 cm may be mounted with screws and "fingers". The carrier may be screwed to a UHV transfer rod for loading and unloading the reactor via the interim chamber.

[7] Note that, dependent on the reactor pressure, the temperature at the surface of the sample is lower. The temperature offset at the surface can be estimated via AlSi eutectics and via calibration curves measured with a pyrometer on reference samples.

Precursors

Gettered N_2 and Pd-purified H_2 can be chosen as carrier gas. Hydrogen is applied during growth for this work. The applied precursors here are silane (SiH_4), tertiarybutylphosphine (TBP), triethylgallium (TEGa), tertiarybutylarsine (TBAs), and 1.1-dimethylhydrazine (UDMHy). TBP and TBAs are less toxic than phosphine and arsine, respectively [248].

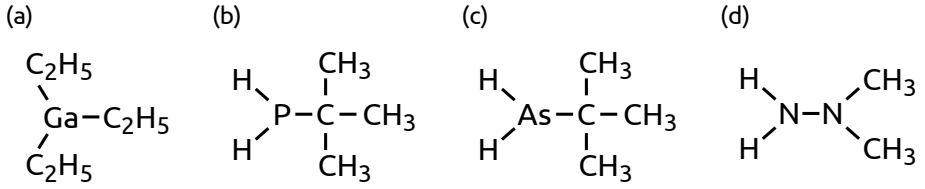

Fig. 2.10 – Structure of the III-V precursors used in this work: (a) TEGa, (b) TBP, (c) TBAs, (d) UDMHy.

The carrier gas is directed into the reactor in two different lines to separate group V and group III precursors in order to avoid pre-reactions (see Fig. 2.9). With a 5/2 way valve, precursor-enriched carrier gas can be directed to the exhaust or in the corresponding line and the reactor. Liquid and solid precursors are stored within so-called "bubblers" in tempered water baths at a temperature T_a and pressure P_{bubbler} (controlled with a pressure controller (PC)). The vapor pressure P_{vap} in the bubbler is given by the August-Antoine equation,

$$P_{\text{vap}} = 1.33322\,\text{mbar} \cdot 10^{A-B/T_a} \quad , \tag{2.3}$$

where A and B are specific for the precursor and T_a refers to the absolute temperature.[8] The amount of carrier gas, which is enriched with the precursor, is called "source flow" q_s and can be controlled by a mass flow controller (MFC). To guarantee a stable flow, carrier gas can be added via the "push" MFC (which usually is balanced with the total flow to avoid dilution). At a total mass flow q_t in the reactor at a reactor pressure P_{react}, the partial pressure P_{part} of the precursor is given by

$$P_{\text{part}} = \frac{q_s}{q_t} \cdot \frac{P_{\text{vap}} \cdot P_{\text{react}}}{P_{\text{bubbler}} - P_{\text{vap}}} \quad . \tag{2.4}$$

The total flow is adjusted for as laminar flow as possible and was $q_s = 5500\,\text{sccm}\,/\,\text{min}$ throughout this work.

[8] The prefactor accounts for converting mm Hg to mbar.

Process parameters used in this work

Prior to every Si process, the reactor was baked at 1010 °C in 950 mbar H_2, typically for 30 min. This process does not completely remove background residuals from previous growth runs present at the reactor walls and susceptor. For entirely "clean" reactor conditions, the quartz parts can be cleaned in nitro-hydrochloric acid (aqua regia) and a separate susceptor and carrier is required. If not stated otherwise, the experiments for this work were performed in systems with GaP residuals.

P-doped n-Si(100) substrates (CrysTec) with 2° misorientation towards [011] were used throughout this work, if not stated otherwise (cf. section 3.5). Optionally, the Si(100) substrates were wet-chemically etched before processing. The etching process is based on Ref.[131] and consists of ultrasonic cleaning in isopropanol, boiling in a basic solution for removal of organic contaminants (NH_4OH (25 %), H_2O_2 (30 %), deionized H_2O at ratios 1:1:3), an HF dip (3 %, 10 s) for deoxidation, and boiling in an acidic solution for controlled re-oxidation of the surface (HCl (32 %), H_2O_2 (30 %), deionized H_2O at ratios 3:1:1). We could not detect an influence of the etching procedure on surface morphology after MOVPE processing and no contamination could be detected with XPS, neither with nor without wet-chemical precleaning. All substrates were thermally deoxidized at 1000 °C in 950 mbar H_2. A homoepitaxial Si buffer (about 250 nm) was grown at 950 °C in 200 mbar with SiH_4 and annealed at 1000 °C / 950 mbar. The final cooling procedure is decisive for the domain structure on the surface and depends on the terrace width, details will be discussed in section 2.10.1.

For GaP/Si(100) heteroepitaxy, a two-step process was applied. GaP was nucleated with alternating (TBP, TEGa) pulses of 1s each (starting with TBP, no pause in between), at 420 °C / 100 mbar with increased V : III ratio compared to growth. GaP epilayers were grown using TBP and TEGa at 595 °C / 100 mbar with V : III = 13. The surface preparation of GaP(100), respectively GaP/Si(100) surfaces is described in section 2.10.2. For $GaP_{0.98}N_{0.02}$, growth temperatures between 570−650 °C at 50−100 mbar were applied, typically with the ratios TBP : TEGa = 13 and UDMHy : TBP = 1-2.5. Optionally, diethylzinc (DEZn) was used for p-doping (carrier concentrations in the range of $5 \cdot 10^{17}\,cm^{-3}$).

Homoepitaxial GaP buffers for reference samples were grown on nominal, Zn-doped p-GaP(100) substrates, which were "epiready" polished (ITME). After thermal deoxidation at 650 °C with TBP stabilization, GaP was grown with TBP and TEGa at between 595 − 620 °C in 100 mbar H_2 with V : III = 13. Optionally, DEZn was used for p-doping analogously to GaP(N)/Si(100) heteroepitaxy.

2.9.2 Reflection anisotropy spectroscopy (RAS)

Reflection anisotropy spectroscopy is a linear optical technique, which enables to study surfaces and interfaces of cubic crystals and can be applied both in vapor phase epitaxy ambient and in UHV. Aspnes and Studna introduced this technique as reflectance difference spectroscopy (RDS) in 1985 probing the optical anisotropies above the bandgap of Si(110) and Ge(110) [9, 15].[9] A broad variety of applications is reviewed in Ref.[286]. In this work, the term reflection anisotropy spectroscopy (RAS) will be used, and reflection $r = r(\lambda)$ here points to the complex Fresnel reflection amplitude and not to the reflectance $R = r^* r$.

The RAS signal

RAS probes the normalized difference $\Delta r = r_x - r_y$ in reflection between two mutually perpendicular directions x and y in the plane of the surface,

$$\frac{\Delta r}{r} = \mathrm{Re}\left(\frac{\Delta r}{r}\right) + \imath\,\mathrm{Im}\left(\frac{\Delta r}{r}\right) = \frac{r_x - r_y}{1/2\,(r_x + r_y)} = 2\,\frac{r_x - r_y}{r_x + r_y} \quad , \tag{2.5}$$

where $\imath$ denotes the imaginary unit, in near normal incident geometry. For $\Delta r \ll r$, it can be shown that [15]

$$\frac{\Delta R}{R} = 2\,\mathrm{Re}\left(\frac{\Delta r}{r}\right) \quad . \tag{2.6}$$

For a crystal with (ideal) cubic symmetry, the optical contribution from the bulk is isotropic and signals arise due to the presence of interfaces or defects that break the symmetry. Aspnes and Studna divided the interfacial contributions in "intrinsic" ones, which are caused by surface many-body screening and bulk spatial dispersion, and "extrinsic" contributions from adsorbed species and microstructured overlayers [15]. In this work, RAS is applied *in situ* in MOVPE ambient. Most surfaces of interest here exhibit atomically well ordered surface reconstructions, which cause characteristic RAS signals, such as the dimerized surfaces of GaP(100) [270] and Si(100) [236] (see also section 2.10). RAS therefore is aligned so that $x = [0\bar{1}1]$ and $y = [011]$,

$$\frac{\Delta r}{r} = 2\,\frac{r_{[0\bar{1}1]} - r_{[011]}}{r_{[0\bar{1}1]} + r_{[011]}} \quad . \tag{2.7}$$

The origin of the optical anisotropies can be manifold. RA spectra can therefore contain rich information of the probed sample. On the other hand, interpretation of the spectra often is not trivial and complementary techniques are beneficial for a detailed understanding. Benchmarking of *in situ* RAS to complementary surface

[9] According to Aspnes and Studna [15], above-band-gap anisotropies were reported by Cardona et al.[48] for Si(110) in 1966, but no further investigation was reported.

science techniques often promotes understanding of the complex RAS signatures and in turn can enable precise *in situ* control. RAS signals of reference surfaces, which are important for this work, are focused in section 2.10.

Besides the surface reconstructions mentioned above, possible contributions to the RAS signal include the following: Mesoscopical structures at the surface can cause large RAS signals [189]; but also microscopic roughness, either at surfaces [10] or interfaces [115] can contribute. Dopants in III-V semiconductors may contribute via the linear electro-optic effect [2, 264]. Anisotropies may also be induced by ordering effects in ternary systems [313] or strain [117, 169]. Dislocations were found to contribute via the piezo-optic effect [164]. In case the transparency of an epilayer enables internal reflection at a buried interface, the RA spectra will be modulated by Fabry-Pérot-like oscillations due to the normalization of the signal [78]. In addition, dielectric interfacial anisotropies may contribute [127, 298, 299] (see also section 2.10.3). Additionally, temperature affects the involved optical transitions: At lower temperatures, spectral features sharpen and shift towards higher photon energies.

Phase-modulation setup

For this work, a commercial RA spectrometer, EpiRAS-200 (LayTec), was used and is described in detail by Haberland [113]. The principal setup corresponds to the phase-modulation approach of Aspnes et al.[12] and the beam path is sketched in Fig. 2.11 on the following page. The incident light of a XBO lamp is linearly polarized with a Rochon prism and directed on the sample by spherical mirrors and a beam splitter. The polarization axis is aligned $\pm 45°$ referred to $[0\bar{1}1]$ and [011] direction of the sample, respectively. Upon anisotropic reflection, the polarization contains an elliptic contribution. The photoelastic modulator (PEM) is aligned such that its periodically strained axis modulates the phase of the light polarized perpendicular to the polarization axis of the former linearly polarized incident light. Hence, only the phase of the anisotropic contribution is modulated. A Glan-Air analyzer prism translates the phase modulation in an amplitude modulation, which can be measured with a Si photodiode located behind a grating monochromator. The measured signal consists of an AC voltage with amplitude ΔU_ω, which relates to the anisotropic contribution, modulated on a constant offset U_{DC}, which relates to the mean reflection. The phase modulation in the PEM may be expressed by Bessel functions, J_1 and J_2, which show a different frequency dependence for the real- and imaginary part [113]. They may be filtered by a lock-in amplifier. Using eq. (2.6), the RAS signal then may be expressed as

$$\mathrm{Re}\left(\frac{\Delta r}{r}\right) \simeq \frac{\sqrt{2}}{2\,J_2(\delta_{\mathrm{PEM}})} \cdot \frac{\Delta U_{2\omega}}{U_{DC}} \quad , \tag{2.8}$$

$$\mathrm{Im}\left(\frac{\Delta r}{r}\right) \simeq \frac{\sqrt{2}}{2\,J_1(\delta_{\mathrm{PEM}})} \cdot \frac{\Delta U_{\omega}}{U_{DC}} \quad , \tag{2.9}$$

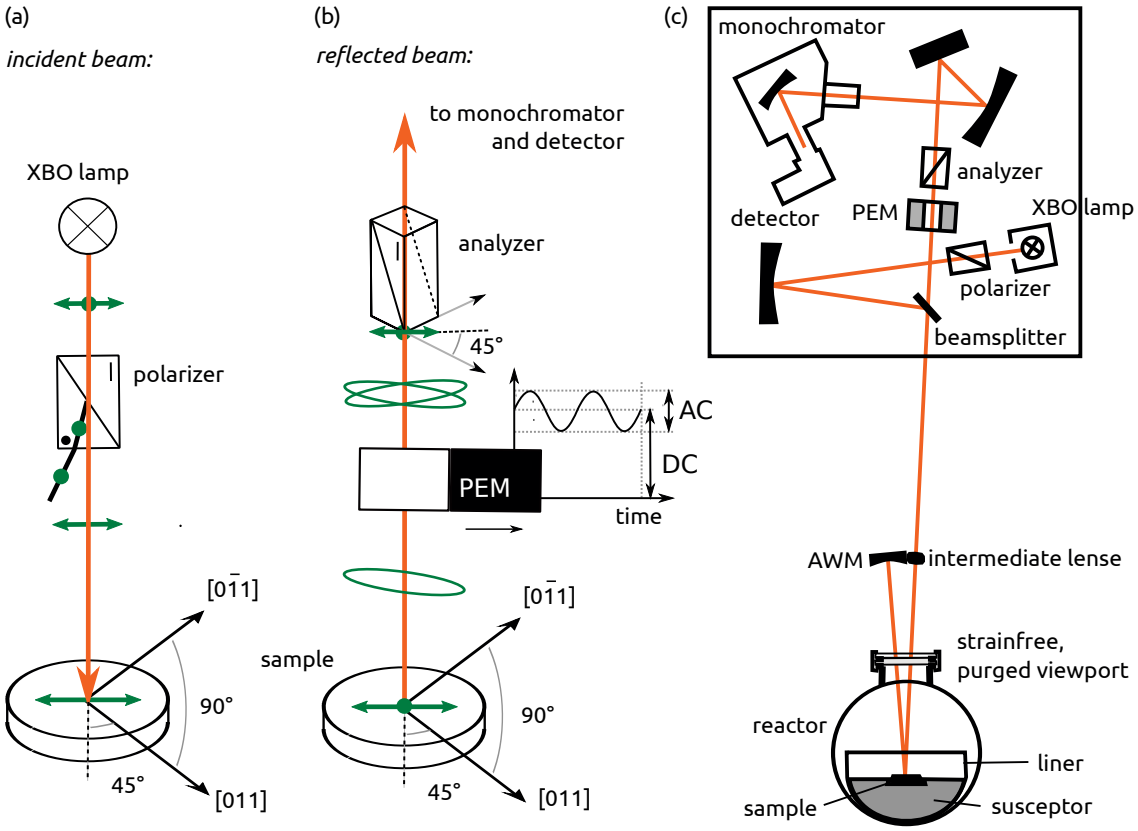

Fig. 2.11 – RAS setup in this work: Polarization of the light for the incoming (a) and reflected (b) beam. (c) Beam path in the EpiRAS-200 setup used in this work (modified after Ref.[113]).

where δ_{PEM} denotes the retardation of the PEM [113]. The retardation is kept constant so that the PEM voltage needs to be adjusted continuously with respect to the wavelength by the measurement software.

In the setup used here, the RAS optics are mounted to the roof of the MOVPE. This requires additional intermediate optics, consisting of a lens to focus the light on the sample (the spot size is about 1 mm^2). An anti-wobble mirror (AWM) compensates tilt and directs the reflected light on the reversed path as the incoming light. When evaluating the detector voltages, it must thus be considered, that the beam is reflected twice on the sample. The optics are cooled by a fan and the IR lamps of the MOVPE are shielded. The optical view-port is strain-free and purged to avoid coating during the MOVPE process.

Baseline subtraction

Since also the optical components themselves inherently contribute to the measured anisotropy, a baseline needs to be subtracted. Commonly, this is done by measuring the sample again after rotation by 90°, which, according to eq. (2.7) on page 26 flips the sign of the signal. Since the optics are not rotated, comparison of the

spectra before and after rotation yields the baseline that needs to be subtracted. In the setup used here, however, the sample would need to be dismounted from the carrier, rotated in air and remounted. In contrast to vicinal Si(100) surfaces [175, 176], oxidized surfaces of Si(100) with both 0.1° and 2° misorientation towards [011] showed no anisotropic contribution from the steps and the measured spectrum only contains the baseline accounting for the optical components themselves. This was carefully checked by comparison to the baseline obtained from measuring the standard reference RA spectrum of oxidized Si(110) [15], which is also referred to when calibrating RAS intensities, before and after rotation by 90°. An advantage of this approach for III-V/Si(100) epitaxy is, that the baseline is measured via the substrate itself and the beam path is not changed anymore.

Measurement modes

The EpiRAS-spectrometer may be operated in three different modes. Spectra can be measured at photon energies in the range from 1.5 to 5 eV, usually with 10 or 20 meV steps at an integration time of 100 ms. To yield a better time resolution, one single energy can be fixed and measured continuously (transient RA). Since spectral shifts (as caused for example by temperature) cannot easily be resolved in the transient mode, entire spectra can also be measured subsequently and then be plotted with color-coded intensities (colorplot mode).

Reflectance measurements

As used for normalization of the RAS signal, the U_{DC} signal also contains the measured reflectance of the sample. Since this is folded to an apparatus function and the spectrum of the lamp, the reflectance cannot be extracted directly. When normalized by a reference measurement with absolute identical setup, the apparatus function cancels. Such "relative reflectance" spectra can be fitted to yield, for example, the thickness of the grown epilayer of a heterostructure [114]. When U_{DC} is measured in transient mode and the dielectric function of the epilayer at that specific energy is known, the growth rate can be obtained by the oscillation period.

2.9.3 Low energy electron diffraction (LEED)

The symmetry of atomically well ordered surfaces can be probed by the diffraction pattern of elastically scattered electrons. For low energy electron diffraction (LEED), the kinetic energies of the incident electrons are in the range of $E_{\mathrm{kin}} \approx 10 - 1000\,\mathrm{eV}$, where their inelastic mean free path is only few atomic layers [232]. Considering the wave character of such a low energetic electron, its de Broglie wavelength [197],

$$\lambda_{dB} = \frac{h}{\sqrt{2 m_e E_{\mathrm{kin}}}} \quad \Rightarrow \quad \lambda_{dB} \approx \frac{12.25\,\text{Å}}{\sqrt{E_{\mathrm{kin}} \,/\, eV}} \quad , \tag{2.10}$$

where h denotes Planck's constant, is in the order of atomic distances in a solid.

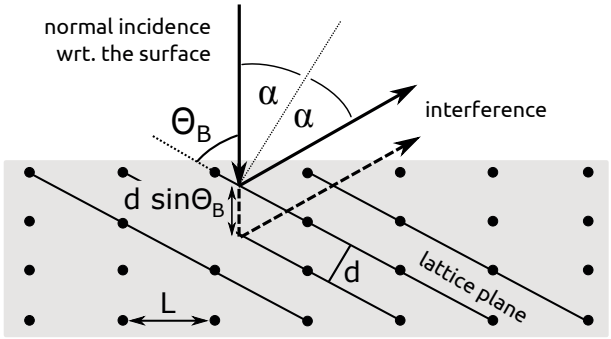

Fig. 2.12 – Bragg's law: Scattering at a solid corresponds to reflection at the lattice planes. Constructive interference occurs when eq. (2.11) is fullfilled (modified after [189]).

Bragg interpreted the elastic scattering process as reflection at the lattice planes of the solid [128]. Constructive interference occurs, when Bragg's equation,

$$n\,\lambda = 2d\,\sin\Theta_B \quad n \in \mathbb{Z} \quad , \tag{2.11}$$

where d is the spacing between the lattice planes and Θ_B the angle of incidence referring to the lattice planes, is fulfilled (see Fig. 2.12). Diffraction spots thus correspond to groups of lattice planes, and the LEED pattern corresponds to the geometry of the surface unit cell in reciprocal space. A (1×2) reconstruction of a surface with symmetric dimers causes diffraction spots at half order along the dimer axis, as shown in Fig. 2.13.[10]

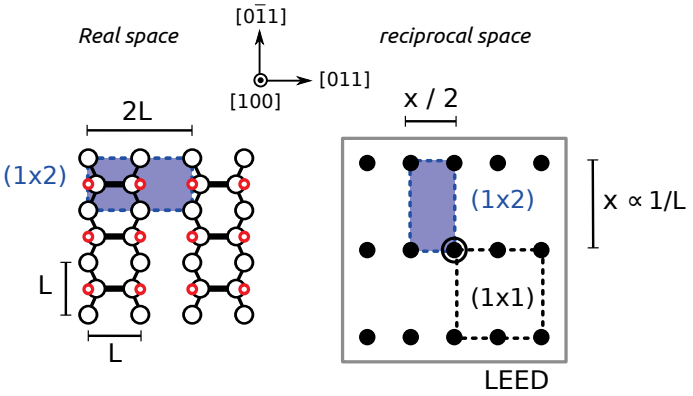

Fig. 2.13 – Dimensions in real space vs. reciprocal space: The LEED pattern of a (1×2) reconstructed surface exhibits spots at half order along the $\times 2$ direction.

[10] In cubic systems, the angles between the basis vectors are identical in real and reciprocal space.

In this work, a commercial LEED setup (Specs ErLEED 100-A) is used. LEED is measured in UHV, the schematic setup is depicted in Fig. 2.14(a). Electrons from a cathode are focused by an electron lens system at normal incidence to the surface of the sample. The scattered electrons move in a field-free space so that they maintain their direction. Inelastically scattered electrons are filtered by a countervoltage. The elastically scattered electrons then get accelerated towards a fluorescent screen, which is viewed by a digital camera situated behind a viewport behind the cathode.

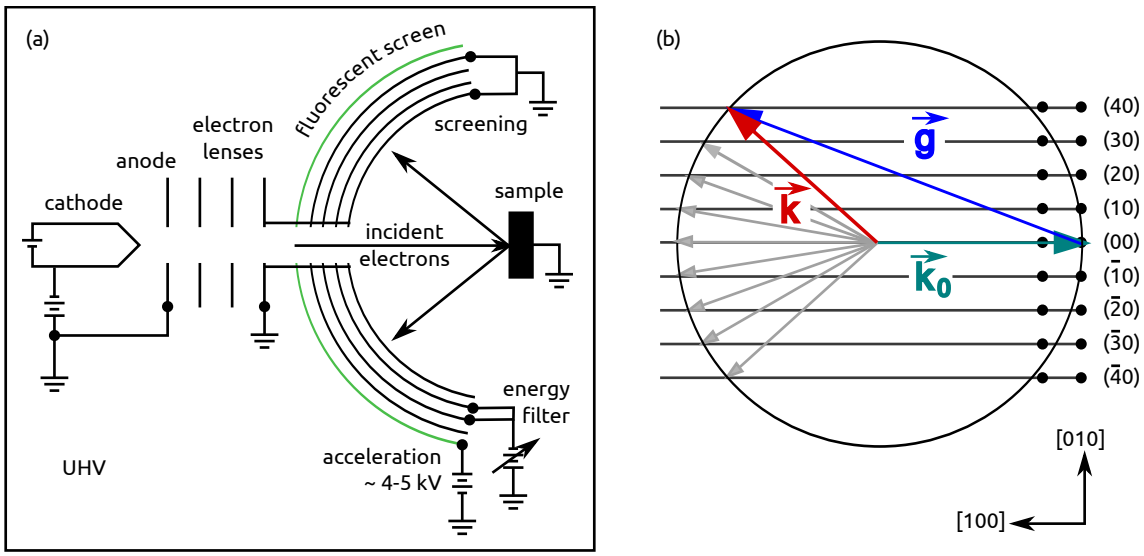

Fig. 2.14 – (a) Schematic drawing of the LEED setup (modified after Ref.[189]). (b) Two-dimensional Ewald construction: The Laue conditions eq. (2.12) are fulfilled for elastically scattered electrons whenever the circle of radius $|\vec{k}_0|$ around $\vec{k}_0$ crosses a reciprocal lattice rod.

According to the Laue condition for constructive interference upon diffraction at a solid [128], the difference $\Delta\vec{k}$ of the incoming wavevector $\vec{k}_0$ and the wavevector of a scattered wave $\vec{k}$ must be a reciprocal lattice vector $\vec{g}$,

$$\Delta\vec{k} = \vec{k} - \vec{k}_0 = \vec{g} \quad . \tag{2.12}$$

For elastically scattered electrons, it holds $|\vec{k}| = |\vec{k}_0|$. Figure 2.14(b) shows a projection of the reciprocal lattice of a (100) surface. Given the surface sensitivity of LEED, $k_\perp$ components are indetermined, which leads to elongated rods along the surface normal. When $\vec{k}_0$ is drawn on the (0,0) rod and a circle with radius $|\vec{k}|$ around $\vec{k}_0$, as shown in Fig. 2.14(b), then the Laue condition for $\vec{k}_\parallel$ is fulfilled whenever the circle crosses a reciprocal lattice rod (Ewald construction).

2.9.4 Photoelectron spectroscopy (PES)

Photoelectron spectroscopy enables determination of the chemical composition of the probed sample. Based on the photoelectric effect [86, 124], electrons in (for example) a solid can be excited to vacuum by photons with an energy $h\,\nu$ larger than the sum of binding energy, E_B, and workfunction, Φ_0. Detection of these photoelectrons enables to study the electronic structure of the materials they escaped from. The measurement of their kinetic energies,

$$E_{\mathrm{kin}} = h\,\nu - \Phi_0 - E_B \quad , \tag{2.13}$$

yields E_B which enables to determine the former binding state of the photoelectron and the chemical composition of the probed material. In case the Fermi levels, E_F, of the sample and the spectrometer are aligned, only the work function of the spectrometer must be known to determine E_B, as depicted in Fig. 2.15(a). In this work, the spectra are plotted as a function of E_B referred to E_F.

The position of a photoemission (PE) line of an element is influenced by the chemical environment of the atom (chemical shift). The information depth is determined by the escape depth of the photoelectron, which is inelastically scattered. This inelastic mean free path depends on the kinetic energy of the electron, i.e. according to eq. (2.13) on the excitation energy $h\,\nu$. While ultraviolet photoelectron spectroscopy (UPS) probes the uppermost layers in depth at Å scale only, several nm may be probed by X-ray photoelectron spectroscopy (XPS). Though, according to Seah and Dench [232], the inelastic mean free path ℓ (in monolayers) as function of E_{kin} for inorganic compounds roughly follows a "universal curve", it may differ for example by a factor two for Si ($\ell \simeq 4\,$Å) and GaAs ($\ell \simeq 8\,$Å) at the minimum around $E_{\mathrm{kin}} \simeq 40\,$eV [267].

For this work, monochromated Al K_α and Ag L_α were used as X-ray sources (Specs Focus 500). Kinetic energies were filtered with a hemispherical analyzer (radius 100 mm) and detected with channeltrons (Specs Phoibos 100). At TU Ilmenau, a 1d delay-line detector was available (Specs 1D-DLD-43-100, Phoibos 150). The quantitative evaluation of the PE spectra was performed by M. M. May (HZB / TU Ilmenau) based on Ref.[180].

XPS only probes occupied states. Unoccupied states may be probed by inverse photoemission. Another option is two-photon photoemission (2PPE) spectroscopy, where laser pulses of photons with energies below the ionization energy are applied. Two photons need to be absorbed during one single pulse to excite an electron above the vacuum level. Absorption of two photons may occur both coherently or via intermediate states, which enables to study occupied and unoccupied states simultaneously. Occupied and unoccupied states may be distinguished by the dependence of E_{kin} on the photon energy $h\,\nu$, as shown in Fig. 2.15(b). In the 2PPE setup, the wavelength $\lambda = 800\,$nm of a Ti:sapphire laser (Coherent, repe-

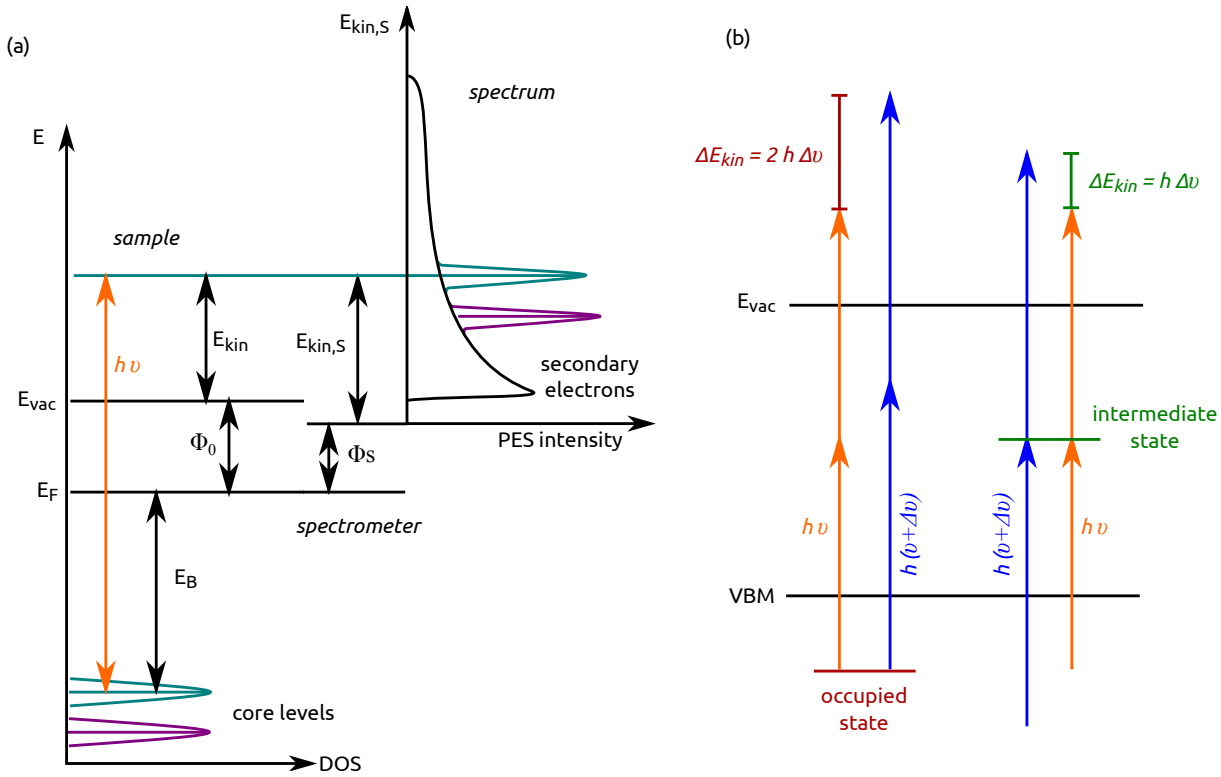

Fig. 2.15 – (a) Schematic relation of the energy levels and a PE spectrum. (b) Different dependence of occupied and unoccupied states on the excitation energy within a 2PPE measurement.

tition rate = 150 kHz, pulse duration = 50 fs, $P_{pulse} = 6\,\mu J$) was converted tunable to $480 - 680$ nm in a noncollinear optical parametric amplifier, which corresponds to $240\,\text{nm} \leq \lambda \leq 340\,\text{nm}$ after frequency doubling. Pulse durations were reduced to < 40 fs at a photon flux in the order of $10^{12}\,\text{cm}^{-2}$ per pulse (see Ref.[238] for more details). Photoelectrons were detected with a time-of-flight spectrometer. The 2PPE experiments were performed in an in-house collaboration by P. Sippel (HZB).

2.9.5 High-resolution X-ray diffraction (HR-XRD)

The information depth of X-rays is higher than that of low energy electrons, certainly when Cu K_α is used as source. Consequently, the bulk of the solid can be probed. Also the diffraction of incoming X-rays can be described by Bragg's equation eq. (2.11). Since $k_\perp$ is no longer indetermined, the reciprocal lattice points are no longer rods, but in case of thin films they are enlarged along the finite direction of the film. The Laue conditions, eq. (2.12), must be fulfilled and the Ewald construction can be used analogously. The Ewald sphere may be extended to the limiting sphere of twofold radius (i.e. $2\,|\vec{k}_0|$), which contains all reflexes that can in

principal be observed, see Fig. 2.17 on the facing page for a side view. The reflexes shown in the gray half spheres are only accessible in transmission.

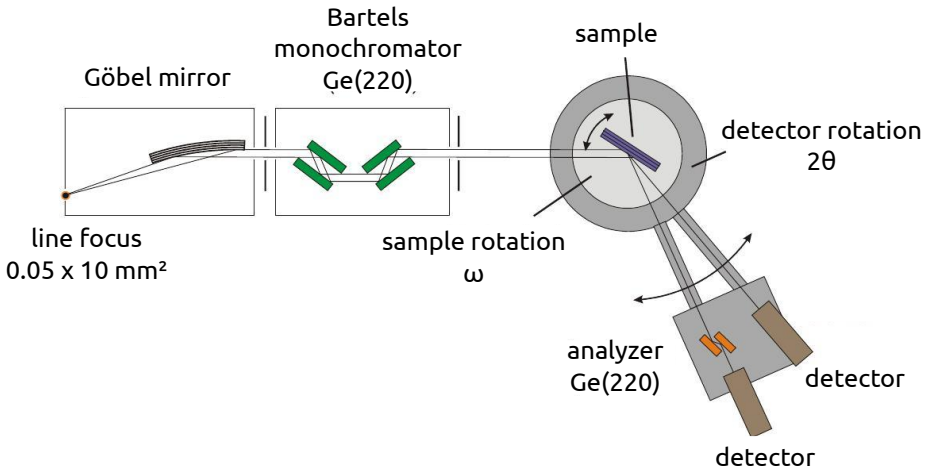

Fig. 2.16 – Schematic drawing of the HR-XRD setup (modified after [224, 245]).

For this work, a Panalytical X'Pert MRD Pro diffractometer was used for high-resolution X-ray diffraction (HR-XRD). Figure 2.16 shows a schematic drawing of the setup. The Cu anode is powered at 45 kV / 40 mA. A line focus (12 mm ×0.04 mm) is collimated by a Göbel mirror to a Ge(220) monochromator, which selects the Cu $K_{\alpha,1}$ emission line with a wavelength $\lambda_0 = (1.5406 \pm 0.0006)$ Å[244]. A cross slit allows to adjust the foci from 0 to 10 mm. The sample is mounted to an Eulerian cradle and the diffracted beam is detected by a PIXcell detector (Panalytical) with a maximum of 255 active channels aligned on 14 mm×14 mm. A Ge(220) analyzer crystal may be used optionally. The angle ω denotes rotation of the sample, while 2θ refers to rotating the detector.

The reciprocal space may either be mapped around a certain reflex (reciprocal space map (RSM)) or scanned along different direction as indicated in Fig. 2.17 on the facing page. A $\omega/2\theta$ scan is performed, when sample and detector are rotated simultaneously, and the reciprocal space is scanned in radial direction. In principle Bragg's equation eq. (2.11) on page 30 enables to determine the lattice constant of a material. For ternary compounds, such as $GaP_{1-x}N_x$, Vegard's law [277] then yields the stoichiometry. Therefore, it is important to determine the degree of relaxation. As pseudomorphic layers maintain the in plane lattice constant $a_\parallel$, the position of their reciprocal lattice points only changes in $k_\perp$ referred to the substrate. Fully relaxed layers, in contrast, cause reciprocal lattice spots shifted radially. In consequence, pseudomorphic and relaxed layers can be distinguished measuring the RSM of an asymmetric reflex.

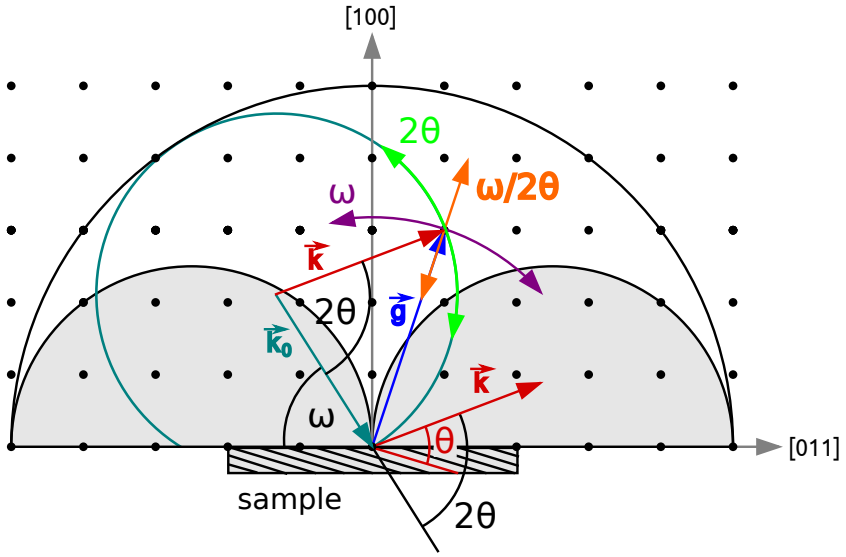

Fig. 2.17 – Ewald construction and limiting sphere in side view (modified after [245]): Reflexes within the limiting sphere (black line), where the Ewald sphere (petrol dashed line) intercepts the reciprocal lattice points, can be observed. The shaded areas are accessible only in transmission. Scan directions for ω, 2θ and $\omega/2\theta$ are indicated. A real space image of the sample indicates the lattice planes for Bragg's condition eq. (2.11) with $\theta = \theta_B$.

Films of finite thickness cause Laue oscillation fringes around the Bragg reflex [233]. In case of sufficient surface and interface smoothness as well as film quality, these fringes can be observed in $\omega/2\theta$ scans and the film thickness may be determined by the period of the side lobes. To reliably yield the N content and the film thickness, the diffractograms were fitted with a software considering dynamical scattering theory.

2.9.6 Mass spectrometry (MS)

Atoms and molecules may be identified by mass spectrometry (MS) according to their mass:charge ratio after ionization. In the setup applied here, a share of the processing gas ambient can be sidelined via a feedthrough in the quartz rod holding the susceptor. A bypass line (about 1.5 m in length) with a fine control valve connects the feedthrough with the main UHV chamber, which is equipped with a Hiden HAL-3F mass spectrometer. A quadrupole analyzer filters the species according to their mass:charge ratio and the ions are detected by a secondary electron multiplier. The measured signal cannot directly be converted to partial pressure in the MOVPE reactor and is therefore given in arbitrary units (a.u.). The multiple ion detection (MID) mode, where only certain mass:ratios are measured, was chosen and single ionization is assumed. *In situ* MS was established at HZB by A. Müller, more details regarding the setup are given in his diploma thesis [191].

2.9.7 Atomic force microscopy (AFM)

The morphology of the surface of a sample can be measured with atomic force microscopy (AFM). In this work, a Park XE-100 AFM with damping stage in an enclosure was used in air. Si tips with a diameter less than 5−10 nm were mounted on a cantilever, which is about 4 μm×100 μm in size. Measurements were performed in non-contact respectively tapping mode. The cantilever is excited close to resonance and its contortion is measured by reflection of a laser and a four segment diode. Van-der-Waals interaction influences the period and phase of the oscillation when approaching the surface. The height of the cantilever is adjusted to maintain a constant amplitude. Scanning the surface then yields a height profile of the surface. Convolution with the tip limits the lateral resolution to the tip diameter, while atomic heights may be resolved perpendicular to the surface.

2.9.8 Scanning tunneling microscopy (STM)

The quantum mechanical tunneling effect is used for imaging in scanning tunneling microscopy (STM). A sharp tip is approached to the surface of the sample, so that electrons may tunnel from the tip through the vacuum gap d to the surface or vice versa. The position of sample and tip can be controlled precisely by piezoelectric scanners. The tunneling current depends exponentially on d [30]. The surface can be scanned either in constant current mode, where the image corresponds to constant local density of states [121], or in constant height mode, where the voltage V_t and d are maintained and the tunneling current I_t is measured. For this work, a Specs Aarhus-150 STM was applied in UHV with electrochemically polished and *in vacuo* sputtered tungsten tips. Measurements were performed in constant current mode probing empty states. The STM measurements were performed by Dr. P. Kleinschmidt (HZB / TU Ilmenau), J. Luczak (HZB) respectively A. Nägelein (TU Ilmenau).

2.9.9 Photoluminescence (PL)

Recombination of photo-generated excitons occurs either radiative or non-radiative. The photoluminescence (PL) signal stems from radiative recombination and can be detected with both time and spectral resolution. The home built PL setup at HZB (Dr. K. Schwarzburg) consists of a laser diode, which is focused on the sample passing a beamsplitting mirror. A wavelength of $\lambda = 405\,\mathrm{nm}$ was used for this work. The PL light is coupled into a fiber optics (directed by the beamsplitter) and monochromatized before being detected by an avalanche photodiode. Gray and long pass filters may be used optionally. The resolution is about $\Delta\lambda \simeq 1\,nm$ at a minimum spot size of 10 μm. The photon density is in the range of $10^{13}\,\mathrm{cm}^{-2}$

per laser pulse at about 50 μW and 10 MHz pulse frequency. For details, see also Ref.[287].

2.10 RAS of Si(100), GaP(100) and GaP/Si(100) reference surfaces

The *in situ* RAS signals, which will be discussed in this work, contain rich information on the structure of the involved interfaces. Given different microscopic origins of anisotropy contributing to the spectra, their lineshapes often are complicated. In order to study the GaP nucleation and subsequent GaPN heteroepitaxy, a detailed understanding of RA spectra of both Si(100) substrates and GaP(100) reference surfaces is indispensable. Therefore, Si(100) preparation in hydrogen-based MOVPE ambient free of III-V residuals (which will be called "clean") and the *in situ* RAS signals will be summarized in section 2.10.1 on the basis of our preliminary work [44, 45]. In section 2.10.2, specific surface reconstructions of GaP(100) and their RA spectra will be introduced as recently reviewed in Ref.[84]. Also the influence of the buried GaP/Si(100) heterointerface on the lineshape of GaP/Si(100) surfaces will be discussed based on preliminary work performed at HZB [73, 78, 81, 83, 251]. In section 2.10.3, a model for separating surface and interface dielectric anisotropies from the measured RA spectra, will be introduced as published in Ref.[252, 254] as basis for the discussion in the main part of this work.

2.10.1 Si(100) surface preparation in clean H ambient

Figure 2.18(a) shows the RA spectra of differently terminated, almost exactly oriented Si(100) surfaces, which were prepared in UHV by Joule heating and subsequent hydrogenation of the surfaces [202]. Strain might contribute to the RA spectrum [125, 225], as Si dimers cause tensile surface strain along the dimer axis, respectively compressive strain along the dimer rows [7]. Also subjacent layers are distorted, at least to the 5th layer [7]. The main bulk-like contribution, however, is supposed to be induced by the anisotropic surface potential, which influences the bulk wave functions [225]. The different lineshapes enable to distinguish the termination of the Si(100) surface *in situ*. The RA spectrum of the monohydride-terminated Si(100) surface (Fig. 2.18(a), black line) is characterized by two peaks at the E_1 and close to the E_2 interband transitions, as well as a shoulder in between. It agrees well with previously published spectra [236]. Sign and intensity of the maximum at E_1 represent a majority T_B surface with a domain ratio of about 60:40 [202]. This feature is attributed to the influence of the surface anisotropy on the bulk states in the vicinity of the dimerized surface [202].

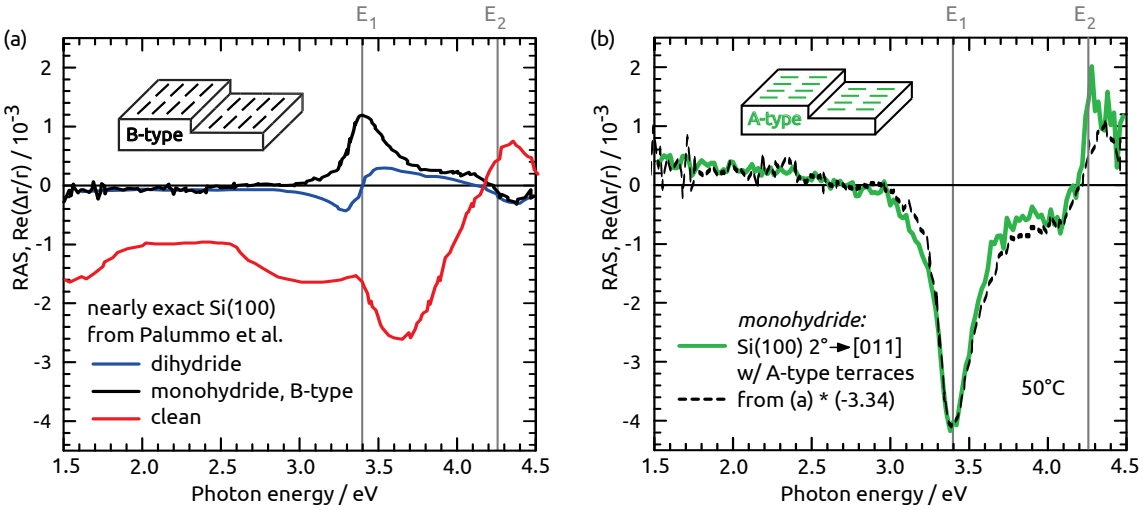

Fig. 2.18 – (a) RA spectra from differently terminated, almost exactly oriented Si(100) surfaces according to data from Palummo et al.[202]: clean (red line), monohydride T_B (black line), and dihydride (blue line) termination. (b) RAS of Si(100) with 2° misorientation towards [011] measured at 50 °C after annealing at 730 °C in 950 mbar H_2 compared to the flipped and scaled black spectrum from (a). The insets indicate the dimer orientation at T_B and T_A terraces, respectively.

Interaction with the process gas H_2 crucially impacts the surface preparation: Applying transient *in situ* RAS, we found that the energetically least favored T_A terraces form during annealing of Si(100) surfaces with 2° misorientation towards [011] at temperatures in the range of 730−750 °C in 950 mbar H_2 [44]. The final RA spectrum of such a surface is juxtaposed with that of the majority T_B surface of Palummo et al.[202] in Fig. 2.18(b). In case the latter is scaled by about $\cdot(-3.34)$, both spectra match well with only minor differences. By definition of the RAS signal, a flip of the sign corresponds to a rotation of the anisotropic structure by 90°. Two equally sized domains thus would sum to a canceled RAS signal. An unequal domain distribution with a minority domain concentration a causes a signal, which is a factor $m = 1/(1-2a)$ less intense compared to a single-domain reference. The spectrum of the 2° misoriented surface thus is caused by a preferential T_A terrace with a domain ratio of about 83:17. The contribution of steps, which are supposed to cause a broad feature at about 3 eV [225], seems negligible at 2° misorientation.

The RA transient in Fig. 2.19 on the facing page was measured during the annealing at 730 °C in 950 mbar H_2 at 3.1 eV, where the dimer-related RAS signal of the final surface exhibits a characteristic extremum, as shown in Fig. 2.18(b). As discussed above, the amplitude increases with an increasing majority domain. We explain this increase in T_A domains by Si vacancy generation at the terraces due to SiH_x formation upon hydrogen desorption [44], similar to previous experiments using Xe-ion bombardment to create vacancies [23, 258]. Anisotropic vacancy diffusion preferably along dimer rows [308] and annihilation of the vacancies at the end of the dimer rows [23, 258, 308] leads to a retreat of T_B terraces at 2° misori-

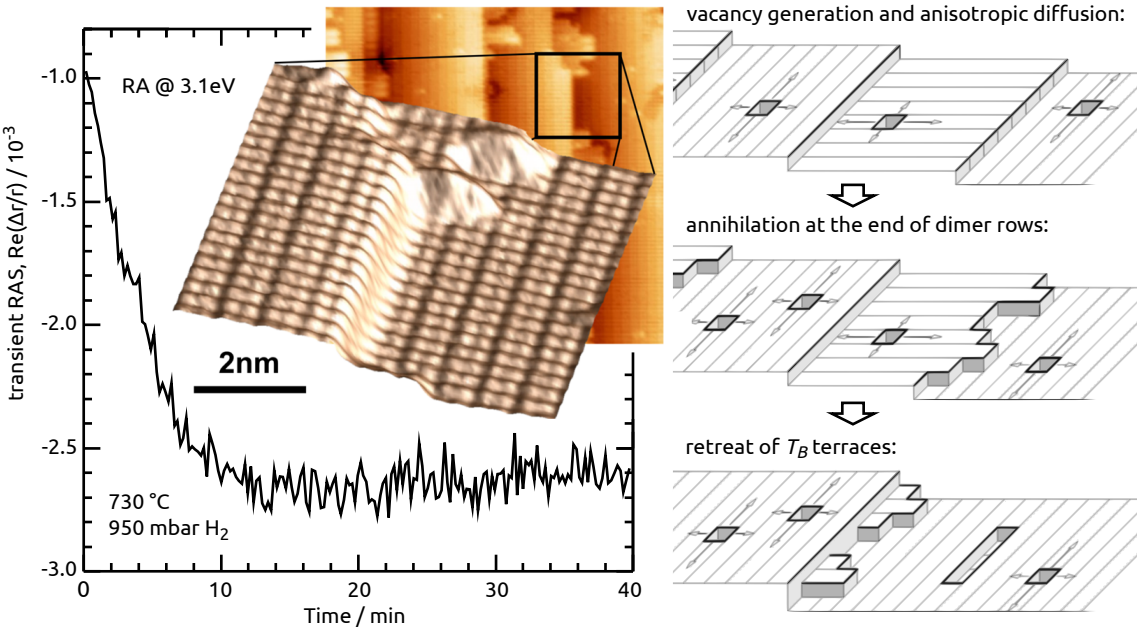

Fig. 2.19 – (left) Transient RAS during annealing of Si(100) 2° misoriented to [011] in 950 mbar H_2 at 730 °C (subsequent to annealing at 1000 °C). The inset shows an STM image (empty states) of the final surface with Si dimer rows parallel to the step edges defined by the misorientation, i.e. T_A terraces. *(right)* Schematic sketch of the anisotropic diffusion of Si vacancies (preferred along the dimer rows indicated by the lines) and their annihilation at the end of the dimer rows, which leads to a retreat of the B-type terrace.

ented substrates, where the diffusion length is large compared to the terrace width. Annealing of these Si(100) 2° surfaces at 730 °C in 950 mbar H_2 for 15 min results reproducibly in $T_A : T_B$ ratios of about 83:13 (as quantified via the amplitude of the RAS signal [44, 202]). The inset of Fig. 2.19 shows an STM image of such a surface, where the dimer rows at the terraces are mainly parallel to $[0\bar{1}1]$ (A-type) and only small residual B-type terraces are left at the step edges.

We found experimental evidence for the crucial role of the generation of Si vacancies studying almost nominal Si(100) surfaces: These have larger terraces, where single Si vacancies may coalesce to vacancy islands [23, 305]. When these islands reach a certain size, continued Si removal may occur also on the next layer. This leads to Si layer-by-layer removal during annealing at 770 °C in 950 mbar H_2, which we observed recently in Ref.[45]. Since the Si dimer orientation is rotated by 90 ° at every subsequently "etched" layer, the dimer-related RAS signal flips sign and the removal process results in monolayer oscillations visible in transient RAS measurements, as shown in Fig. 2.20 on the following page. Small residual domains are left before etching the next layer, which leads to a decrease in amplitude with time. Studying the removal at different temperatures, we could deduce an activation energy of (2.75±0.20) eV from the transient *in situ* RAS measurements via the Arrhenius equation, which agrees with SiH_x formation [45, 98]. Both preferential A-

type and B-type surfaces can be prepared when cooling rapidly at the corresponding stage of the removal process [45]. Figure 2.20(c) shows an STM images of a majority T_A surface, where vacancy islands are visible at the terraces. Continued Si removal, however, results in disordered terraces with rough step edges, as observed by STM in Fig. 2.20(d).

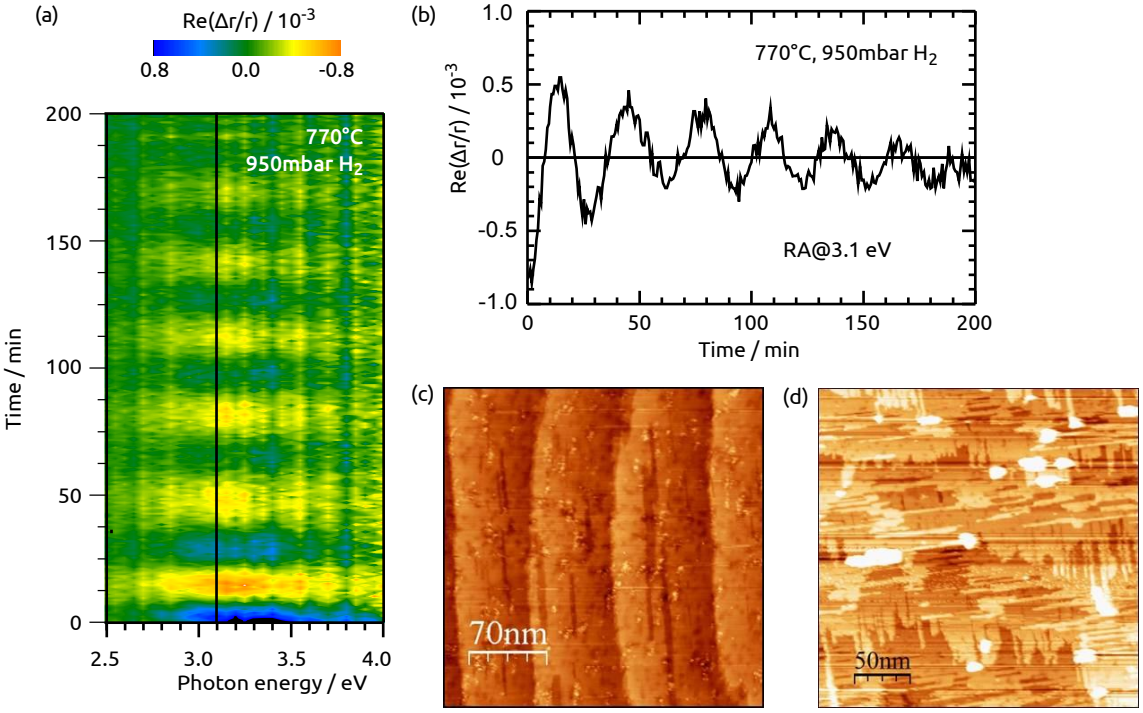

Fig. 2.20 – (a) RAS colorplot during annealing of Si(100) with 0.1° misorientation towards [011] in 950 mbar H_2 at 770 °C (subsequent to annealing at 1000 °C). (b) Transient at 3.1 eV from the colorplot shown in (a). (c) STM image of a final majority A-type Si(100) 0.1° surface (empty states) which was cooled rapidly to avoid layer-by-layer removal. (d) STM image of a Si(100) 0.1° surface (empty states) after annealing at 770 °C.

Consequently, the desired process conditions for T_A terraces are completely different for 2° and 0.1° misoriented Si(100) surfaces: While annealing at 730°C is necessary at Si(100) with 2° misorientation, it needs to be avoided at Si(100) with 0.1° misorientation. Figure 2.21 on the next page sketches the required temperature (straight lines) reactor pressure P_{react} (dashed lines) to yield preferentially A-type Si(100) surfaces for 0.1° (blue) and 2° misoriented towards [011] (red).[11] For both misorientations, the substrate is deoxidized thermally for 30 min at 1000 °C (950 mbar) prior to growth of an about 250 nm thick Si buffer with SiH_4 for 15 min at 950 °C (200 mbar), which is annealed for 10 min at 1000 °C (950 mbar) to yield a

[11] For simplicity, gradients of temperature and pressure ramps are only roughly estimated here.

smooth surface. Details on the thermal deoxidation process are discussed in Ref.s[73, 75–77, 80]. Subsequently, the process routes depend on the misorientation: Si(100) 2° misoriented to [011] is annealed for 15 min at 730 °C (950 mbar), while both pressure and temperature are ramped quickly for Si(100) 0.1° misoriented to [011] to avoid layer-by-layer removal.

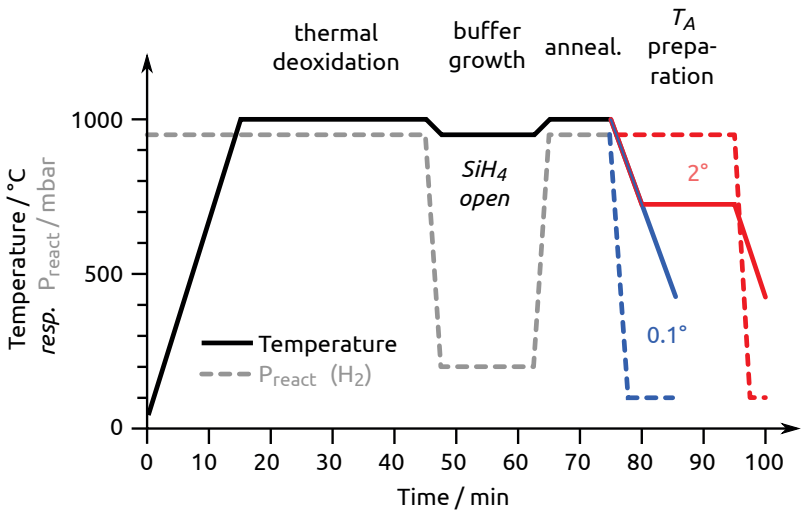

Fig. 2.21 – Temperature (straight lines) and H_2 reactor pressure P_{react} (dashed lines) required for T_A preparation of 0.1° (blue) and 2° (red) misoriented Si(100) in clean H_2 ambient.

The almost single-domain Si(100) surfaces with 2° misorientation serve as ideal starting point for this work. They can be reliably prepared in clean MOVPE ambient and RAS enables *in situ* control over the atomic order at the surface.

2.10.2 GaP(100) and GaP/Si(100) surface preparation

GaP(100)

Figure 2.22(a) shows the phase diagram of the surface reconstructions of GaP(100), which was calculated by Hahn et al.[116] in dependence on the chemical potential H (referred to molecular hydrogen) and (Ga, P). Two different surface reconstructions are typical for MOVPE preparation in hydrogen ambient:[12]

1. The “P-rich” surface, which consists of buckled P dimers stabilized by one H atom each (and a lone pair at the second P atom of the dimer) [116, 229, 270],

[12] For preparation in N-based ambient, see Ref.[82].

occurs during growth. Along the dimer rows, the buckled dimers are aligned in zig zag chains, as shown in Fig. 2.22(b). Different domains coexist, where those lines may arrange either in phase, causing a (2×2) reconstruction, or out of phase, leading to a $c(4 \times 2)$ reconstruction. Thermal excitation at room temperature causes flipping of the buckling [149]. Since P desorbs preferentially at temperatures above about 470 °C [78, 270], surfaces are commonly cooled with TBP stabilization after growth. This results in excess P and TBP fragments on the surface, which desorb during annealing without TBP stabilization at 420 ° [78, 270]. The (2×1)-like P dimers cause spots at half order along the dimer axis parallel to $[0\bar{1}1]$ in the LEED pattern and their buckling leads to streaks along $[0\bar{1}1]$ [270] (cf. Fig. 2.23 on page 44).

2. Desorption of P from the surface creates a "Ga-rich" surface, where a mixed Ga-P dimer is on top of a layer of Ga dimers [96, 173] (cf. Fig. 2.22(c). Commonly, this surface is prepared by annealing at 700 °C without precursor supply [78, 270].

Both surfaces can be distinguished *in situ* by their characteristic RA spectra, which were benchmarked by Töben et al.[270] to LEED and STM. Figure 2.22(d) compares experimental data from Ref.[270], which was measured at 20 K after contamination-free transfer to UHV (where the samples were mounted on the cold finger of a He cryostat) with calculated spectra from Hahn et al.[116] and Schmidt et al.[226, 230], respectively. Though the predicted intensities and lineshapes differ from the measured ones, the principal features of the experimentally observed spectra are reflected in the calculated spectra.

The main characteristics of the RAS signal of the "P-rich" $(2 \times 2)/c(4 \times 2)$ reconstructed GaP(100) surface are a sharp minimum, P_1, at about 2.6 eV, a shoulder at E_0^{GaP}, a maximum, P_2, about 100 meV below E_1^{GaP}, and a broad peak, P_3, beyond $E_0^{|}$. Hahn et al. attributed P_1 to a transition from the lone pair of the P dimer (located at the dimerized P atom which is not bound to H) into a surface resonant state. In analogy to InP(100) [278], P_2 is associated with a surface modified bulk E_1 transition.

The "Ga-rich" (2×4) mixed dimer reconstructed GaP(100) surface exhibits a rather broad minimum, Ga_1, around 2.45 eV, a smaller maximum, Ga_2 at 3.3 eV, a minimum, Ga_3 close to the E_1 transition, and a maximum, Ga_4, close to $E_0^{|}$. Schmidt et al.[226] showed that Ga_1 is the result of transitions from the Ga–Ga bonds below the mixed dimer into a series of surface states. Similar to InP(100) [227], Ga_2 arises from transitions between dimer states and surface resonances [226]. Ga_3 and Ga_4 in, contrast, stem from surface modified bulk states [96, 226].

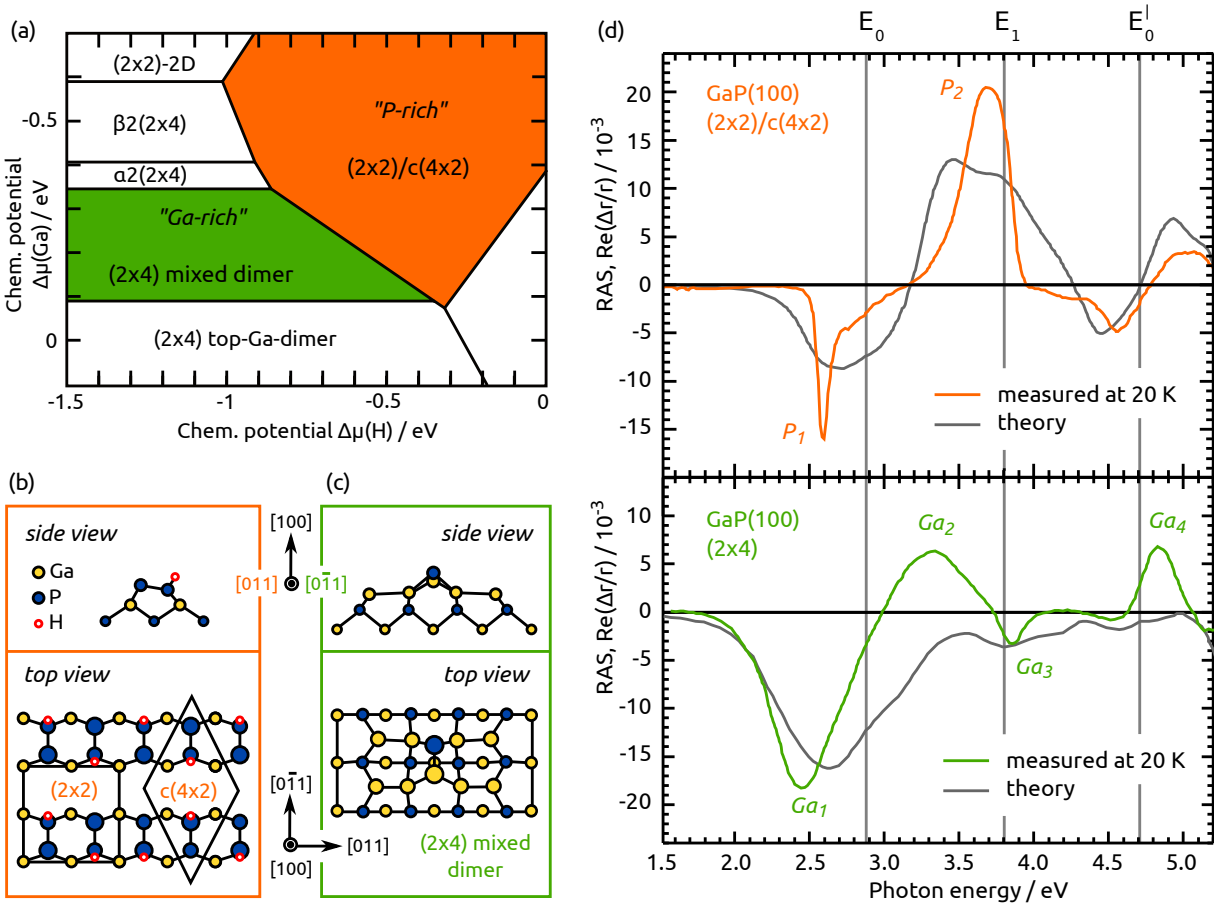

Fig. 2.22 – (a) Phase diagram of GaP(100) surface reconstructions in hydrogen based ambient (modified after [116]). (b) Side view (facing [011]) and top view of the $(2 \times 2)/c(4 \times 2)$ surface reconstruction of GaP(100). (c) Side view (facing $[0\bar{1}1]$) and top view of the (2×4) surface reconstruction of GaP(100). (d) RA spectra of GaP(100) with $(2 \times 2)/c(4 \times 2)$ reconstruction (orange) and (2×4) reconstruction (green) measured at 20 K in comparison to calculated spectra (gray, dash-dotted) for the according surface reconstruction (data from Ref.[116, 230, 270]). Grey vertical lines indicate the interband transition energies of GaP at 20 K [311].

GaP/Si(100)

RA spectra of pseudomorphic GaP/Si(100) heterostructures are GaP(100)-like in the sense that the identical surface reconstruction causes the main spectral features, which are superimposed by anisotropies arising at the GaP/Si(100) heterointerface and Fabry-Pérot-like interference due to internal reflection [78, 79, 81, 83, 254]. Figure 2.7 on page 14 shows that antiphase disorder leads to two inverted GaP sublattice domains. Due to the tetrahedral coordination of the zincblende crystal, this results in a rotation of the unit cell of the surface by 90°. Despite that rotation, the uppermost atoms at the terraces form identical reconstructions. Figure 2.23 on the following page visualizes this comparing the LEED pattern of GaP(100) with that of a two-domain GaP/Si(100) surface. The RA spectra shown in Fig. 2.22 are

also related to the dimers at the surface. Given the definition of the RAS signal in eq. (2.7) on page 26, a rotation of anisotropic structures by 90° flips the sign of the RAS signal caused by that structure. Since RAS inherently integrates over the entire spot size (in mm^2 range), this allows to quantify the APD concentration *in situ* analogously to Si(100) in section 2.10.1, as exemplified in Fig. 2.24. Scaling the spectrum by m to a single-domain reference yields the APD concentration $a = 0.5\,(1 - 1/m)$ at the GaP/Si(100) surface [78]. Note that this not necessarily corresponds to the domain concentration at the Si(100) surface prior GaP growth, since APDs may annihilate within the GaP epilayer [139, 194]. In order to study the Si(100) surface indirectly via the GaP/Si(100) surface, growth conditions for straight APD propagation must be chosen, as done in Ref.[83]. Instead of scaling the spectra directly [79], interference at the buried heterointerface needs to be considered for pseudomorphic GaP films, since absorption is small for photon energies below E_1 so that both P_1 and P_2 may be affected by interference [73, 252]. Figure 2.24(c) juxtaposes the RA spectrum of a $(2\times2)/c(4\times2)$ reconstructed GaP/Si(100) surface with that of GaP(100). While the amplitudes match at P_1, the amplitudes at P_2 do not match. APD quantification by RAS is not directly possible here. The main reason is Fabry-Pérot-like interference at the buried heterointerface: Even with the assumption of identical anisotropies Δr for GaP(100) and GaP/Si(100), interference enters the RAS signal via the normalization with r. Within an empirical model [73, 78, 81], this can be accounted for by the relative reflectance $R_{\mathrm{rel}} = R_{\mathrm{GaP/Si}}/R_{\mathrm{GaP}}$ (with the assumption of an identical apparatus function for the measurements of GaP(100) and GaP/Si(100), which cancels in R_{rel}): The corrected signal $\mathrm{Re}\,(\Delta\hat{r}/\hat{r})$

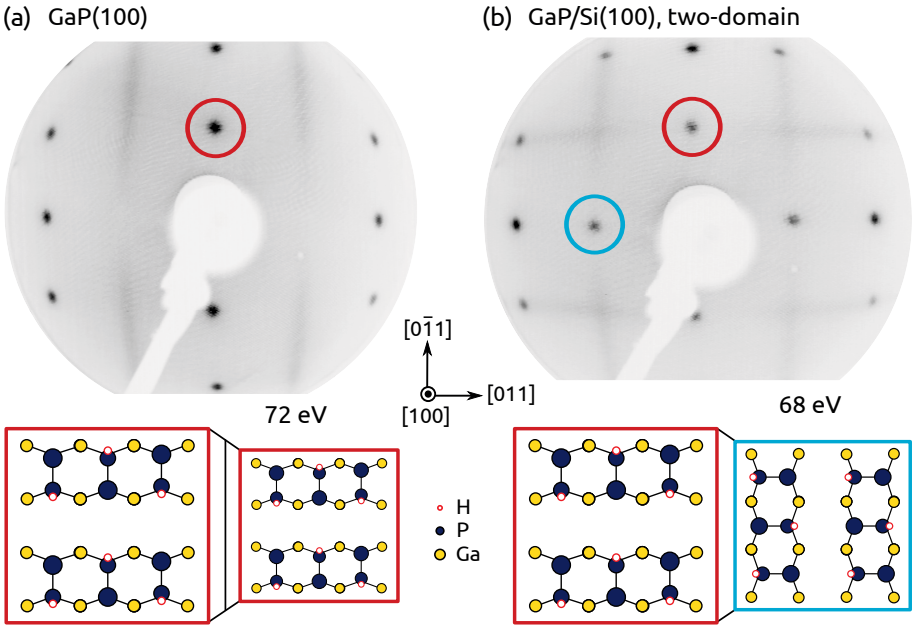

Fig. 2.23 – LEED patterns of $(2\times2)/c(4\times2)$ reconstructed surfaces of (a) GaP(100) and (b) two-domain GaP/Si(100). Circles mark spots at half order.

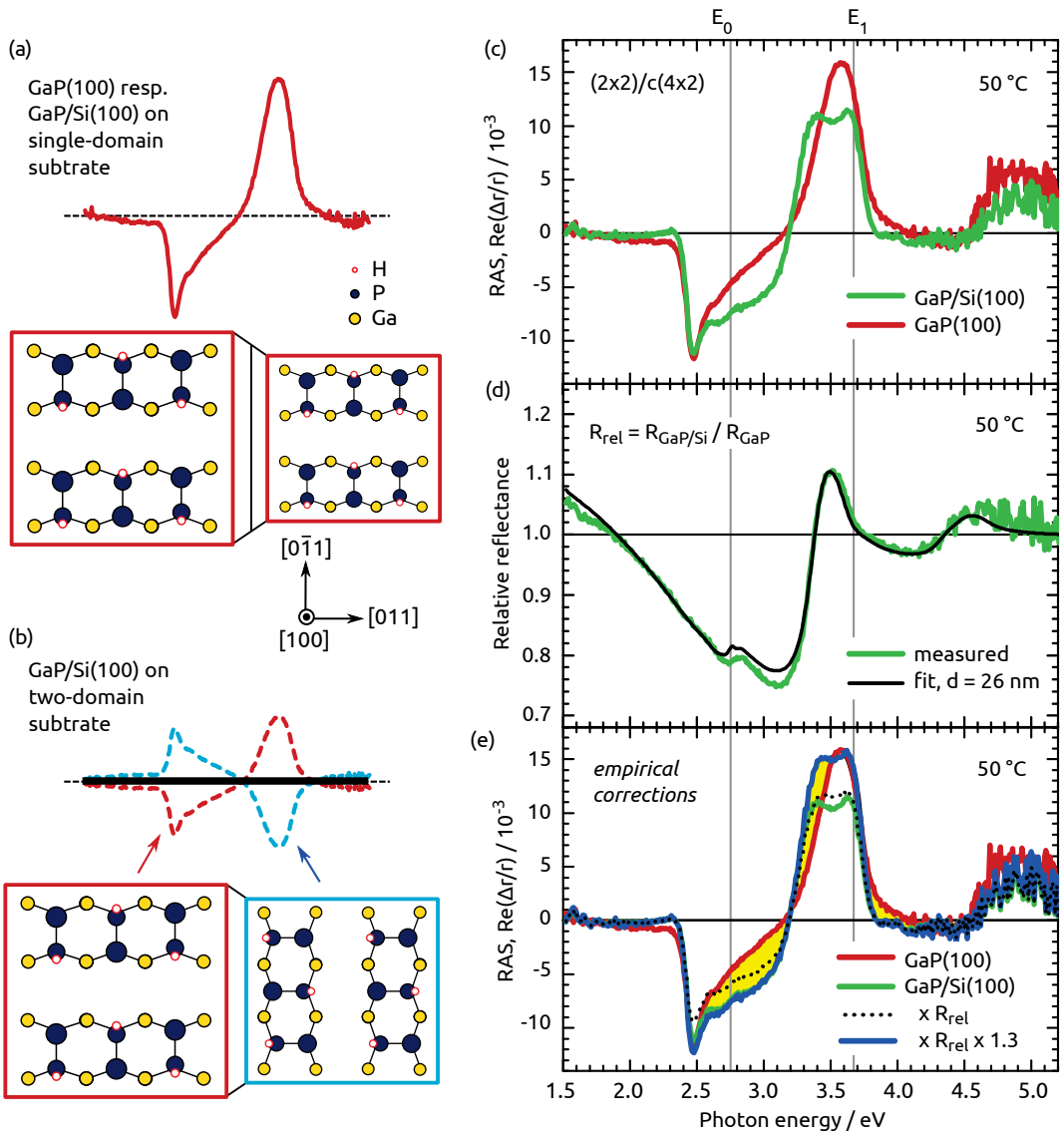

Fig. 2.24 – RAS of $(2 \times 2)/c(4 \times 2)$ reconstructed GaP/Si(100) and empirical APD quantification: (a) APD-free GaP epilayers can be grown on single domain Si(100) substrates. The dimer contribution to the RAS signal is identical to that of GaP(100) (red terrace). (b) Two-domain substrates with single-layer steps induce antiphase disorder. The dimer orientation of the antiphase domain is rotated by 90° referring to GaP(100) (blue terrace). Accordingly, dimer-induced anisotropies exhibit a RAS signal of opposite sign. In case the both domains are equally in size, the RAS signal cancels (black line). (c) RAS of $(2 \times 2)/c(4 \times 2)$ reconstructed GaP/Si(100) (green) in comparison to GaP(100) (red). (d) Relative reflectance spectra R_{rel} for the samples shown in (c) (green). The fit (black) yields a GaP epilayer thickness of 26 nm. (e) Empirical interference correction (by multiplication of the GaP/Si(100) RAS signal with R_{rel}, black dots) and subsequent scaling with a factor $m = 1.3$ to account for an APD concentration of 11.5 % at the GaP/Si(100) surface. (modified after [251])

is normalized by the signal of the GaP(100) reference,

$$\begin{aligned} \mathrm{Re}\left(\frac{\Delta\hat{r}}{\hat{r}}\right) &= \mathrm{Re}\left(\frac{\Delta r_{\mathrm{GaP/Si}}}{r_{\mathrm{GaP/Si}}}\right)\cdot R_{\mathrm{Rel}} = \mathrm{Re}\left(\frac{\Delta r_{\mathrm{GaP/Si}}}{r_{\mathrm{GaP/Si}}}\right)\cdot\frac{R_{\mathrm{GaP/Si}}}{R_{\mathrm{GaP}}} \\ &\approx \mathrm{Re}\left(\frac{\Delta r_{\mathrm{GaP/Si}}}{r_{\mathrm{GaP}}}\right) \quad , \end{aligned} \tag{2.14}$$

where $\Delta R/R \approx 2\,\mathrm{Re}(\Delta r/r)$ for $\Delta r \ll r$ and the assumption $\Delta r_{\mathrm{GaP/Si}} = \Delta r_{\mathrm{GaP}}$ is used. Fitting R_{rel} with dielectric functions from literature [14] also yields the thickness of the GaP epilayer [113, 114]. Figure 2.24(e) shows the resulting $\mathrm{Re}\,(\Delta\hat{r}/\hat{r})$ spectrum (black dots) for the samples from Fig. 2.24(e) and R_{rel} from Fig. 2.24(d). Subsequent scaling by a factor $m = 1.3$ results in matching amplitudes at both P_1 and P_2 (blue line). The corresponding APD concentration is $a = 11.5\,\%$. Note, however, that even the scaled spectrum differs from that of the GaP(100) reference (yellow area), most prominent in between P_1 and P_2. This indicates that the assumption $\Delta r_{\mathrm{GaP/Si}} = \Delta r_{\mathrm{GaP}}$ does not hold. Besides possible contributions from crystal defects or strain in the GaP epilayer, the GaP/Si(100) heterointerface is a potential source for dielectric anisotropies.

2.10.3 Surface and interface dielectric anisotropies

Parts of this section are reprinted in part, with permission from Phys. Rev. B 86, 35308 [254], ©2012 American Physical Society.

In general, the RA spectrum of a thin transparent film grown on an optically isotropic crystal contains signal contributions from different sources of optical anisotropy, including those from the surface $\Delta r_{\mathrm{sf}}/r_{\mathrm{sf}}$, the interface $\Delta r_{\mathrm{if}}/r_{\mathrm{if}}$, and the bulk Δn of the film.

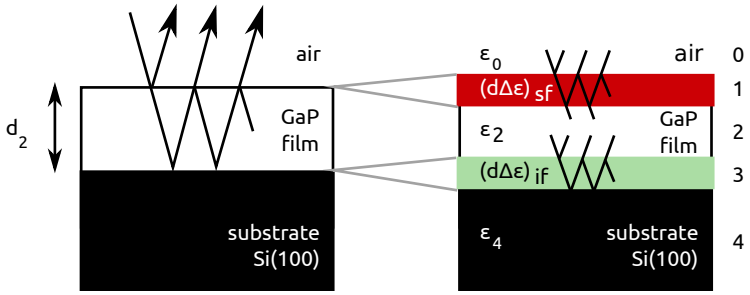

Fig. 2.25 – Three and five layer model as suggested by Yasuda[298].

Yasuda [298] modeled the dielectric response assuming small anisotropic contributions, i.e. by expressing them as partial derivatives of the (complex) three layer Fresnel reflection coefficient. Hunderi et al.[127] developed a five layer model following Yasuda's suggestion to treat both the anisotropic surface and interface as

independent layers. The derivation given by Hunderi et al. requires both transmission and reflection coefficients [127]. The complex (amplitude) transmission and reflection coefficient of a three layer system is denoted t_{ijk} and r_{ijk}, respectively, where the indices (ijk) number the different media (Fig. 2.25) in the sequence of light propagation.[13] For the transmission amplitude coefficients t_{ijk} of the two sub stacks (012) and (234), the interference of multiple transitions must be taken into account considering the phase compared to the incoming light. In analogy to the well-known Fresnel reflection coefficient for a non-magnetic three layer stack under normal incidence [17], this is fulfilled by

$$t_{ijk} = \frac{t_{ij}\, t_{jk}\, \exp(\imath\, \beta_j)}{1 + r_{ij}\, r_{jk}\, \exp(2\imath\, \beta_j)} \quad , \tag{2.15}$$

where $\imath$ denotes the imaginary unit and $\beta_j = 2\pi n_j d_j/\lambda$ with the (complex) index of refraction $n = n(\lambda)$ and the thickness d_j of the intermediate layer. Assuming $\beta \ll 1$, i.e. very thin layers, a Taylor expansion around $\beta = 0$ in first order leads to

$$\frac{t_{ijk}}{t_{ik}} = 1 + \imath\, \beta_j \frac{n_j^2 + n_i n_k}{n_j(n_i + n_k)} \quad , \tag{2.16}$$

where $t_{ik} = t_{ijk}(d_j = 0)$. Further simplification using the corresponding reflection ratios r_{ijk}/r_{ik}, given by Hunderi et al.[127] in reference to McIntyre and Aspnes [183], leads to

$$\frac{t_{ijk}}{t_{ik}} = \frac{1}{2}\left(\frac{r_{ijk}}{r_{ik}} + \frac{r_{kji}}{r_{ki}}\right) = \frac{t_{kji}}{t_{ki}} \quad . \tag{2.17}$$

In contrast to the derivation of Hunderi et al.[127], eq. (2.17) does not contain an additional anisotropic contribution $\delta_t = \beta_1$.[14] Neglecting bulk contributions and applying $\delta_t = 0$ to eq. (10) of Ref.[127], the RAS signal can be expressed as

$$\frac{\Delta r}{r} = w_s(d_2, \lambda) \cdot\, d\Delta\varepsilon|_{\mathrm{sf}}(\lambda) + w_i(d_2, \lambda) \cdot\, d\Delta\varepsilon|_{\mathrm{if}}(\lambda) \quad , \tag{2.18}$$

with the weighting coefficients

$$w_s(d_2, \lambda) = \frac{4\pi}{\imath\lambda} \frac{n_0}{\varepsilon_2 - \varepsilon_0} \left[1 - \frac{n_2}{n_0} \cdot v(d_2, \lambda)\right] \quad , \tag{2.19}$$

$$w_i(d_2, \lambda) = \frac{4\pi}{\imath\lambda} \frac{n_2}{\varepsilon_4 - \varepsilon_2} \cdot v(d_2, \lambda) \quad , \tag{2.20}$$

$$v(d_2, \lambda) = \frac{r_{24}\,(1 - r_{02}^2)\, \exp(2\imath\, \beta_2)}{[r_{02} + r_{24} \exp(2\imath\, \beta_2)][1 + r_{02} r_{24} \exp(2\imath\, \beta_2)]} \quad , \tag{2.21}$$

[13] Hunderi et al. use the notation t_{ij} [r_{ij}] for the transmission [reflection] coefficient at the interface (ij) and τ_{ik} [ϱ_{ik}] for three layers [127]. The notation of McIntyre and Aspnes [183] is used here, so that $\tau_{ik} \equiv t_{ijk}$, $\varrho_{ik} \equiv r_{ijk}$, $t_{ik} = t_{ijk}(d_j = 0)$, and $r_{ik} = r_{ijk}(d_j = 0)$.

[14] Assuming a factor 2 in the (nominator) exponential of t_{012} in eq. (2) would lead to $\delta_t = \imath\, \beta_1$.

and the (complex) dielectric function $\varepsilon = \varepsilon(\lambda)$. In this notation, the imaginary parts of the surface dielectric anisotropy $d\Delta\varepsilon|_{\mathrm{sf}}$ (SDA) and interface dielectric anisotropy $d\Delta\varepsilon|_{\mathrm{if}}$ (IDA) are related to the real part of the surface and interface signal, $\Delta r_{\mathrm{sf}}/r_{\mathrm{sf}}$ and $\Delta r_{\mathrm{if}}/r_{\mathrm{if}}$, respectively [183]. The thickness of the thin anisotropic surface and interface layers is denoted with d (without index). Beyond a certain film thickness $d_2 \gg d$, SDA and IDA are expected to be independent of d_2 [127]. In eq. (2.18), d_2 contributes to the RAS signal only via β_2 in the weighting coefficients $w_s(d_2, \lambda)$ and $w_i(d_2, \lambda)$, which can be calculated from bulk optical properties.

This leads to an analytically solvable equation system for the SDA and the IDA, when evaluating eq. (2.18) with two RA spectra of similar samples with different film thickness d_2, but identically prepared surfaces and interfaces. According to eq. (2.18), the result obtained for a pair of samples $\chi = (\mu, \nu)$ is the SDA

$$d\Delta\varepsilon|_{\mathrm{sf}} = \frac{w_{i,\mu} \cdot \dfrac{\Delta r_\nu}{r_\nu} - w_{i,\nu} \cdot \dfrac{\Delta r_\mu}{r_\mu}}{w_{s,\nu} \cdot w_{i,\mu} - w_{s,\mu} \cdot w_{i,\nu}} \quad , \tag{2.22}$$

and the IDA

$$d\Delta\varepsilon|_{\mathrm{if}} = \frac{w_{s,\mu} \cdot \dfrac{\Delta r_\nu}{r_\nu} - w_{s,\nu} \cdot \dfrac{\Delta r_\mu}{r_\mu}}{w_{s,\mu} \cdot w_{i,\nu} - w_{s,\nu} \cdot w_{i,\mu}} \quad . \tag{2.23}$$

For consideration of antiphase disorder, sample specific linear factors m_χ can be introduced for the SDA,[15]

$$d\Delta\varepsilon|^{m}_{\mathrm{sf}} = \frac{w_{i,\mu} \cdot \dfrac{\Delta r_\nu}{r_\nu} - w_{i,\nu} \cdot \dfrac{\Delta r_\mu}{r_\mu}}{m_\nu \cdot w_{s,\nu} \cdot w_{i,\mu} - m_\mu \cdot w_{s,\mu} \cdot w_{i,\nu}} \quad . \tag{2.24}$$

Antiphase disorder can then be quantified numerically by a least square fit of the SDA of GaP/Si(100) from eq. (2.24) to the SDA of a GaP(100) reference SDA under variation of $m_\chi \geq 1$.

Assuming that the SDA of GaP/Si(100) equals the SDA of homoepitaxial GaP(100), denoted $d\Delta\varepsilon|^{\mathrm{GaP}}_{\mathrm{sf}}$, IDA spectra can be obtained directly from the RAS data of individual samples applying $m^{-1} \cdot\ d\Delta\varepsilon|^{\mathrm{GaP}}_{\mathrm{sf}}$ as additional input,

$$d\Delta\varepsilon|_{\mathrm{if}} = \frac{1}{w_i}\left(\frac{\Delta r}{r} - \frac{w_s}{m} \cdot\ d\Delta\varepsilon|^{\mathrm{GaP}}_{\mathrm{sf}}\right) \quad . \tag{2.25}$$

[15] A similar influence on the IDA could be taken into account as well. However, due to identical nucleation procedure, the interface formation should be similar on all samples and in this case such a factor would cancel out in eq. (2.22).

3

On the atomic structure of GaP/Si(100) heterointerfaces

In the following, the atomic structure of the GaP/Si(100) heterointerface and its impact on subsequent GaP heteroepitaxy will be investigated. At first, surface states at GaP(100) reference surfaces will be discussed. The focus is then on surface preparation of Si(100) surfaces with 2° misorientation towards [011] in "realistic" GaP processing ambients, which contain III-V residuals. The dependence of the sublattice orientation of GaP epilayers on the type of Si(100) substrate surface will be referred to. This leads to a model of the heterointerface structure deduced indirectly via surface dimers. Subsequently, time-resolved RAS measurements during pulsed GaP nucleation are benchmarked by XPS to resolve the chemical composition of the heterointerface. The corresponding interface dielectric anisotropy is calculated from thicker GaP epilayers. Then, experimental results will be compared to DFT calculations of interface formation energies. Subsequently, the influence of (Ga, P) background residuals on GaP/Si(100) heteroepitaxy will be discussed. Finally, As-terminated Si(100) surfaces and subsequent GaP heteroepitaxy will be in focus. Parts of this work have been published in Ref.s[239, 253, 256].

3.1 Surface states at GaP(100) surfaces

The GaP(100) surface is an important reference for this work, as pseudomorphic GaP epilayers grown on Si(100) reconstruct analogously to GaP(100) [78]. In section 2.10.2, the two different surface reconstructions, which are typical for GaP(100) in MOVPE ambient, were introduced: (i) the $(2\times2)/c(4\times2)$ reconstructed GaP(100) surface, which is terminated by buckled P dimers that are stabilized by one H atom each, and (ii) the (2×4) reconstructed GaP(100) surface, which is formed by a mixed P–Ga dimer atop on a layer of Ga atoms. The RA spectra of those two GaP(100) surfaces have been established and benchmarked to surface science techniques in previous studies [270]. Spectral RA features have been assigned to transitions involving surface states by comparison to density functional theory calculations [116, 226]. We studied GaP(100) surface states with two-photon-photoemission (2PPE) to give also experimental evidence for those assignments.[16] Parts of these results have been published in Ref.[239].

$(2 \times 2)/c(4 \times 2)$ and (2×4) reconstructed GaP(100) surfaces were prepared after homoepitaxial buffer growth (see section 2.10.2 for experimental details) and transferred contamination-free from the MOVPE reactor to a mobile UHV chamber [119], which exhibits a base pressure of about $4 \cdot 10^{-10}$ mbar. After transfer to another UHV chamber at an optical table, we performed 2PPE measurements on the freshly prepared GaP(100) surfaces. The basic principle of 2PPE is that the photon energy is lower than the ionization energy. Two photons thus need to be absorbed during one laser pulse to reach the vacuum level. Both coherent absorption of two photons or excitation via intermediate states are possible, which enables the simultaneous study of occupied and unoccupied states [238]. We identified surface states by comparing 2PPE spectra before and after O_2 exposure. Surface states show no dispersion in $k_\perp$ perpendicular to the surface and only normal emission is detected. Hence, unoccupied surface states (i.e. intermediate states) retain their energy upon variation of the excitation energy [143, 239]. Virtual intermediate state energies (related to occupied surface states), in contrast, depend linearly on the photon energy [143, 239].

We are able to identify one occupied surface state, $SS^{\mathrm{O}}_{\mathrm{P}}$, for the $(2\times2)/c(4\times2)$ reconstructed GaP(100) surface as well as one occupied surface state, $SS^{\mathrm{O}}_{\mathrm{Ga}}$, and two unoccupied surface states, $SS^{\mathrm{U1}}_{\mathrm{Ga}}$ and $SS^{\mathrm{U2}}_{\mathrm{Ga}}$, respectively, for the (2×4) mixed dimer GaP(100) surface. Their energetic positions are given in Fig. 3.1 on the next page.[17] It is likely that the identified surface states are also anisotropic along [011] and [0$\bar{1}$1]

[16] 2PPE was performed by P. Sippel and the according measurements will be discussed in detail in his Ph.D. thesis [238].

[17] The accuracy for the alignment of 2PPE peaks with respect to the bulk bands here is about 0.2 eV, as discussed in Ref.[239].

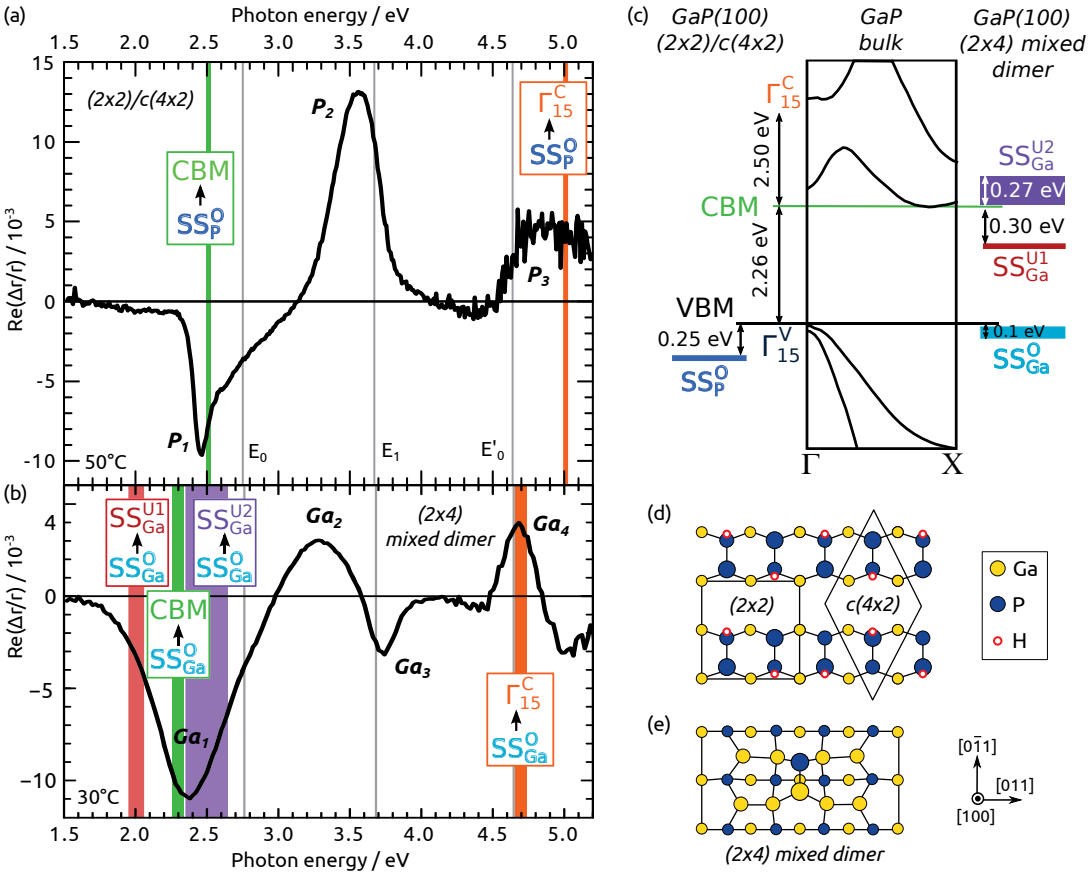

Fig. 3.1 – RA spectra of (a) $(2 \times 2)/c(4 \times 2)$ reconstructed GaP(100) and (b) (4×2) reconstructed GaP(100) surfaces (from Ref.[182]). Vertical lines indicate the critical point energies of GaP[310] (gray) as well as possible transitions involving surface states that were measured with 2PPE (see text, colored according to the final state drawn in (c)). (c) Energetic positions of surface states for both GaP(100) surface reconstructions [239] and a sketch of the bulk band structure (after Fraj et al.[94]). (d) Top view of the $(2 \times 2)/c(4 \times 2)$ GaP(100) surface reconstruction (after Hahn et al.[116] resp. Kleinschmidt et al.[149]). (e) Top view of the (4×2) mixed dimer GaP(100) surface reconstruction (after Frisch et al.[96]).

direction, since the atomic arrangements of both GaP(100) surface reconstructions discussed here are unsymmetric. In case they are indeed anisotropic, and in case transitions involving them are allowed in terms of dipole selection rules, they can contribute to the RAS signal of the corresponding GaP(100) surfaces. Figure 3.1 shows the RA spectra (a) of $(2 \times 2)/c(4 \times 2)$ reconstructed GaP(100) and (b) of (4×2) reconstructed GaP(100), which were measured at about 50 °C and 30 °C, respectively. The corresponding surface reconstructions [96, 116] are sketched in (d) and (e), respectively. The spectral features are described in detail in section 2.10.2. In Fig. 3.1(a,b), we marked energetic positions of electronic transitions involving at least one of the $SS^{\mathrm{O}}_{\mathrm{P}}$, $SS^{\mathrm{O}}_{\mathrm{Ga}}$, $SS^{\mathrm{U1}}_{\mathrm{Ga}}$ or $SS^{\mathrm{U2}}_{\mathrm{Ga}}$ surface states. The transition energy from $SS^{\mathrm{O}}_{\mathrm{P}}$ to the conduction band minimum (CBM) (resp. a resonant state) agrees well with the position of P_1. We find no transition involving surface states for P_2, as

is expected for a surface modified bulk transition. P_3 could be related to a transition between $SS^{\mathrm{O}}_{\mathrm{P}}$ and states resonant to Γ^{c}_{15}. Ga_1 coincides with a series of transitions each involving $SS^{\mathrm{O}}_{\mathrm{Ga}}$ as initial and $SS^{\mathrm{U1}}_{\mathrm{Ga}}$, $SS^{\mathrm{U2}}_{\mathrm{Ga}}$ or a CBM resonant state as final state, which could explain the broad peak width compared to P_1. Though Ga_2 is predicted to be related to dimer states [226], we find no transitions that could be related to Ga_2 and neither for the surface modified bulk transition Ga_3. Ga_4 could be caused by either a surface modified $\mathrm{E}^{|}_{0}$ bulk transition or a transition from $SS^{\mathrm{O}}_{\mathrm{Ga}}$ to Γ^{c}_{15} resonant states. We find that Ga_4 partly remains after exposing the surface to O_2 [239], which indicates that both transitions may be involved here. Also, polarization dependent 2PPE measurements on the (2×4) reconstructed GaP(100) surface were performed. For $SS^{\mathrm{O}}_{\mathrm{Ga}}$, we could prove anisotropic behavior [238].

In consequence, we found experimental evidence for predicted surface states, which induce the characteristic RA spectra of $(2 \times 2)/c(4 \times 2)$ and (2×4) GaP(100) surfaces: $SS^{\mathrm{O}}_{\mathrm{Ga}}$ agrees with the predicted Ga–Ga related states below the mixed Ga–P dimer [226]. $SS^{\mathrm{U1}}_{\mathrm{Ga}}$ and $SS^{\mathrm{U2}}_{\mathrm{Ga}}$ likely arise from the dangling bonds of the Ga atoms which were predicted as final states causing Ga_1 [226]. Analogously, we identify $SS^{\mathrm{O}}_{\mathrm{P}}$ as caused by the lone pair of the P dimer predicted in the vicinity of the valence band maximum (VBM). Future 2PPE experiments to probe also the interface states of GaP/Si(100) heterostructures are planned.

3.2 Si(100) surface preparation prior to nucleation

The atomic order and step structure at the Si(100) surface prior III-V nucleation is of essential importance regarding the formation of III-V/Si(100) heterointerfaces. Antiphase disorder, for example, is inherently introduced at single-layer substrate steps, as discussed in section 2.4. Though appropriate growth conditions can lead to a kinking of antiphase boundaries (APBs) and their annihilation when they converge [139, 193, 194], double-layer (resp. even-numbered) steps at the substrate surface prior to heteroepitaxy enable single-domain III-V growth from the first monolayers. Besides antiphase disorder, also the electronic structure across the interface will depend on the atomic structure of the GaP/Si(100) heterointerface.

In the following, our previous results from "clean" MOVPE ambient free of III-V residuals (cf. section 2.10.1) will be transferred to "realistic" III-V processing ambient. Regarding dimer orientations at the involved surfaces, the notation of Chadi [52] will be used (see section 2.3). For convenience, the same labels will be used for P dimers at the $(2 \times 2)/c(4 \times 2)$ reconstructed GaP/Si(100) surfaces.[18]

[18] Focusing on the P dimers only (i.e. neglecting the H atom and the lone pair), the $(2 \times 2)/c(4 \times 2)$ reconstruction of GaP(100) can be considered "(2×1)-like". Note that the terms "A polarity" resp. "B polarity", which are common for III-V(111) material, are defined differently.

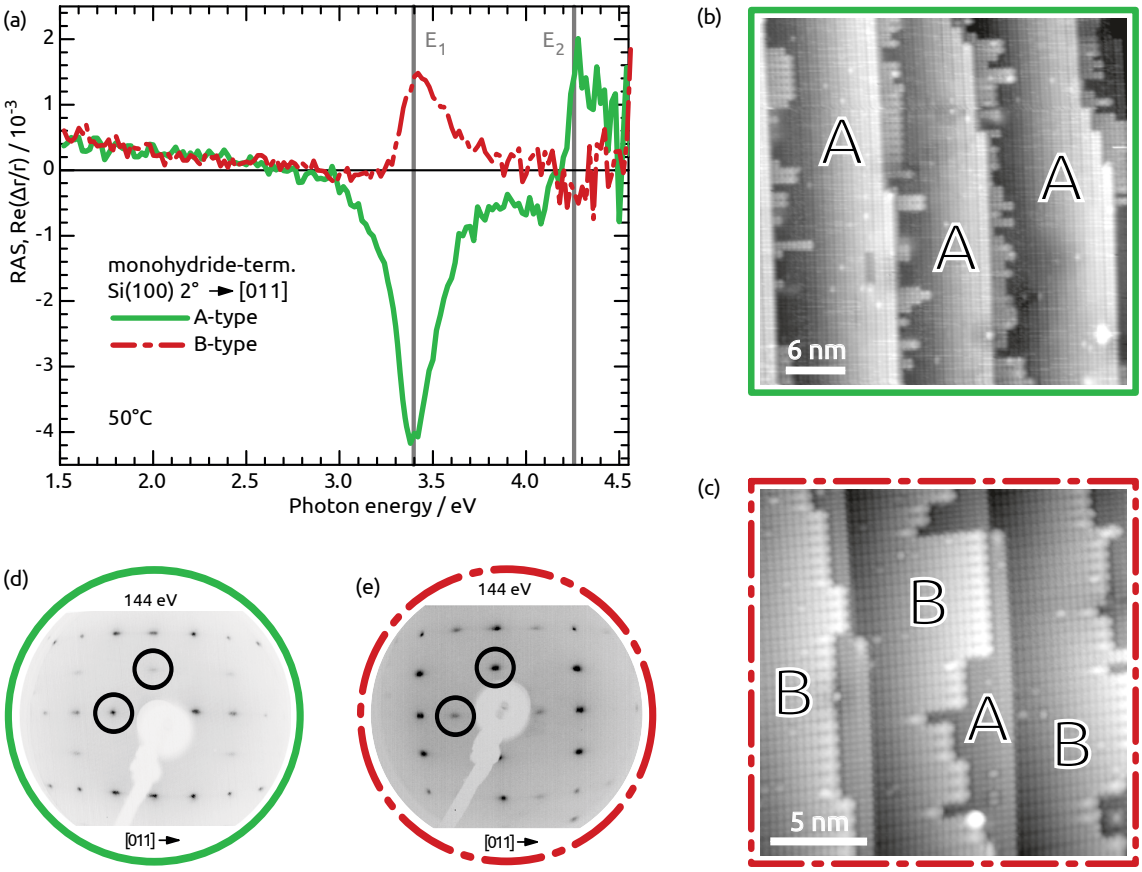

Fig. 3.2 – (a) RA spectra of monohydride-terminated Si(100) with 2° misorientation towards [011] exhibiting A-type majority domains (green line) and B-type majority domains (red broken line), respectively (both measured at 50 °C). Vertical gray lines mark the critical point energies of Si.[165] (b) STM image (empty states, $I_t = 170\,\mathrm{pA}$, $V_t = 1.24\,\mathrm{V}$) of the A-type sample. (c) STM image (empty states) of the of the B-type sample. Letters in the STM images denote the terrace type. (d) LEED pattern of the A-type sample. (e) LEED pattern of the B-type sample. Spots at half-order (marked with circles) occur along the dimer orientation of the majority domain.

As discussed in section 2.10.1, annealing of Si(100) with 2° misorientations towards [011] in 950 mbar H_2 at temperatures around 730 °C leads to a retreat of T_B towards the step edges. Subsequent cooling stabilizes the T_A surfaces with constant H termination [43]. The green line in Fig. 3.2 shows the *in situ* RAS signal of such an A-type Si(100) surface, which will be abbreviated *Si-A* in the following. Characteristic features are a pronounced local minimum at E_1, a shoulder between 3.6 eV and 4.0 eV, as well as a local maximum at the E_2 critical point energy [44, 202]. The corresponding STM image in Fig. 3.2(b), which was measured after contamination-free transfer to UHV, shows mainly A-type terraces with dimer rows oriented parallel to the step edges along $[0\bar{1}1]$ direction. Only small residuals of B-type terraces are visible, which indicates an almost single-domain surface. Accordingly, the diffraction spots at half order in the corresponding LEED pattern in Fig. 3.2(d) are intense along [011] direction.

The kinetically-driven formation of *Si-A* crucially depends on the Si–H interaction. A reduction of the H_2 pressure from 950 mbar to 50 mbar and omitting of the annealing at 730 °C leads to increasing T_B domains, which are energetically more favored [163]. The red line in Fig. 3.2(a) depicts the RAS signal of such a Si(100) surface, where T_B domains even prevail (called *Si-B* in the following). While the lineshapes of the RA spectra are similar, their sign and amplitude differ. Regarding *Si-B*, both sign and lineshape of the RA spectrum agree with theoretical predictions performed by Palummo et al.[202], as well as with the RA spectra presented by Shioda and van der Weide for surface preparation in UHV [236]. The corresponding STM image in Fig. 3.2(c) shows a prevalence of dimer rows perpendicular to the step edges (B-type domains) and smaller A-type domains on subjacent terraces (marked B and A, respectively). The associated LEED pattern (see Fig. 3.2(e)) shows enhanced intensity of the spots at half-order along $[0\bar{1}1]$ direction compared to [011] direction, which evidences (2×1) majority domains. RAS inherently integrates over the probed area at mm^2 scale. In consequence, both types of domains contribute to the spectrum and the RAS amplitude is a measure for the domain ratio [78, 202]. The domain imbalance can thus be quantified *in situ* directly before III-V nucleation. The dashed red RA spectrum in Fig. 3.2(a) corresponds to a $T_B : T_A$ domain imbalance of about 62:38 [202]. A quicker cooling ramp at pressures below 50 mbar might increase the domain ratio further towards B-type.

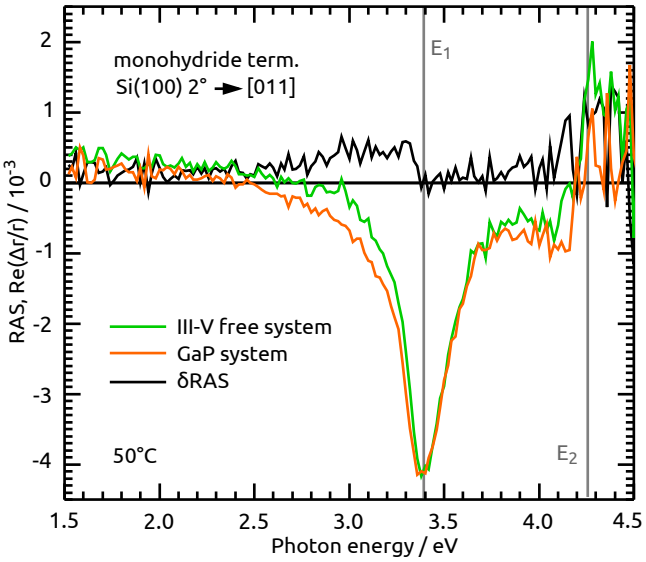

Fig. 3.3 – Comparison of RA spectra of *Si-A* prepared in a clean MOVPE system (green, broken line) and in a GaP processing MOVPE system (orange line) together with their difference spectrum δRAS (black dotted line). Vertical gray lines mark the critical point energies of Si [165] at 50 °C.

Figure 3.3 juxtaposes RA spectra of *Si-A* prepared in a clean Si system (green, broken line), $(\Delta r/r)^{Si\text{-}A}_{\text{III-V free}}$, and of *Si-A* prepared in a system with GaP residuals

from prior processes[19] (orange line), $(\Delta r/r)^{Si\text{-}A}_{\mathrm{GaP}}$. The spectra and, in particular, the amplitude of the minimum at E_1 of Si are very similar. Nevertheless, the difference spectrum,

$$\delta\mathrm{RAS} = \left(\frac{\Delta r}{r}\right)^{Si\text{-}A}_{\text{III-V free}} - \left(\frac{\Delta r}{r}\right)^{Si\text{-}A}_{\mathrm{GaP}} \quad , \tag{3.1}$$

shows small differences (in the order $\lesssim 0.5 \cdot 10^{-3}$, black dotted line) between about 2.5 eV and E_1^{Si}. This could be caused by roughness or small amounts of residual contamination. While traces of As cannot be avoided even in nominal III-V free systems, As cannot be detected by XPS on *Si-A* prepared in GaP processing systems. The latter, in contrast, contains traces of Ga at the surface. The domain concentration of *Si-A* prepared in GaP containing MOVPE system, however, is comparable to that in clean systems. Preparation of *Si-B* in GaP processing systems did not succeed. This is probably related to enhanced residual diffusion, when the reactor pressure is reduced at elevated temperatures to avoid T_A formation, as will be discussed in section 3.5.

3.3 Nucleation in P-rich conditions

A two-step process, consisting of pulsed GaP nucleation (five pulse pairs) at 420 °C (see section 2.9.1) and subsequent epilayer growth at 595 °C, is applied for GaP growth on the *Si-A* and *Si-B* surfaces. These conditions are considered "P-rich", since pulsing starts with TBP at high partial pressures. The state of the Si(100) surface was confirmed by *in situ* RAS directly before nucleation (cf. Fig. 3.2 on page 53).[20] GaP epilayer thicknesses were obtained here by fitting relative reflectance data, which is obtained during the RAS measurement (cf. Haberland et al.[114]) using optical constants from literature [14].[21] Finally, the $(2\times2)/c(4\times2)$ reconstructed surface was prepared (see section 2.10.2 on page 41). AFM images typically show RMS roughnesses below 5 Å, two examples are shown in Fig. 3.4 on the next page.

[19] After the standard bakeout procedure described in section 2.9.1.

[20] As discussed above, *Si-B* had to be prepared in a previously clean silicon system.

[21] In contrast to the procedure in Ref.s[78, 252], the ratio

$$R_{\mathrm{rel}} = \frac{R_{\mathrm{GaP/Si}}}{R_{\mathrm{Si}}} = \sqrt{\frac{U_{\mathrm{DC}}^{\mathrm{GaP/Si}}}{U_{\mathrm{DC}}^{\mathrm{Si}}}} \quad , \tag{3.2}$$

is used here, where the detector voltage $U_{\mathrm{DC}}^{\mathrm{Si}}$ was measured prior processing so that both signals stem from the very same alignment with an identical spot size and the apparatus function cancels more reliably. As pointed out in Ref.[252], the square root (which is not considered in Ref.[78]) accounts for the twofold reflection on the sample since an additional anti-wobble mirror is used in our setup (cf. section 2.9.2).

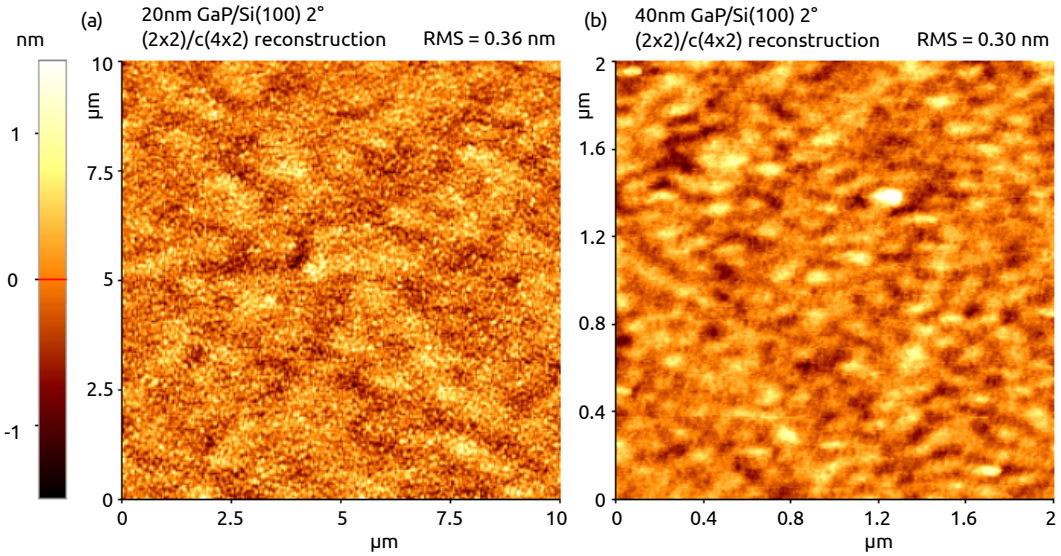

Fig. 3.4 – AFM images (tapping mode, measured in air). (a) $10\,\mu\text{m} \times 10\,\mu\text{m}$ image of 20 nm thick, $(2 \times 2)/c(4 \times 2)$ reconstructed GaP/*Si-A* with a RMS roughness of 0.36 nm. (b) $2\,\mu\text{m} \times 2\,\mu\text{m}$ image of 40 nm thick, $(2 \times 2)/c(4 \times 2)$ reconstructed GaP/*Si-A* with a RMS roughness of 0.30 nm.

3.3.1 RAS of GaP/Si(100) surfaces

GaP/Si(100) growth on *Si-A* and *Si-B*

The RAS signal of the heteroepitaxial GaP/Si-A sample (Fig. 3.5(a), red line) is very similar to that of P-rich GaP(100) [270] regarding both lineshape and, in particular, sign of the signal: The sign of the surface state related peak P_1 at about 2.35 eV and P_2 at about 3.4 eV clearly correspond to a B-type $(2 \times 2)/c(4 \times 2)$ reconstructed GaP/Si(100) surface as known for GaP(100) [116, 270] (see also Fig. 3.6). Fig. 3.5(c) shows the LEED pattern of such a T_B GaP(100) reference surface, where the P dimers are aligned (2×1)-like leading to half-order spots along $[0\bar{1}1]$ direction. Modulations of the amplitude of the RAS signal between P_1 and P_2 are related to internal reflection of the incoming light at the heterointerface, which causes interference [78] and is convoluted with possible interface dielectric anisotropies [298]. Identical GaP growth conditions applied on a *Si-B* substrate result in a RAS signal of opposite sign (Fig. 3.5, broken green line). Since a flipped sign in the RAS signal implies a mutually perpendicular anisotropic structure giving rise to the spectral features, this corresponds to a (1×2)-like reconstruction of the GaP/*Si-B* surface, where the P dimers form T_A terraces, as is also evidenced in the LEED pattern in Fig. 3.5(b). When flipped in sign (Fig. 3.5, dotted blue line), the RAS signal of GaP/*Si-B* is almost identical with that of GaP/*Si-A* up to about 4 eV. The amplitude of both signals indicates single-domain surfaces implying self-annihilation [139,

194] of anti-phase boundaries during GaP growth on *Si-B*. Consequently, the orientation of the P dimers at the GaP/Si(100) surface depends on that of the Si(100) substrate.

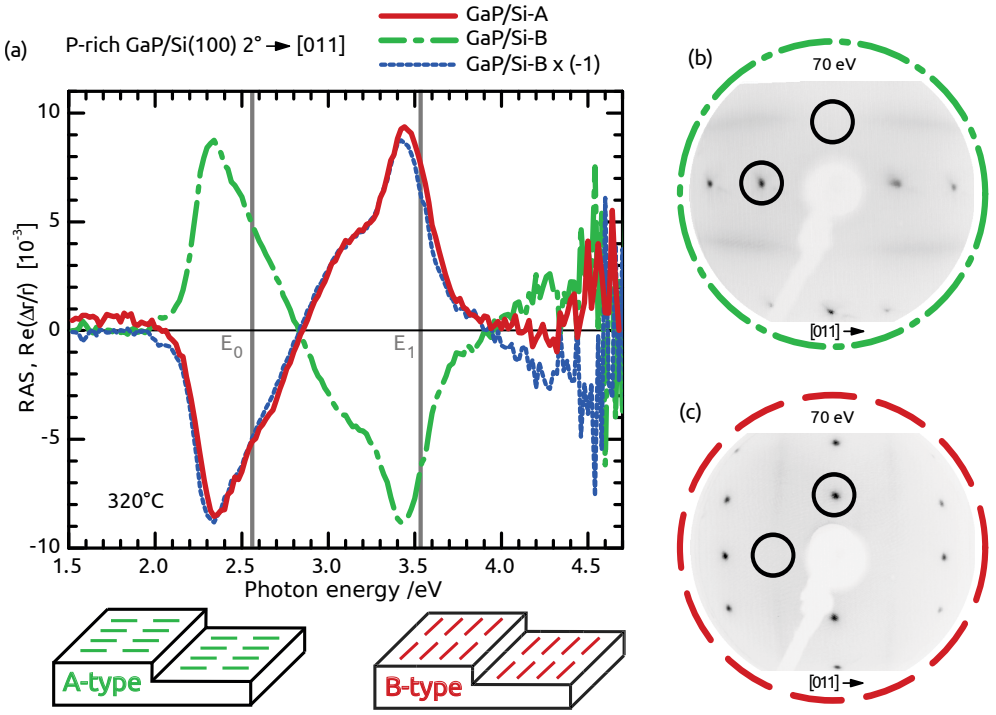

Fig. 3.5 – RA spectra of about 40 nm thin GaP films grown on *Si-A* (red line) and *Si-B* (broken green line) surfaces, as well as the latter spectrum flipped in sign (dotted blue line) for comparison. The line color corresponds to the P dimer orientation while the line style indicates the substrate (in reference to Fig. 3.2(a)). Insets indicate the prevailing P dimer orientation at the P-rich GaP/Si(100) surface. Vertical gray lines mark critical point energies of GaP [310]. (b) LEED pattern of the GaP/*Si-B* sample. (c) LEED pattern of a $(2 \times 2)/c(4 \times 2)$ reconstructed GaP(100) reference sample. Circles mark spots at half order.

The orientation of the P dimers at the $(2\times2)/c(4\times2)$ reconstructed GaP/Si(100) surface reflects the sublattice orientation of the GaP epilayer, as explained in Fig. 3.6 on the following page. The surface consists of P dimers on top of Ga atoms. Every subjacent monolayer, the (100) projected bond orientation changes by 90° due to the tetrahedral coordination within the zincblende lattice. An inversion of the GaP sublattice thus corresponds to a rotation of the P dimers by 90°. The GaP sublattice orientation thus determines the sign of the RAS signal of GaP/Si(100). Consequently, the GaP sublattice orientation with respect to the step edges can be chosen via the Si(100) substrate preparation as intended for further processing.

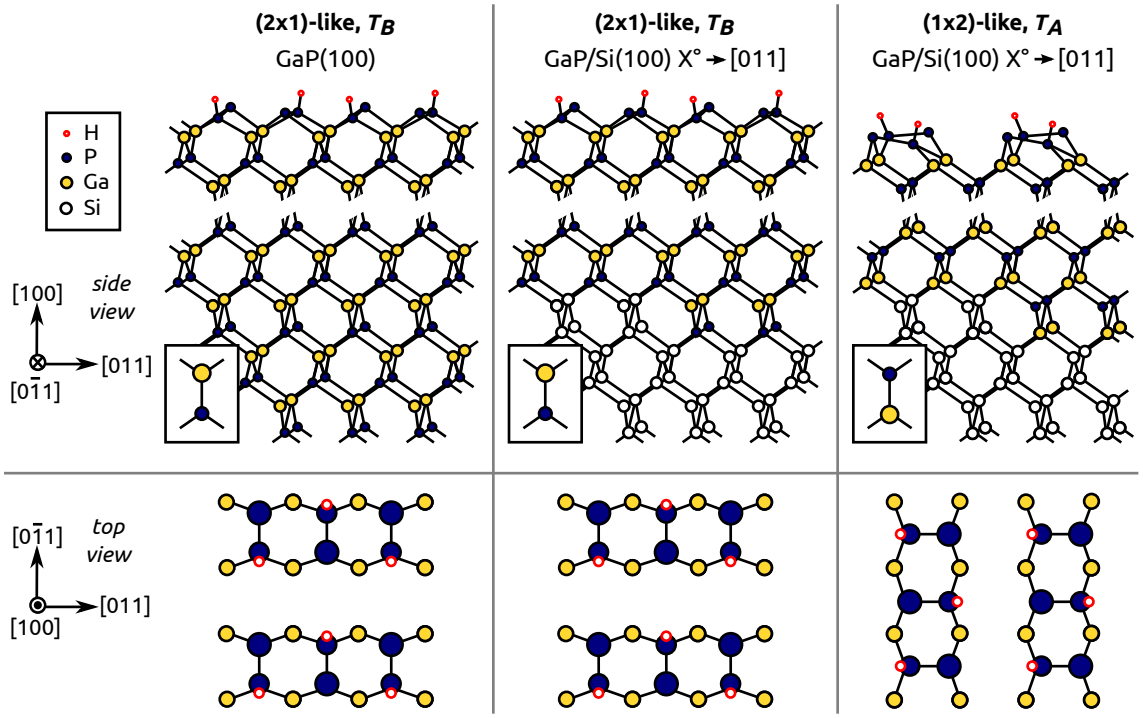

Fig. 3.6 – Sublattice orientation vs. dimer orientation: Not considering their buckling, P dimers at GaP(100)-$(2 \times 2)/c(4 \times 2)$ surfaces reconstruct "(2×1)-like" (left). In analogy to the notation used for Si(100) surfaces, these terraces are denoted as T_B. In [0$\bar{1}$1] projection, Ga is atop on P in the barbell-like structure shown in the inset. Growth on double-layer stepped Si(100) with a misorientation towards [011] (shown here for *Si-A*) results in single-domain GaP epilayers. Depending on the structure of the heterointerface, the sublattice orientation with respect to the step edges can be identical (middle) or inverted (right) to that of GaP(100). Inverted GaP(100) epilayers exhibit "(1×2)-like" T_A terraces. Note that, for the sake of simplicity, the GaP/Si(100) surface is drawn without steps and interfaces are assumed to be abrupt.

From surface dimers to bonds at the heterointerface

The GaP sublattice orientation is correlated with the structure of the heterointerface. Recently, Beyer et al.[28] published idealized abrupt interface structure models with either Si–Ga or Si–P interface bonds. The interface structure model is based on an abrupt interface, where the uppermost Si atoms are not replaced and GaP layers form strictly on top of the formerly dimerized Si atoms during nucleation. The interfacial bonds are then deduced from the GaP sublattice orientation (which was obtained applying *ex situ* TEM [28]) and the orientation of the Si dimer prior to nucleation. The latter was measured by LEED from a reference Si(100) surface after transfer to UHV in a nitrogen chamber [28] under the assumption of an identical surface during actual processing. Both information, however, can also be obtained with *in situ* RAS, as discussed above.

Considering the prevalent dimer orientation of *Si-A* and *Si-B* substrates and the tetrahedral coordination in the crystal lattice, an inverted sublattice in the GaP film would result depending on whether bonds between Si and Ga or Si and P are preferred for both *Si-A* and *Si-B*. Table 3.1 displays all possible substrate/film orientations for abrupt heterointerfaces. Si–Ga interfaces at *Si-A* (*Si-B*) substrates would lead to A-type (B-type) P dimers at the GaP/Si(100) surface, while Si–P interfaces at *Si-A* (*Si-B*) substrates correspond to B-type (A-type) P dimers at the GaP/Si(100) surface.

Tab. 3.1 – Principally possible orientations of dimers at the Si(100) resp. GaP/Si(100) surface starting with either Ga or P at an abrupt heterointerface. Note, that all samples were prepared with P dimers terminating the surface.

substrate	*GaP epilayers*	*orientation*	*case*
Si-A	Ga–P–[...]–Ga–P	A-type	$A \rightarrow A$
Si-A	P–Ga–[...]–P	B-type	$A \rightarrow B$
Si-B	Ga–P–[...]–Ga–P	B-type	$B \rightarrow B$
Si-B	P–Ga–[...]–P	A-type	$B \rightarrow A$

Abrupt interface model

First, the abrupt interface will be assumed, which is also discussed by Beyer et al.[28]. This configuration is not necessarily the energetically most favored one. Growth in MOVPE, however, takes place under highly non-equilibrium conditions and even energetically less favored states may result and be "frozen" in the following process (cf. the kinetically driven A-type Si(100) preparation discussed above). Note that only the terraces are considered here. As obvious from Fig.s 3.2 and 3.5, the cases A→B and B→A (Tab. 3.1) are observed experimentally. Following the idealized abrupt interface model [28], Fig. 3.7(a),(b) shows that the experiments suggest Si–P interfaces both for *Si-A* and *Si-B*. In contrast, Beyer et al.[28] reported that Si–Ga bonds are created on Si(001) with 0.1° misorientation towards [110] direction and A-type majority domains during a pulsed GaP nucleation. The growth of inverted GaP epilayers required a modified nucleation with a higher temperature (about 680 °C) during the first TBP pulse, which was attributed to TBP decomposition [28]. Particularly in this temperature range, however, *in situ* control is of utmost importance regarding almost nominal Si(100) substrates, where the majority domain changes periodically from A-type to B-type due to layer-by-layer removal in H_2 process ambient (cf. section 2.10.1). The Si(100) substrates with 2° misorientation towards [011], which are used here, form stable A-type or B-type terraces depending on the annealing procedure as confirmed *in situ* by RAS directly prior nucleation.

DFT calculations of Steinbach et al.[246] performed for GaP/Si(100) superlattices reveal that abrupt Si–P interfaces are energetically more stable than Si–Ga interfaces. This agrees with experimental findings by Wright et al.[292], who re-

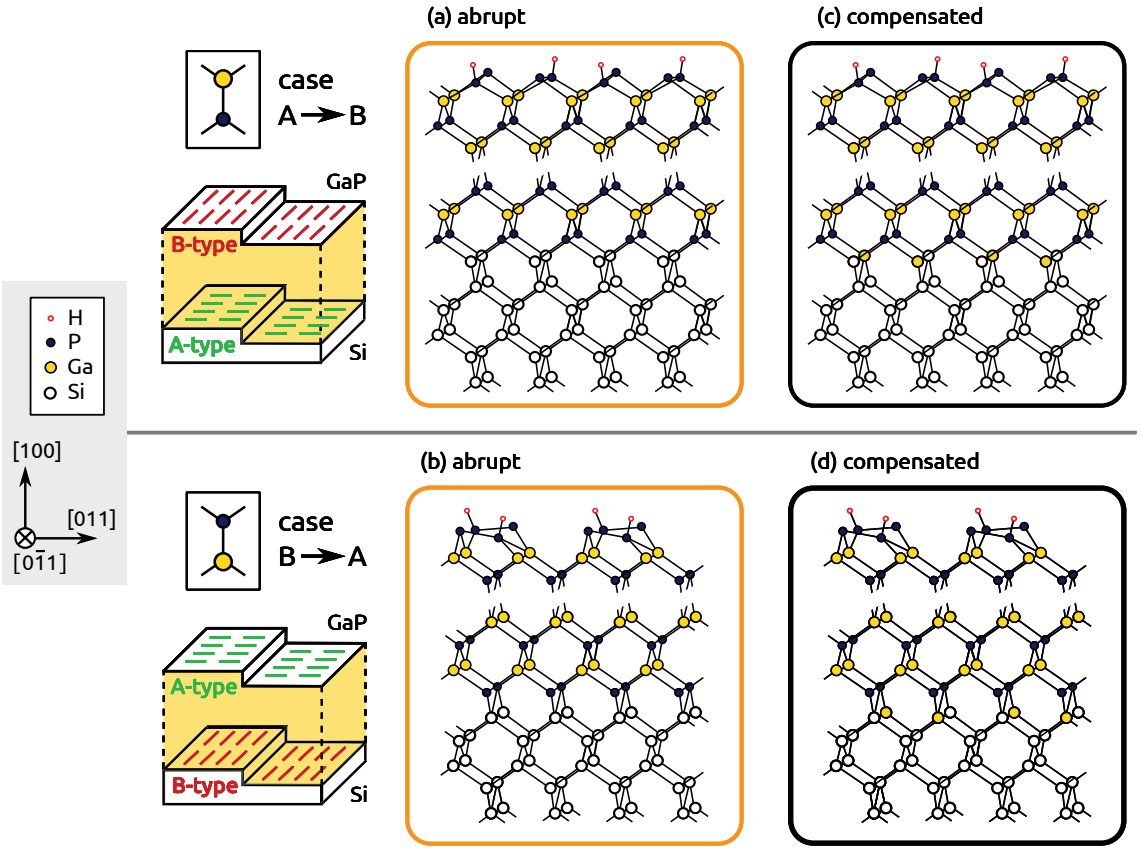

Fig. 3.7 – Abrupt interface model (in side view) for the experimentally observed cases A→B (left) and B→A (right). The sketch on the left hand side indicates the dimer orientations of the Si(100) substrate prior to GaP nucleation and of the final P-rich GaP/Si(100) surface as obtained by *in situ* RAS (cf. Fig. 3.2 and 3.5) and the inset illustrates the corresponding sublattice orientation of the GaP film. In an idealized abrupt interface model, both (a) B-type GaP grown on Si-A and (b) A-type GaP grown on Si-B require Si–P bonds at the heterointerface. (c),(d) visualize the binding situation at compensated 0.5 Si : 0.5 Ga–P interfaces.

ported for GaP nucleation on Si(211) that P binds preferred to Si atoms having two backbonds and that P might even displace Ga atoms occupying such sites due to the weaker Si–Ga bond strength. Considering that the Si dimers at the substrate will break during nucleation, this agrees with a prevalence of Si–P bonds at the GaP/Si(100) heterointerface and such group-IV–group-V bonds at the heterointerface similarly occur for GaAs growth on both Si(100) [37] and Ge(100) [268]. Bringans even argues that in earlier GaAs/Si(100) studies, which included Ga prelayer deposition before actual growth, the Ga atoms may have been displaced by As atoms [38]. Replacive P adsorption, as observed for PH_3 exposed to clean Si(100) surfaces [285], would not explain the GaP sublattice orientation (assuming Ga to bind to P that replaced the Si dimers).

Intermixing at the GaP/Si(100) heterointerface

Ideally abrupt interfaces are not charge compensated (see section 2.5). The smallest in-plane interface unit cell for GaP/Si(100), where charge can be compensated (see section 2.5), is a (2×2) cell with a Si to P (Ga) atomic mixing ratio of 0.5:0.5. A mixed heterointerface structure model for GaP/Si(100), where every second Si atom is substituted by a Ga atom at the interface ($0.5\,\mathrm{Si} : 0.5\,\mathrm{Ga}$–P model) would also agree with the observed cases A→B and B→A as shown in Fig. 3.7(c,d). Note, that a compensated interface must not be confused with cross-diffusion of atoms at typical doping concentrations.

The correlation of surface dimers alone cannot resolve the actual atomic structure of the heterointerface. In order to find direct evidence for the bonding situation at the GaP/Si(100) heterointerface, time-resolved RAS measurements and XPS at intermediate states of nucleation will be discussed in the following.

3.3.2 Time-resolved RAS during pulsed GaP nucleation

The following experiments were started with an almost single-domain *Si-A* surface with its characteristic RAS signal (see inset of Fig. 3.8 on the following page, broken violet line), where the sign corresponds to the Si dimer orientation [45, 202, 236]. During nucleation, pulse pairs (PP) consisting of alternating TBP and TEGa pulses were offered for 1 s each at 420 °C in 100 mbar H_2. Transient RA was measured at 3.25 eV, i.e. slightly below the E_1 interband transition of Si.

Figure 3.8 shows that the anisotropy related to the monohydride-terminated Si(100) surface vanishes with the first TBP pulse and an anisotropy of opposite sign establishes during further pulsing. Within about the first ten PP, this anisotropy of different sign is increasing while subsequent pulsing leads to a decreasing RAS signal with a modulated oscillation of slightly increasing amplitude. Note that RAS signals depend on a variety of influences, such as temperature, strain, internal electric fields, and spectral shifts must be considered when interpreting RA transients. The extinction of the Si(100) dielectric anisotropy during the very first pulse probably is caused by TBP (or fragments of it) being adsorbed on the surface. The arising dielectric anisotropy of opposite sign indicates formation of an ordered surface or well-defined interface. A decreasing RA amplitude, in contrast, could correspond to an increased degree of disorder or a spectral shift, while modulated oscillations probably are related to a periodically created and consumed surface reaction layer [65, 219]. XPS quantification (see below) indicates that one pulse increases the GaP epilayer thickness by about one monolayer (after initial heterointerface formation). The modulation follows indeed the pulsing sequence. The oscillation period seems slightly enlarged, which could be related to an increased amount of unreacted species [219]. Spectral resolution, however, would be useful to strengthen this observation.

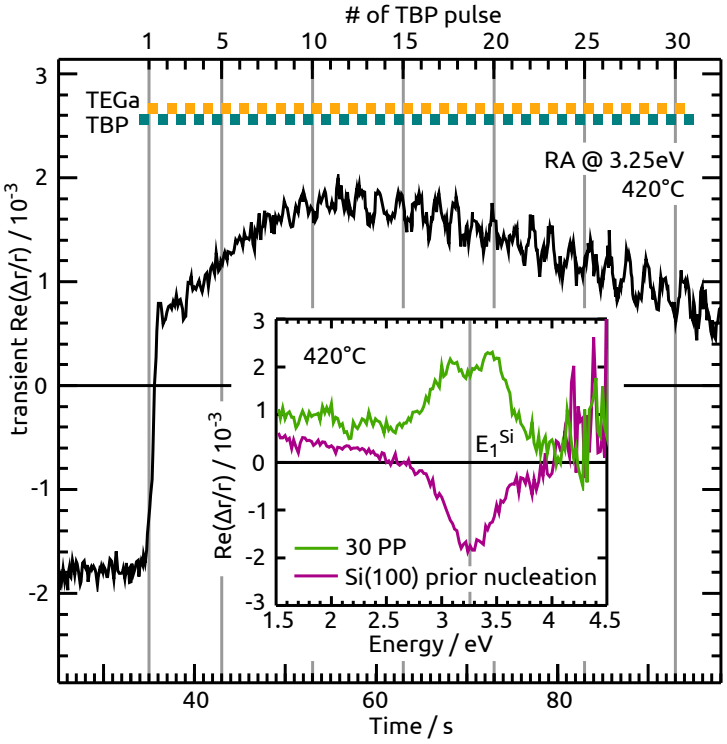

Fig. 3.8 – Transient RA measurement at 3.25 eV during 30 pulse pairs consisting of alternating TBP and TEGa pulses (1 s each) on A-type Si(100). The time scale refers to the starting of the measurement after recording the Si(100) RA spectrum shown in the inset (red dash-dotted line), with the first TBP pulse starting at about 34 s. The inset also shows the RA spectrum after 30 (TBP, TEGa) PP (green line).

The inset in Fig. 3.8 also shows the resulting RA spectrum after 30 PP (green line) with two peak-like contributions at about 3.1 eV and 3.5 eV. A partly similar feature was observed during pulsed chemical beam epitaxy of GaP on Si(113) [65, 66] and assumed to stem from a P-rich surface reconstruction.

3.3.3 RAS after pulsed nucleation and benchmarking to LEED

Parts of this section are reprinted in part, with permission from J. Phys. Chem. Lett. 6, 464 [256], ©2015 American Chemical Society.

In order to resolve the temporal evolution over the whole spectral range, pulsing was stopped after 5 and 10 PP, respectively, to measure RAS at 50 °C and benchmark the spectra to LEED and XPS (see section 3.3.4). Desorption of excess P and precursor residuals was applied at 420 °C analogously to surface preparation of thicker GaP epilayers [78]. Carbon was not detectable with XPS.

After 5 PP, the RA spectrum exhibits one clear peak centered at 3.3 eV (see Fig. 3.9(a), blue line) and already a shoulder at the E_1 interband transition of

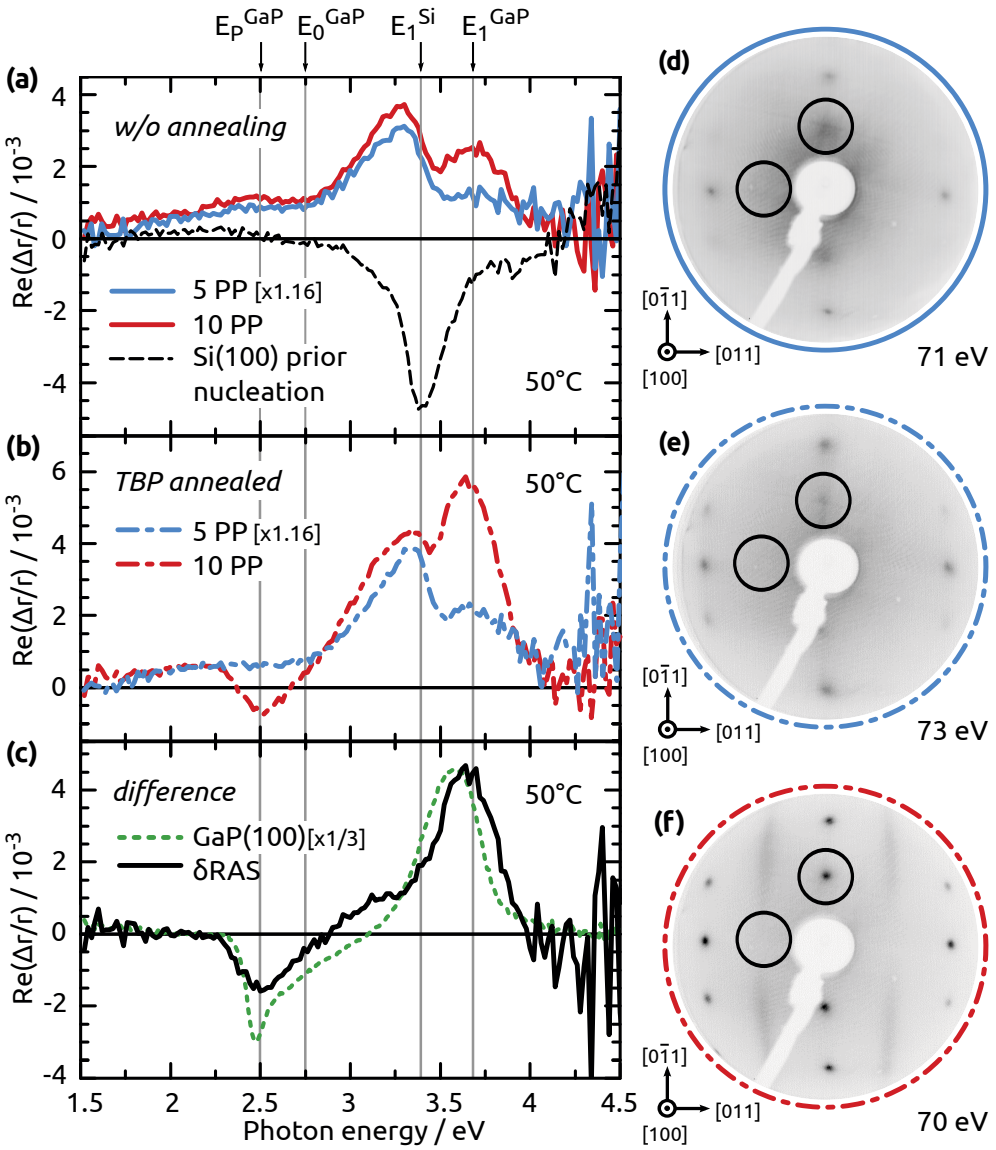

Fig. 3.9 – (a-c) RA spectra measured at 50 °C: (a) After 5 (blue) resp. 10 (red) PP, scaled so that the Si(100) spectra (black dashed line) prior to pulsing match. (b) Identical samples as in (a) which where subsequently heated to 595 °C with TBP supply. (c) Difference RA spectrum (blue line in (a) subtracted from red line in (b)) in comparison to a $(2 \times 2)/c(4 \times 2)$ reconstructed GaP(100) reference (green dashed line). Gray vertical lines indicate critical point energies of GaP [310] and Si [165] as well as a transition E_P^{GaP} between a surface state of $(2 \times 2)/c(4 \times 2)$ reconstructed GaP(100) and a state resonant to the X-valley CBM [116, 239]. *(d-f) LEED patterns corresponding to the RA spectra:* (d) after 5 PP, (e) after 5 PP plus annealing in TBP, (f) after 10 PP plus annealing in TBP. Circles mark spots at half order.

GaP as well as around 2.5 eV. This RAS signal will be called "nucleation RAS signal" $(\Delta r/r)_{\text{nucleation}}$ in the following. Compared to monohydride-terminated Si(100)

(dashed black line), $(\Delta r/r)_{\text{nucleation}}$ is shifted about 100 meV towards lower energies and flipped in sign. After 10 PP (dashed red line), the dielectric anisotropy increases slightly and is superimposed by an increased contribution at the E_1 interband transition of GaP (spectra were scaled to Si(100) of the 10 PP sample to compensate slight differences in intensity caused by the domain ratio). In order to compare to the nucleation layer directly before actual GaP layer growth, both samples were heated subsequently to 595 °C under TBP supply before cooling to 420 °C for desorption of excess P [78], see Fig. 3.9(b). The contribution at E_1 of GaP increases, in particular for the 10 PP sample, while that at 3.3 eV almost remains unchanged. The LEED pattern of the 5 PP sample in Fig. 3.9(e) are less diffuse compared to prior annealing and show a weak spot at half order along $[0\bar{1}1]$. In the RA spectrum after 10 PP, $(\Delta r/r)_{10\,\text{PP}}$, an additional anisotropic contribution occurs at the electronic transition E_P^{GaP} involving a surface state related to the $(2 \times 2)/c(4 \times 2)$ reconstruction of GaP(100) (see section 3.1). Here, the beginning formation of an ordered GaP/Si(100) surface just by pulsed nucleation at low temperature and subsequent annealing in TBP is monitored. This surface also exhibits a LEED pattern with streaks and spots at half order along $[0\bar{1}1]$ in Fig. 3.9(f) just as for a corresponding GaP(100) surface [270]. Consequently, $\left.\frac{\Delta r}{r}\right|_{10\,\text{PP}}$ is a superposition of a GaP surface signal and $(\Delta r/r)_{\text{nucleation}}$. This becomes more evident, when comparing the difference spectrum

$$\delta\text{RAS} = \left(\frac{\Delta r}{r}\right)_{10\,\text{PP}} - \left(\frac{\Delta r}{r}\right)_{\text{nucleation}} \tag{3.3}$$

with that of a $(2\times2)/c(4\times2)$ reconstructed GaP(100) reference in Fig. 3.9(c). There are differences in the lineshape, but the general features are reproduced. The lower intensity of δRAS compared to the GaP reference is not caused by antiphase disorder [79], since the LEED pattern do not show spots related to the T_A domain. Probably, the surface of the very thin layer (about 4 a_{GaP} according to XPS, see Tab. 3.2 on page 67) is not yet fully ordered. The majority GaP sublattice orientation already corresponds to that observed above for GaP growth on *Si-A*. Note that neither C nor O were found on the surface by XPS.

The dielectric anisotropy stemming from the surface-modified bulk E_1^{GaP} transition develops faster than the surface-state related anisotropy at E_P^{GaP} (see Fig. 3.9 on the preceding page). While the GaP/Si(100) surface is not yet well-ordered after 5 pulses, the anisotropy at 3.3 eV is already mostly established [cf. Fig. 3.9(b)]. This indicates that the interface forms already during the first pulses at low temperature and not during annealing at higher temperatures, which supports the possibility of a kinetically limited interface formation.

3.3.4 Chemical composition of the heterointerface probed by XPS

Parts of this section are reprinted in part, with permission from J. Phys. Chem. Lett. 6, 464 [256], ©2015 American Chemical Society.

In order to resolve the chemical composition of the heterointerface, XPS measurements of 5 and 10 PP GaP on *Si-A* samples (including annealing in TBP), were performed after contamination-free sample transfer to UHV. Si–P and Si–Ga interfacial bonds are expected to give additional, chemically shifted contributions in the photoemission (PE) lines of the two species involved in the bond at the interface. Indeed, XPS reveals distinct components for both the Si 2p and P 2p core levels (see fits[22] in Fig. 3.10). For the P 2p line in Fig. 3.10(a), a second component, P_2, which also show spin-orbit splitting, occurs after 5 and 10 PP. The P_2 components are chemically shifted towards higher binding energies (E_B) and vanish for thicker epilayers of GaP (cf. gray spectrum in Fig. 3.10(a)). P_2 therefore is related to the interface, as also verified by measurements at 30° exit angle.

Based on Fadley [87], the coverage C of an overlayer (L) on a substrate (S) can according to May et al.[180] be quantified via

$$C = \frac{I}{I + 1 - \exp\left(-\frac{d\,\cos\theta}{\lambda_0(E_L)}\right) - I\,\exp\left(-\frac{d\,\cos\theta}{\lambda_0(E_S)}\right)} \quad ; \quad I = \frac{I_L}{I_S}\,\frac{I_S^\infty}{I_L^\infty} \quad , \qquad (3.4)$$

where d is one quarter of the lattice constant of Si (defined as 1 monolayer (ML)), $\lambda_0(E_{S,L})$ is the electron attenuation length calculated from the NIST database [210] for the energy of the PE line of the substrate or overlayer, respectively, θ is the rotation against normal exit angle, $I_{S,L}$ denotes the measured intensity of the PE line, and $I_{S,L}^\infty$ is calculated for an infinitely thick layer with photoelectron ionization cross sections from Ref.[300]. Quantification applying eq. (3.4) is given in Tab. 3.2 on page 67. The relative error for this quantification without standard is estimated to $\pm(10-20)\%$ for the 5 PP sample, but will be larger for thicker GaP coverages due to increased attenuation of the interfacial signal.

The smaller P contribution, P_2, corresponds to about 1 ML for 5 PP. The first P contribution, P_1, matches energetically the line position of the thicker sample (70 s GaP growth) (129.54 eV for P $2p_{3/2}$, see dotted line in Fig. 3.10(a)) and is therefore assigned to P in GaP. This is in line with a direct evaluation of the Ga 3p and P 2p peak contributions with atomic sensitivity factors: P_2 after 5 and 10 PP quantitatively matches the minor Si_2 signal. P_1 is at least a factor of 3 stronger, and the intensity ratio of Ga 3p to P_1 of 1 ± 0.15 indicates that P_1 relates to GaP.

[22] The quantitative XPS analysis was performed by M. M. May (HZB / TU Ilmenau) applying the open-source software *fityk* [290]. Voigt profiles were used as model functions and the background was approximated by a linear function. For each set of fit functions (such as the four components of a Si 2p fit), the full width at half-maximum was set identical for all peak components. The intensity ratio of each 2p doublet pair was fixed to 2:1.

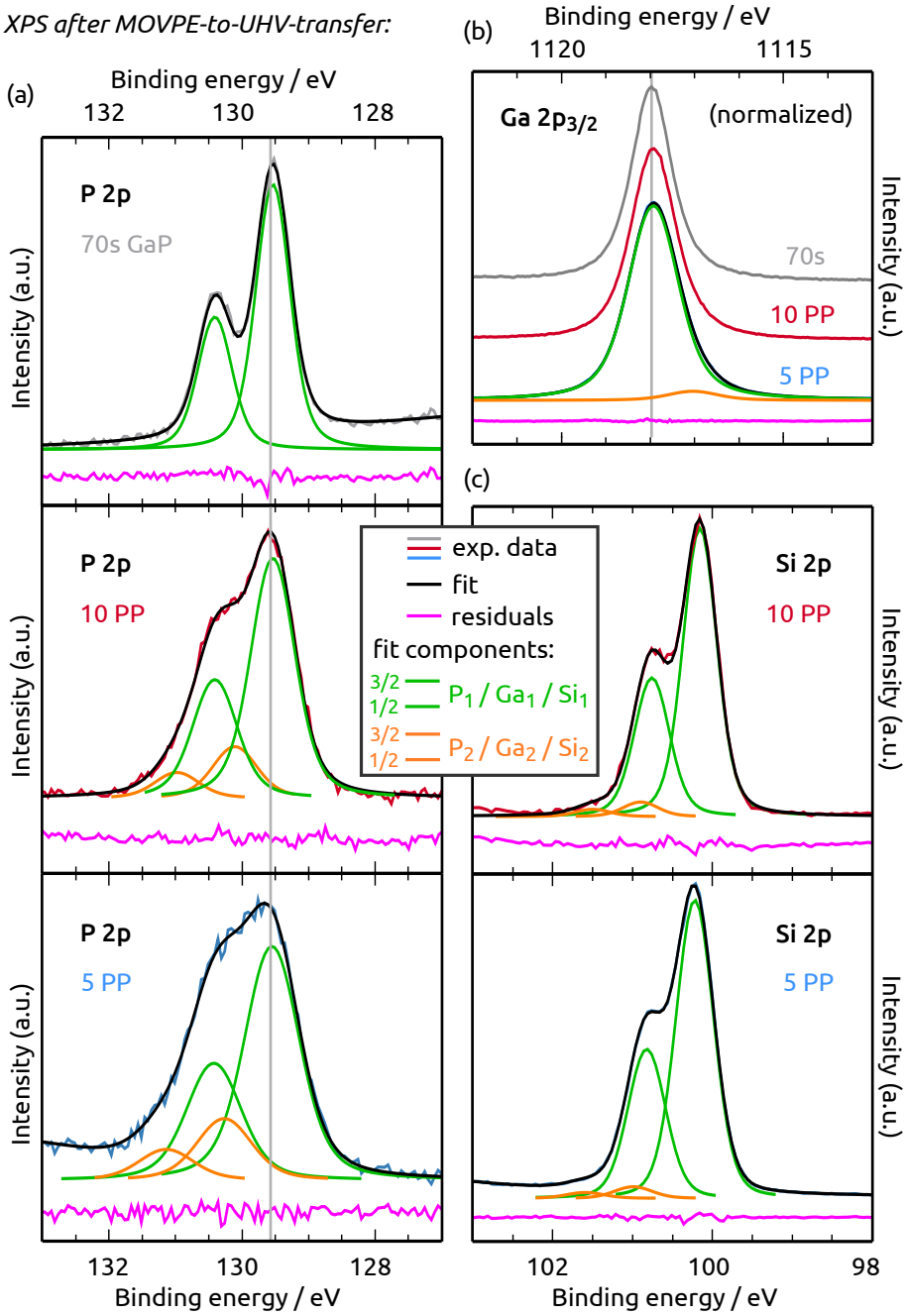

Fig. 3.10 – XPS (monochromated Al K_α) at different stages of nucleation (after annealing in TBP; blue for 5 PP, red for 10 PP and gray for 70 s GaP growth). (a) P 2p core level region, the vertical dotted line indicates $E_B = 129.54$ eV. (b) Ga $2p_{3/2}$ PE line (the fit is only shown for 5 PP). The vertical dotted line indicates $E_B = 1117.97$ eV. (c) Si 2p core level region. Fitted components to the PE lines are shown in green (P_1, Ga_1 resp. Si_1) and orange (P_2, Ga_2 resp. Si_2). Solid and dashed lines represent $2p_{3/2}$ and $2p_{1/2}$ components, respectively. The fit envelope (black line) shown in (a) also includes fitted components for the Si 2p plasmon around 135 eV and the Ga 3p PE line was included for the fit in (c). Residuals are plotted with an offset in pink.

Tab. 3.2 – Quantification by XPS after 5 and 10 PP GaP nucleation on *Si-A* and annealing in TBP. Coverages C were estimated using calculated cross-sections and electron attenuation lengths, see eq. (3.4) [180]. Ratios R were calculated directly from the peak areas considering the detector transmission function and atomic sensitivity factors.

	5 PP E_B / eV	5 PP C / ML	10 PP E_B / eV	10 PP C / ML
P_1	129.55	3.30	129.54	8.1
P_2	130.27	0.99	130.11	1.4
Si_1	100.22	–	100.16	–
Si_2	100.99	0.87	100.89	1.36
	ΔE_B / eV	R	ΔE_B / eV	R
P_1:Si_1	28.56	4.5	28.65	9.97
P_2:Si_2	29.28	1.18	29.22	1.09

For the Si 2p PE line [Fig. 3.10(c)], there also exist two peak components after 5 and 10 PP. The larger component, Si_1, corresponds to bulk Si. The smaller component, Si_2, is shifted towards higher E_B. This is expected for Si–P bonds [171]. Similarly, the Si 2p core-level was shifted towards higher E_B for Si bound to As in GaAs-on-Si heteroepitaxy [39, 40]. Both oxide species [75] and carbon related species [62], which might lead to similar shifts, are ruled out by XPS measurements. Si–Ga bonds, in contrast, are expected to induce a chemical shift towards lower E_B [39, 40]. Quantitatively, a coverage of about 1 ML for Si_2 is estimated, in agreement with P_2. After 10 PP, the Si_2 and P_2 components seem to increase. As the relative error of the quantification here is increased due to the larger attenuation by the GaP layers on top, we conclude that the coverage of Si_2 and P_2 corresponds to roughly one interfacial layer. Consequently, both Si_2 and P_2 are attributed to the GaP/Si interface.

The Ga $2p_{3/2}$ PE line of the 5 PP sample in Fig. 3.10(b) contains a small second component (orange line, about 4 % of the main peak), which is shifted 0.87 eV to lower E_B. This component could not be detected in the other Ga $2p_{3/2}$ and Ga 3p PE lines (not shown here). A possible origin for this second component include Ga–Ga bonds at antiphase boundaries, since the preferential A-type Si(100) surface contains small residual B-type domains at the step edges, see Fig. 3.5(b), and antiphase boundaries which will not annihilate within the very first MLs. Another possible origin are minority Si–Ga bonds at the heterointerface. These could result from residual Ga on the surface prior to nucleation (see section 3.5) or a non-ideally abrupt heterointerface. A corresponding Si–Ga component in the Si 2p peak cannot be detected, however, due to the low intensity.

In consequence, a minority of Si–Ga bonds cannot be excluded, but XPS gives strong, quantitative evidence for about 1 ML Si–P bonds at the GaP/Si(100) interface. This finding supports the abrupt interface model. Similarly, Si–As bonds were found dominantly at the GaAs/Si(100) interface [39].

The difference in P coverage of about 5 ML between 5 and 10 PP fits to adding half a lattice constant of GaP per PP (note that surfaces were TBP stabilized, so that the uppermost P layer is not to be counted as a pulse here). Assuming growth of one bilayer per PP, the interface would form during 3 PP. The GaP coverage of about 3 GaP bilayers, i.e. $1.5\,a_{GaP} \approx 0.82\,\text{nm}$, which is estimated by XPS for 5 PP agrees with the thickness of the nucleation layer of $(0.6 \pm 0.3)\,\text{nm}$ estimated from a linear fit of the growth rate from the GaP/Si(100) (see Fig. 3.13(b) and eq. (3.6) on page 71).

According to Ref.[284], the XPS measurements allow estimation of the valence band offset (VBO) from

$$\text{VBO} = E^{\text{Si}}_{10\,\text{PP}} - E^{\text{Ga}}_{10\,\text{PP}} + \text{VBM}_{\text{Si(100)}} - E^{\text{Si}}_{\text{Si(100)}} - \left(\text{VBM}_{\text{GaP(100)}} - E^{\text{Ga}}_{\text{GaP(100)}}\right) \quad , \quad (3.5)$$

where the $E^{\text{PEline}}_{\text{sample}}$ denotes the measured Si resp. Ga $2p_{3/2}$ core level energy of the 10 PP sample, a Si(100) and a thicker GaP/Si(100) reference, respectively, and VBM is the according valence band maximum (see Fig. 3.11). The resulting value of $\text{VBO} = (600 \pm 150)\,\text{meV}$ is lower than reported in literature [205, 222] and corresponds to an almost symmetric Type I heterostructure as sketched in Fig. 3.11. Note that the VBO will depend on the actual electronic interface structure [123] so that comparison to theoretical modeling will enable further insight on the atomic interface structure. In future studies, we will therefore perform DFT calculations in combination with VBO measurements from differently prepared heterointerfaces.

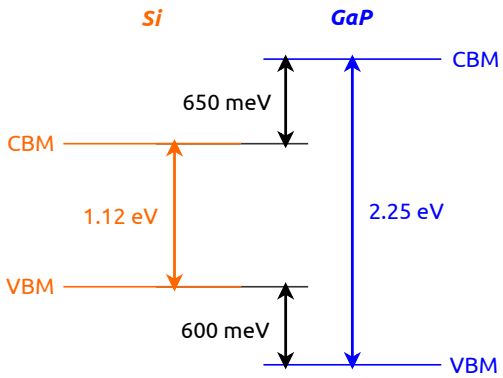

Fig. 3.11 – Type I heterostructure of GaP/*Si-A* sketched for a VBO of 600 meV.

3.3.5 Interface dielectric anisotropy of GaP/Si(100) heterointerfaces

If the nucleation-related RAS signal $(\Delta r/r)_{\text{nucleation}}$, which was observed in section 3.3.3, originates indeed from the GaP/Si(100) interface rather than from an ordered surface, it will persist during subsequent GaP epilayer growth and contribute to the RA spectra due to internal reflection at the buried interface [298]. The interface dielectric anisotropy (IDA), however, is convoluted with interference and absorption in the RA spectra and needs to be separated from the surface dielectric anisotropies (SDA). Within a dielectric model based on Ref.s[127, 183, 298], SDA and buried IDA can be extracted from the RAS data of two GaP epilayers with different thicknesses i and j using eq. (2.22) and eq. (2.23) on page 48. This deconvolution approach requires (i) the real part of GaP/Si(100) RA spectra of two differently thick GaP epilayers, (ii) the corresponding imaginary RAS signals, (iii) the thicknesses of the epilayers, and (iv) the dielectric functions of Si and GaP as input.

Interrupted GaP growth on *Si-A*

Here, the real parts of RAS are measured during interrupted growth of one single sample and their imaginary counterparts are calculated self-consistently via the Kramers-Kronig relation [303]. The spectra are displayed in Fig. 3.12.[23] In contrast to Ref.[254], interrupted growth is chosen here in order to avoid any run-to-run discrepancy effects and to minimize the influence of slightly different alignment.[24]

The GaP epilayer thickness results from the fit of the measured relative reflectance $R_{\text{rel}} = R_{\text{GaP/Si}} \,/\, R_{\text{Si}}$ for each growth step (as discussed on page 55). The corresponding spectra are shown in Figure 3.13 on the next page.[25] According to Fig. 3.13(b), interrupted growth with a total growth time t leads to comparable total epilayer thickness as growing the same time continuously with identical parameters

[23] In previous studies [252], the RAS imaginary part was found to be very sensitive to slightly changed alignment and strain in the optical components. Yasuda highlighted the importance of minimizing the influence of e.g. the viewport [298]. Though the anti-wobble mirror and lenses above the reactor are air-cooled and the optical view port is nominally strain-free, we observed shifts in the spectra in the range $5 \cdot 10^{-3}$ changing with temperature [252]. Using the Kramers-Kronig relations instead was more reliabe and is, for example, justified in Ref.[303] and also done for RAS in Ref.s[105, 113].

[24] For comparability, GaP was nucleated pulsed at 420 °C on 2° misoriented Si(100) with A-type terraces in analogy to the blue RA spectra in Fig. 3.2 on page 53. Subsequent GaP growth was interrupted by $(2 \times 2)/c(4 \times 2)$ surface preparation [78] and RAS measurements at 50 °C after 5 nm, 21 nm, 27 nm, 36 nm, and 48 nm total epilayer thickness.

[25] The thickness dependent fit was performed using dielectric function from Ref.[14]. Introducing variable surface and interface roughness (according to Bruggeman's model) in the fit did not considerably increase the quality of the fit. The error boundary for the fit is roughly estimated to 2 nm as indicated in Fig. 3.13.

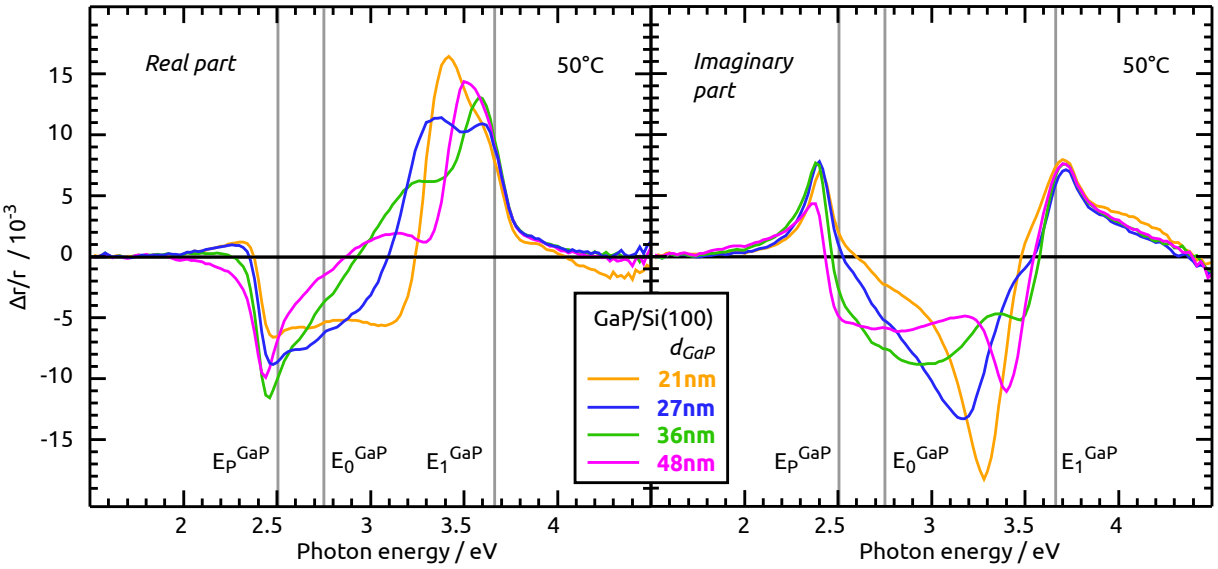

Fig. 3.12 – RAS of differently thick, $(2 \times 2)/c(4 \times 2)$ reconstructed GaP epilayers grown with interruptions on one single *Si-A* substrate. *(left)* Real part of the RAS signals. *(right)* Kramers-Kronig imaginary parts calculated from the real parts of the RAS signals. Gray vertical lines indicate critical point energies of GaP [310] as well as a transition E_P^{GaP} involving a surface state of $(2 \times 2)/c(4 \times 2)$ reconstructed GaP(100) [116, 239].

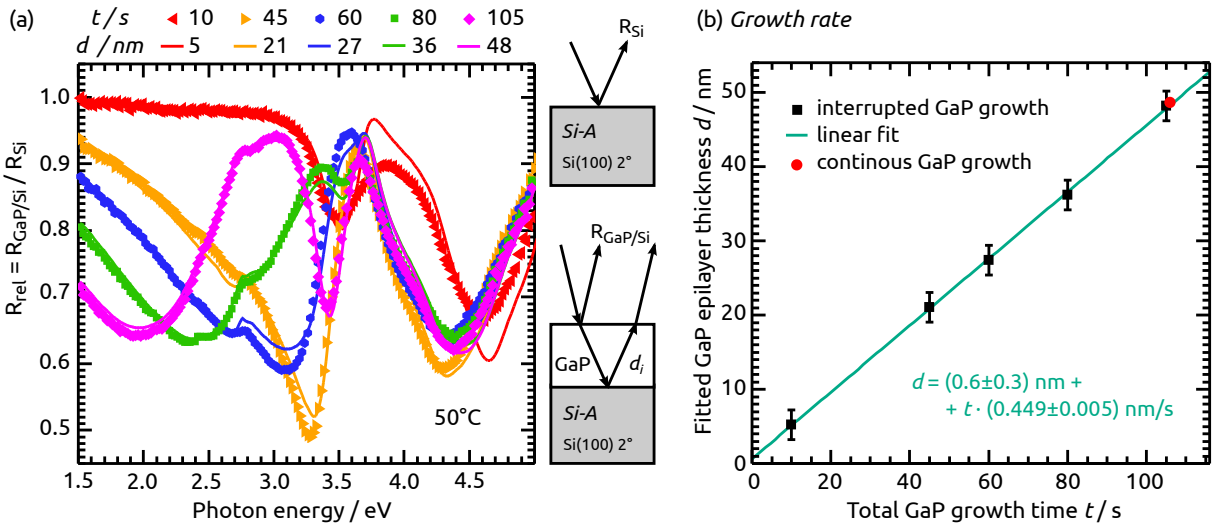

Fig. 3.13 – (a) Measured $R_{\mathrm{rel}} = R_{\mathrm{GaP/Si}} / R_{\mathrm{Si}}$ spectra obtained during interrupted GaP growth on *Si-A* (total GaP growth time t, indicated by the symbols) and fit yielding the GaP epilayer thickness d (lines, see legend for colors). (b) Growth rate obtained from a linear regression of the values given in (a). The red dot marks the growth time and thickness of a GaP epilayer which was continuously grown on *Si-A* with identical growth parameters.

(red circle). Both R_{rel} and the RA spectra in Fig. 3.12 in comparison to continuously grown GaP/Si(100) samples show no indications for additional interference caused by the interruptions, indicating growth of one single continuous epilayer. According to the linear regression (Fig. 3.13(b), turquoise line),

$$d = (0.6 \pm 0.3)\,\mathrm{nm} + t \cdot (0.449 \pm 0.005)\,\mathrm{nm\,s^{-1}} \quad , \tag{3.6}$$

the growth rate was $(0.449 \pm 0.005)\,\mathrm{nm\,s^{-1}}$ with an offset of $(0.6 \pm 0.3)\,\mathrm{nm}$, which results from the pulsed low-temperature nucleation before layer growth.

Calculated surface and interface dielectric anisotropies

Figure 3.14 on the following page shows the weights $w_{i,s}$ calculated for the according thicknesses for evaluation of eq. (2.22) and 2.23 to extract the SDA and the IDA from pairs of the differently thick GaP epilayers plotted in Fig. 3.12 on the preceding page. The dielectric functions are taken from literature [133, 134].[26] Antiphase disorder was considered negligible due to the quasi single-domain character of the samples.

The resulting SDA and IDA, respectively, for different pairs of GaP epilayer thicknesses (d_i, d_j) grown on A-type Si(100) with 5 PP nucleation[27] are shown Fig. 3.15 on the following page. Note that the imaginary parts are plotted, because they relate in first order to the real parts of the corresponding RAS signals [183]. As expected, the lineshape of the SDA for all pairs of samples matches that of $(2 \times 2)/c(4 \times 2)$ reconstructed GaP(100) (cf. Ref.[254]). The slight differences between the two main peaks possibly are due to the uncertainty in the GaP epilayer thickness. The IDA of all pairs is almost zero up to 2.2 eV, where the anisotropy starts rising before peaking slightly below the E_1 transition of Si. This is followed by a minimum at about 3.5 eV and a maximum at 3.7 eV. The lineshape of the IDA per pair differs slightly below E_1^{Si}, which is most visible for $(d_i, d_j) = (21\,\mathrm{nm}, 27\,, \mathrm{nm})$ (red line). This is could be an artifact, as also the SDA of this pair differs most prominently. "Features" at about 2.4 eV possibly originate in small differences of the amount of residual APD, which annihilate [139, 194] during epilayer growth. The derivative-like feature in the IDA around the E_1 transition of GaP could originate in an interface modification of the bulk transition caused by the truncation of the GaP resp. Si lattice at the interface [220, 243] or by strain. Differences between the spectra might be related to the strain that builds up in the pseudomorphic layers. However, at higher photon energies, interpretation of the IDA becomes more difficult due to higher absorption beyond E_1^{GaP} and possible artifacts in the calculation of the IDA [254]. In the following, the spectral region around the E_1 transition of Si will be focused.

[26] In Ref.[254], IDA calculations using dielectric functions from different literature data [14, 133, 134] were compared. The difference in the resulting IDA was found to be negligible.

[27] To guarantee spatial separation of surfaces and interfaces [127], the 5 nm sample was not considered for the calculation of IDA and SDA.

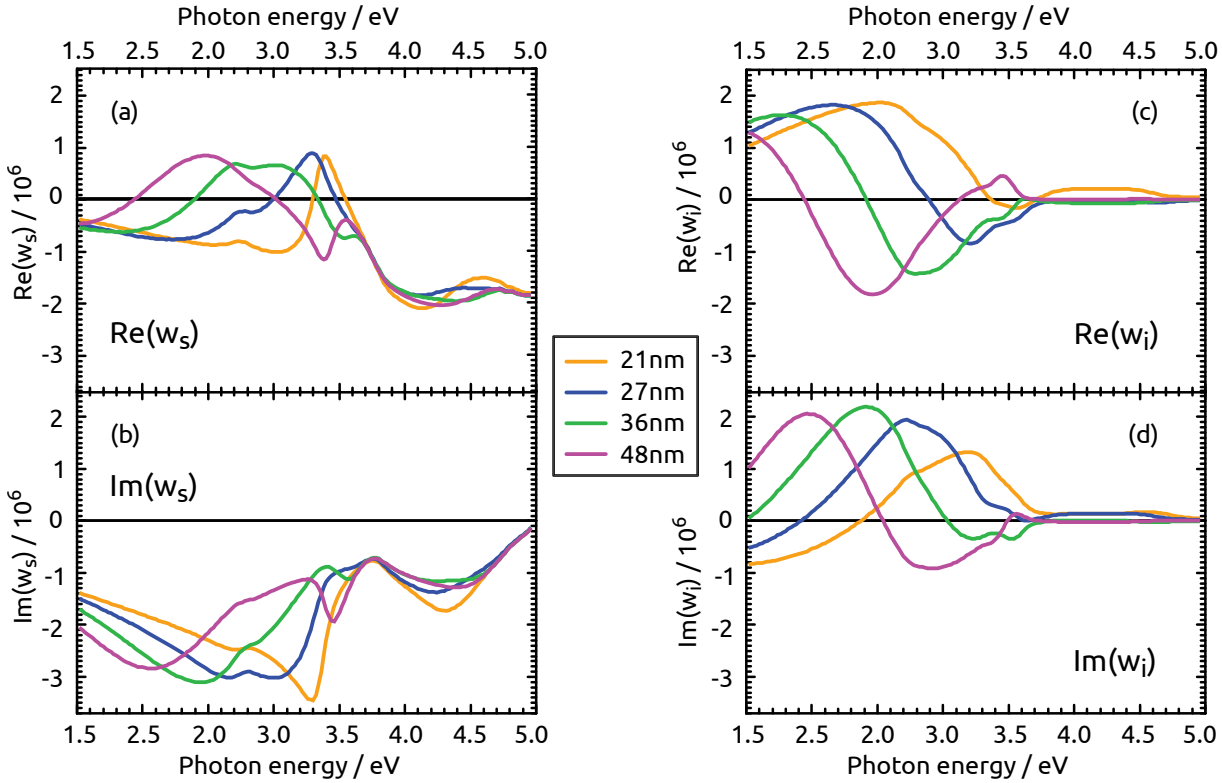

Fig. 3.14 – Spectral weights $w_{i,s}$ of the SDA and IDA ("RAS = w_s SDA + w_i IDA", cf. eq. (2.18) on page 47) for the GaP epilayer thicknesses from Fig. 3.13 on page 70. (a) Real part of w_s. (b) Imaginary part of w_s (c) Real part of w_i. (d) Imaginary part of w_i.

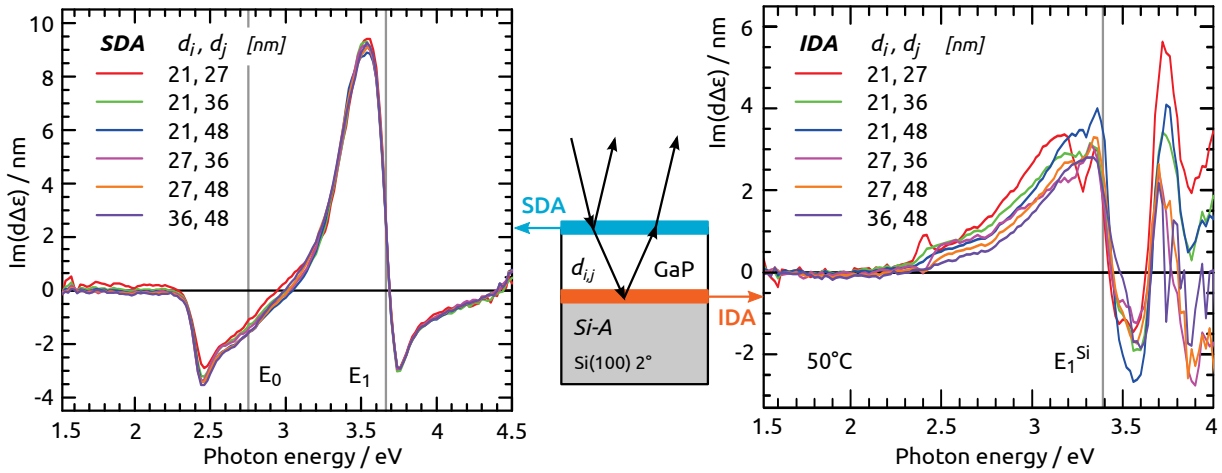

Fig. 3.15 – Calculated surface dielectric anisotropies *(left)* and interface dielectric anisotropies *(right)* from pairs of the differently thick, $(2 \times 2)/c(4 \times 2)$ reconstructed GaP epilayers on *Si-A* which are shown in Fig. 3.12. Gray vertical lines indicate critical point energies of GaP [310] and Si [165], respectively.

In order to compare the IDA extracted from GaP/Si(100) to $(\Delta r/r)_{\text{nucleation}}$ (cf. Fig. 3.9(a), solid blue line) and *Si-A* prior nucleation, the arithmetic mean of the IDA spectra shown in Fig. 3.15(b), and the SDA of the 5 PP sample ($\text{SDA}_{5\,\text{PP}}$) and of *Si-A* ($\text{SDA}_{Si\text{-}A}$) are calculated according to

$$\text{SDA} = d\,\Delta\varepsilon = \frac{\lambda}{4\pi\,\imath}\,\frac{\varepsilon_0 - \varepsilon_{\text{Si}}}{n_0}\,\frac{\Delta r}{r} \quad , \tag{3.7}$$

where the thickness d of the anisotropic layer fulfills $d \ll \lambda$ [183]. The resulting spectra are show in Fig. 3.16.

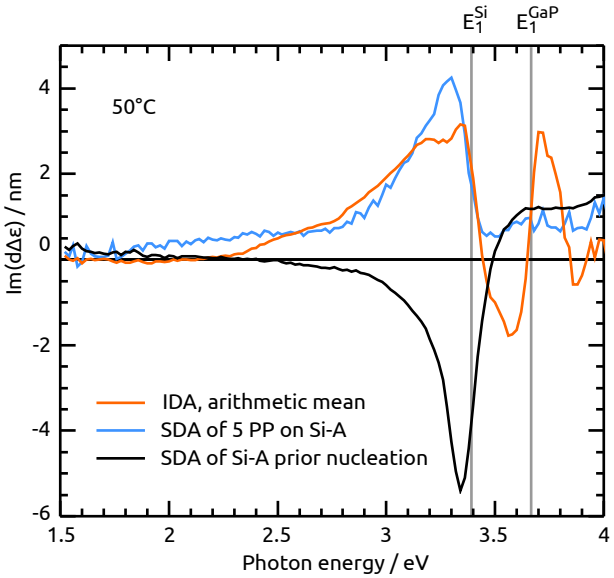

Fig. 3.16 – Comparison of the arithmetic mean of the IDA spectra from Fig. 3.15 (orange line) with the SDA calculated for the 5 PP sample from Fig. 3.9(a) (blue line) and the SDA of *Si-A* prior GaP nucleation (dashed black line). Gray vertical lines indicate the E_1 interband transition of GaP [310] and Si [165], respectively.

The lineshape of the maximum in the IDA below the E_1 transition of Si does not perfectly match that of $\text{SDA}_{5\,\text{PP}}$. Considering the experimental uncertainties and modeling imperfections, however, a certain similarity is noticeable. This suggests that the nucleation anisotropy may indeed arise at the actual GaP/Si(100) heterointerface. The minimum and maximum around E_1^{GaP} has not yet established in the $\text{SDA}_{5\,\text{PP}}$ spectrum. Possibly, this is due to the low GaP coverage. Considering a flip of the sign and the slight energetical shift, the lineshape of the peak in the $\text{SDA}_{\text{Si-A}}$ below E_1^{Si} is also similar. Neither $\text{SDA}_{5\,\text{PP}}$ nor the IDA can, however, be caused by Si dimers rotated from A-type towards B-type at Si(100), since this dimer-related anisotropy would not persist but vanish, when the dimers break during nucleation (note that GaP coverages beyond 3 ML were detected with XPS, cf. Tab. 3.2 on page 67). The IDA could be caused by transitions involving interface perturbed bulk

states, in analogy to what is known for surfaces [228, 243]. Strain was, for example, suggested to cause the RAS signal of UHV-prepared Si(100) [125]. DFT calculations [246, 253], however, revealed interplane relaxations along the [100] direction close to the interface, whereas in-plane relaxations were small for the abrupt interfaces.

Nucleation on Si(100) B-type leads to a flip in sign of $(\Delta r/r)_{\mathrm{nucleation}}$ at 3.3 eV, which implies that this dielectric anisotropy is terrace-related. It may also be caused by transitions involving anisotropic states at the interface, as was suggested for AlAs/GaAs [127]. Due to the tetrahedral lattice coordination, the Si–P bonds, which were found by XPS (cf. section 3.3.4), only exist along [011] direction at abrupt interfaces with (formerly) A-type Si single-domain terraces and even-numbered atomic step height. The existence of an anisotropic density of states at abrupt GaP/Si(100) interfaces was indeed evidenced by DFT [246]. Calculations of the interface-related interband transitions and the corresponding RA spectra, however, are not available. Further modeling and calculation of RA spectra are necessary to understand the microscopic origin of the IDA. Also studying the influence of varying the chemical ambient during nucleation by different sequences seems highly instructive.

Concluding the experimental part of this section, it was shown that a characteristic, nucleation-related dielectric anisotropy establishes already during the first alternating (TBP, TEGa) pulses at low temperature (420 °C). This optical anisotropy is probably also reflected in the interface dielectric anisotropy calculated from RA spectra of thicker GaP/Si(100) heterostructures. Si–P bonds could be evidenced with *in system* XPS and quantitatively correspond to about 1 ML. These findings agree with rather abrupt Si–P heterointerfaces, which can also explain the correlation of GaP sublattice orientation and Si(100) domain type. In the following, DFT calculations of formation energies of abrupt and intermixed GaP/Si(100) interface structures will be discussed.

3.4 DFT calculations of GaP/Si(100) interface formation energies

Ab initio density functional theory (DFT) calculations were performed in collaboration with Dr. F. Grosse (PDI Berlin, Germany) and Dr. O. Romanyuk (ASCR Prague, Czech Republic), who calculated interface formation energies of both abrupt and compensated GaP/Si(100) interface structures.[28] Figure 3.17 on the next page shows the slab used here, which consists of 5 bilayers of GaP and 10 resp. 9 layers of Si. The surface is modeled by the (2×2) surface reconstruction consisting of

[28] Dr. O. Romanyuk performed the DFT calculations discussed here using the ABINIT program [106, 107]. A summary of the computational details is given in the supplementary on page 123.

two P dimers and two hydrogen atoms per (2×2) surface cell [116]. The surface reconstruction does obey the ECM [203]. Dangling bonds of the Si layer backside were passivated by hydrogen atoms. A vacuum region of 20 Å was used to avoid surface interaction with the bottom layer. For the calculations of the relative interface formation energies, $\Delta\gamma$, of abrupt Si–Ga, Si–P, and compensated 0.5 Si : 0.5 P–Ga, 0.5 Si : 0.5 Ga–P interface structure models (shown in Fig. 3.17), the surface structure to the P-terminated (2×2) reconstruction was fixed for both sublattice orientations of the GaP film and the atomic stoichiometry at the interface was varied: The Si–P (Si–Ga) abrupt interface consists of four Si and four P (Ga) atoms per (2×2) in-plane cell. A compensated Si–P (Ga) interface is formed when two Si atoms are substituted by two Ga (P) atoms per (2×2) cell with a Si:P (Ga) ratio of 0.5:0.5 within the interfacial layer. The calculations were carried out for $T = 0$ K assuming thermodynamic equilibrium during initial stages of interface formation. These

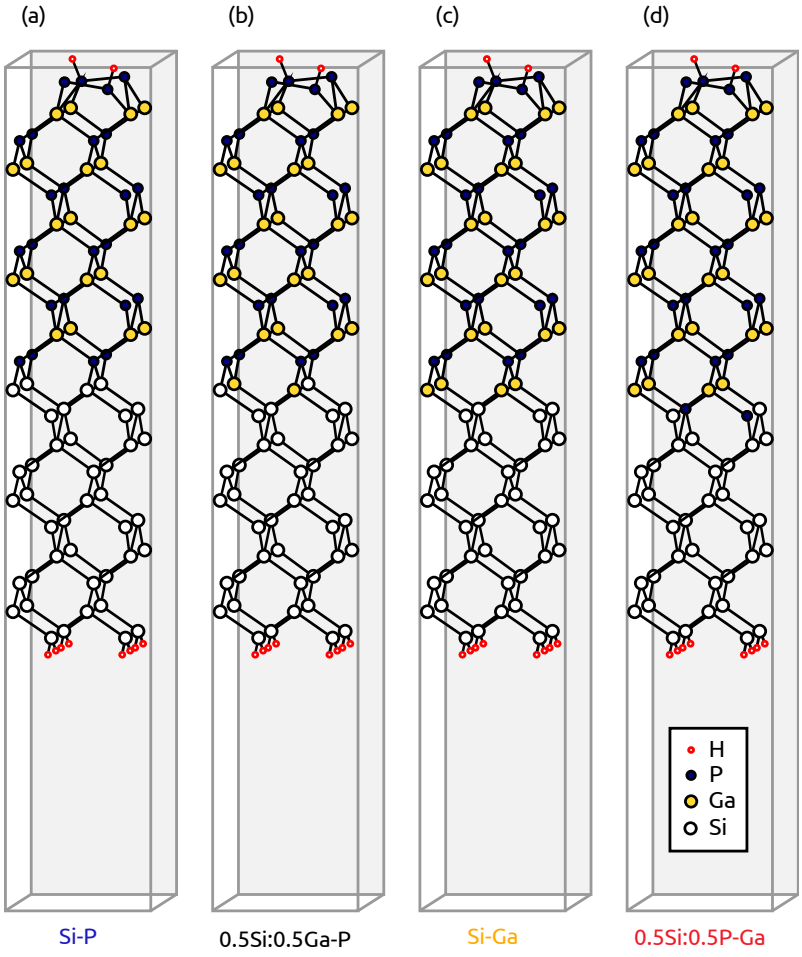

Fig. 3.17 – Slab for the DFT calculations of GaP/Si(100) interface formation energies: (a) Abrupt Si–P interface. (b) Compensated 0.5 Si : 0.5 Ga–P interface. (c) Abrupt Si–Ga interface. (d) Compensated 0.5 Si : 0.5 P–Ga interface. Note, that there is no preferential ⟨011⟩ direction in the DFT model and steps were not included. (Modified graphic after Dr. O. Romanyuk)

equilibrium interface structures are regarded as reference points, even though real atomic interface arrangements can deviate, for example due to kinetically limiting and non-equilibrium growth processes as well as hydrogen interaction at elevated temperatures.

Figure 3.18(c) shows the resulting dependence of $\Delta\gamma$ on the P chemical potential. The compensated interface structure with a 0.5 Si : 0.5 Ga–P atomic interfacial layer is found to be the most energetical favorable in thermodynamic equilibrium. Atomic intermixture of Si and P at the interface is found to be less energetically favorable. Similar to other semiconductor heterostructures [54, 55, 150, 162, 206], abrupt interfaces are found to be less energetically stable in equilibrium than the compensated interfaces. Abrupt Si–P and Si–Ga interfaces, however, could be realized under non-equilibrium growth conditions, such as MOVPE preparation. The formation energy of the abrupt interfaces depends on the chemical potential: for P-rich conditions (which are typical during MOVPE preparation), Si–P bonds are favored and $\Delta\gamma$ increases linearly with decreasing P chemical potential. From a certain threshold value towards Ga-rich conditions, Si–Ga bonds are lower in energy. The energy of the Si–P interface is much lower at P-rich conditions, than the energy of the Si–Ga interface under Ga-rich conditions. This result is in agreement with the previous theoretical work on the abrupt GaP/Si(100) interface[246] predicting a higher stability of Si–P bonds compared to Si–Ga bonds and also agrees with earlier experimental results regarding thermal stability [293].

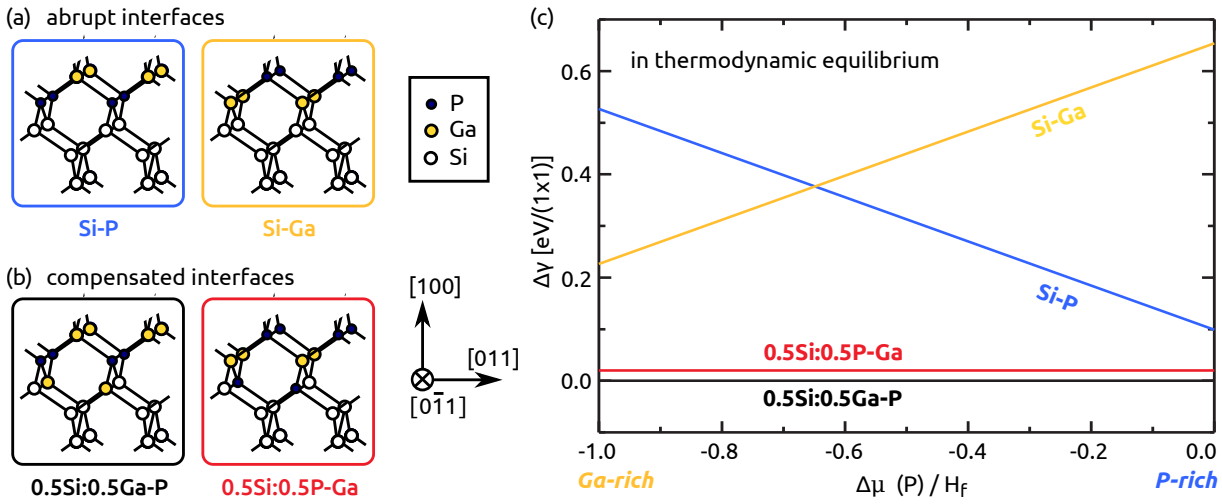

Fig. 3.18 – Structural models for (a) abrupt and (b) compensated GaP/Si(100) interfaces. (c) Relative interface formation energy diagram of these heterostructures. The interface energy of the 0.5 Si : 0.5 Ga–P structure, which is the most stable configuration at thermodynamic equilibrium, was used as reference energy and was set to zero.

These results are in line with section 3.3.1, where it was shown that the observed GaP sublattice orientation after growth on both *Si-A* and *Si-B* can be caused by either abrupt Si–P interfaces or the compensated 0.5 Si : 0.5 Ga–P structure (cf. Fig. 3.7 on page 60). In section 3.3.4, a minority of Si–Ga bonds could not be ruled out. However, Si–P bonds were found by XPS. Nucleation at the rather low temperature of 420 °C (cf. Fig. 3.8 on page 62) thus leeds to a kinetically limited formation of preferential Si–P interfaces.

We initiated a collaboration with Dr. A. Lenz at TU Berlin in order to find further direct evidence for abruptness vs. intermixing applying cross-sectional STM at the interface. Currently, we also work on DFT calculations at nucleation temperature.

3.5 Nucleation in dependence on the (Ga, P) chemical potential

At abrupt interfaces, Si–Ga bonds should become more favored towards Ga-rich nucleation conditions, as depicted in Fig. 3.18 on the preceding page. III-rich conditions are generally critical in MOVPE since droplet formation needs to be avoided. In the following, the aim is to realize Ga-rich nucleation conditions experimentally and it will be shown that already sub-monolayer coverages of (Ga, P) from previous processes highly impact GaP nucleation.

3.5.1 Local variations of the majority sublattice orientation

As discussed in section 2.10.1, annealing at about 730 °C under high H_2 pressure is crucial for preparation of single-domain A-type terraces on 2° misoriented Si(100). However, here quick pressure ramps from 950 mbar to 100 mbar after Si buffer growth are desired to increase desorption from (Ga,P) background residuals. As we showed in Ref.[45], the same is needed to avoid layer-by-layer Si removal and to prepare preferential A-type terraces on 0.1° misoriented Si(100) substrates. Therefore, Si(100) substrates with 0.1° misorientation towards [011] will be used in the following.

Starting pulsing with the precursor TEGa had no effect on the GaP sublattice orientation. Moreover, when increasing the TEGa partial pressure or prolonging the pulses, we could not measure any of the well-known GaP(100) in situ RAS signals during GaP growth. It turned out to be more practical to vary reactor preconditioning and Si preparation to control the amount of (Ga, P) residuals at the Si(100) surface: (1) Samples prepared in a GaP reactor under rather “clean” conditions (including well-defined baking of the reactor and carrier prior to processing)

are marked with the index *clean*. (2) Samples prepared in presence of intentionally higher amounts of residual (Ga,P) species (e.g. by shorter baking) are indexed with *cont*. Identical process parameters were applied for thermal deoxidation and Si homoepitaxy with silane [43], see Fig. 2.21 on page 41. In case of GaP/Si samples, the 5 PP nucleation sequence discussed above was applied prior to pseudomorphic growth of about 40 nm GaP.

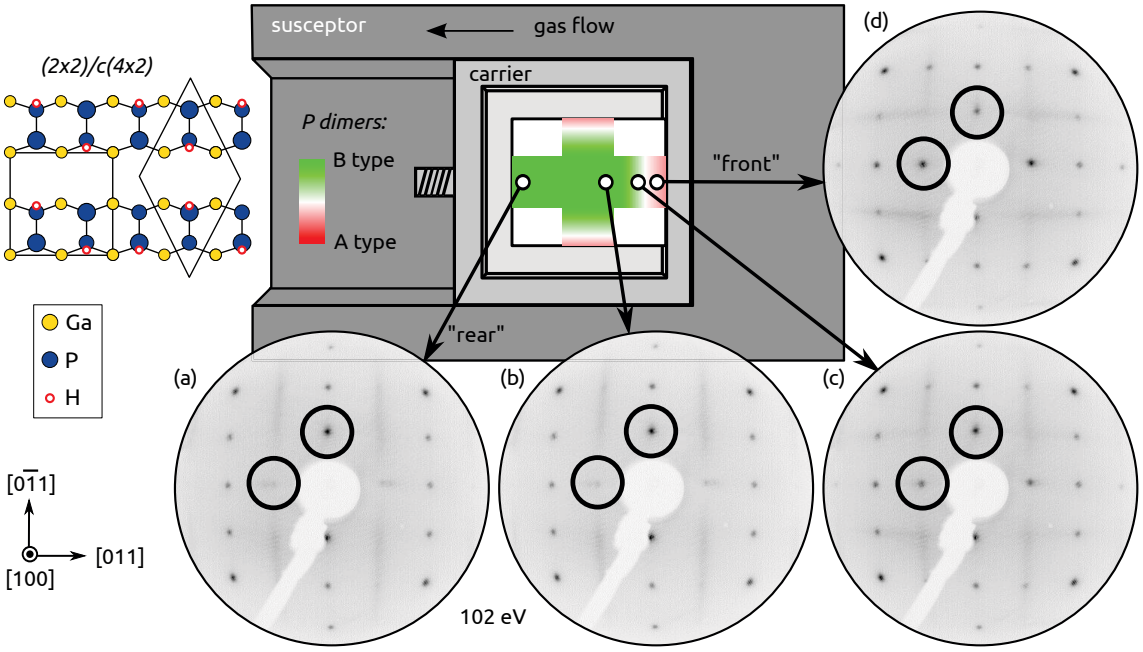

Fig. 3.19 – Schematic drawing of the susceptor and carrier together with LEED patterns (E=102 eV) of $(2 \times 2)/c(4 \times 2)$ reconstructed GaP/Si$_{clean}$. The sketch of the sample (length $\approx$ 2 cm) indicates the domain imbalance, which was roughly estimated applying LEED, color-coded along a scan parallel (a,b,c,d) and perpendicular to the flow direction. Circles mark spots at half order.

Figure 3.19 shows LEED patterns of $(2\times2)/c(4\times2)$ reconstructed GaP/Si$_{clean}$.[29] At about the center of the sample, the GaP/Si(100) surface is almost single-domain B-type as indicated by spots at half order along [0$\bar{1}$1] in Fig. 3.19(b), which would be expected for GaP/*Si-A*. These LEED patterns do not change significantly over large areas of the sample. Towards the front edge, however, the spots at half order along [011] increase in intensity (cf. Fig. 3.19(c)) and at the very edge, the A-type domain even prevails (cf. Fig. 3.19(d)). Similar behavior is observed at the top and bottom edges. At the rear, in contrast, the B-type majority domains persist (cf. Fig. 3.19(a)). These findings clearly point to an effect at edges close to the

[29] Note that the spot position of in situ RAS setup at the MOVPE reactor is fixed, which hinders locally resolved domain quantification via the RAS intensity.

susceptor. Two possible explanations are that (i) already the corresponding domain ratio at the Si(100) surface is affected analogously, or (ii) that diffusion of residual atoms influences the chemical ambient during GaP nucleation.

Figure 3.20 demonstrates that out-gassing of both Ga and P species from reactor parts needs to be considered: After a typical GaP/Si growth run, the reactor was heated to 1010 °C (950 mbar H_2) monitoring the mass:charge ratios, which relate to P and Ga, with a mass spectrometer connected to the reactor outlet. While the measured ionization currents cannot directly be translated to partial pressures in the reactor, both Ga, GaH_x, P and PH_x species are clearly present in the gas phase.

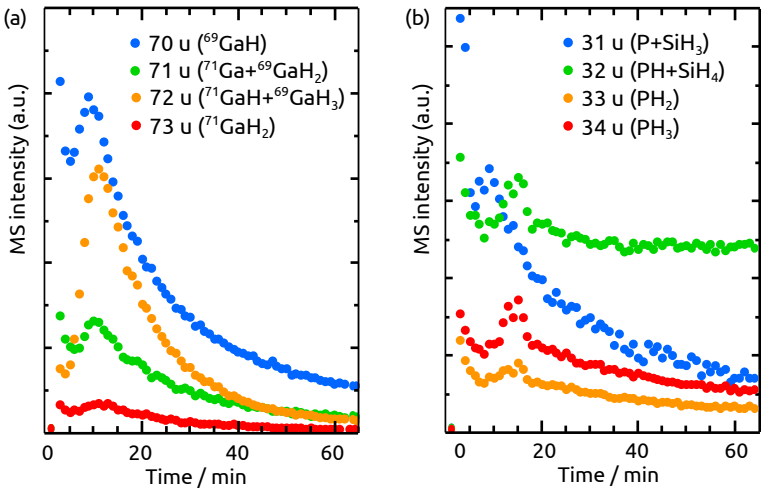

Fig. 3.20 – Mass spectrometry during heating of the MOVPE reactor (no sample, 950 mbar H_2, 1010 °C reached at 16 min) after a typical GaP/Si(100) process. (a) Ga-related species. (b) P-related species.

3.5.2 Si(100) surfaces preparation

In order to study the effect of background residuals quantitatively, we performed XPS measurements. Coverages were estimated applying the model described in eq. (3.4) on page 65, including Si plasmons for substrate intensity. One ML would correspond to the thickness of a quarter of a lattice constant with every atomic substrate site replaced by the overlayer species. Here, Si_{clean} is compared to Si_{cont}, where a faster pressure ramp after Si buffer growth from 950 mbar to 100 mbar was applied. Both samples were transferred to XPS[119] after Si(100) processing and prior to pulsed GaP nucleation. Fig. 3.10 shows selected PE lines and Tab. 3.3 on the following page gives binding energies (E_B) and coverages. The Ga $2p_{3/2}$ PE line (Fig. 3.10(a)) clearly consists of two components: a bigger component (Ga_2) and a smaller one at lower binding energies (Ga_1). Compared to the quantification

Tab. 3.3 – Coverage $\mathcal{C}$ in ML (according to eq. 3.4 based on Ref.[180], see also section 3.3.4), binding energies E_B and intensity ratios (corrected with atomic sensitivity factors) of the $2p_{3/2}$ PE components shown in Fig. 3.21

	Si_{clean}		Si_{cont}				
PE line	E_B/eV	$\mathcal{C}$/ML	E_B/eV	$\mathcal{C}$/ML	*ratio*	90°	30°
Ga_1	1116.53	0.4 %	1116.28	1.3 %	Ga_1:Ga_2	0.17	0.39
Ga_2	1117.58	0.7 %	1117.48	8.6 %	Ga_1:P	0.10	0.11
P	129.38	8 %	129.09	17 %	Ga_2:P	0.68	0.28
Si	99.76	-	99.65	-			

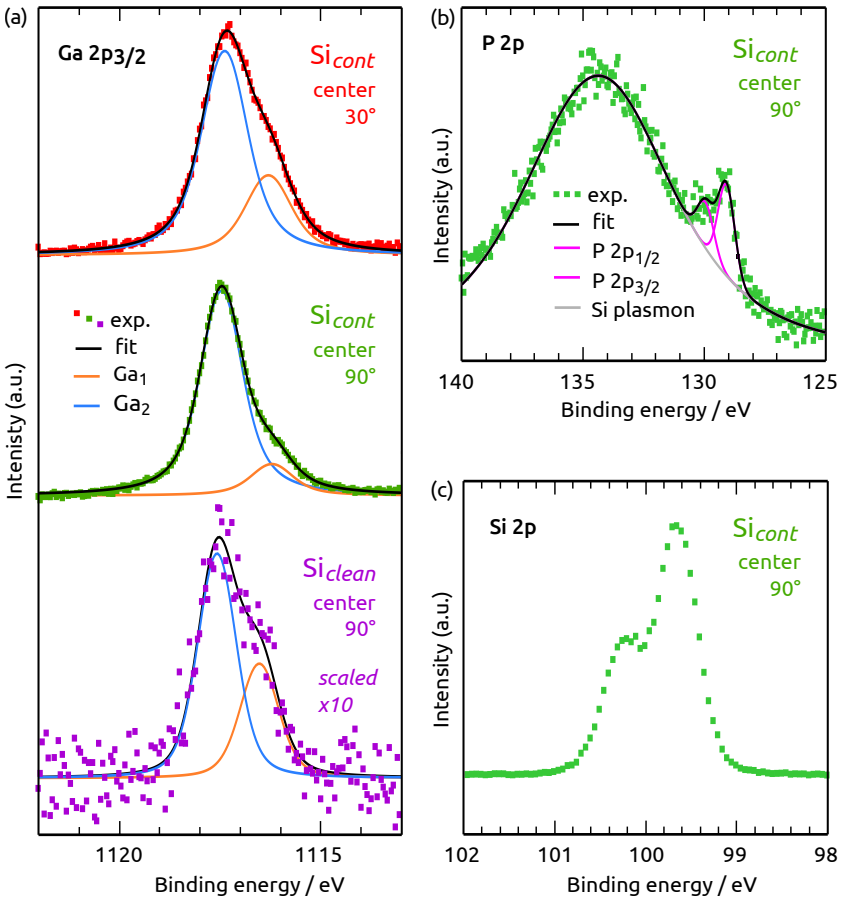

Fig. 3.21 – XPS measurements (monochromated Al K_α). (a) Ga $2p_{3/2}$ PE line (symbols) and fitted components (see legend) of Si_{cont} measured at normal exit angle (green) and 30° exit angle (red), as well as of Si_{clean} (violet). (b) P 2p PE line of Si_{cont} measured at normal exit angle and fit components (see legend). (c) Si 2p PE line of Si_{cont} measured at normal exit angle.

in Tab. 3.2 on page 67, the Si PE lines of Si_{clean} and Si_{cont} are shifted in E_B by 0.45 and 0.55 eV, respectively. Considering that shift, Ga_2 matches the position of GaP. Due to the small cross-section and lower surface-sensitivity, the P 2p PE line (Fig. 3.10(b)) is not intense enough to reliably distinguish between the existence of two or just one component. The different ratio of Ga_2:P between the two samples could explain the shift of the P 2p line position, as the two chemically shifted components, one would expect, cannot be reliably resolved. Si_{cont}, however, is covered by about 9 times more Ga and about 2 times more P compared to Si_{clean}. When measured at 30° exit angle to raise surface sensitivity, the ratio Ga_1:Ga_2 increases, whereas Ga_1:P remains constant.[30] This implies that Ga_2 is covered by another species, while Ga_1 and P are not. One possible explanation is that three different adsorbate species coexist at the surface: (i) about 9 % of a monolayer (ML) GaP, where Ga is situated below P, (ii) about 8 % ML of P-species not bound to Ga, and (iii) about 1 % ML Ga-species not bound to P. The Si 2p PE line (Fig. 3.10(c)) cannot sufficiently be fitted by one single component. Due to the low coverages, the Si 2p PE line does not allow a clear conclusion on whether the Ga or the P species are chemically bound to Si. Position-dependent measurements at Si_{cont} show a decreasing Ga:P ratio in flow direction with higher amounts of Ga at the front and more P at the rear of the sample. This supports the assumption of Ga residuals causing the local variation of antiphase disorder in Fig. 3.19 on page 78. The general trend was reproduced, though run-to-run discrepancies in the absolute residual coverages occur.

3.5.3 GaP/Si(100) heterointerface structure

Figure 3.22 on the next page shows the RA spectra of a Si_{cont} sample directly prior to nucleation as well as of $(2\times2)/c(4\times2)$ reconstructed GaP/Si_{cont} after heteroepitaxy. The Si(100) signal (green, solid line) is similar to that of H-terminated Si(100), though there are slight differences: Beyond 3.9 eV, RAS of Si_{cont} does not clearly show the peak-like contribution known from clean H-terminated Si(100) [44, 202], but an additional broad peak seems present around 2.2 eV. The latter might be related to Ga, as sub-monolayer coverage of Ga on UHV-prepared (vicinal) Si(100) was found to contribute to the RAS signal at photon energies below 2.2 eV [53]. The clear peak at the E_1 interband transition of Si, however, corresponds to the A-type Si dimer orientation, which is indicated in the inset (b), as was also proved by LEED. The GaP/Si_{cont} RA spectrum measured here (orange, dash-dotted line) corresponds to A-type P dimers at the $(2\times2)/c(4\times2)$ reconstructed surface. Hence, RAS evidences growth of A-type GaP on A-type Si. Within the abrupt interface

[30] Intensity ratios were calculated using atomic sensitivity factors [283] assuming a homogeneous element distribution. For thin layers, this underrates PE lines at higher kinetic energies, which explains the different ratio when compared to the more reliable ML coverage.

model discussed above, this implies Si–Ga bonds at the heterointerface as indicated in the inset (c) of Fig. 3.22.

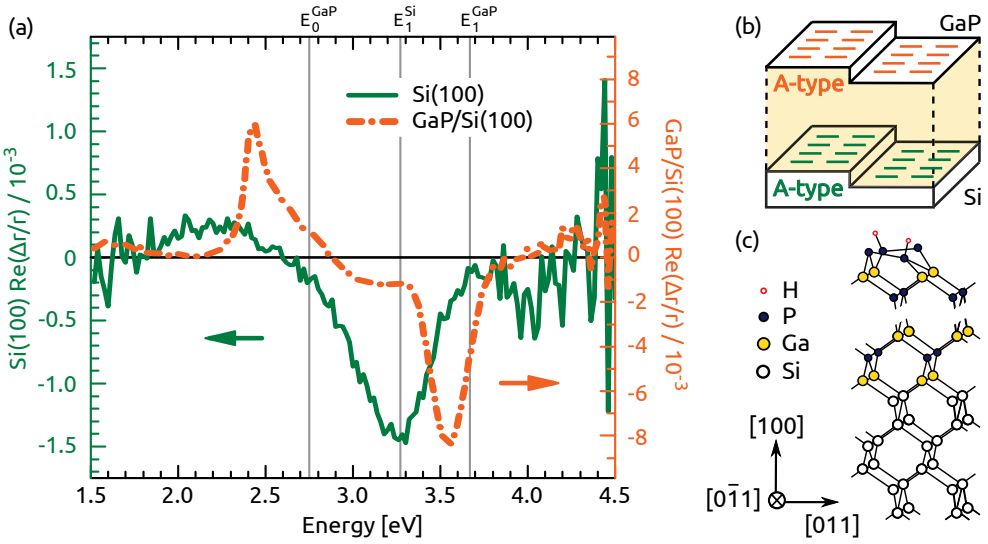

Fig. 3.22 – (a) RA spectra of Si_{cont} directly prior to GaP nucleation (420 °C, green line) and of subsequently grown, $(2 \times 2)/c(4 \times 2)$ reconstructed GaP (50 °C, orange line). Vertical gray lines indicate the critical point energies of Si [165] and GaP [310], respectively. (b) Corresponding orientations of P and Si dimers (prior to nucleation). (c) Sketch of the heterointerface in the idealized abrupt model.

Both for GaP growth on Si_{clean} (see Fig. 3.19(a)) and Si(100) with 2° misorientation, in contrast, the GaP sublattice orientation is inverted, which implies Si–P bonds at the heterointerface assuming abrupt interfaces. In principle, the inversion of the GaP sublattice for GaP/Si_{cont} could also be explained by Si–P bonds combined with either (i) B-type Si(100), (ii) substitutional P adsorption or (iii) an additional Ga/P interlayer forming one ML below the uppermost Si atoms. However, these processes would then only occur during pulsed nucleation on Si_{cont} and not on Si_{clean}.[31] Si–P bonds and a GaP sublattice orientation in disagreement with substitutional P adsorption of an entire ML of Si was observed in section 3.3 during GaP nucleation in comparably clean systems. In case of Si_{cont}, XPS analysis also indicates that P is adsorbed on top of Si. Consequently, it seems unlikely that P will substitute Si atoms during subsequent GaP nucleation. Ga was found to promote B-type Si(100) terraces at Si(100), which was Joule-heated to 600 °C in UHV [122]. To explain our findings, rearrangement towards Ga-covered B-type Si terraces [122] would have to take place during pulsed nucleation together with replacement of the

[31] Note that our experiments differ from As-terminated Ge(100) [46, 268]. Here, the amount of sub-ML residuals on Si with A-type majority domains is varied. Subsequently, pulsed nucleation with precursor supply is performed identically here.

uppermost Ga atoms by P. Ga droplet growth on Si(100) terraces with precursor supply may lead to pyramidal etching [24, 288]. The droplet formation was found to be significantly above 1 ML of Ga and can be reduced by higher V:III ratios [279]. Here, Ga coverages prior to nucleation are clearly below 1 ML and XPS results even imply that the larger Ga_2 component, which is not located at the very surface, is bound to P whereas the Ga_1 component is on top. Regarding Ga coverages below 0.5 ML, UHV studies suggest that Ga–Ga dimers form on top of Si dimers which remain unbroken [22, 34, 221]. Though experimental conditions are quite different here (monohydride-terminated Si, presence of P), intact A-type Si dimers below the adsorbed Ga could explain the Si dimer related RAS minimum at E_1^{Si} (Fig. 3.22) and possibly also the slight differences in lineshape above and below E_1^{Si} compared to Si(100) prepared in absence of III-V residuals.

The increased amount of Ga available during GaP nucleation also shifts the (P, Ga) chemical potential towards more Ga-rich conditions. The *ab initio* density functional theory calculations in section 3.4 showed that the energetically favorable binding situation at the ideally abrupt GaP/Si(100) heterointerface changes from Si–P to Si–Ga for more Ga-rich nucleation conditions (cf. section 3.4). It cannot directly be translated, at which value of chemical potential the nucleation takes place here. However, qualitatively this could explain the observation of inverted GaP sublattice growth on Si_{clean} resp. Si_{cont}. It may also explain the Si–Ga bonds suggested recently [28].

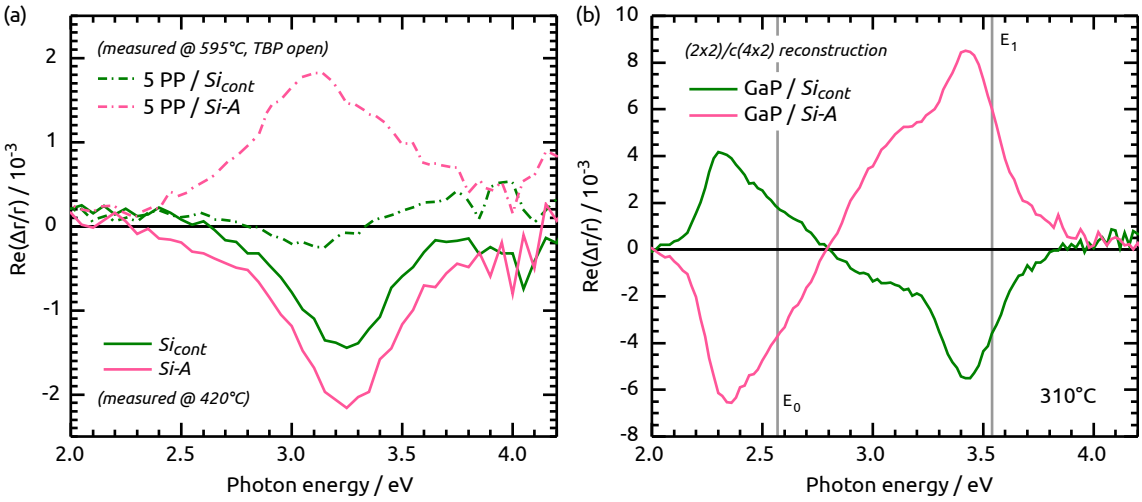

Fig. 3.23 – RA spectra extracted from colorplots during processing: (a) *Si-A* (pink) and Si_{cont} (green) directly prior to GaP nucleation (straight lines, measured 420 °C) and after 5 PP nucleation directly prior GaP growth (dash-dotted lines, measured at 595 °C with TBP stabilization). (b) RAS of GaP grown on the samples shown in (a), measured at 311 °C after preparation of the $(2\times2)/c(4\times2)$ reconstructed GaP/Si(100) surface. Vertical gray lines indicate the critical point energies of GaP [310].

Figure 3.23(a) illustrates that already the nucleation related RAS signal flips sign when the 5 PP nucleation sequence is applied on Si_{cont}. Moreover, the amplitude of the RAS signal after nucleation on Si_{cont} (green line) is strongly reduced compared to that in a clean system (pink line). As discussed in section 3.3, the RA spectrum after 5 PP is terrace-related. This could be caused by the presence of two domains with a stronger domain imbalance for cleaner systems. Assuming residual Ga at the Si(100) surface to be responsible, the sub-monolayer coverage will lead to local variations of the amount of Ga available. Even though it turned out, that the precise amount of the background residuals diffusing on the Si(100) surface is difficult to adjust in terms of negligible run-to-run discrepancies, we found indeed indications for a stronger domain imbalance with increasing background Ga. Assuming further the argument given above, that Ga residuals lead to a more Ga-rich chemical potential, domains of Si–P and Si–Ga bonds could result in case of abrupt interfaces. Consequently, antiphase disorder would be introduced in the GaP epilayer even in case of single-domain T_A Si(100) substrate surfaces.

Regarding the microscopic origin of the nucleation related RAS signal, Dr. O. Romanyuk performed preliminary calculations of interfacial density of states (DOS) for abrupt Si–P and Si–Ga interfaces (not shown here). More precise calculations are required for a definite conclusion, but these preliminary results indicate an anisotropic DOS both for the Si–P and the Si–Ga abrupt interface with opposite dispersion along [011] and $[0\bar{1}1]$, respectively. Whether these states also result in the nucleation related RAS signal for both cases, however, needs further theoretical modeling. Besides transitions involving Si–P resp. Si–Ga bonds, also interface perturbed transitions, either in the thin GaP film itself or its influence on the Si substrate, might account for the observed RA spectra.

3.5.4 Consequence for the choice of Si(100) substrate misorientation

The Si surface preparation step after Si buffer growth is decisive here for the amount of residuals found on the surface. Annealing at 730 °C in 950 mbar H_2 after thermal deoxidation at 1000 °C is crucial for single-domain, A-type surface preparation of Si(100) with 2° misorientation (cf. Fig. 2.19 on page 39). Quick temperature and pressure ramps, however, are necessary to avoid layer-by-layer removal on Si(100) 0.1° occurring in this temperature range (cf. Fig. 2.20 on page 40). Particularly the pressure ramp is complicating Si(100) 0.1° surface preparation in reactors contaminated with III-V residuals: The rate of residuals desorbing from reactor parts (liner, susceptor, carrier) is increasing with decreasing pressure. This becomes particularly important at elevated temperatures, where desorption of residuals from reactor parts and diffusion of residuals on the sample are high while the H termination [43] is not stable yet. The consequence is that single-domain surface formation and avoidance of contamination conflict for nominal Si(100) substrates regarding process parame-

ters. The residual atoms may in principle also influence Si vacancy generation and diffusion, but *in situ* RAS reveals an A-type majority domains even for Si_{cont} so that the vacancy kinetics are assumed to be comparable to systems free of residuals.

Nucleation with a starting TEGa pulse (not shown here) was not sufficient to grow GaP with majority A-type P dimers. Nucleation with high residual amounts or high TEGa precursor supply–in order to reach high amounts of Si–Ga bonds for single-domain GaP–is not easy to control. The co-existence of areas with Si–P and Si–Ga bonds at single-domain Si(100) terraces, however, would cause antiphase disorder analogously to the existence of either Si–P or Si–Ga bonds at two-domain Si(100) terraces. We never observed A-type GaP/Si(100) surfaces in case of A-type Si(100) 2° misoriented substrates. Cooling to temperatures in the range of 730 °C in 950 mbar H_2 (for annealing to prepare A-type terraces), prior to decreasing the reactor pressure for GaP nucleation, seems to effectively hinder excessive Ga diffusion on the surface. Both decreased desorption rates from reactor parts and the H termination of the Si(100) surface [43] are beneficial here.

Nucleation on nominally oriented Si(100) may also benefit from even higher TBP partial pressures. In case nominal Si(100) surfaces are not required for the final device structure, Si(100) surfaces with 2° misorientation are favored regarding a more robust surface and single-domain GaP nucleation process in processing ambient which contains (Ga, P) residuals.

3.6 The influence of arsenic on GaP/Si(100) heteroepitaxy

Regarding III-V/Si(100) heteroepitaxy of III-V compounds containing As, such as lattice-matched GaPNAs epilayers or GaAsP graded buffer layers, the influence of As on Si(100) preparation and GaP/Si(100) heteroepitaxy is important. As termination of Si(100) was also found to hinder out-diffusion of Si in the GaP epilayer [151]. On the other hand, arsenic is highly interesting regarding the preparation of a Si pn-junction by As in-diffusion in the homoepitaxial Si buffer.[32]

Though arsenic is mostly present in realistic MOVPE growth process ambient, be it As_4 from background residuals or in form of the precursor, its influence on GaP/Si heterointerface formation and GaP epilayer growth has been studied much less compared to GaP/Si preparation in clean H_2 ambient [43–45, 71, 77, 202] and As-free GaP nucleation [28, 253, 256, 279].

[32] A pn-junction within the Si substrate can serve as bottom cell in tandem PV absorbers. The MOVPE preparation and characterization of these pn-junction is part of A. Paszuk's ongoing Ph.D. work in our group at TU Ilmenau and will not be discussed here.

Here, Si(100) 2° misoriented substrates will be used. In contrast to Ref.s[32, 118, 184], where TBAs or AsH_3 was supplied during thermal deoxidation of the Si substrate to decrease the required temperature below 900 °C, the established process for preparation of *Si-A* will be applied to decrease etching and roughening of the surface. This yields well-defined starting conditions before offering TBAs at 420 °C. The surface will then be heated in TBAs ambient to 670 °C, which is an interesting temperature range for As in-diffusion. Subsequently, an As-modified Si(100) surface, will be prepared by annealing in background arsenic at 850 °C. The resulting surface will be abbreviated *Si-As* in the following.

3.6.1 Preparation of As-modified Si(100) surfaces

Fig. 3.24(a) shows a RAS colorplot, where RA spectra were measured continuously with color-coded amplitude. Arrows mark spectra which are compared in Fig. 3.24(b). Before offering any III-V precursor, a preferentially A-type, monohydride-terminated Si(100) surface (*Si-A*, see section 2.10.1) was prepared and cooled to 420 °C in 100 mbar H_2. The corresponding RAS signal (green, dash-dotted line) demonstrates that *Si-A* can also be prepared in MOVPE processing ambient, where As (and Ga, P) was involved in previous processes. The amplitude of the RAS signal implies a $T_A : T_B$ domain imbalance of about 7:3. [44, 202]. Directly upon opening the TBAs source,[33] the dielectric anisotropy changes drastically (blue, dashed line): A broad peak centered at about 3.7 eV (labeled A_1) emerges and the Si dimer related minimum peak at E_1 has almost vanished, with a remaining amplitude of only $0.2 \cdot 10^{-3}$ shifted about 100 meV to lower energies (A_2). Despite a temperature related shift and decrease in amplitude, these features retain when heating to 670 °C under continuous TBAs supply. A_2 seems to increase only slightly during continuous annealing at 670 °C. A_2 is more pronounced in the RA spectra of As-terminated A-type Si(100) in literature [32, 147] (see discussion below). To test the influence of background arsenic, TBAs was switched off and the sample was heated towards 850 °C. At first, the RAS signal does not change (apart from temperature effects on the optical transitions). A_1, however, seems to sharpen beyond about 800 °C and, simultaneously, a second local minimum becomes apparent at about 4 eV (A_3). Reaching 850 °C, both A_2 and A_3 increase rather suddenly in amplitude and remain stable at 850 °C. After cooling back to 420 °C, the RA spectrum (orange line, abbreviated *Si-As*) clearly shows A_2 about 100 meV below E_1^{Si}, A_1 of similar amplitude at 3.7 eV as well as A_3 at 4.1 eV and a small broad contribution below 2.7 eV (A_4). The thermal blueshift of A_2 is larger than that of A_1.

[33] $P_{part}^{TBAs} = 0.4$ mbar, $P_{reactor} = 950$ mbar H_2

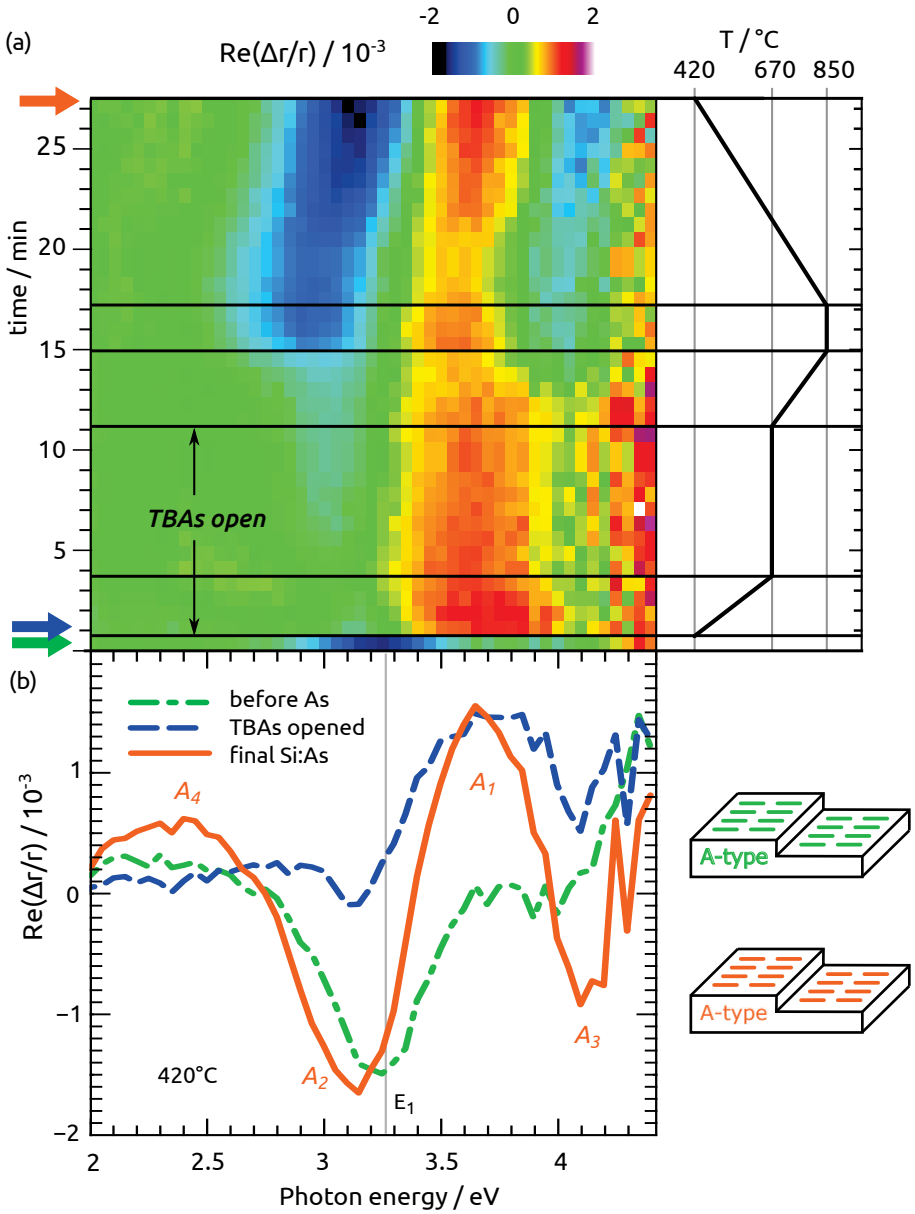

Fig. 3.24 – (a) RAS colorplot of Si(100) with 2° misorientation towards [011] in H_2 at temperatures indicated at the right hand side. The black arrow marks TBAs supply and bold green/blue/orange arrows mark particular spectra which are compared in (b). The models at the right bottom side indicate the majority dimer orientations according to LEED measurements. The vertical gray line indicates the E_1 transition of Si [165].

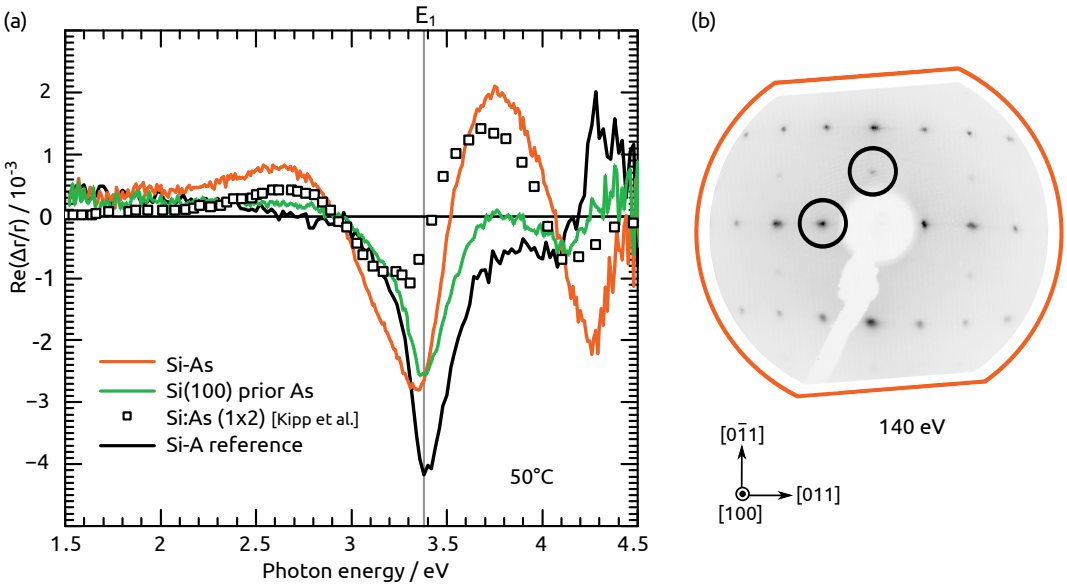

Fig. 3.25 – (a) RA spectra of 2° misoriented Si(100) prior (green line) and after (orange line) As-modification in comparison to the UHV-prepared, (1 × 2) A-type Si(100):As sample from Kipp et al.[147] and *Si-A* prepared in As-free H_2 ambient. (b) LEED pattern of *Si-As*. Circles mark spots at half order.

Figure 3.25 compares the RAS signal of a *Si-As* sample with the spectrum measured by Kipp et al.[147] after additive As_4 adsorption on B-type Si(100) with 4° misorientation towards [011] in UHV (see section 2.3), and with our standard *Si-A* reference prepared in an As-free system. Referring to calculated RAS signals, Kipp et al.[147] ascribed the spectral features to transitions between surface modified bulk states and antibonding As dimer states, respectively to transitions between bonding and antibonding As dimer states. However, their calculations do not resemble A_2. Patterson and Herrendörfer assign A_2 to Si–As bonds and As lone pairs [204]. *Si-As* measured here exhibits more intense peaks compared to the sample of Kipp et al. A_2, in particular, is more than twice as intense. The spectrum measured by Bork et al. after TBAs annealing in MOVPE-ambient shows an almost identical lineshape compared to that measured by Kipp et al., but it is enhanced in intensity by a factor of five. Both surfaces were terminated with 1 ML As [32, 147]. While Kipp et al.[147] claim a domain ratio of $T_A : T_B = 9{:}1$, Bork et al.[32] refer to LEED showing two-domain patterns.[34] A flip of the RAS signal, however, was observed by Kipp et al.[147] for B-type As dimers, which implies a dimer-related signal.

[34] The published pattern in Ref.s[119] clearly show qualitatively that the surface is not single-domain. The absence of temperature-dependence in the RAS signal, which is stated by Bork et al.[32], cannot be reproduced here.

According to the RAS signal in Fig. 3.24, *Si-A* prior to As-modification was monohydride-terminated. A small contribution at the position of A_1, however, already seems present. Since H was found to limit As adsorption [271], the formation of A_2 at temperatures above 850 °C could be related to an increase in H desorption rates facilitating replacive adsorption of Si by As present in the reactor. This would, however, not explain the early appearance of A_1. During the annealing at 850 °C, As will also desorb from the surface [4]. Indeed, we monitored a decrease of amplitude of the RAS signal during longer annealing at 850 °C, when the amount of background As is insufficient to compensate As desorption. STM and XPS of the intermediate surface (Fig. 3.24, blue line) would be of great benefit here. Regarding the final *Si-As* surface, XPS measurements indicate an As coverage of only about 0.5 ML according to eq. 3.4. Possibly, the RAS signal of *Si-As* contains a contribution from As dimers Si(100) (as discussed by Kipp et al.[147]) and monohydride-terminated Si dimers (as for *Si-A*), both with majority T_A domains.

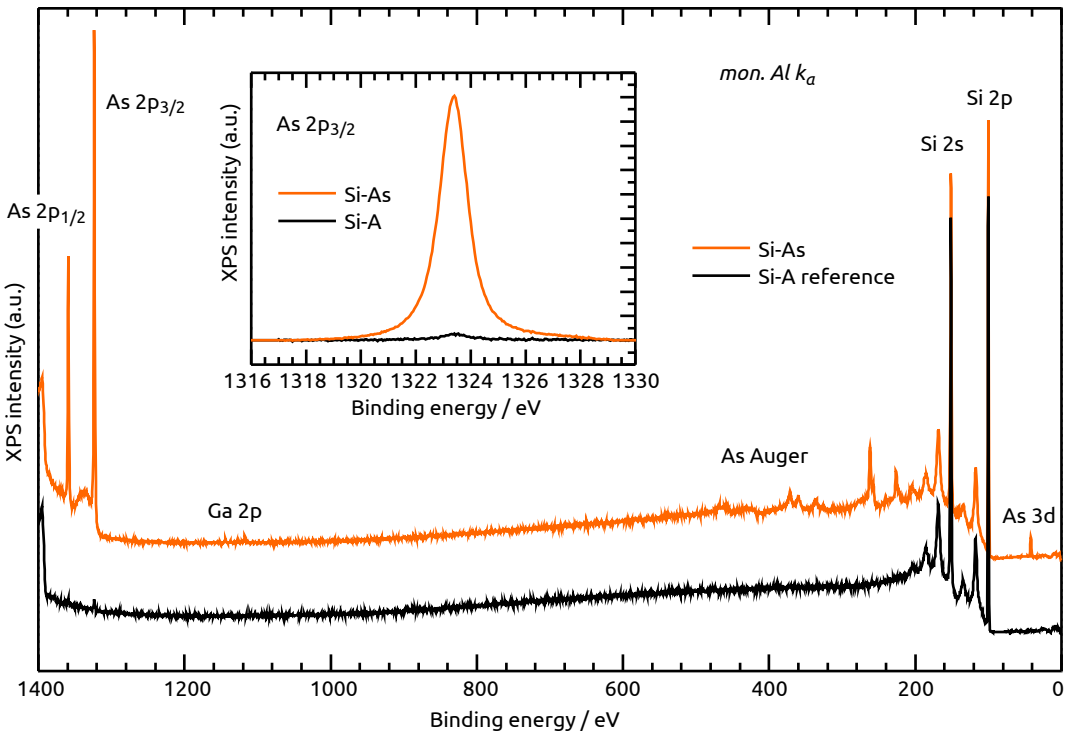

Fig. 3.26 – XPS survey spectra of *Si-As* (orange line) and the *Si-A* reference (black line) measured with mon. Al k_α. The inset shows the As $2p_{3/2}$ PE line.

Figure 3.26 shows the XPS survey spectra of the *Si-A* reference and *Si-As*. Also *Si-A* contains traces of As.[35] Neither O 1s nor C 1s could be detected. In addition to about 0.5 ML As, little amounts of Ga are detectable on *Si-As*.

[35] Residual As close to the detection limit of XPS is usually present even after preparation in the

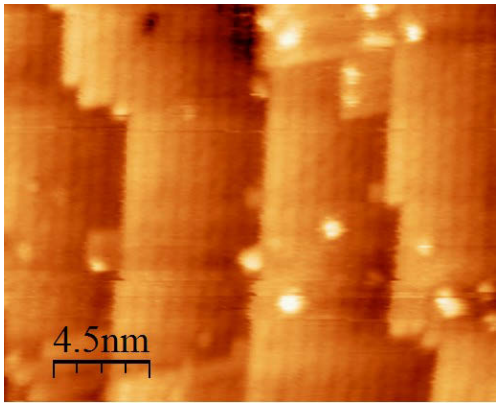

Fig. 3.27 – STM image (empty states) of *Si-As*.

A-type dimer rows are clearly visible in the STM image of *Si-A* in Fig. 3.27, where both terrace width and step height correspond to a double-layer stepped surface. While steps reached maximum 4-fold atomic step heights, single-, double- and triple-layer steps where most prominent and significant step bunching was not observed. We could not yet resolve, whether these dimers are Si dimers, As dimers or possibly even Si–As heterodimers. Interestingly, the steps separating T_A terraces are mostly of "real" even-numbered step height without the small T_B residuals, which were found at *Si-A* (cf. Fig. 3.2 on page 53).

3.6.2 GaP growth on Si(100):As

According to *in situ* RAS, *Si-A* preparation and subsequent As-modification succeeds also in MOVPE ambient which may contain (Ga,As,P) residuals from previous processes. In the following, the focus is on subsequent GaP heteroepitaxy. Interrupted GaP growth was performed on *Si-As* analogously to the growth in *Si-A* discussed in section 3.3.5. The RAS signal of differently thick, $(2 \times 2)/c(2 \times 4)$ reconstructed GaP/*Si-As* epilayers is displayed in Fig. 3.28(a). Epilayer thicknesses were fitted via the relative reflectance data as in Fig. 3.13 on page 70. Just as for GaP/*Si-A* (cf. Fig. 3.12 on page 70), the RAS lineshape results from a convolution of the GaP(100) SDA, thickness dependent interference and the buried IDA. The sign of GaP/*Si-As* corresponds to P dimers aligned in rows parallel to $[0\bar{1}1]$ direction (A-type), as shown in the sketch in Fig. 3.28(c). This implies an inverted GaP sublattice compared to growth on *Si-A* (see Fig. 3.28(d)). The amplitude of the RA spectra indicates single-domain surfaces.

"clean" Si system. Note that the wafers are not doped with As. Possibly, this is a contamination from the run lines of the MOVPE system or As out-diffusing from the exhaust.

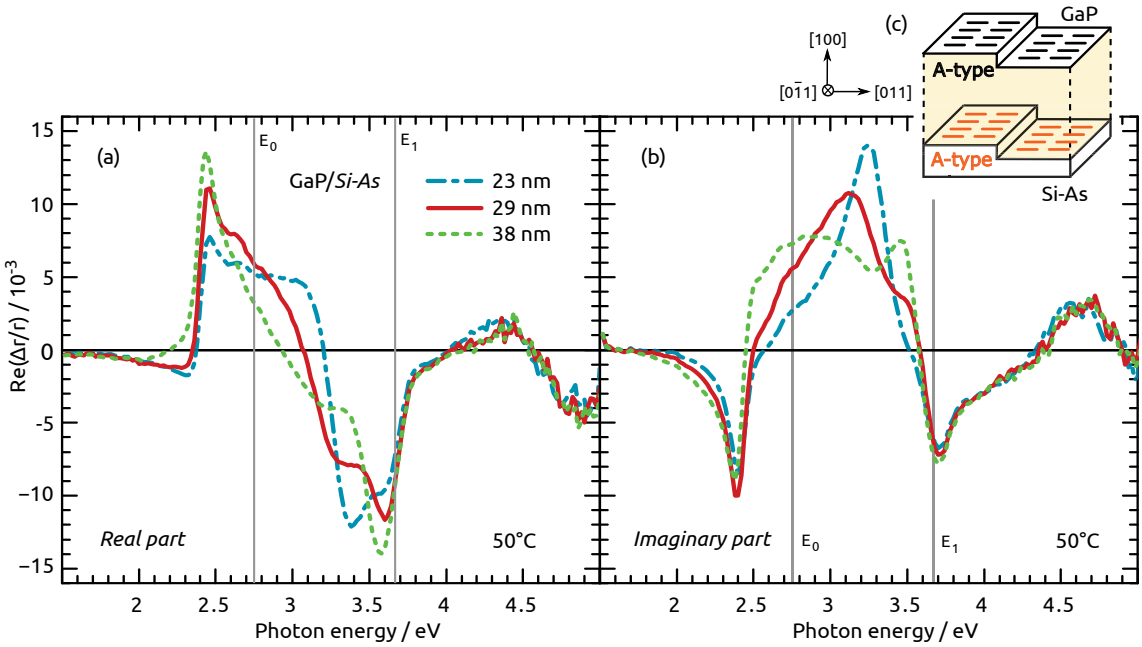

Fig. 3.28 – (a) Real part of the RA spectra of $(2 \times 2)/c(2 \times 4)$ reconstructed, pseudomorphic GaP epilayers grown on A-type Si:As. Fitted epilayer thicknesses are given in the legend. Vertical gray lines indicate the critical points energies of GaP [310]. (b) Imaginary part of the RAS signals obtained by a self-consistent Kramers-Kronig transformation of the spectra shown in (a). (c) As dimer orientation of *Si-As* prior to heteroepitaxy and of the P dimers at the final GaP/*Si-As* surface.

3.6.3 The GaP/Si(100):As heterointerface

Analogously to section 3.3.5, the IDA of the GaP/*Si-As* heterointerface can be calculated from eq. (2.23) on page 48 using the RA spectra from Fig. 3.28 obtained during interrupted growth on one single *Si-As* substrate surface. Fig. 3.29 shows the arithmetic mean of the GaP/Si:As IDA (orange line) calculated from three pairs of the differently thick GaP epilayers in comparison to the arithmetic mean of the GaP/*Si-A* IDA from Fig. 3.16 on page 73 (dash-dotted, green line), which was flipped in sign. Both IDAs increase between 2.3 eV and about 3.3 eV with a slightly different lineshape, as depicted in the difference spectrum (black, dashed line),

$$\delta\mathrm{IDA} = \mathrm{IDA}_{GaP/Si\text{-}As} - \mathrm{IDA}_{GaP/Si\text{-}A} \quad . \tag{3.8}$$

At about 3.6 eV, δIDA resembles a peak-like structure. The rather broad difference below 3.3 eV could be caused by interface roughness or by the step structure. Note, however, that small deviations can also be artificial [254]. The difference around

3.6 eV, in contrast, is much more distinct. It possibly is related to Si–As bond states, As–Ga bonds or a fingerprint of different step reconstructions.

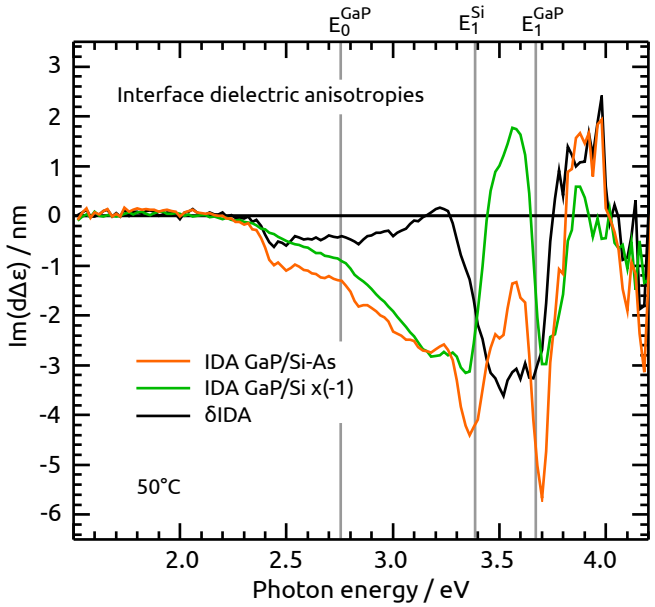

Fig. 3.29 – Interface dielectric anisotropies of GaP/*Si-A* (dash-dotted green line, flipped signal from Fig. 3.16 on page 73) and GaP/*Si-As* (orange line) heterointerfaces, as well as their difference spectrum according to eq.3.8 (black, dashed line). Vertical gray lines indicate the critical points energies of bulk Si [165] and GaP [310], respectively.

As the similar IDA suggests, pulsed nucleation with 5 PP on Si–As leads to RAS signal similar to 5 PP nucleation on *Si-A* but with a flipped sign. Both spectra are juxtaposed in Fig. 3.30 on the facing page directly before starting GaP growth. The difference in lineshape between 3.3 and 3.4 eV probably is caused by a contribution of the P dimers at the 5 PP/Si(100) surface that start to order (cf. Fig. 3.9). We cannot yet conclude on the atomic structure of the heterointerface, but assuming a terrace-related origin as for nucleation on *Si-A*, the amplitude of the signal would imply a similarly high domain ratio, which is promising regarding APD-free GaP growth already within the very first monolayers. More importantly, RAS here indicates that the pulsed nucleation succeeds also on *Si-As* after processing comparable to that used for As in-diffusion. Both As-doping of Si(100) and single-domain GaP growth can thus be performed in one single growth run.

To conclude on the atomic structure of the GaP/*Si-As* heterointerface is not straightforward since both Ga, As, and P are present during GaP nucleation. The As-modified Si(100) surface was covered with about 0.5 ML prior to nucleation. The observed sublattice orientation would agree with the sequence Ga–P on top of *Si-As*. In case of a 0.5 : 0.5 intermixing of Si and As in the interfacial layer, which is followed by Ga, also charge compensation would be fulfilled. We cannot yet

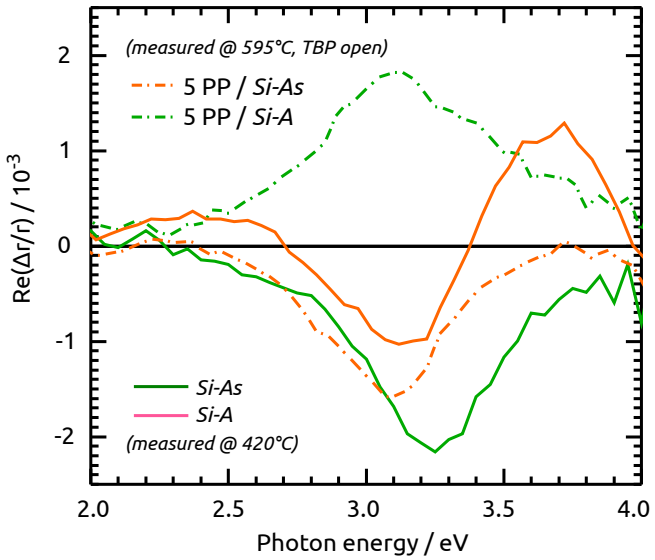

Fig. 3.30 – RA spectra extracted from colorplots during processing: (a) *Si-A* (green) and *Si-As* (orange) directly prior to GaP nucleation (straight lines, measured 420 °C) and after 5 PP nucleation directly prior GaP growth (dash-dotted lines, measured at 595 °C with TBP stabilization).

prove the existence of that structure. However, As-modified Si(100) surfaces remain highly exciting as they may combine single-domain GaP growth with compensated interfaces.

Time-resolved RAS measurements as well as a detailed XPS analysis of the GaP/*Si-As* interface will be performed in upcoming projects. DFT calculations of interface formation energies involving As are planned. Just as for the GaP/*Si-A* heterointerface, cross-sectional STM experiments would highly beneficial to resolve the atomic structure directly.

3.7 Comparison of GaP/Si(100) RA spectra

RA spectra of the different Si(100) and GaP/Si(100) surfaces, which were obtained in this work, are juxtaposed in Fig. 3.31 on the next page in the left and center column, respectively. The ball-and-stick model in the right column visualizes the corresponding interface structure in an idealized abrupt interface model.

GaP growth on *Si-A* and *Si-B* surfaces results in epilayers with mutually inverted sublattice orientation (cf. RAS in Fig. 3.31(a,b) resp. (e,f)). XPS reveals about 1 ML of Si–P located at the heterointerface, which agrees with DFT calculations for abrupt interfaces and the observed GaP sublattice orientation (cf. model in Fig. 3.31(i,j)). The formation of compensated GaP/Si(100) interfaces with a 0.5 : 0.5 intermixing of Ga resp. P and Si in the interfacial layer, in consequence, is kinetically hindered at nucleation temperature.

A-type Si(100) surfaces with 2° misorientation towards [011] can be prepared reliably in (Ga,P,As) processing MOVPE ambient after a standard bakeout procedure of the reactor. Processing conditions for almost nominal A-type Si(100) surfaces, in contrast, promote Ga diffusion on the surface (cf. RAS in Fig. 3.31(c)). GaP growth on such a surface leads to an inverted majority GaP sublattice orientation (cf. RAS in Fig. 3.31(g)), even though coverages were clearly below one monolayer. In an abrupt interface model, this agrees with a change from Si–P to Si–Ga bonds (cf. Fig. 3.31(k)). This change at abrupt interfaces is supported by DFT calculations for Ga-rich chemical potentials. Co-existence of Si–P and Si–Ga domains at A-type terraces may cause antiphase disorder, which results in a decreased amplitude of the GaP/Si(100) RAS signal.

Regarding 2° misoriented substrates, both monohydride-terminated Si(100) surfaces and As-modified Si(100) surfaces with preferentially A-type terraces can be prepared in MOVPE reactors containing background arsenic. GaP growth on such A-type *Si-As* surfaces leads to an inverted GaP sublattice compared to GaP growth on monohydride-terminated A-type Si(100) (cf. Fig. 3.31(d,k)). The GaP/*Si-As* surfaces are single-domain and already the nucleation-related RAS signal is flipped in sign. We could not yet resolve the binding situation at the heterointerface. However, an equal amount of Si and As in the former *Si-As* surface plane, followed by a Ga layer would explain the observed sublattice orientation. Such an interface could also be charge compensated.

Currently, ongoing investigations aim at finding further direct evidence for the bond structure at the heterointerface. Cross-sectional STM measurements will be performed in order to resolve the atomic structure of the GaP/Si(100) heterointerfaces. Theoretical predictions of the dependence of the VBO of GaP/Si(100) on the interface structure as well as the calculation of interface formation energies at nucleation temperature would help to complete the picture.

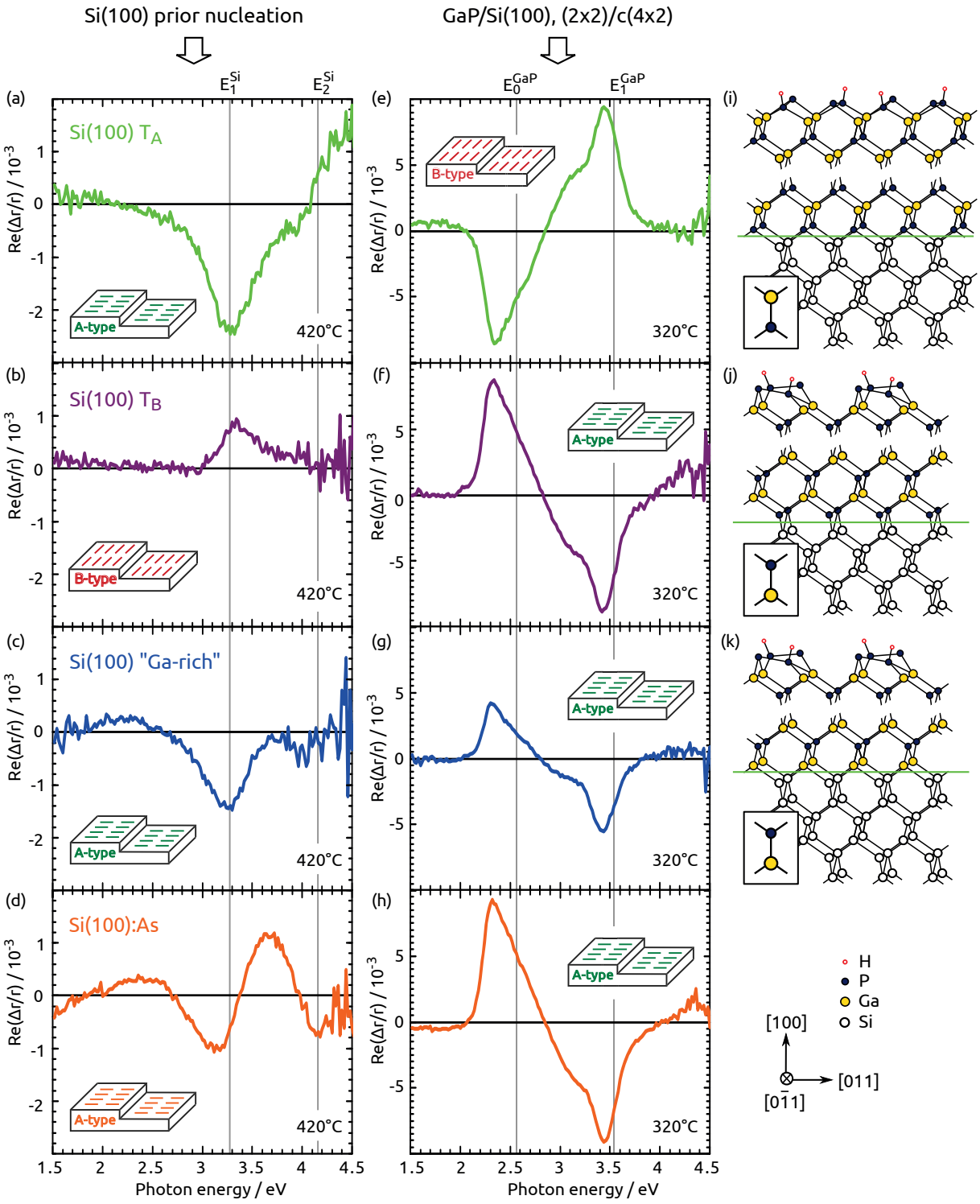

Fig. 3.31 – RAS of Si(100) surfaces prior GaP nucleation at 420 °C *(left column)*: (a) A-type Si(100), (b) (b) B-type Si(100), (c) A-type Si(100) with an increased amount of (Ga, P) residuals, (d) As-modified Si(100). *(center column, e-h)* $(2 \times 2)/c(4 \times 2)$ reconstructed GaP/Si(100) surface after growth of about 40 nm GaP on the surfaces in (a-d). Insets indicate the orientation of the majority domains of Si resp. P dimers at the surface. *(right column, i-k)* Ball-and-stick model sketching the orientation of the majority GaP sublattice and the corresponding interface structure in an idealized abrupt model. The interface is marked with a green line.

4

Dilute nitride GaPN/Si(100) heteroepitaxy

The goal of this chapter is to establish optical in situ signals of the GaPN/Si(100) surfaces relevant for lattice-matched GaPN heteroepitaxy on Si(100). RA spectra are important both for monitoring the GaPN growth process and for the final surface preparation itself, as the surface reconstruction of GaP(100) highly impacts the formation of the interface towards water [182]. At first, UDMHy decomposition will be briefly discussed. In situ RAS signals of thin GaPN/GaP/Si(100) layers will then be compared to GaP/Si(100). The preparation of both the $(2\times2)/c(4\times2)$ *and the* (2×4) *reconstructed surface will be discussed. Subsequently, bulk properties are addressed with ex situ characterization techniques. Parts of these results have been published in Ref.s[84, 255].*

4.1 UDMHy precursor decomposition

The N incorporation efficiency into GaP is very low with only about 2 % N at TBP:UDMHy ratios in the order of one [160].[36] To make optimal use of the UDMHy precursor, we studied its decomposition *in situ* with mass spectrometry (MS).[37] The pyrolysis of UDMHy was previously studied by Lee and Stringfellow [166] as well as by Bourret-Courchesne et al.[35]. Breaking of the intramolecular N–N bond is suggested as first reaction step in Ref.[35] and this is supported by a recent study [266] published during our work being in progress. Copyrolysis with TEGa is suggested to form an adduct at about 150 °C [35], but the behaviour at high temperatures is not fully understood.

During both GaN and GaPN growth, where the group-V precursors are offered prior to TEGa, the MS intensities of the 15 u signal (NH/CH_3) and the 16 u signal (NH_2/CH_4) decrease when TEGa is released in the reactor.[38] Though this could in principle be caused by copyrolysis of UDMHy and TEGa, decomposition of TEGa should rather increase the CH-related signals. The observed decrease of the 15 u and 16 u signal hints to incorporation of N from NH or NH_2 as active growth component. However, a NH signal might also be caused by decomposition of NH_2 in the mass spectrometer. Since NH_2 is predicted to occur upon breaking of the N–N precursor bond [35], NH_2 seems feasible as active growth component.

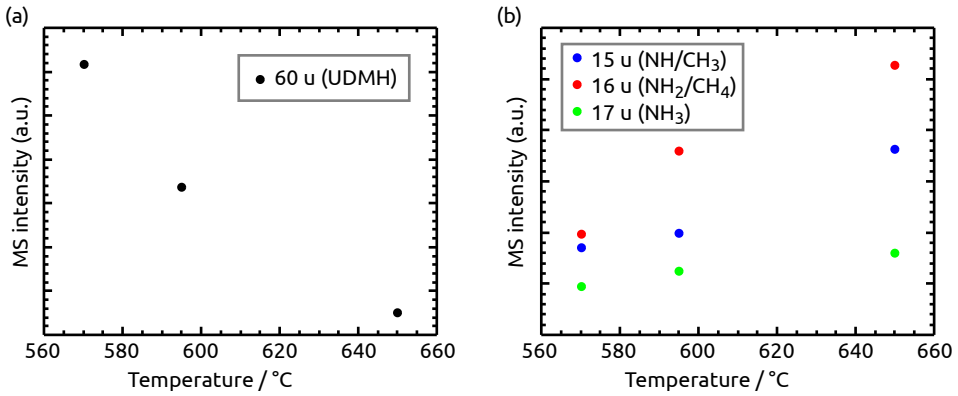

Fig. 4.1 – MS of (a) UDMHy-related and (b) NH_x-related masses during variation of the temperature.

[36] UDMHy is used due to its lower pyrolysis temperature compared to NH_3 [166, 188].

[37] These MS experiments were performed by Helena Stange during her M.Sc. thesis [245], which I co-supervised at HZB. The main thesis advisers were Prof. Dr. R. Manzke (HU Berlin) and Prof. Dr. T. Hannappel (HZB/TU Ilmenau).

[38] Note that only the ratio mass : charge can be measured. Temperatures here are ≤ 650 °C, where NH_3 is not yet decomposed [166].

Figure 4.1 on the facing page shows that the decomposition of UDMHy is largely increased at 650 °C compared to 570 °C (90% decrease in signal intensity), while the NH_x-related signals increase. Particularly, NH- and NH_2-related signals rise drastically compared to NH_3. In section 4.2.1, it will be shown that N is not diffusing out from the surfaces even at 700 °C. Growth at 650 °C ($P_{\text{reactor}} = 50\,\text{mbar}$) was thus chosen for most GaPN/Si(100) growth experiments.

4.2 GaPN/Si(100) surface preparation

Parts of this section are reprinted in part, with permission from J. Appl. Phys. 115, 113509 [255], ©2014 AIP Publishing LLC.

On the one hand, the influence of N on the atomic order of the GaP/Si(100) surface is interesting regarding *in situ* controlled growth of dilute nitride GaP layers. On the other hand, the surface reconstruction of GaP(100) highly impacts the initial formation of the semiconductor:water interface [182]. In order to establish the MOVPE growth of dilute nitride GaPN on Si(100) at HZB, the first experiments were based on the detailed studies by Kunert et al.[160], who in contrast to Miyoshi et al.[188] also used the precursors TEGa, TBP, and UDMHy for Ga, P, and N, respectively. *In situ* RAS and *in situ* reflectance measurements were used to obtain growth conditions leading to similar spectra compared to GaP/*Si-A*, i.e. without signatures of 3d structures or tilting of the spectra. After studying GaPN growth on GaP(100) and Si(100) substrates initially in parallel, we decided to focus on the GaP/*Si-A* substrates discussed in section 3.3.1, since the experiments showed that N incorporation is decreased by the increasing strain caused by growing non-lattice matched on GaP(100).

In the following, the MOVPE-preparation of GaPN/GaP/Si(100) surfaces in comparison to that of established GaP(100), respectively GaP/Si(100), surfaces will be discussed. The preparation of the surfaces is described in section 2.10.2. GaP/Si(100) and GaPN/GaP/Si(100) samples with similar total III-V epilayer thicknesses will be compared to yield comparable interference modulations.

4.2.1 (2×4) reconstructed surface

Figure 4.2(a) compares RA spectra of GaP/Si(100) and GaPN/GaP/Si(100) samples after annealing at 700 °C for preparation of the (2×4) surface reconstruction. The minimum peak around 2.3 eV of the GaPN/GaP/ Si(100) sample, which stems from the dimerized surface reconstruction, is blue-shifted about 50 meV with respect to GaP/Si(100) and about 1 RAS unit less intense. While both spectra match well at the maximum around 3 eV and beyond 3.9 eV, the lineshape around the E_1 transition is different. The LEED patterns in Fig. 4.2(b,c) show the (2×4) diffraction

pattern expected for GaP(100), without signs of a mutually perpendicular structure. The spots and especially the streaks along [011], however, are slightly brighter for the GaP/Si(100) sample (Fig. 4.2(b)) than for the GaPN/GaP/Si(100) sample (Fig. 4.2(c)). A decreased amplitude of the minimum peak around 2.3 eV, Ga_1 could

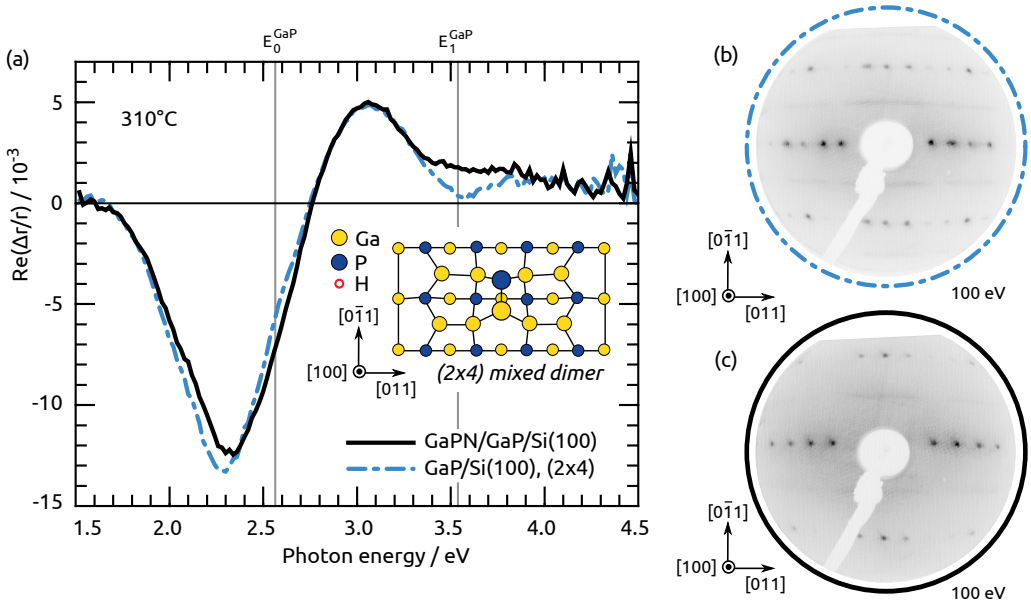

Fig. 4.2 – (a) RA spectra of (2 × 4) reconstructed GaP/Si(100) (blue line) and GaPN/GaP/Si(100) (black line) measured at 310 °C. Gray lines indicate the critical point energies of GaP[310]. The inset shows the (2 × 4) surface reconstruction. LEED pattern of (b) the Ga-rich GaP/Si(100) surface and (c) the GaPN/GaP/Si(100) surface from (a) after transfer to UHV.

be caused by both excess nitrogen (resp. precursor residuals) on the surface, a disordering effect by nitrogen incorporated into the surface or different anti-phase domain contents [79]. Anti-phase disorder as the origin of the reduced RAS peak intensity is unlikely, since almost single-domain Si(100) surfaces were prepared prior to GaP nucleation and small residual anti-phase domains will annihilate during GaP growth [139, 194]. Also, the LEED pattern are single-domain. Regarding excess atoms at the surface, carbon could not be detected (as signature of precursors residuals) on the GaPN/GaP/Si(100) surface with XPS so that excess nitrogen seems more likely. Furthermore, slight differences in the film thickness or modified interference modulation due to the GaPN/GaP interface [254] might influence the lineshape of the peak. To exclude contributions from the GaP/Si(100) or the GaPN/GaP heterointerface, thicker GaPN epilayers were grown to exploit higher absorption. Figure 4.3 on the next page shows real and imaginary part of the spectral weight w_i calculated for a 300 nm thick GaP/Si epilayer (cf. section 3.3.5). Assuming that GaPN absorbs at least as good as GaP, no photons from the buried heterointerfaces of 300 nm GaPN grown on silicon will contribute to the RAS signal at E_1. The RAS signal around

E_1 of such a 300 nm thick epilayer grown on Si(100) can therefore be compared to a GaP(100) reference surface.

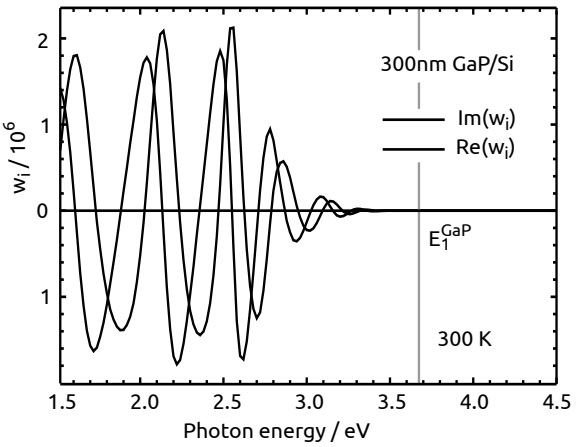

Fig. 4.3 – Real and imaginary part of the spectral weight w_i calculated for a 300 nm thick GaP/Si epilayer (cf. section 3.3.5. The gray line indicates the E_1 critical point energy of GaP[310].

Figure 4.4 on the following page juxtaposes the spectra from Fig. 4.2 with a GaP(100) reference and a 300 nm GaPN/GaP/Si(100) sample. Interference modulations are clearly visible up to about 3 eV in the RAS signal of the latter sample. The difference spectra,

$$\delta\mathrm{RAS} = \left(\frac{\Delta r}{r}\right)_{\mathrm{GaPN/GaP/Si(100)}} - \left(\frac{\Delta r}{r}\right)_{\mathrm{reference}} , \tag{4.1}$$

are shown in Fig. 4.4(b), where the index reference refers to GaP/Si(100) and GaP(100) in case of thin GaPN/GaP/Si(100) and thick GaPN/GaP/Si(100), respectively.

A peak-like structure is clearly visible for both δRA spectra in Fig. 4.4(b). As that peak occurs centered at the E_1 bulk transition of GaP, it may possibly be caused by N incorporation. Zorn et al.[312] demonstrated that the composition of GaAsP can be obtained by RAS due to the transition of the different surface reconstructions of GaAs and GaP. This was suggested also for GaNAs [211]. In Fig. 4.4 on the following page, however, the fingerprints of the (2×4) reconstructed surface seem mainly to be preserved but superimposed with an additional contribution. Possibly this is related to the linear electro-optic effect [1, 2, 264] (the samples shown in Fig. 4.4 were not intentionally doped). In He-I UPS measurements, (2×4)-reconstructed GaPN/Si(100) surfaces show an increased density of states compared to GaP/Si(100)-(2×4) between $E_B = 1.5 - 2.5$ eV [181]. Whether these are surface or bulk related states, however, remained unclear [181].

The annealing step at 700 °C during Ga-rich preparation might in principle also lead to N depletion in the GaPN film. To check the nitrogen content, XRD measurements were performed on the samples from Fig. 4.2. Figure 4.5 on page 103

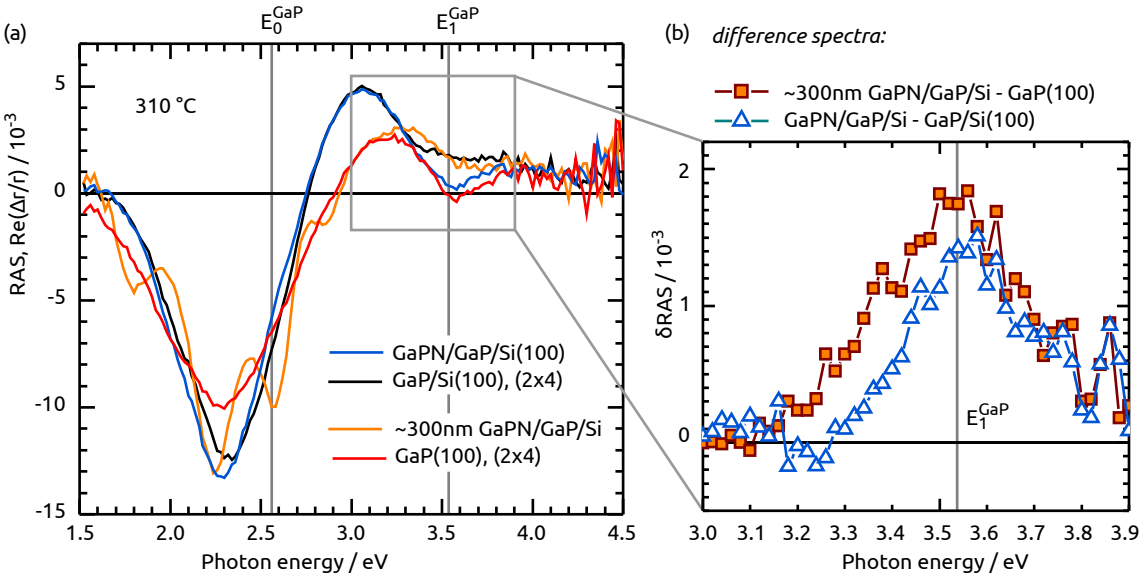

Fig. 4.4 – (a) RA spectra of Ga-rich GaP(100) (red dashed line) and about 300 nm thick GaPN/GaP/Si(100) (orange line) in comparison to the spectra of the thinner GaP(N)/Si(100) samples from Fig. 4.2 on page 100 (thin black resp. dash-dotted blue line). (b) Difference of the spectra shown in (a) around E_1: δRAS (eq. (4.1)) of the thicker GaPN/GaP/Si sample and the GaP(100) reference (orange squares) as well as δRAS of the thinner samples from Fig. 4.2 (blue triangles). Gray lines indicate the critical point energies of GaP [310].

shows the $\omega/2\theta$ scan and according fits relative to the Si(400) peak position of the substrate. From RSMs, we know that the films are not relaxed. Fitting the thickness fringes accordingly, yields a GaP film thickness of about 39 nm as expected for the growth parameters used here. The diffractogram of the GaPN/GaP/Si(100) sample can be fitted with good agreement yielding about 17 nm GaPN with 2.2 % of nitrogen and a GaP buffer thickness of about 16 nm. Nitrogen thus seems not to desorb remarkably from the bulk of the GaPN film, which is in line with Ref.[160] where sticking limited N incorporation is found for GaPN.

Since XRD probes mainly the bulk, XPS was applied as a complementary method mainly sensitive to the surface nitrogen concentration. Monochromated Ag L_α X-rays ($h\nu = 2984.3$ eV) were used, because, in contrast to Al K_α, the Ga LMM Auger lines are not superimposed to the N 1s photoemission line. The intensity of this source is, however, almost two orders of magnitude lower than the typically employed monochromated Al K_α source. Together with the nitrogen content of only $x \approx 0.02$ and the low cross-section of N 1s, this results in a relatively noisy signal when compared to Al K_α. Therefore, a sample with higher N content was prepared and characterized with XPS at first after $(2\times2)/c(4\times2)$ preparation and a second time after preparation of the (2×4) reconstructed surface. Nitrogen is clearly present at the surfaces and the N 1s emission (inset of Fig. 4.6) does not de-

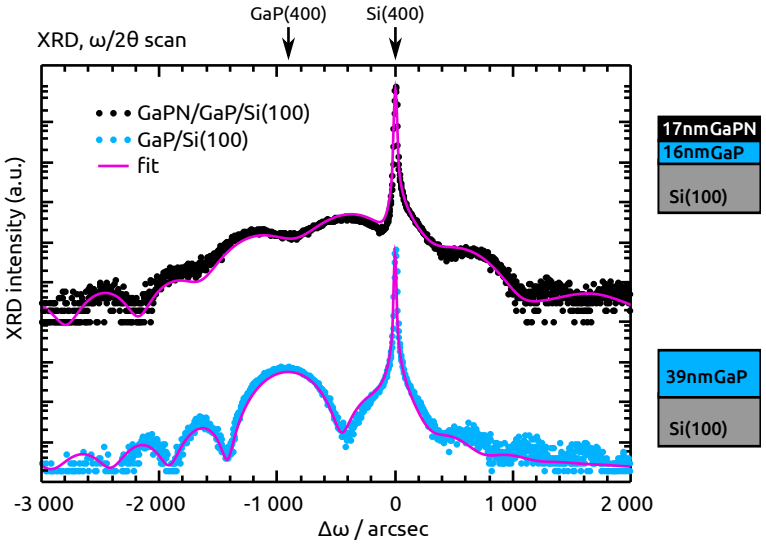

Fig. 4.5 – $\omega/2\theta$ scan of GaP/Si(100) and GaPN/GaP/Si(100) relative to ω of Si(400). The fit yields the thicknesses indicated in the insets and a N content of 2.2 % in the GaPN epilayer. Arrows indicate the peak positions for Si(400) and pseudomorphic, not-relaxed GaP(400) [240].

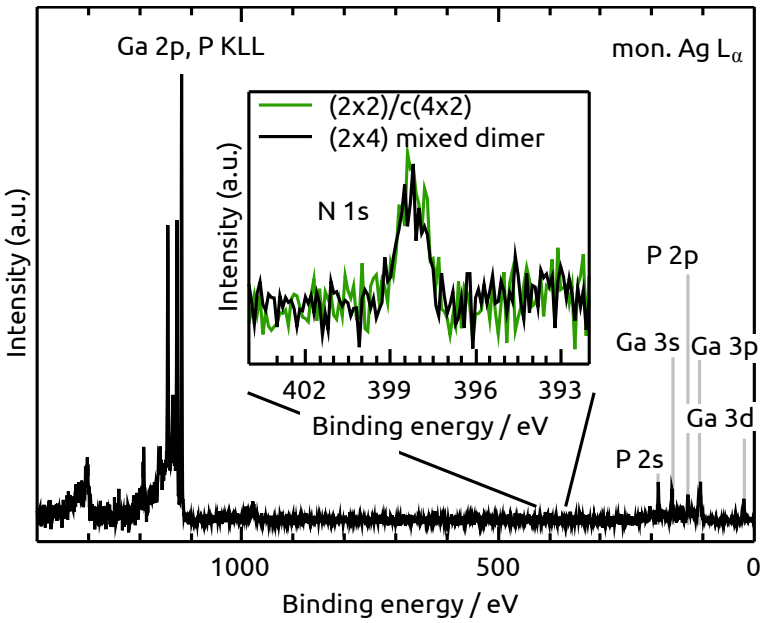

Fig. 4.6 – XPS survey spectrum of GaPN/GaP/Si(100) employing a monochromated Ag L_α source. The insets shows a detail spectrum of the N 1s emission of a $(2\times2)/c(4\times2)$ reconstructed sample prepared without UDMHy stabilization after growth, as well as the same sample after preparation of the (2×4) reconstructed surface.

crease even during annealing at 700 °C, further emphasizing that N is not desorbing significantly during the annealing steps for the according surface preparation.

4.2.2 $(2 \times 2)/c(4 \times 2)$ reconstructed surface

Figure 4.7(a) juxtaposes the RA spectra of GaPN/GaP/Si(100) (black line) and of GaP/Si(100) (red line), which were measured at 310 °C after $(2 \times 2)/c(4 \times 2)$ surface preparation (including group–V stabilization after growth and annealing without precursor supply at 420 °C and 470 °C, respectively). These are the identical samples, which were annealed at 700 °C (see Fig. 4.2) after being transferred back to the MOVPE via the UHV shuttle). After annealing at 420 °C without precursor supply, the intensity of the maximum around the E_1 transition was decreased for GaPN/GaP/Si(100) compared to GaP/Si(100) (not shown here). Further annealing at 470 °C lead to an increasing signal, but still a factor of 1.7 less amplitude than the spectrum of the GaP/Si(100) surface (cf. gray line in Fig. 4.7(a)), i.e. significantly less than in the according Ga-rich case. The peak position is shifted about 70 meV towards blue.

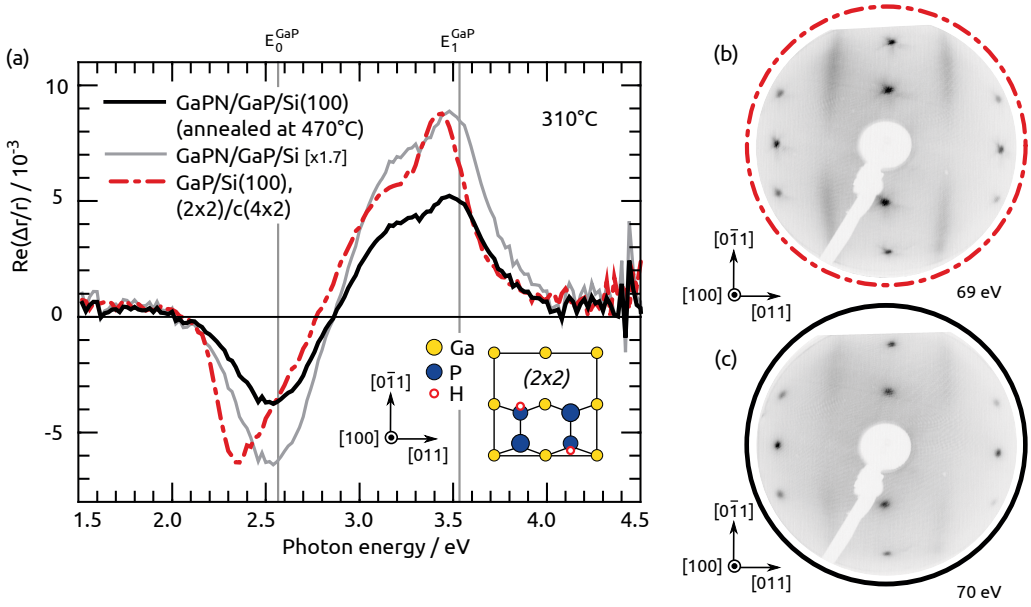

Fig. 4.7 – (a) RA spectra of GaP/Si(100) (red line), GaPN/GaP/Si(100) after annealing at 470 °C without precursor supply (black line) and the latter scaled by 1.7 (gray line), all measured at 310 °C. Dashed gray lines indicate the critical point energies of GaP[310]. The inset sketches the p(2×2) surface reconstruction of P-rich GaP(100). LEED pattern of (b) the P-rich GaP/Si(100) surface and (c) the GaPN/GaP/Si(100) surface from (a) after transfer to UHV.

The discussion ties in with that of the (2×4) reconstructed surfaces: antiphase disorder can be ruled out by the LEED patterns (cf. Fig. 4.7(b) and (c)), which show single-domain (2×1)-like diffraction patterns with a spot at half-order only along $[0\bar{1}1]$ direction. The spots and, in particular, the streaks along $[0\bar{1}1]$, which are related to the c(4×2)-like order of buckled dimers and their flipping at room temperature [149], are less pronounced at the GaPN/GaP/Si(100) surface compared to GaP/Si(100). Excess nitrogen or UDMHy residuals adsorbed on the surface during stabilization might influence the buckling of the P dimers. The minimum in the RA spectrum at about 2.3 eV, P_1, originates in anisotropic transitions between surface states related to these P–H bonds resp. the lone pair [116], as also discussed in section 3.1. The difference in the RA spectra in Fig. 4.7 on the facing page is significant at P_1. Compared to GaP/Si(100), the peak is more symmetric, shifted about 200 meV towards the E_0 transition and less intense for GaPN/GaP/Si(100). This behavior is similar to P-rich GaP(100), which we observed after water exposure [181, 182]. The P-H bonds probably were modified upon water adsorption. The P_1 peak shape of P-rich GaP(100) could only be restored, when offering hydrogen to the surface. This hints to excess N present at the surface. As for the (2×4) surface, carbon could not be detected in XPS (as signature of UDMHy precursor residuals) on the GaPN/GaP/Si(100) surface so that nitrogen seems to be the origin of changes on the surface here. Since both spectra differ less after Ga-rich preparation, a pure interference effect caused by the GaPN/GaP heterointerface or the slightly different total film thickness is unlikely.

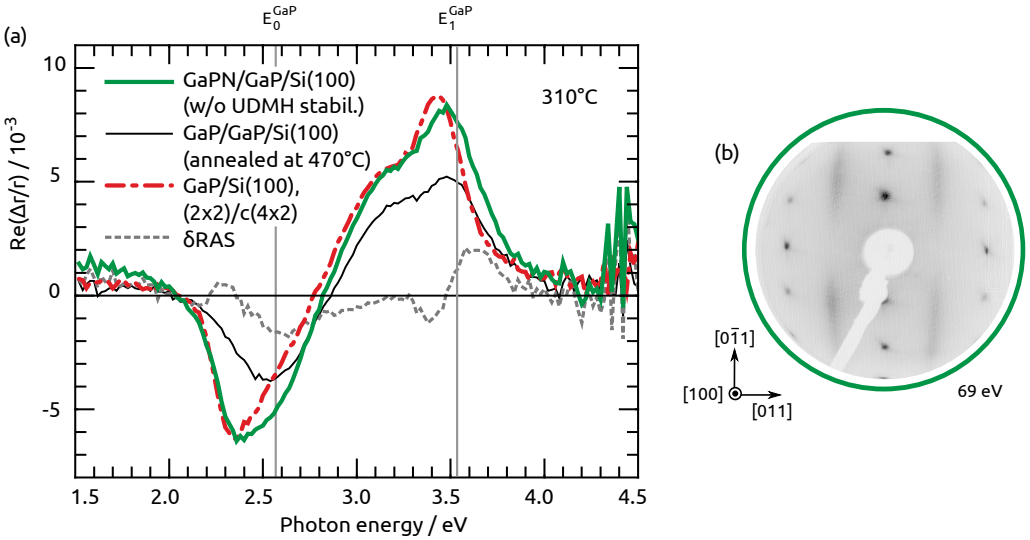

Fig. 4.8 – RA spectra of P-rich GaP/Si(100) and GaPN/GaP/Si(100) from Fig. 4.7 and GaPN/GaP/Si(100) annealed at 420 °C after cooling with TBP supply only (black line), all measured at 310 °C. The difference between the spectra at E_1 is highlighted in yellow. Dashed gray lines indicate the critical point energies of GaP[310]. The inset shows the LEED pattern of GaPN/GaP/Si(100) cooled with TBP supply only.

Annealing temperatures above 470 °C in order to prepare atomically well-defined group–V-rich GaPN(100) surfaces seem feasible, since annealing at 700 °C does not lead to N depletion in the GaPN epilayer but to rather well-defined Ga-rich surfaces. Regarding group–V-rich surface preparation, temperatures above 490 °C are, however, critical since P will desorb preferentially from the surface [78]. Therefore, UDMHy stabilization was omitted after growth while cooling with TBP supply only. Figure 4.8(a) compares the RA spectrum of GaPN/GaP/Si(100) (green line), which was prepared analogously as in Fig. 4.7, despite cooling with only TBP supply and subsequent annealing at 420 °C to desorb excess P, with the spectra shown in Fig. 4.7(a). The amplitude of the GaPN/GaP/Si(100) spectrum matches now almost that of GaP/Si(100) and the shift of the minimum peak P_1 is drastically decreased. The lineshape, however, is broader respectively more symmetric. The δRA spectrum (gray line) indicates an additional contribution at about the E_0 transition. This could be either caused by interference or a N-modified bulk transition close to E_0 as well as on the influence of nitrogen on the anisotropic surface state transition of P-rich GaP(100). The growth of samples with different GaPN epilayer thicknesses and comparison to growth on GaP(100) could clarify this point in future studies. The shift of the maximum close to E_1 is hardly reduced by the changed surface preparation, which supports the assumption of a bulk-like contribution to the spectrum caused by nitrogen incorporation. The incorporated nitrogen could modify the E_1 bulk transition and thereby influence the surface modification of this transition to which the maximum of the P-rich GaP(100) RAS signal is ascribed. The δRA spectrum (cf. eq. (4.1)) around E_1 stems partly from the shift of the peak position. A peak-like structure at about E_1, similar to that observed for the Ga-rich surface in Fig. 4.4, is superimposed. Accordingly, this feature seems not to be related purely to a specific surface reconstruction. The LEED pattern (inset Fig. 4.8) clearly shows the (2×1)-like reconstruction with both spots and streaks as bright as for P-rich GaP/Si(100) (inset Fig. 4.7(b)), which indicate a well-ordered surface terminated with buckled dimers.

4.2.3 GaPN/Si(100) growth with and without GaP buffer layer

In a final device design, the pseudomorphic GaP buffer layer could serve as electron barrier due the conduction band offset referred to GaPN. It might also be one part of the tunnel-junction interconnecting the GaPN-based top absorber and the Si bottom absorber. From recent theoretical considerations [217], n-GaP/p-Si and p-Si/n-Si tunnel-junctions are predicted to perform much better than p-GaP/n-Si and p-GaP/n-GaP tunnel-junctions. Locating the tunnel-junction in the GaPN-based layers could also be an option. The rather broad n-GaPN/p-GaP tunnel-junction in the GaNPAs/Si cell of Geisz et al., however, was identified to be one of the limiting factors regarding solar conversion efficiency [103].

However, GaP buffer growth can also be omitted: Growing GaPN directly after 5 PP of pulsed GaP nucleation on *Si-A* was not successful. RAS and *in situ* reflectance signals immediately broke down upon offering UDMHy, which probably is related with N reaching the Si substrate. After 10 PP, however, where an ordered GaP surface already establishes (see section 3.3.2) and GaP thickness is about two lattice constants, GaPN growth results in epilayers comparable to GaPN grown on GaP buffers with $10 - 40$ nm buffer thickness regarding RAS, XRD, PL and AFM measurements.

4.2.4 RAS during GaPN growth

Figure 4.9 on the next page shows color-coded RA spectra (a) and DC detector voltages (b), which were measured continuously during $GaP_{0.98}N_{0.02}$ growth on *Si-A* (650 °C, 50mbar H_2) after 10 PP GaP nucleation.[39] Transients at photon energies indicated by the dashed vertical lines are shown in (c) and (d) on the right side. The RA spectra correspond to a growth surface, which is group-V rich exhibiting the dimerized $(2 \times 2)/c(4 \times 2)$ reconstruction. The presence of dimers might benefit site-selective N incorporation [304]. The required process parameters, however, do not allow different reconstructions to test that effect here. During the 36 min long GaPN growth, oscillations in the transient measurements are caused by interference due to reflection of light at the buried heterointerface. The modulation intensities are dampened by absorption. At 3.32 eV, for example, interference has vanished already before one oscillation period was completed. The DC signal transient at 2.62 eV shows no significant roughening of the surface, as the mean intensity remains almost constant. In the RA transients, however, a slight downward tilting of the spectra towards higher photon energies is visible. As the intensity recovers upon turning of UDHMy after growth (while TBP remains opened for stabilization), this probably is caused by excess N on the growth surface.

Together with Dr. M. Pristovsek, we measured the dielectric constants of a homoepitaxial GaP buffer (no intentional doping) with spectroscopic ellipsometry (SE) at different temperatures *in situ* in a PH_3-based Aix-200 MOVPE reactor at TU Berlin (see [231] for details regarding the setup). The dielectric functions and constants are displayed in Fig. 4.10 on page 109. Unfortunately, GaPN growth was not possible during that growth run. Constructive interference in the transient DC detector signal of the GaPN/Si(100) sample occurs for normal incidence, when

$$2d\,\mathrm{Re}\Big(n(\lambda)\Big) = m\,\lambda \tag{4.2}$$

[39] The DC signal contains the reflectance of the sample, which is folded to the apparatus function, see section 2.9.2. A slight modulation with a period of 10 spectra/datapoints is visible both in the RAS and DC signals. This is an artifact caused by the measurement settings.

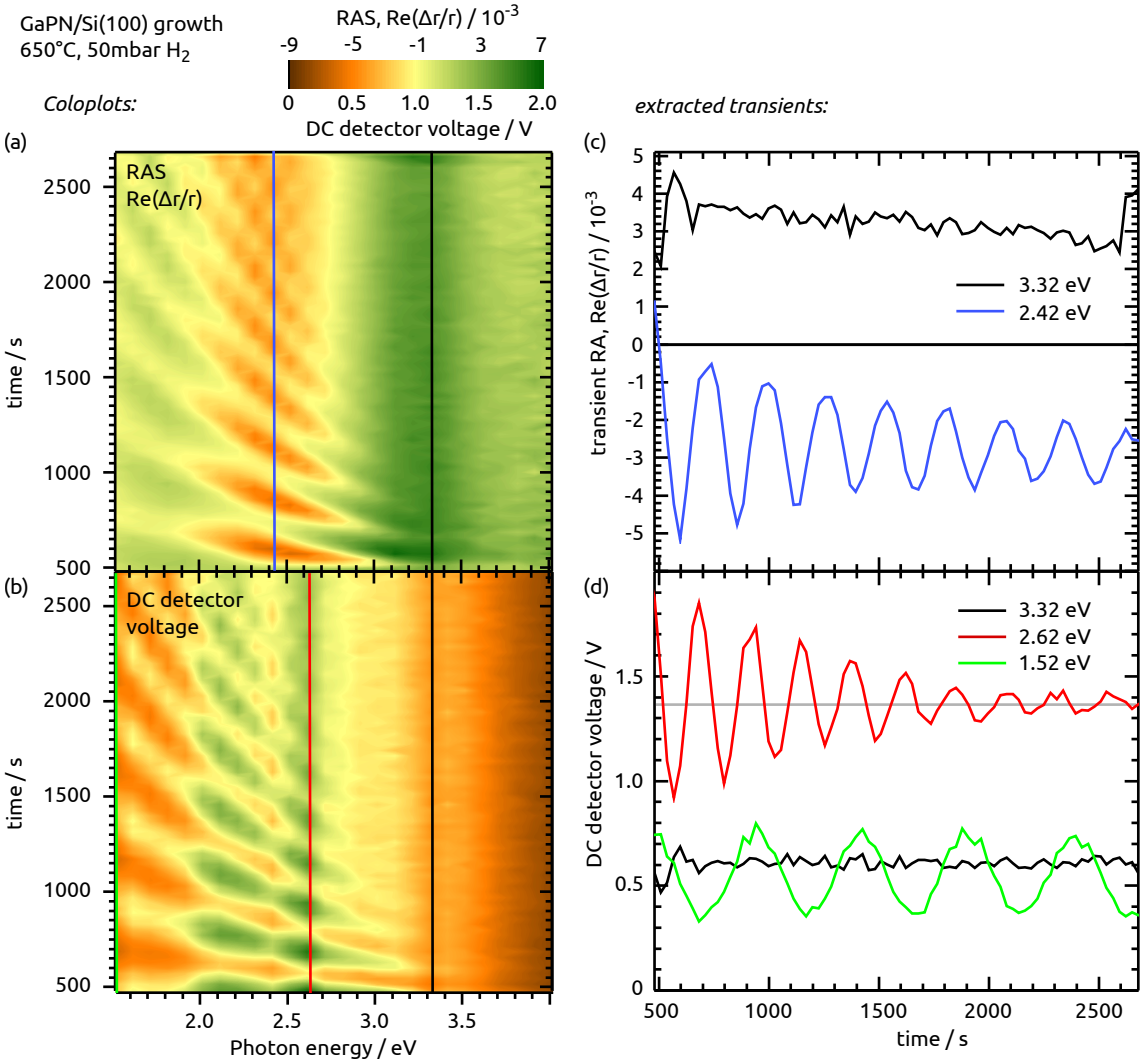

Fig. 4.9 – RAS during 36 min long growth of $GaP_{0.98}N_{0.02}$ on *Si-A* at 650 °C after 10 PP nucleation. (a) Continuously measured, color-coded RA spectra. (b) Continuously measured, color-coded DC detector voltage spectra ("reflectance", see section 2.9.2). (c,d) Transients extracted from (a,b) at photon energies indicated by the dashed lines. The colorplot was measured with $\Delta E = 100$ meV to increase temporal resolution, the transient at 3.32 eV is close to $E_1^{GaP}(650\,°C) = 3.35$ eV [310].

is fulfilled for $m \in \mathbb{N}$. The growth rate can be determined by XRD measurements to 2.5 Å / s, which is also in line with the GaP/Si growth rate (eq. (3.6) on page 71), where the TEGa flow was twice as high as here. Evaluating the transient at 2.62 eV from Fig. 4.9(d), for example, with a GaPN epilayer thickness of 540 nm, we get $\mathrm{Re}(n) \approx 4.0 \pm 0.3$, which is in the range of what would be expected for GaP at 650 °C. The precision of estimating $\mathrm{Re}(n)$ for GaPN via eq. (4.2) on the preceding page, however, is not sufficient to reliably resolve the influence of N here. Transient measurements at one single photon energy would result in better precision but only one wavelength per sample. Therefore, we plan to install a multichan-

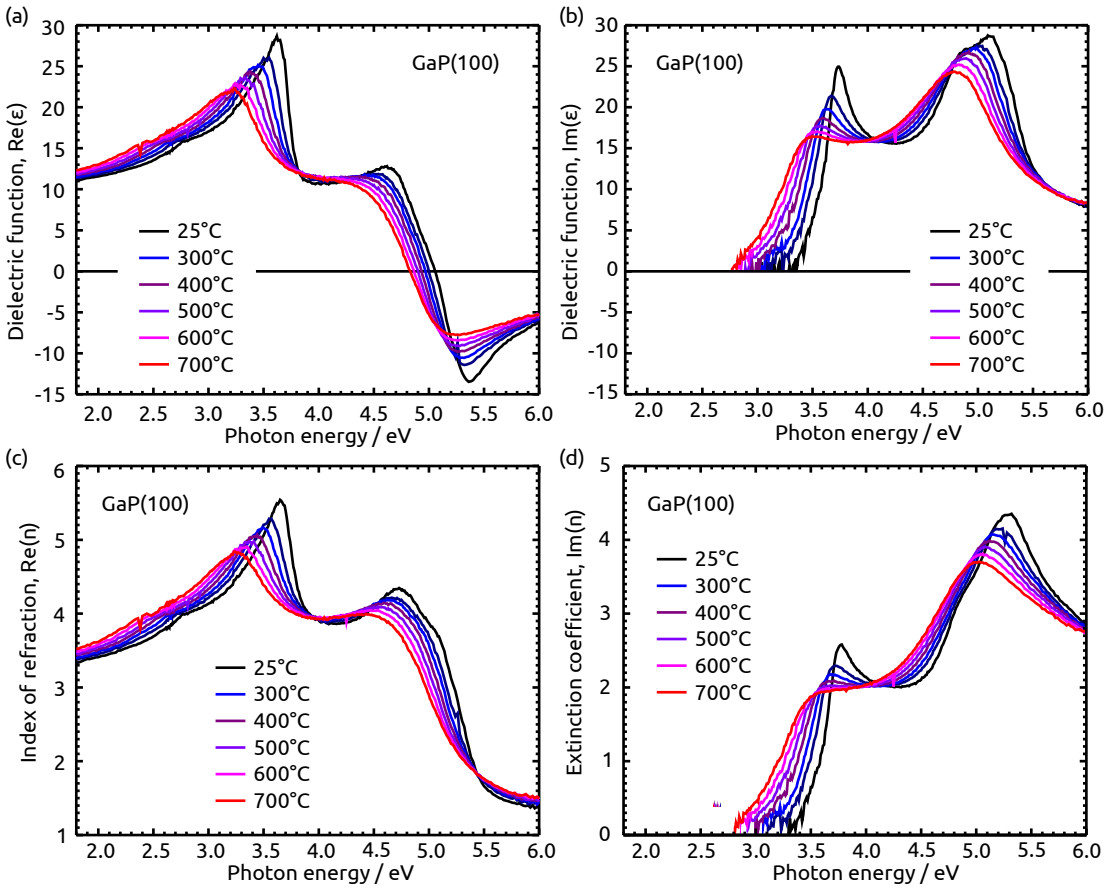

Fig. 4.10 – Dielectric functions of GaP(100) at different temperatures: (a) Real part of the dielectric function, Re(ε). (b) Imaginary part of the dielectric function, Im(ε). (c) Real part of the dielectric constant (index of refraction), Re(n). (d) Imaginary part of the dielectric constant (extinction coefficient), Im(n). Note that low-energetic data is omitted for Im(n) and Im(ε) due to measurement artifacts and increasing noise.

nel RA spectrometer at TU Ilmenau. Also, the complex dielectric functions of our GaPN epilayers will be measured *ex situ* by SE in a future collaboration with Dr. S. Shokhovets at TU Ilmenau. First preliminary results indicate an absorption edge in $GaP_{0.98}N_{0.02}$ slightly below 2 eV.

4.3 *Ex situ* high-resolution X-ray diffraction

The N content x of $GaP_{1-x}N_x$ can be obtained via its lattice constant applying Vegard's law [277]. We measured the lattice constant by fitting $\omega/2\theta$ scans measured

with high-resolution X-ray diffraction (HR-XRD).[40] For a better reliability of the fit, reciprocal space map (RSM) measurements were performed to estimate the residual strain in the epilayers. Varying the azimuth angle φ showed that tilting of the GaPN lattice planes with respect to the Si substrate, as observed for GaP growth on Si(100) with higher misorientation [262], is negligible here [245]. Single $\omega/2\theta$ scans are therefore used for fitting the GaPN lattice constant. Considering uncertainties in the input parameters, the error in determining the N concentration is estimated to $\Delta x \leq \pm 0.2\%$ [245].

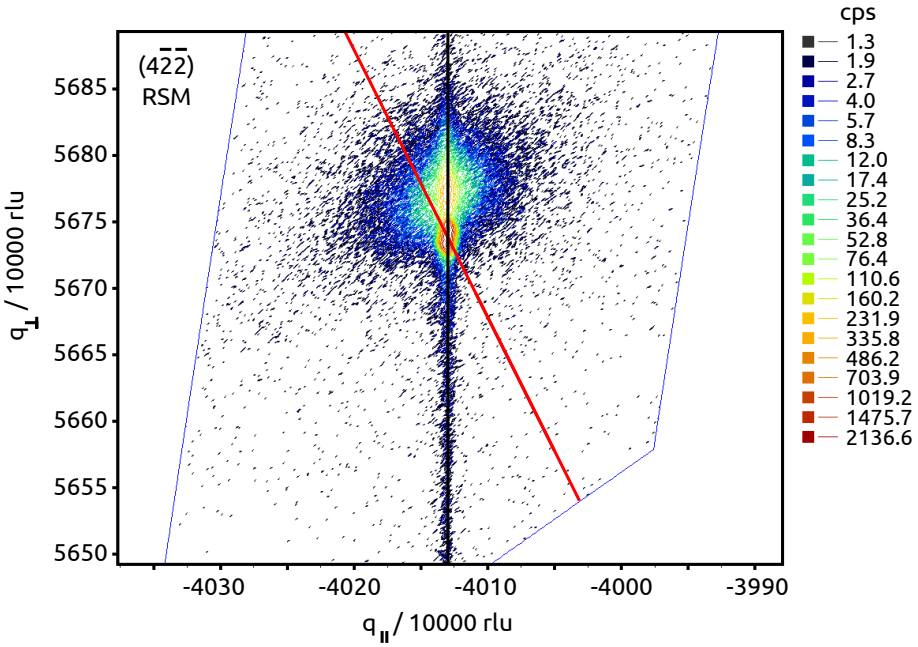

Fig. 4.11 – RSM around the (4$\bar{2}\bar{2}$) reflex of GaPN/*Si-A*. The black line indicates [400] and the red line connects the Si substrate peak with the origin of the reciprocal space. The reciprocal coordinates q are denoted in reciprocal lattice units (rlu).

Figure 4.11 shows the RSM of about 550 nm GaPN / 16 nm GaP / *Si-A* around the Si (4$\bar{2}\bar{2}$) reflex. Pseudomorphic layers (fulfilling $a_\parallel = a_{\mathrm{Si}}$) lead to diffraction spots along the black line, which corresponds to the [400] direction. Diffraction spots of completely relaxed layers, in contrast, are expected to occur on the red line which connects the (4$\bar{2}\bar{2}$) reflex of the Si(100) substrate with the origin of the reciprocal space. The position of the GaPN peak above Si in $q_\perp$ indicates that $a_{\mathrm{GaPN}} < a_{\mathrm{Si}}$ and negligible relaxation.[41] From the $\omega/2\theta$ scan, the N content was estimated to 2.3 %.

[40] The HR-XRD measurements were performed together with Helena Stange during her M.Sc. thesis [245], which I co-supervised at HZB. The main thesis advisers were Prof. Dr. R. Manzke (HU Berlin) and Prof. Dr. T. Hannappel (HZB/TU Ilmenau).

[41] Due to the broken symmetry along $k_\perp$, diffraction peaks of thin layers are elongated along the growth direction. For the RSM measurements, the analyzer crystal was removed for higher

Figure 4.12 shows $\omega/2\theta$ scans of differently thick GaPN layers, which were grown on (16±2) nm GaP / *Si-A*, and the according fits of the Laue oscillations yielding the GaPN epilayer thickness, d_{GaPN} and N content, x.

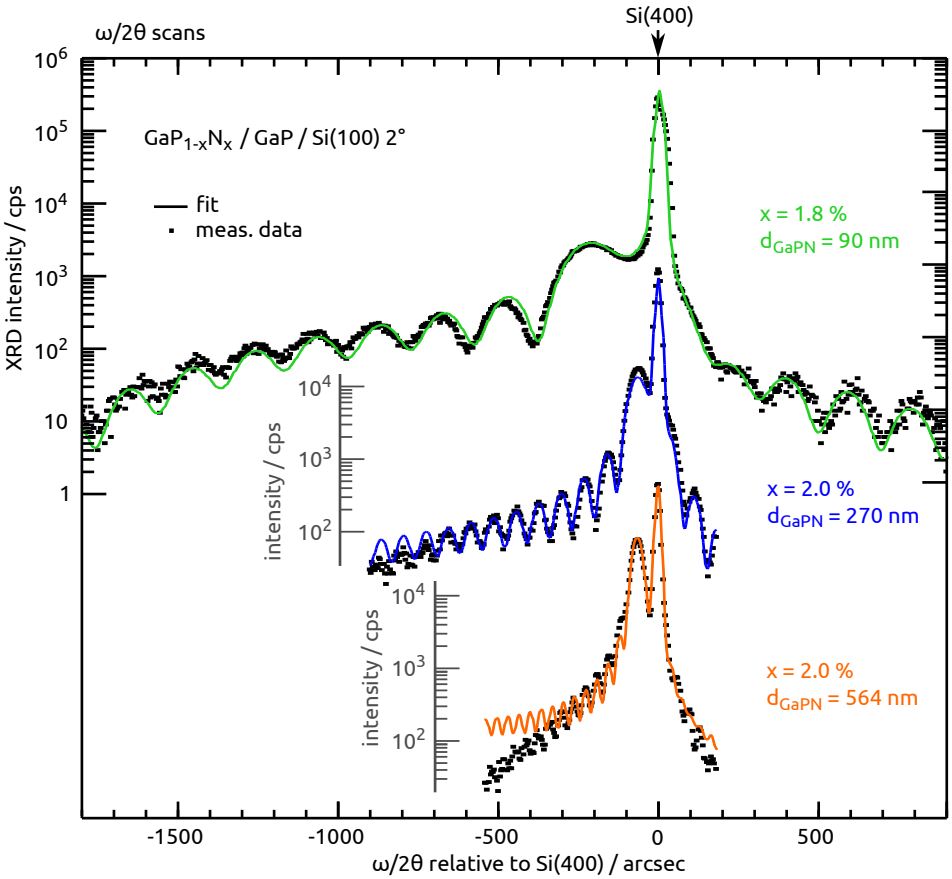

Fig. 4.12 – $\omega/2\theta$ scans of the (400) reflex of three differently thick $GaP_{1-x}N_x$ epilayers grown on GaP/*Si-A* (rectangles). Two diffractograms are shown with an offset as indicated by gray ordinates. The fits (lines) yield the given numbers for x and d_{GaPN}.

The fit of the GaPN/GaP/Si structures also indicates that N is not diffusing significantly in the pseudomorphic GaP buffer layer. To test this, a multilayer structure consisting of four repetitions of (40 GaP / 50 nm GaPN) on 40 nm GaP on *Si-A* was grown (40 resp. 50 nm estimated referring to the growth rate). The (400) $\omega/2\theta$ scan and the RSM around $(4\bar{2}\bar{2})$ are depicted in Fig. 4.13 and Fig. 4.14, respectively. Pseudomorphic GaP and lattice-matched GaPN epilayers with $x = 2.1-2.2\,\%$ can clearly be distinguished in the fit and the anticipated layer thicknesses are reproduced.

intensities. This causes a slight symmetrically distortion of the reflexes tilted from [004] [224, 245].

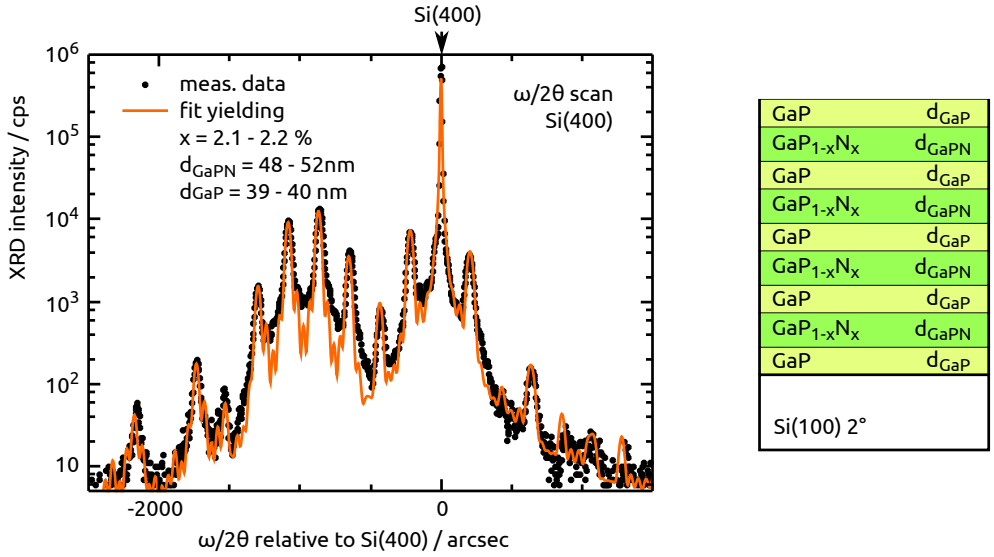

Fig. 4.13 – $\omega/2\theta$ scan of the (400) reflex of a GaP / 4x(GaPN / GaP) multilayer structure grown lattice-matched on *Si-A*.

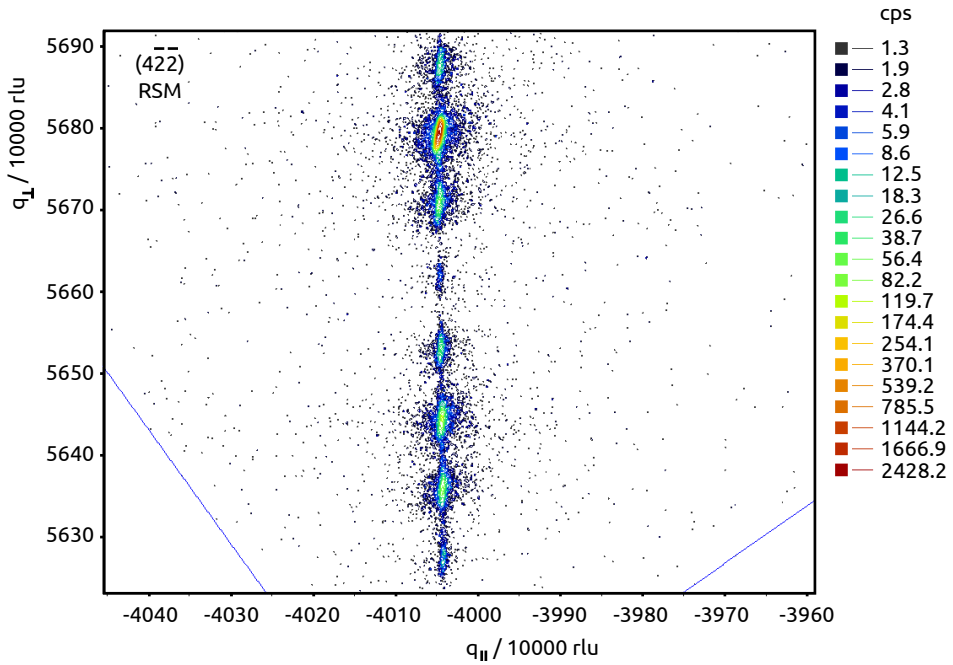

Fig. 4.14 – RSM around the $(4\bar{2}\bar{2})$ reflex of the identical sample shown in Fig. 4.13.

4.4 Cu contamination in the bulk and surface roughness

On some GaPN/Si samples, we were facing seriously enhanced roughness with "hillocks" reaching diameters in the order of 100 nm and 50 nm height even at nominally 100 nm layer thickness. In between the hillocks, the surfaces were much smoother with RMS in the order of 1 nm. First, we thought to optimize growth conditions, but the irreproducibility of the rough surfaces hindered determined and well-structured approaches. In a collaboration with Dr. G. Lilienkamp and Prof. Dr. W. Daum (TU Clausthal, Germany), such a GaPN/GaP/Si sample was measured with a scanning Auger nano-probe (nanoSAM). The hillocks were found to be related to Cu contamination, which could be traced back to the heterointerface by sputtering. Cu at the surfaces could also be verified by energy dispersive X-ray spectroscopy (EDX).[42] We are still determining the actual origin of this contamination. Secondary ion mass spectrometry (SIMS) measurements, for example, indicate Cu being present in unprocessed substrate wafers. The amount of about $10^{17}\,\mathrm{cm}^{-3}$ in the uppermost 100 nm and less than $5 \cdot 10^{15}$ in the bulk, as measured by SIMS, is high enough to seriously deteriorate Si-based devices but cannot explain the high amount of Cu which was observed. We believe that some sort of carry-over contamination on our carriers is more realistic. GaPN growth in new susceptors and carriers, which are thought to be free of that contamination, resulted in mirror-like surfaces with highly reduced hillock density. Decontamination of the entire MOVPE system is currently work in progress.

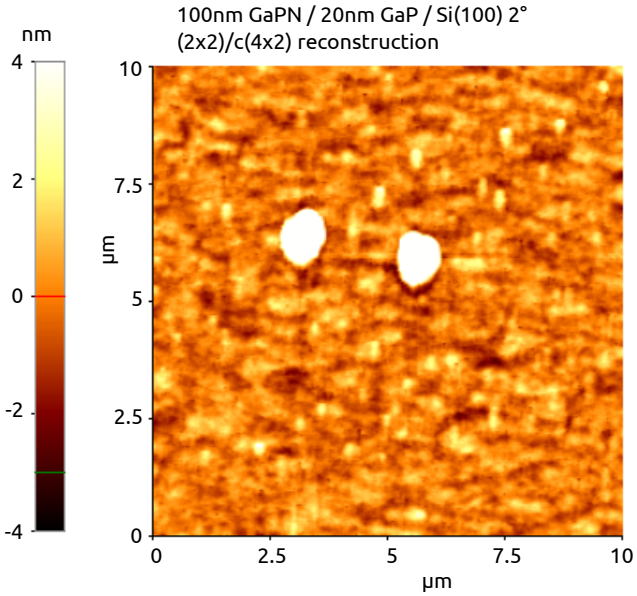

Fig. 4.15 – 10 μm × 10 μm AFM image (tapping mode, measured in air) of 100 nm thick GaPN grown on 20 nm GaP/*Si-A*. The height of the two hillocks is almost 50 nm.

[42] EDX was performed by M. Steidl at TU Ilmenau.

4.5 Photoluminescence

Figure 4.16 shows photoluminescence (PL) spectra of about 550 nm thick, Zn-doped $GaP_{0.98}N_{0.02}$ grown on GaP/*Si-A* measured at room temperature (orange) and 7 K (petrol).[43] As expected, the emission line is below 2 eV at room temperature. Preliminary SE measurements also indicate the existence of the expected absorption edge in $GaP_{1-x}N_x$ below 2 eV. The shape of the PL lines in Fig. 4.16 is asymmetric, as most obvious in the spectrum measured at 7 K. While recombination from energetic levels above the CBM or into states below the VBM, respectively, would result in a tail towards higher energies, we observe a tail towards lower energies. This hints to states below the CBM edge in agreement with previous studies: Zhang et al.[305] observed absorption bands in GaPN, which they assigned to N pairs and clusters. Indeed, the temporal behavior of PL spectra of GaPNAs/Si and GaPN/GaP was explained by exciton hopping via tunneling between such localized states [132, 195].

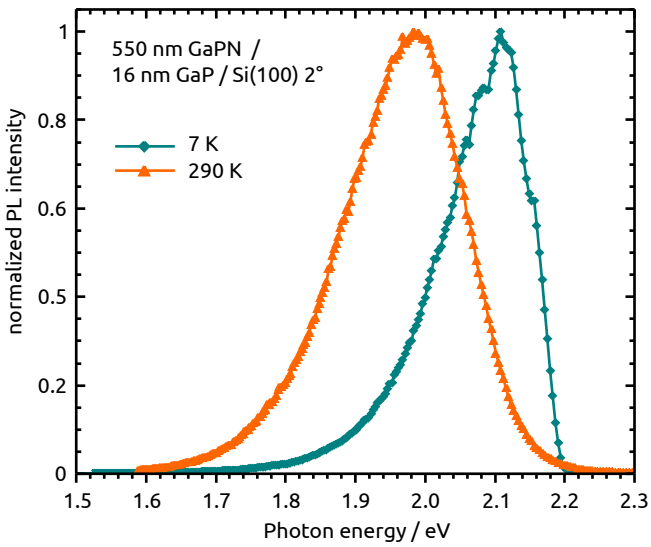

Fig. 4.16 – PL spectra of about 550 nm GaPN/GaP/*Si-A* measured at room temperature (orange line) and at 7 K (petrol line).

With TRPL, we observed a bi-exponential decay of the PL signal at room temperature [287]. The fast component showed lifetimes in the order of 10^{-10} s and the slower one in the order of 10^{-9} s. Measurements at 7 K indicate lifetimes in the

[43] Photoluminescence (PL) and time-resolved PL (TRPL) measurements were performed by Jonas Weinrich for his Bachelor thesis [287], which I co-supervised at HZB. The main thesis advisers were Prof. Dr. R. Manzke (HU Berlin) and Prof. Dr. T. Hannappel (HZB/TU Ilmenau). The measurements discussed here were assisted by Dr. K. Schwarzburg, who designed the TRPL setup at HZB.

order of 10^{-8} s, which is two orders of magnitude less than observed in Ref.[195]. Besides N clusters, also interstitial Ga defects related to the presence of hydrogen [57, 59, 60] may be involved here.[44] We can, however, neither rule out the Cu contamination discussed above. Recent MBE studies of GaPN growth on GaP(100) also indicate increased substitutional N incorporation and N pair formation at the step edges [56]. Note also that our samples were measured as grown. Recently, Gies et al.[104] showed that post-growth rapid thermal annealing (RTA) is beneficial regarding PL of GaPNAs quantum wells grown on Si(100) for laser applications. Thermal annealing is also expected to suppress defects related to Ga interstitials [58] and will be part of dedicated future experiments.

4.6 Sb as surfactant

High solar conversion efficiencies can indeed be achieved with N-containing III-V films, as recently demonstrated with MBE-grown GaInNAs subcells in triple junction cells, which reach efficiencies of 44 % under concentrated sunlight [111]. Antimony is suggested to act as surfactant reducing N-related defects during dilute nitride III-V films and was found to increase N incorporation during MBE growth [280]. In our experiments, however, the presence of TESb (which was available as Sb precursor) resulted in highly reduced N incorporation both when TESb was offered prior to GaPN growth and when TESb was offered during growth. This agrees with observations for MOVPE growth of GaAs [67] and GaInNAs [99]. Future work will focus on the effect of trimethylantimony (TMSb) on the GaPN structures discussed here, since TMSb promises better performance as shown recently for GaInNAs [146].

[44] Defects evolving during growth of strained GaPN epilayers on GaP(100) as in Ref.s[57, 59, 60], however, may be different compared to lattice-matched growth on Si.

5

Conclusion

Photochemical diodes based on GaPN/Si(100) tandem absorber structures are considered for high-efficient direct solar water splitting. However, preparation of the involved heterostructures and well-defined interfaces is challenging in industrially scalable MOVPE ambient due to the presence of process gas, precursor molecules and fragments, as well as residual III-V species from previous processes. *In situ* monitoring is inevitable for a precise understanding of the involved complex processes, where energetics and kinetics compete. In this work, essential stages of the heteroepitaxy were studied *in situ* with optical spectroscopy: (i) the preparation of Si(100) surfaces in H_2-based MOVPE ambient in presence of III-V residuals, (ii) subsequent formation of GaP/Si(100) heterointerfaces, and (iii) lattice-matched GaPN heteroepitaxy. The *in situ* spectra were benchmarked to complementary, electron-based surface science techniques, such as LEED and XPS, applying a dedicated MOVPE-to-UHV transfer system. Supported by DFT calculations, the separation of different contributions to the RAS signal led to detailed insights into the formation of the involved surface and interface structures: The heterointerface establishes during pulsed nucleation and its atomic structure depends on the (Ga, P) chemical potential during nucleation. Antiphase disorder can be suppressed by single-domain Si(100) surfaces, where the dimer orientation prior nucleation determines the GaP sublattice orientation. Single-domain GaP/Si(100) quasisubstrates with selectable sublattice orientation, which are suitable for further generic III-V integration, can reliably be prepared in MOVPE ambient.

The kinetically driven formation of Si(100) T_A surfaces succeeds in MOVPE reactors, which contain residual (Ga, P, As) species from previous growth runs, when a standard bakeout procedure is performed. Domain imbalances beyond $80:20$ were achieved. The energetically more favorable preferential T_B surface, in contrast, could only be prepared in H_2 ambient free of III-V residuals. An optical anisotropy contributing to the RAS signal is induced during subsequent pulsed GaP nucleation at low temperature, which is important to suppress twin defects and stacking faults. Calculations of the dielectric anisotropy of the buried heterointerface from thicker GaP/Si(100) samples indicate that this anisotropy remains during GaP growth and it is therefore attributed to the heterointerface. This signal scales with the domain imbalance of the Si(100) surface prior to nucleation, which points to an origin related to the terraces at the interface. Both intrinsic contributions by interface perturbed bulk transitions and extrinsic contributions related to the binding situation at the heterointerface come into consideration. Further pulsing and annealing at higher temperatures with phosphorus stabilization induces a superposition of GaP(100) surface-related features to the RAS signal. LEED evidences an atomically well-ordered, single-domain (2×1)-like reconstruction, which is well-known from H stabilized, buckled P dimers at GaP(100) surfaces.

Charge compensation at the heterointerface may be achieved with an equal number of Si–Ga and Si–P bonds. Such intermixed interfaces are predicted by DFT calculations to exhibit lower formation energies than abrupt interfaces. However,

XPS measurements after pulsed nucleation on 2° misoriented Si(100) reveal chemically shifted components in the Si 2p and P 2p PE lines, which can be attributed to the heterointerface and quantitatively correspond to about 1 monolayer. Even though a minority contribution from Si–Ga bonds cannot be excluded, the XPS results suggest rather abrupt interfaces consisting mainly of Si–P bonds. Such an abrupt Si–P interface can explain the sublattice orientation of the GaP epilayer, which is observed with RAS. According to DFT calculations, it also is energetically favored over an abrupt Si–Ga interface for wide ranges of (Ga, P) chemical potential.

Preparation of nominal Si(100) surfaces in presence of (Ga, P) residuals is more critical than for 2° misoriented surfaces. Formation of single-domain surfaces requires low H_2 pressures and quick cooling after homoepitaxial buffer growth. This promotes diffusion of background residuals on the Si(100) surface, as evidenced by XPS. The amount of sub-monolayer coverages of residual species at the Si(100) surface prior to pulsed nucleation highly impacts the structure of the heterointerface and subsequent GaP growth. Beyond a certain amount of Ga species present during nucleation, GaP growth proceeds with an inverted majority sublattice orientation. Also for these more "Ga-rich" conditions, RAS proves a preferential T_A Si(100) surface directly prior to nucleation. Already the nucleation related anisotropy, however, is inverted and reduced in amplitude. The inversion of the GaP sublattice depending on the amount of Ga would agree with a change from Si–P to Si–Ga bonds, which is predicted at abrupt interfaces by DFT for nucleation in Ga-rich conditions. Within that picture, local variations of the chemical potential might cause domains of Si–P and Si–Ga bonds resulting in antiphase disorder. Preparation routes for Si(100) surfaces with 2° misorientation, in contrast, effectively hinder background diffusion on the surface.

Single-domain GaP epilayers can be grown also on As-modified Si(100) surfaces with preferential T_A terraces. Compared to growth on monohydride-terminated Si(100) with T_A terraces, the GaP sublattice orientation is inverted. The interface dielectric anisotropy is flipped in sign and contains an additional contribution, possibly related to Si–As bonds. The successful GaP nucleation on As-modified Si(100) is very promising regarding growth on MOVPE-prepared Si pn-junctions. Moreover, intermixing of As and Si in the interfacial layer might lead to a compensated interface structure.

Future studies will include XPS after nucleation on Si(100) prepared in "Ga-rich" conditions and on As-modified Si(100). Cross-sectional STM studies are planned to directly visualize the atomic structure of the GaP/Si(100) heterointerfaces and to directly analyze their abruptness. Further theoretical calculations will focus the density of interface states. Calculations of corresponding RAS signals would be highly instructive towards a microscopic understanding of the interface dielectric anisotropy.

Regarding dilute nitride GaPN heteroepitaxy, *in situ* mass spectrometry proved that decomposition of the N precursor UDMHy is largely enhanced at 650 °C compared to 570 °C, resulting in a high proportion of NH_2, which is suggested being the active growth component. Lattice-matched $GaP_{0.98}N_{0.02}$ epilayers were successfully grown on Si(100) both involving a pseudomorphic GaP buffer layer and directly after pulsed GaP nucleation with ten pulse pairs. While a growth rate half as high as applied for GaP reduced the GaPN/Si(100) surface roughness, Cu-related defects were inevitable. Excluding these hillocks, RMS roughness values in the order of 1 nm were achieved. The presence of Sb resp. the precursor TESb was found to reduce the N incorporation efficiency. Zn-doped $GaP_{0.98}N_{0.02}$/Si(100) exhibits PL below 2 eV and a lineshape of the spectra which is related to N clusters. Lifetimes in the order of 10^{-8} s were found with TRPL at 7 K, which is two orders of magnitude below published data. Beneficial effects of post-growth annealing, which were reported in literature, will be investigated in future studies after complete Cu decontamination, as well as the surfactant behavior of Sb using TMSb.

$GaP_{0.98}N_{0.02}$/Si(100) surfaces exhibit analogous surface reconstructions as the GaP(100) reference. The (2×4) reconstructed surfaces can be prepared identically. Excess N at the surface preparation of an atomically well-ordered $(2 \times 2)/c(4 \times 2)$ reconstruction requires avoidance of excess N at the surface, which was achieved by repealing stabilization with UMDHy after growth. RA spectra of both surfaces exhibit an additional contribution at the E_1 interband transition of GaP, which is related to N incorporation. There is no significant N out-diffusion upon annealing GaPN epilayers at 700 °C, and GaP / GaPN multilayers could be clearly discriminated by XRD.

The detailed understanding of the presented RA spectra allows for precise *in situ* monitoring of the entire GaPN/Si(100) growth process. In general, the presented approach can be analogously applied for investigations of different III-V/IV heterostructures and interfaces. In particular, III-V growth on Ge(100) is of interest, where we already established MOVPE-preparation of atomically well ordered surfaces [21, 42, 46]. The next crucial steps towards a GaPN/Si(100)-based device include the design of an appropriate tunnel-junction and electrical characterization of the subcells. The electronic structure may benefit from additional incorporation of As. Electrochemical experiments involving the GaPN structures are currently ongoing. We will also follow alternative approaches for further III-V epitaxy on the GaP/Si(100) quasisubstrates discussed in this work. These include grading towards higher lattice-constants as well as strain-balanced quantum well structures.

Supplementary

Computational: DFT calculations

The DFT calculations of the interface formation energies in section 3.4, which are shown in Fig. 3.18 on page 76, were performed by Dr. O. Romanyuk (ASCR Prague), who communicated the computational details given in the following paragraph. Details are also given in Ref.s[218, 253].

The generalized gradient approximation (GGA) for the exchange correlation energy functional was used. Norm-conserving pseudopotentials [97] of the Troullier-Martins type [273] were used to describe the atomic species. The electronic wave functions were expanded in a plane wave basis with a converged kinetic energy cutoff of 12 Hartree (Ha). k point sets [190] corresponding to 12×12 points per (1×1) Brillouin zone were used. Periodic boundary conditions were applied along the in-plane and out-of-plane directions, the slab is shown in Fig. 3.17 on page 75. Equilibrium lattice constants were computed for bulk Si ($a_{Si} = 5.46\,\text{Å}$) and GaP ($a_{GaP} = 5.50\,\text{Å}$) [218]. The Si lattice constant was used for the GaP/Si slab. The atomic positions were adjusted until the interatomic forces became smaller than 10^{-3} Ha/Bohr, whereas atomic positions of two Si layers and passivating hydrogen atoms were fixed. The relative interface formation energy $\Delta\gamma$, as a function of the chemical potential variation in thermodynamic equilibrium is defined as: [150, 206]

$$\Delta\gamma\,\mathcal{A} = E_{\text{tot}} - (\hat{n}_{\text{P}} - \hat{n}_{\text{Ga}})\Delta\mu_{\text{P}} - \hat{n}_{\text{Ga}}\mu^{\text{bulk}}_{\text{GaP}} - \hat{n}_{\text{Si}}\mu^{\text{bulk}}_{\text{Si}} \quad , \tag{1.1}$$

where E_{tot} is the total energy of the slab, $\hat{n}_{\text{P}}$, $\hat{n}_{\text{Ga}}$, $\hat{n}_{\text{Si}}$ are the number of P, Ga, and Si atoms in a slab, respectively, μ_i is the chemical potential of species i, $\Delta\mu_{\text{P}} = \mu_{\text{P}} - \mu^{\text{bulk}}_{\text{P}}$, and $\mathcal{A}$ is the surface unit cell area. The boundary conditions for the chemical potential variation were expressed as

$$H_f^{\text{GaP}} \leq \Delta\mu_{\text{P}} \leq 0 \quad , \tag{1.2}$$

where H_f^{GaP} is the heat of formation of GaP. The corresponding bulk chemical potentials were calculated for the orthorhombic α-Ga phase [26] and the orthorhombic black phosphorous [263] phase. The computed value of the GaP heat of formation is H_f^{GaP}= -0.91 eV [158].[45]

[45] The DFT calculations were carried out for the ground state, which refers to the solid Ga phase and not to liquid Ga. The experiments are carried out under P-rich conditions at elevated temperatures. There will be single Ga atoms at the surface, but Ga droplets need to be avoided in the experiments during growth for high epilayer crystal quality. Large Ga droplets seem not to appear on the surface, as indicated by AFM, LEED and RAS. One could, however, consider the Ga chemical potential of single Ga atoms [138], which would decrease H_f so that the Si–Ga interface would become more favorable at Ga-rich conditions (at $T = 0\,\text{K}$). Nevertheless, Ga single atoms are thermodynamically less stable than solid Ga in the ground state. Therefore, liquid Ga was not considered here.

List of Abbreviations

2PPE	two-photon photoemission
AFM	atomic force microscopy
AM	air mass
APB	antiphase boundary
APD	antiphase domain
ASF	atomic sensitivity factor
AsH_3	arsine
ATR	total attenuation reflection
AWM	anti-wobble mirror
BAC	band anticrossing model
CBE	chemical beam epitaxy
CBM	conduction band minimum
CPE	critical point energy
CPV	concentrating photovoltaics
DEZn	diethylzinc
DOS	density of states
ECM	electron-counting rule model
EDX	energy dispersive X-ray spectroscopy
FME	flow modulated epitaxy
FTIR	Fourier-transform infrared spectroscopy
HR-XRD	high-resolution X-ray diffraction
HZB	Helmholtz-Zentrum Berlin für Materialien und Energie GmbH
IDA	interface dielectric anisotropy
JDOS	joint density of states
LED	light emitting diode
LEED	low energy electron diffraction
LEEM	low energy electron microscopy
MEE	migration enhanced epitaxy
MFC	mass flow controller
MID	multiple ion detection

MOCVD	metalorganic chemical vapor deposition
MOVPE	metalorganic vapor phase epitaxy
MS	mass spectrometry
OMVPE	organometallic vapor phase epitaxy
PC	pressure controller
PE	photoemission
PEM	photoelastic modulator
PES	photoelectron spectroscopy
PH_3	phosphine
PL	photoluminescence
PP	pulse pairs
PV	photovoltaics
RAS	reflection anisotropy spectroscopy
RDS	reflectance difference spectroscopy
rlu	reciprocal lattice units
RMS	root mean square
RSM	reciprocal space map
RTA	rapid thermal annealing
SDA	surface dielectric anisotropies
SE	spectroscopic ellipsometry
SiH_4	silane
SIMS	secondary ion mass spectrometry
STM	scanning tunneling microscopy
TBAs	tertiarybutylarsine
TBP	tertiarybutylphosphine
TEGa	triethylgallium
TEM	transmission electron microscopy
TESb	triethylantimony
TMGa	trimethylgallium
TMSb	trimethylantimony
TRPL	time-resolved PL
TU	Technische Universität (Technical University)
UDMHy	1.1-dimethylhydrazine
UHV	ultra-high vacuum
UPS	ultraviolet photoelectron spectroscopy
VBM	valence band maximum
VBO	valence band offset
XPS	X-ray photoelectron spectroscopy

List of Figures

List of Tables

References

Given URLs were checked on March, 10th, 2015.

[1] Acosta-Ortiz, S. E.; Lastras-Martínez, A.: *Measurements of above-bandgap optical anisotropies in the (001) surface of GaAs*. Solid State Communications, **64**:809, 1987.

[2] Acosta-Ortiz, S. E.; Lastras-Martínez, A.: *Electro-optic effects in the optical anisotropies of (001) GaAs*. Physical Review B, **40**:1426, 1989.

[3] Alamo, J. A. del: *Nanometre-scale electronics with III–V compound semiconductors*. Nature, **479**:317, 2011.

[4] Alstrin, A. L.; Strupp, P. G.; Leone, S. R.: *Direct detection of atomic arsenic desorption from Si(100)*. Applied Physics Letters, **63**:815, 1993.

[5] American Society for Testing and Materials (ASTM): *Terrestrial Reference Spectra for Photovoltaic Performance Evaluation*. Obtained via Renewable Resource Data Center at National Renewable Energy Laboratory. http://rredc.nrel.gov/solar/spectra/am1.5/.

[6] Aoyama, T.; Goto, K.-i.; Yamazaki, T.; Ito, T.: *Silicon (001) surface after annealing in hydrogen ambient*. Journal of Vacuum Science & Technology A, **14**:2909, 1996.

[7] Appelbaum, J. A.; Baraff, G. A.; Hamann, D. R.: *The Si (100) surface. III. Surface reconstruction*. Physical Review B, **14**:588, 1976.

[8] Aspnes, D. E.: *Optical properties of thin films*. Thin Solid Films, **89**:249, 1982.

[9] Aspnes, D. E.: *Above-bandgap optical anisotropies in cubic semiconductors: A visible-near ultraviolet probe of surfaces*. Journal of Vacuum Science & Technology B, **3**:1498, 1985.

[10] Aspnes, D. E.: *Optical response of microscopically rough surfaces*. Physical Review B, **41**:10334, 1990.

[11] Aspnes, D. E.: *Real-time optical diagnostics for epitaxial growth*. Surface Science, **307–309**:1017, 1994.

[12] Aspnes, D. E.; Harbison, J. P.; Studna, A. A.; Florez, L. T.: *Application of reflectance difference spectroscopy to molecular-beam epitaxy growth of GaAs and AlAs*. Journal of Vacuum Science and Technology A, **6**:1327, 1988.

[13] Aspnes, D. E.; Ihm, J.: *Biatomic steps on (001) silicon surfaces.* Physical Review Letters, **57**:3054, 1986.

[14] Aspnes, D. E.; Studna, A. A.: *Dielectric functions and optical parameters of Si, Ge, GaP, GaAs, GaSb, InP, InAs, and InSb from 1.5 to 6.0 eV.* Physical Review B, **27**:985, 1983.

[15] Aspnes, D. E.; Studna, A. A.: *Anisotropies in the above-band-gap optical spectra of cubic semiconductors.* Physical Review Letters, **54**:1956, 1985.

[16] Ayers, W.: *Photolytic Production of Hydrogen.* US Patent No. 4,466,869, 1984.

[17] Azzam, R. M. A.; Bashara, N. M.: *Ellipsometry and polarized light.* North-Holland, 1987. ISBN: 9780444870162.

[18] Bachmann, K. J.; Rossow, U.; Sukidi, N.; Castleberry, H.; Dietz, N.: *Heteroepitaxy of GaP on Si(100).* Journal of Vacuum Science & Technology B, **14**:3019, 1996.

[19] Baillargeon, J. N.; Cheng, K. Y.; Hofler, G. E.; Pearah, P. J.; Hsieh, K. C.: *Luminescence quenching and the formation of the $GaP_{1-x}N_x$ alloy in GaP with increasing nitrogen content.* Applied Physics Letters, **60**:2540, 1992.

[20] Barrigón, E.; Brückner, S.; Supplie, O.; Döscher, H.; Rey-Stolle, I.; Hannappel, T.: *In situ study of Ge(100) surfaces with tertiarybutylphosphine supply in vapor phase epitaxy ambient.* Journal of Crystal Growth, **370**:173, 2013.

[21] Barrigón, E.; Brückner, S.; Supplie, O.; Kleinschmidt, P.; Rey-Stolle, I.; Hannappel, T.: *Optical in situ monitoring of hydrogen desorption from Ge(100) surfaces.* Applied Physics Letters, **102**:111608, 2013.

[22] Baski, A. A.; Nogami, J.; Quate, C. F.: *Gallium growth and reconstruction on the Si(100) surface.* Journal of Vacuum Science & Technology A, **8**:245, 1990.

[23] Bedrossian, P.; Klitsner, T.: *Anisotropic vacancy kinetics and single-domain stabilization on Si(100)-2×1.* Physical Review Letters, **68**:646, 1992.

[24] Bell, K. A.; Ebert, M.; Yoo, S. D.; Flock, K.; Aspnes, D. E.: *Real-time optical characterization of heteroepitaxy by organometallic chemical vapor deposition.* Journal of Vacuum Science & Technology A, **18**:1184, 2000.

[25] Bender, H.; Verhaverbeke, S.; Caymax, M.; Vatel, O.; Heyns, M. M.: *Surface reconstruction of hydrogen annealed (100) silicon.* Journal of Applied Physics, **75**:1207, 1994.

[26] Bernasconi, M.; Chiarotti, G. L.; Tosatti, E.: *Ab initio calculations of structural and electronic properties of gallium solid-state phases.* Physical Review B, **52**:9988, 1995.

[27] Beyer, A.; Haas, B.; Gries, K. I.; Werner, K.; Luysberg, M.; Stolz, W.; Volz, K.: *Atomic structure of (110) anti-phase boundaries in GaP on Si(001).* Applied Physics Letters, **103**:032107, 2013.

[28] Beyer, A.; Ohlmann, J.; Liebich, S.; Heim, H.; Witte, G.; Stolz, W.; Volz, K.: *GaP heteroepitaxy on Si(001): Correlation of Si-surface structure, GaP growth conditions, and Si-III/V interface structure.* Journal of Applied Physics, **111**:083534, 2012.

[29] Bi, W. G.; Tu, C. W.: *N incorporation in GaP and band gap bowing of* GaN_xP_{1-x}. Applied Physics Letters, **69**:3710, 1996.

[30] Binnig, G.; Rohrer, H.; Gerber, C.; Weibel, E.: *Tunneling through a controllable vacuum gap.* Applied Physics Letters, **40**:178, 1982.

[31] Boland, J. J.: *Structure of the H-saturated Si(100) surface.* Physical Review Letters, **65**:3325, 1990.

[32] Bork, T.; McMahon, W.; Olson, J.; Hannappel, T.: *Surface science studies including low-temperature RDS on MOCVD-prepared, As-terminated Si(100) surfaces.* Journal of Crystal Growth, **298**:54, 2007.

[33] Borkenhagen, B.: *Oberflächen-Elektronenmikroskopie von anwendungsrelevanten Materialien für heterogene Katalyse, III-V-Heteroepitaxie und polykristalline Werkstoffe.* Ph.D. thesis. Technische Universität Clausthal (Germany) / Papierflieger-Verlag Clausthal-Zellerfeld, 2012. ISBN: 978-3-86948-239-2.

[34] Bourguignon, B.; Carleton, K. L.; Leone, S. R.: *Surface structures and growth mechanism of Ga on Si(100) determined by LEED and Auger electron spectroscopy.* Surface Science, **204**:455, 1988.

[35] Bourret-Courchesne, E; Ye, Q; Peters, D. W; Arnold, J; Ahmed, M; Irvine, S. J. C; Kanjolia, R; Smith, L. M; Rushworth, S. A.: *Pyrolysis of dimethylhydrazine and its co-pyrolysis with triethylgallium.* Journal of Crystal Growth, **217**:47, 2000.

[36] Breyer, C.; Gerlach, A.: *Global overview on grid-parity.* Progress in Photovoltaics: Research and Applications, **21**:121, 2013.

[37] Bringans, R. D.: *Arsenic passivation of Si and Ge surfaces.* Critical Reviews in Solid State and Materials Sciences, **17**:353, 1992.

[38] Bringans, R. D.; Biegelsen, D.; Swartz, L.-E.: *Atomic-step rearrangement on Si(100) by interaction with arsenic and the implication for GaAs-on-Si epitaxy.* Physical Review B, **44**:3054, 1991.

[39] Bringans, R. D.; Olmstead, M. A.; Uhrberg, R. I. G.; Bachrach, R. Z.: *Interface formation of GaAs with Si(100), Si(111), and Ge(111): Core-level spectroscopy for monolayer coverages of GaAs, Ga, and As.* Physical Review B, **36**:9569, 1987.

[40] Bringans, R. D.; Olmstead, M. A.; Uhrberg, R. I. G.; Bachrach, R. Z.: *Summary abstract: Core level spectroscopy of the GaAs-on-Si interface.* Journal of Vacuum Science & Technology A, **5**:2141, 1987.

[41] Brückner, S.: *Atomic scale in situ control of Si(100) and Ge(100) surfaces in CVD ambient*. Ph.D. thesis. Humboldt-Universität zu Berlin / Helmholtz-Zentrum Berlin (Germany), 2014.
http://edoc.hu-berlin.de/docviews/abstract.php?id=40487.

[42] Brückner, S.; Barrigón, E.; Supplie, O.; Kleinschmidt, P.; Dobrich, A.; Löbbel, C.; Rey-Stolle, I.; Döscher, H.; Hannappel, T.: *Ge(100) surfaces prepared in vapor phase epitaxy process ambient*. physica status solidi (RRL)—Rapid Research Letters, **6**:178, 2012.

[43] Brückner, S.; Döscher, H.; Kleinschmidt, P.; Hannappel, T.: *In situ investigation of hydrogen interacting with Si(100)*. Applied Physics Letters, **98**:211909, 2011.

[44] Brückner, S.; Döscher, H.; Kleinschmidt, P.; Supplie, O.; Dobrich, A.; Hannappel, T.: *Anomalous double-layer step formation on Si(100) in hydrogen process ambient*. Physical Review B, **86**:195310, 2012.

[45] Brückner, S.; Kleinschmidt, P.; Supplie, O.; Döscher, H.; Hannappel, T.: *Domain-sensitive in situ observation of layer-by-layer removal at Si(100) in H_2 ambient*. New Journal of Physics, **15**:113049, 2013.

[46] Brückner, S.; Supplie, O.; Barrigón, E.; Luczak, J.; Kleinschmidt, P.; Rey-Stolle, I.; Döscher, H.; Hannappel, T.: *In situ control of As dimer orientation on Ge(100) surfaces*. Applied Physics Letters, **101**:121602, 2012.

[47] Buyanova, I. A.; Izadifard, M.; Chen, W. M.; Xin, H. P.; Tu, C. W.: *Experimental evidence for N-induced strong coupling of host conduction band states in GaN_xP_{1-x} : Insight into the dominant mechanism for giant band-gap bowing*. Physical Review B, **69**:201303, 2004.

[48] Cardona, M.; Pollak, F. H.; Shaklee, K. L.: *Electroreflectance in semiconductors*. Journal of the Physical Society of Japan, Suppl. **S21**:89, 1966. Cited after [15].

[49] Chabal, Y. J.; Harris, A. L.; Raghavachari, K.; Tully, J. C.: *Infrared spectroscopy of H-terminated silicon surfaces*. International Journal of Modern Physics B, **7**:1031, 1993.

[50] Chabal, Y. J.; Raghavachari, K.: *Surface infrared study of Si(100)-(2×1)H*. Physical Review Letters, **53**:282, 1984.

[51] Chabal, Y.: *High-resolution infrared spectroscopy of adsorbates on semiconductor surfaces: Hydrogen on Si(100) and Ge(100)*. Surface Science, **168**:594, 1986.

[52] Chadi, D. J.: *Stabilities of single-layer and bilayer steps on Si(001) surfaces*. Physical Review Letters, **59**:1691, 1987.

[53] Chandola, S.; Power, J.; Farrell, T.; Weightman, P.; McGilp, J.: *The effect of submonolayer coverages of Ga on the optical anisotropy of vicinal Si(001)*. Applied Surface Science, **123–124**:233, 1998.

[54] Chetty, N.; Martin, R. M.: *First-principles energy density and its applications to selected polar surfaces.* Physical Review B, **45**:6074, 1992.

[55] Chetty, N.; Martin, R. M.: *GaAs(111) and ($\bar{1}\bar{1}\bar{1}$) surfaces and the GaAs/AlAs (111) heterojunction studied using a local energy density.* Physical Review B, **45**:6089, 1992.

[56] Cornet, C.; Nguyen Thanh, T.; Quinci, T.; Almosni, S.; Rohel, T.; Kuyyalil, J.; Rambaud, A.; Létoublon, A.; Bertru, N.; Durand, O.; Le Corre, A.: *Preferential incorporation of substitutional nitrogen near the atomic step edges in diluted nitride alloys.* Applied Physics Letters, **101**:251906, 2012.

[57] Dagnelund, D.; Stehr, J.; Yu. Egorov, A.; Chen, W. M.; Buyanova, I. A.: *Optically detected magnetic resonance studies of point defects in quaternary GaNAsP epilayers grown by vapor phase epitaxy.* Applied Physics Letters, **102**:021910, 2013.

[58] Dagnelund, D.; Tu, C. W.; Polimeni, A.; Capizzi, M.; Chen, W. M.; Buyanova, I. A.: *Effect of thermal annealing on defects in post-growth hydrogenated GaNP.* physica status solidi (c), **10**:561, 2013.

[59] Dagnelund, D.; Vorona, I. P.; Nosenko, G.; Wang, X. J.; Tu, C. W.; Yonezu, H.; Polimeni, A.; Capizzi, M.; Chen, W. M.; Buyanova, I. A: *Effects of hydrogenation on non-radiative defects in GaNP and GaNAs alloys: An optically detected magnetic resonance study.* Journal of Applied Physics, **111**:023501, 2012.

[60] Dagnelund, D.; Wang, X. J.; Tu, C. W.; Polimeni, A.; Capizzi, M.; Chen, W. M.; Buyanova, I. A.: *Effect of postgrowth hydrogen treatment on defects in GaNP.* Applied Physics Letters, **98**:141920, 2011.

[61] De Vos, A.; Pauwels, H.: *On the thermodynamic limit of photovoltaic energy conversion.* Applied Physics, **25**:119, 1981.

[62] Delplancke, M. P.; Powers, J. M.; Vandentop, G. J.; Salmeron, M.; Somorjai, G. A.: *Preparation and characterization of amorphous SiC:H thin films.* Journal of Vacuum Science & Technology A, **9**:450, 1991.

[63] Deutsch, T. G.; Head, J. L.; Turner, J. A.: *Photoelectrochemical characterization and durability analysis of GaInPN epilayers.* Journal of The Electrochemical Society, **155**:B903, 2008.

[64] Deutsch, T. G.; Koval, C. A.; Turner, J. A.: *III-V nitride epilayers for photoelectrochemical water splitting: GaPN and GaAsPN.* Journal of Physical Chemistry B, **110**:25297, 2006.

[65] Dietz, N.; Rossow, U.; Aspnes, D. E.; Bachmann, K. J.: *Real-time optical monitoring of epitaxial growth: Pulsed chemical beam epitaxy of GaP and InP homoepitaxy and heteroepitaxy on Si.* Journal of Crystal Growth, **164**:34, 1996.

[66] Dietz, N.; Rossow, U.; Aspnes, D. E.; Bachmann, K. J.: *Real-time optical monitoring of heteroepitaxial growth processes on Si under pulsed chemical beam epitaxy conditions.* Applied Surface Science, **102**:47, 1996.

[67] Dimroth, F.; Howard, A.; Shurtleff, J. K.; Stringfellow, G. B.: *Influence of Sb, Bi, Tl, and B on the incorporation of N in GaAs.* Journal of Applied Physics, **91**:3687, 2002.

[68] Dimroth, F.; Grave, M.; Beutel, P.; Fiedeler, U.; Karcher, C.; Tibbits, T. N. D.; Oliva, E.; Siefer, G.; Schachtner, M.; Wekkeli, A.; Bett, A. W.; Krause, R.; Piccin, M.; Blanc, N.; Drazek, C.; Guiot, E.; Ghyselen, B.; Salvetat, T.; Tauzin, A.; Signamarcheix, T.; Dobrich, A.; Hannappel, T.; Schwarzburg, K.: *Wafer bonded four-junction GaInP/GaAs//GaInAsP/GaInAs concentrator solar cells with 44.7% efficiency.* Prog. Photovolt: Res. Appl. **22**:277, 2014.

[69] Dixit, V. K.; Ganguli, T.; Sharma, T. K.; Singh, S. D.; Kumar, R.; Porwal, S.; Tiwari, P.; Ingale, A.; Oak, S. M.: *Effect of two-step growth process on structural, optical and electrical properties of MOVPE-grown GaP/Si.* Journal of Crystal Growth, **310**:3428, 2008.

[70] Dobrich, A.: *Wasserstoffbindungen an Silizium-Halbleiteroberflächen aus MO-CVD-Präparation.* Diploma thesis. Freie Universität Berlin / Helmholtz-Zentrum Berlin (Germany), 2009.

[71] Dobrich, A.; Kleinschmidt, P.; Döscher, H.; Hannappel, T.: *Quantitative investigation of hydrogen bonds on Si(100) surfaces prepared by vapor phase epitaxy.* Journal of Vacuum Science & Technology B, **29**:04D114, 2011.

[72] Doi, T.; Ichikawa, M.; Hosoki, S.; Ninomiya, K.: *Anisotropic diffusion between the step-up and the step-down directions on a Si(001) surface.* Physical Review B, **53**:16609, 1996.

[73] Döscher, H.: *Benchmarking surface signals when growing GaP on Si in CVD ambients.* Ph.D. thesis. Humboldt-Universität zu Berlin / Helmholtz-Zentrum Berlin (Germany), 2010.
http://edoc.hu-berlin.de/docviews/abstract.php?id=37409.

[74] Döscher, H.; Borkenhagen, B.; Lilienkamp, G.; Daum, W.; Hannappel, T.: *III-V on silicon: Observation of gallium phosphide anti-phase disorder by low-energy electron microscopy.* Surface Science, **605**:L38, 2011.

[75] Döscher, H.; Brückner, S.; Dobrich, A.; Höhn, C.; Kleinschmidt, P.; Hannappel, T.: *Surface preparation of Si(100) by thermal oxide removal in a chemical vapor environment.* Journal of Crystal Growth, **315**:10, 2011.

[76] Döscher, H.; Brückner, S.; Hannappel, T.: *Investigation of oxide removal from Si(100) substrates in dependence of the MOVPE process gas ambient.* Journal of Crystal Growth, **318**:563, 2011.

[77] Döscher, H.; Dobrich, A.; Brückner, S.; Kleinschmidt, P.; Hannappel, T.: *Si(100) surfaces in a hydrogen-based process ambient.* Applied Physics Letters, **97**:151905, 2010.

[78] Döscher, H.; Hannappel, T.: *In situ reflection anisotropy spectroscopy analysis of heteroepitaxial GaP films grown on Si(100).* Journal of Applied Physics, **107**:123523, 2010.

[79] Döscher, H.; Hannappel, T.; Kunert, B.; Beyer, A.; Volz, K.; Stolz, W.: *In situ verification of single-domain III-V on Si(100) growth via metal-organic vapor phase epitaxy.* Applied Physics Letters, **93**:172110, 2008.

[80] Döscher, H.; Kleinschmidt, P.; Hannappel, T.: *Atomic surface structure of Si(100) substrates prepared in a chemical vapor environment.* Applied Surface Science, **257**:574, 2010.

[81] Döscher, H.; Kunert, B.; Beyer, A.; Supplie, O.; Volz, K.; Stolz, W.; Hannappel, T.: *In situ antiphase domain quantification applied on heteroepitaxial GaP growth on Si(100).* Journal of Vacuum Science & Technology B, **28**:C5H1, 2010.

[82] Döscher, H.; Möller, K.; Hannappel, T.: *GaP(100) and InP(100) surface structures during preparation in a nitrogen ambient.* Journal of Crystal Growth, **318**:372, 2011.

[83] Döscher, H.; Supplie, O.; Brückner, S.; Hannappel, T.; Beyer, A.; Ohlmann, J.; Volz, K.: *Indirect in situ characterization of Si(100) substrates at the initial stage of III-V heteroepitaxy.* Journal of Crystal Growth, **315**:16, 2011.

[84] Döscher, H.; Supplie, O.; May, M. M.; Sippel, P.; Heine, C.; Muñoz, A. G.; Eichberger, R.; Lewerenz, H.-J.; Hannappel, T.: *Epitaxial III–V films and surfaces for photoelectrocatalysis.* ChemPhysChem, **13**:2899, 2012.

[85] Dupuis, R. D.; Dapkus, P. D.: *Room-temperature operation of $Ga_{(1-x)}Al_xAs$ / GaAs double-heterostructure lasers grown by metalorganic chemical vapor deposition.* Applied Physics Letters, **31**:466, 1977.

[86] Einstein, A.: *Über einen die Erzeugung und Verwandlung des Lichtes betreffenden heuristischen Gesichtspunkt.* Annalen der Physik, **322**:132, 1905.

[87] Fadley, C. S.: *Angle-resolved x-ray photoelectron spectroscopy.* Progress in Surface Science, **16**:275, 1984.

[88] Fang, S. F.; Adomi, K.; Iyer, S.; Morkoc, H.; Zabel, H.; Choi, C.; Otsuka, N.: *Gallium arsenide and other compound semiconductors on silicon.* Journal of Applied Physics, **68**:R31, 1990.

[89] Felici, M.; Polimeni, A.; Miriametro, A.; Capizzi, M.; Xin, H. P.; Tu, C. W.: *Free carrier and/or exciton trapping by nitrogen pairs in dilute $GaP_{1-x}N_x$.* Physical Review B, **71**:045209, 2005.

[90] Fischer, R.; Masselink, W. T.; Klem, J.; Henderson, T.; McGlinn, T. C.; Klein, M. V.; MorkoÃ§, H.; Mazur, J. H.; Washburn, J.: *Growth and properties of GaAs/AlGaAs on nonpolar substrates using molecular beam epitaxy.* Journal of Applied Physics, **58**:374, 1985.

[91] Fischer, T. E.: *Photoelectric Emission and Work Function of InP.* Physical Review, **142**:519, 1966.

[92] Fluegel, B.; Zhang, Y.; Geisz, J. F.; Mascarenhas, A.: *Comment on "Experimental evidence for N-induced strong coupling of host conduction band states in GaN_xP_{1-x}: Insight into the dominant mechanism for giant band-gap bowing"*. Physical Review B, **72**:197301, 2005.

[93] Fluegel, B.; Zhang, Y.; Geisz, J. F.; Mascarenhas, A.: *Confirmation of the impurity-band model for $GaP_{1-x}N_x$*. Physical Review B, **72**:073203, 2005.

[94] Fraj, N.; Saidi, I.; Ben Radhia, S.; Boujdaria, K.: *Band structures of AlAs, GaP, and SiGe alloys: A 30 $k\times p$ model*. Journal of Applied Physics, **102**:053703, 2007.

[95] Franciosi, A.; Walle, C. G. V. de: *Heterojunction band offset engineering*. Surface Science Reports, **25**:1, 1996.

[96] Frisch, A. M.; Schmidt, W. G.; Bernholc, J.; Pristovsek, M.; Esser, N.; Richter, W.: (2×4) *GaP(001) surface: Atomic structure and optical anisotropy*. Physical Review B, **60**:2488, 1999.

[97] Fuchs, M.; Scheffler, M.: *Ab initio pseudopotentials for electronic structure calculations of poly-atomic systems using density-functional theory*. Computer Physics Communications, **119**:67, 1999.

[98] Gallois, B. M.; Besmann, T. M.; Stott, M. W.: *Chemical etching of silicon (100) by hydrogen*. Journal of the American Ceramic Society, **77**:2949, 1994.

[99] Garrod, T.; Kirch, J.; Dudley, P.; Kim, S.; Mawst, L.; Kuech, T.: *Narrow band gap GaInNAsSb material grown by metal organic vapor phase epitaxy (MOVPE) for solar cell applications*. Journal of Crystal Growth, **315**:68, 2011.

[100] Geisz, J. F.; Friedman, D. J.: *III-N-V semiconductors for solar photovoltaic applications*. Semiconductor Science and Technology, **17**:769, 2002.

[101] Geisz, J. F.; Olson, J. M.; Romero, M. J.; Jiang, C.-S.; Norman, A. G.: *Lattice-mismatched GaAsP solar cells grown on silicon by OMVPE*. Proceedings of the 4th IEEE World Conference on Photovoltaic Energy Conversion, **1**:772, 2006.

[102] Geisz, J. F.; Reedy, R. C.; Keyes, B. M.; Metzger, W. K.: *Unintentional carbon and hydrogen incorporation in GaNP grown by metal-organic chemical vapor deposition*. Journal of Crystal Growth, **259**:223, 2003.

[103] Geisz, J.; Olson, J.; Friedman, D.; Jones, K.; Reedy, R.; Romero, M.: *Lattice-matched GaNPAs-on-Silicon Tandem Solar Cells*. Proceedings of the IEEE Photovoltaics Specialists Conference, **31**:695, 2005.

[104] Gies, S.; Zimprich, M.; Wegele, T.; Kruska, C.; Beyer, A.; Stolz, W.; Volz, K.; Heimbrodt, W.: *Annealing effects on the composition and disorder of Ga(N,As,P) quantum wells on silicon substrates for laser application*. Journal of Crystal Growth, **402**:169, 2014.

[105] Goletti, C.; Arciprete, F.; Almaviva, S.; Chiaradia, P.; Esser, N.; Richter, W.: *Analysis of InAs(001) surfaces by reflectance anisotropy spectroscopy.* Physical Review B, **64**:193301, 2001.

[106] Gonze, X.; Beuken, J.-M.; Caracas, R.; Detraux, F.; Fuchs, M.; Rignanese, G.-M.; Sindic, L.; Verstraete, M.; Zerah, G.; Jollet, F.; Torrent, M.; Roy, A.; Mikami, M.; Ghosez, P.; Raty, J.-Y.; Allan, D.: *First-principles computation of material properties: the ABINIT software project.* Computational Materials Science, **25**:478, 2002.

[107] Gonze, X.; Rignanese, G.-M.; Verstraete, M.; Beuken, J.-M.; Pouillon, Y.; Caracas, R.; Jollet, F.; Torrent, M.; Zerah, G.; Mikami, M.; Ghosez, P.; Veithen, M.; Raty, J.-Y.; Olevano, V.; Bruneval, F.; Reining, L.; Godby, R.; Onida, G.; Hamann, D. R.; Allan, D. C.: *A brief introduction to the ABINIT software package.* Zeitschrift für Kristallographie, **220**:558, 2005.

[108] Gowers, J. P.: *TEM image contrast from antiphase domains in GaAs:Ge(001) grown by MBE.* Applied Physics A, **34**:231, 1984.

[109] Grassman, T. J.; Brenner, M. R.; Rajagopalan, S.; Unocic, R.; Dehoff, R.; Mills, M.; Fraser, H.; Ringel, S. A.: *Control and elimination of nucleation-related defects in GaP/Si(001) heteroepitaxy.* Applied Physics Letters, **94**:232106, 2009.

[110] Green, M. A.: *Third generation photovoltaics–Advanced solar energy conversion.* Springer Verlag (Berlin/Heidelberg), 2006. ISBN: 13978-3-540-26562-7.

[111] Green, M. A.; Emery, K.; Hishikawa, Y.; Warta, W.; Dunlop, E. D.: *Solar cell efficiency tables (version 41).* Progress in Photovoltaics: Research and Applications, **21**:1, 2013.

[112] Green, M. A.; Emery, K.; Hishikawa, Y.; Warta, W.; Dunlop, E. D.: *Solar cell efficiency tables (version 44).* Progress in Photovoltaics: Research and Applications, **22**:701, 2014.

[113] Haberland, K.: *Optical in-situ studies during metal-organic vapor phase epitaxy with respect to III-V device production.* Ph.D. thesis. Technische Universität Berlin (Germany), 2002.

[114] Haberland, K.; Kurpas, P.; Pristovsek, M.; Zettler, J.-T.; Weyers, M.; Richter, W.: *Spectroscopic process sensors in MOVPE device production.* Applied Physics A, **68**:309, 1999.

[115] Haberland, K.; Zorn, M.; Klein, A.; Bhattacharya, A.; Weyers, M.; Zettler, J.-T.; Richter, W.: *In-situ determination of interface roughness in MOVPE-grown visible VCSELs by reflectance spectroscopy.* Journal of Crystal Growth, **248**:194, 2003.

[116] Hahn, P. H.; Schmidt, W. G.; Bechstedt, F.; Pulci, O.; del Sole, R.: *P-rich GaP(001)*$(2 \times 1)/(2 \times 2)$ *surface: A hydrogen-adsorbate structure determined from first-principles calculations.* Physical Review B, **68**:033311, 2003.

[117] Hanada, T.; Yasuda, T.; Ohtake, A.; Hingerl, K.; Miwa, S.; Arai, K.; Yao, T.: *In situ observation of strain-induced optical anisotropy of ZnS_xSe_{1-x} / GaAs(110) during molecular-beam epitaxy.* Physical Review B, **60**:8909, 1999.

[118] Hannappel, T.; McMahon, W. E.; Olson, J. M.: *An RDS, LEED, and STM Study of MOCVD-Prepared Si(100) surfaces.* Journal of Crystal Growth, **272**:24, 2004.

[119] Hannappel, T; Visbeck, S; Töben, L; Willig, F: *Apparatus for investigating metalorganic chemical vapor deposition-grown semiconductors with ultrahigh-vacuum based techniques.* Review of Scientifc Instruments, **75**:1297, 2004.

[120] Hansen, W. N.; Kolb, D. M.: *The work function of emersed electrodes.* Journal of Electroanalytical Chemistry and Interfacial Electrochemistry, **100**:493, 1979.

[121] Hansma, P. K.; Tersoff, J.: *Scanning tunneling microscopy.* Journal of Applied Physics, **61**:R1, 1987.

[122] Hara, S.; Irokawa, K.; Miki, H.; Kawazu, A.; Torii, H.; Fujishiro, H. I.: *Behavior of Ga atoms on Si(001) surface at high temperature.* Journal of Applied Physics, **98**:083513, 2005.

[123] Harrison, W. A.; Kraut, E. A.; Waldrop, J. R.; Grant, R. W.: *Polar heterojunction interfaces.* Physical Review B, **18**:4402, 1978.

[124] Hertz, H.: *Ueber einen Einfluss des ultravioletten Lichtes auf die electrische Entladung.* Annalen der Physik, **267**:983, 1887.

[125] Hingerl, K.; Balderas-Navarro, R. E.; Bonanni, A.; Tichopadek, P.; Schmidt, W. G.: *On the origin of resonance features in reflectance difference data of silicon.* Applied Surface Science, **175–176**:769, 2001.

[126] Hu, S.; Xiang, C.; Haussener, S.; Berger, A. D.; Lewis, N. S.: *An analysis of the optimal band gaps of light absorbers in integrated tandem photoelectrochemical water-splitting systems.* Energy & Environmental Science, **6**:2984, 2013.

[127] Hunderi, O.; Zettler, J.-T.; Haberland, K.: *On the AlAs/GaAs (001) interface dielectric anisotropy.* Thin Solid Films, **472**:261, 2005.

[128] Ibach, H.; Lüth, H.: *Festkörperphysik.* Springer Verlag (Berlin/Heidelberg), 2009. ISBN: 978-3-54-085795-2.

[129] Ibach, H.: *Physics of Surfaces and Interfaces.* Springer Verlag (Berlin/Heidelberg), 2006. ISBN: 978-3-540-34709-5.

[130] Ioffe Physico-Technical Institute: *Electronic archive: New semiconductor materials, characteristics and properties—Physical properties of semiconductors: Basic parameters of Si.*
http://www.ioffe.ru/SVA/NSM/Semicond/Si/basic.html.

[131] Ishizaka, A.; Shiraki, Y.: *Low temperature surface cleaning of silicon and its application to silicon MBE.* Journal of The Electrochemical Society, **133**:666, 1986.

[132] Jandieri, K.; Jurecka, C.; Ohlmann, J.; Beyer, A.; Kunert, B.; Baranovskii, S. D.; Volz, K.; Stolz, W.; Gebhard, F.: *Hopping relaxation of photoexcited excitons in Ga(NAsP) bulk structure.* physica status solidi (c), **8**:163, 2011.

[133] Jellison Jr., G.: *Optical functions of GaAs, GaP, and Ge determined by two-channel polarization modulation ellipsometry.* Optical Materials, **1**:151, 1992.

[134] Jellison Jr., G.: *Optical functions of silicon determined by two-channel polarization modulation ellipsometry.* Optical Materials, **1**:41, 1992.

[135] Jeong, S.; Oshiyama, A.: *Structural stability and adatom diffusion at steps on hydrogenated Si(100) surfaces.* Physical Review Letters, **81**:5366, 1998.

[136] Kaiser, B.; Jaegermann, W.; Fiechter, S.; Lewerenz, H.-J.: *Direct photoelectrochemical conversion of sun light into hydrogen for chemical energy storage.* Bunsen-Magazin, **4**:104, 2011.

[137] Kaiser, B.; Fertig, D.; Ziegler, J.; Klett, J.; Hoch, S.; Jaegermann, W.: *Solar hydrogen generation with wide-band-gap semiconductors: GaP(100) photoelectrodes and surface modification.* ChemPhysChem, **13**:3053, 2012.

[138] Kangawa, Y.; Ito, T.; Taguchi, A.; Shiraishi, K.; Ohachi, T.: *A new theoretical approach to adsorption–desorption behavior of Ga on GaAs surfaces.* Surface Science, **493**:178, 2001.

[139] Kawabe, M.; Ueda, T.: *Self-Annihilation of Antiphase Boundary in GaAs on Si(100) Grown by Molecular Beam Epitaxy.* Japanese Journal of Applied Physics, **26**:L944, 1987.

[140] Kenney, M. J.; Gong, M.; Li, Y.; Wu, J. Z.; Feng, J.; Lanza, M.; Dai, H.: *High-Performance Silicon Photoanodes Passivated with Ultrathin Nickel Films for Water Oxidation.* Science, **342**:836, 2013.

[141] Kent, P. R. C.; Zunger, A.: *Evolution of III-V nitride alloy electronic structure: The localized to delocalized transition.* Physical Review Letters, **86**:2613, 2001.

[142] Kent, P. R. C.; Zunger, A.: *Theory of electronic structure evolution in GaAsN and GaPN alloys.* Physical Review B, **64**:115208, 2001.

[143] Kentsch, C.; Kutschera, M.; Weinelt, M.; Fauster, T.; Rohlfing, M.: *Electronic structure of Si(100) surfaces studied by two-photon photoemission.* Physical Review B, **65**:035323, 2001.

[144] Khaselev, O.; Turner, J. A.: *A monolithic photovoltaic-photoelectrochemical device for hydrogen production via water splitting.* Science, **280**:425, 1998.

[145] Khaselev, O.; Turner, J. A.: *Electrochemical stability of p-GaInP$_2$ in aqueous electrolytes toward photoelectrochemical water splitting.* Journal of The Electrochemical Society, **145**:3335, 1998.

[146] Kim, T. W.; Garrod, T. J.; Kim, K.; Lee, J. J.; LaLumondiere, S. D.; Sin, Y.; Lotshaw, W. T.; Moss, S. C.; Kuech, T. F.; Tatavarti, R.; Mawst, L. J.: *Narrow band gap (1eV) InGaAsSbN solar cells grown by metalorganic vapor phase epitaxy.* Applied Physics Letters, **100**:121120, 2012.

[147] Kipp, L.; Biegelsen, D.; Northrup, J.; Swartz, L.-E.; Bringans, R. D.: *Reflectance Difference Spectroscopy: Experiment and Theory for the Model System Si(001):As and Application to Si(001).* Physical Review Letters, **76**:2810, 1996.

[148] Kitahara, K.; Ueda, O.: *Observation of atomic structure by scanning tunneling microscopy of vicinal Si(100) surface annealed in hydrogen gas.* Japanese Journal of Applied Physics, **33**:L1571, 1994.

[149] Kleinschmidt, P.; Döscher, H.; Vogt, P.; Hannappel, T.: *Direct observation of dimer flipping at the hydrogen-stabilized GaP(100) and InP(100) surfaces.* Physical Review B, **83**:155316, 2011.

[150] Kley, A.; Neugebauer, J.: *Atomic and electronic structure of the GaAs / ZnSe (001) interface.* Physical Review B, **50**:8616, 1994.

[151] Kohama, Y.; Uchida, K.; Soga, T.; Jimbo, T.; Umeno, M.: *Quality improvement of metalorganic chemical vapor deposition grown GaP on Si by AsH_3 preflow.* Applied Physics Letters, **53**:862, 1988.

[152] Kolasinski, K. W.; Nessler, W.; Meijere, A. de; Hasselbrink, E.: *Hydrogen adsorption on and desorption from Si: Considerations on the applicability of detailed balance.* Physical Review Letters, **72**:1356, 1994.

[153] Komeda, T.; Kumagai, Y.: *Si(001) surface variation with annealing in ambient H_2.* Physical Review B, **58**:1385, 1998.

[154] Kondow, M.; Kitatani, T.; Nakatsuka, S.; Larson, M. C.; Nakahara, K.; Yazawa, Y.; Okai, M.; Uomi, K.: *GaInNAs: a novel material for long-wavelength semiconductor lasers.* IEEE Journal of Selected Topics in Quantum Electronics, **3**:719, 1997.

[155] Krames, M. R.; Shchekin, O. B.; Mueller-Mach, R.; Mueller, G. O.; Zhou, L.; Harbers, G.; Craford, M. G.: *Status and future of high-power light-emitting diodes for solid-state lighting.* Journal of Display Technology, **3**:160, 2007.

[156] Kroemer, H.: *Polar-on-nonpolar epitaxy.* Journal of Crystal Growth, **81**:193, 1987.

[157] Kroemer, H.: *Nobel lecture: Quasielectric fields and band offsets: Teaching electrons new tricks.* Reviews of Modern Physics, **73**:783, 2001.

[158] Kumar, V.; Sastry, B. S. R.: *Heats of formation of binary semiconductors.* physica status solidi (b), **242**:869, 2005.

[159] Kunert, B.; Németh, I.; Reinhard, S.; Volz, K.; Stolz, W.: *Si (001) surface preparation for the antiphase domain free heteroepitaxial growth of GaP on Si substrate.* Thin Solid Films, **517**:140, 2008.

[160] Kunert, B.; Koch, J.; Torunski, T.; Volz, K.; Stolz, W.: *MOVPE growth experiments of the novel (GaIn)(NP)/GaP material system.* Journal of Crystal Growth, **272**:753, 2004.

[161] Kurtz, S. R.; Allerman, A. A.; Jones, E. D.; Gee, J. M.; Banas, J. J.; Hammons, B. E.: *InGaAsN solar cells with 1.0 eV band gap, lattice matched to GaAs*. Applied Physics Letters, **74**:729, 1999.

[162] Laks, D. B.; Zunger, A.: *Theory of interfacial stability of semiconductor superlattices*. Physical Review B, **45**:14177, 1992.

[163] Laracuente, A. R.; Whitman, L. J.: *Step structure and surface morphology of hydrogen-terminated silicon: (001) to (114)*. Surface Science, **545**:70, 2003.

[164] Lastras-Martínez, L. F.; Lastras-Martínez, A.: *Reflectance anisotropy of GaAs (100): Dislocation-induced piezo-optic effects*. Physical Review B, **54**:10726, 1996.

[165] Lautenschlager, P.; Garriga, M.; Vina, L.; Cardona, M.: *Temperature dependence of the dielectric function and interband critical points in silicon*. Physical Review B, **36**:4821, 1987.

[166] Lee, R.; Stringfellow, G.: *Pyrolysis of 1,1 dimethylhydrazine for OMVPE growth*. Journal of Electronic Materials, **28**:963, 1999.

[167] Leibiger, G.; Gottschalch, V.; Schubert, M.; Benndorf, G.; Schwabe, R.: *Evolution of the optical properties of III-V nitride alloys: Direct band-to-band transitions in* GaN_yP_{1-y} $(0 \leq 0.029)$. Physical Review B, **65**:245207, 2002.

[168] Létay, G.; Bett, A. W.: *EtaOpt–A program for calculating limiting efficiency and optimum bandgap structure for multi-bandgap solar cells and TPV cells*. Proceedings of the European Photovoltaic Solar Energy Conference and Exhibition, **17**:178, 2001. http://www.ise.fraunhofer.de/de/geschaeftsfelder/iii-v-und-konzentrator-photovoltaik/themen/iii-v-epitaxie-und-solarzellen/fueleistungen/simulation/etaopt.

[169] Liarokapis, E.; Papadimitriou, D.; Rumberg, J.; Richter, W.: *Raman and RAS Measurements on Uniaxially Strained Thin Semiconductor Layers*. physica status solidi (b), **211**:309, 1999.

[170] Liebich, S.; Zimprich, M.; Beyer, A.; Lange, C.; Franzbach, D. J.; Chatterjee, S.; Hossain, N.; Sweeney, S. J.; Volz, K.; Kunert, B.; Stolz, W.: *Laser operation of Ga(NAsP) lattice-matched to (001) silicon substrate*. Applied Physics Letters, **99**:071109, 2011.

[171] Lin, D.-S.; Ku, T.-S.; Sheu, T.-J.: *Thermal reactions of phosphine with Si(100): a combined photoemission and scanning-tunneling-microscopy study*. Surface Science, **424**:7, 1999.

[172] Liu, X.; Kim, I. K.; Aspnes, D. E.: *Initial stages of GaP heteroepitaxy on nanoscopically roughened (001)Si*. Journal of Vacuum Science & Technology B, **25**:1448, 2007.

[173] Lüdge, K.; Vogt, P.; Pulci, O.; Esser, N.; Bechstedt, F.; Richter, W.: *Clarification of the GaP(001)*(2×4) *Ga-rich reconstruction by scanning tunneling microscopy and ab initio theory*. Physical Review B, **62**:11046, 2000.

[174] Manasevit, H. M.; Simpson, W. I.: *The use of metal-organics in the preparation of semiconductor materials: I. Epitaxial Gallium-V compounds*. Journal of The Electrochemical Society, **116**:1725, 1969.

[175] Mantese, L.; Rossow, U.; Aspnes, D.: *Surface-induced optical anisotropy of oxidized, clean, and hydrogenated vicinal Si(001) surfaces*. Applied Surface Science, **107**:35, 1996.

[176] Mantese, L.; Xue, Q. K.; Sakurai, T.; Aspnes, D. E.: *Analysis of high-index Si(001) surfaces by reflectance difference spectroscopy*. Journal of Vacuum Science & Technology A, **17**:1652, 1999.

[177] Martí, A.; Araújo, G. L.: *Limiting efficiencies for photovoltaic energy conversion in multigap systems*. Solar Energy Materials and Solar Cells, **43**:203, 1996.

[178] Matthews, J. W.; Blakeslee, A. E.: *Defects in epitaxial multilayers: II. Dislocation pile-ups, threading dislocations, slip lines and cracks*. Journal of Crystal Growth, **29**:273, 1975.

[179] Matthews, J.; Blakeslee, A.: *Defects in epitaxial multilayers: I. Misfit dislocations*. Journal of Crystal Growth, **27**:118, 1974.

[180] May, M. M.; Lewerenz, H.-J.; Hannappel, T.: *Optical in situ study of InP(100) surface chemistry: dissociative adsorption of water and oxygen*. Journal of Physical Chemistry C, **118**:19032, 2014.

[181] May, M. M.: *GaP- and InP-based surfaces for solar water splitting*. Ph.D. thesis. Humboldt-Universität zu Berlin / Helmholtz-Zentrum Berlin (Germany), defended 11/2014, to be published.

[182] May, M. M.; Supplie, O.; Höhn, C.; Krol, R. van de; Lewerenz, H.-J.; Hannappel, T.: *The interface of GaP(100) and H_2O studied by photoemission and reflection anisotropy spectroscopy*. New Journal of Physics, **15**:103003, 2013.

[183] McIntyre, J. D. E.; Aspnes, D. E.: *Differential reflection spectroscopy of very thin surface films*. Surface Science, **24**:417, 1971.

[184] McMahon, W.; Batyrev, I.; Hannappel, T.; Olson, J.; Zhang, S.: *5-7-5 line defects on As/Si(100): A general stress-relief mechanism for V/IV surfaces*. Physical Review B, **74**:033304, 2006.

[185] Men, F. K.; Packard, W. E.; Webb, M. B.: *Si(100) surface under an externally applied stress*. Physical Review Letters, **61**:2469, 1988.

[186] Mermin, W.; Ashcroft, N.: *Solid State Physics*. Harcourt, Inc., 1976. ISBN: 978-0030839931.

[187] Merwe, J. H. van der: *Misfit dislocation generation in epitaxial layers*. Critical Reviews in Solid State and Materials Sciences, **17**:187, 1991.

[188] Miyoshi, S.; Yaguchi, H.; Onabe, K.; Ito, R.; Shiraki, Y.: *Metalorganic vapor phase epitaxy of $GaP_{1-x}N_x$ alloys on GaP*. Applied Physics Letters, **63**:3506, 1993.

[189] Möller, K.: *In situ Überwachung der MOCVD-Präparation von Gallium- und Indiumantimonid*. Ph.D. thesis. Universität Duisburg-Essen / Helmholtz-Zentrum Berlin (Germany), 2006.

[190] Monkhorst, H. J.; Pack, J. D.: *Special points for Brillouin-zone integrations*. Physical Review B, **13**:5188, 1976.

[191] Müller, A.: *In-Situ Massenspektrometrie bei der metallorganischen Gasphasenabscheidung*. Diploma thesis. Fachhochschule Brandenburg / Helmholtz-Zentrum Berlin (Germany), 2011.

[192] Nakagawa, N.; Hwang, H. Y.; Muller, D. A.: *Why some interfaces cannot be sharp*. Nature Materials, **5**:204, 2006.

[193] Németh, I.; Kunert, B.; Stolz, W.; Volz, K.: *Heteroepitaxy of GaP on Si: Correlation of morphology, anti-phase-domain structure and MOVPE growth conditions*. Journal of Crystal Growth, **310**:1595, 2008.

[194] Németh, I.; Kunert, B.; Stolz, W.; Volz, K.: *Ways to quantitatively detect antiphase disorder in GaP films grown on Si(001) by transmission electron microscopy*. Journal of Crystal Growth, **310**:4763, 2008.

[195] Niebling, T.; Rubel, O.; Heimbrodt, W.; Stolz, W.; Baranovskii, S. D.; Klar, P. J.; Geisz, J. F.: *Hopping energy relaxation of localized excitons in GaP(N)*. physica status solidi (c), **5**:768, 2008.

[196] Nishiyama, N.; Caneau, C.; Guryanov, G.; Liu, X. S.; Hu, M.; Zah, C.-E.: *High efficiency long wavelength VCSEL on InP grown by MOCVD*. Electronics Letters, **39**:437, 2003.

[197] Nolting, W.: *Grundkurs Theoretische Physik 5/1: Quantenmechanik – Grundlagen*. Springer Verlag (Berlin/Heidelberg), 2009. ISBN: 978-3-540-68868-6.

[198] Northrup, J. E.: *Structure of Si(100)H: Dependence on the H chemical potential*. Physical Review B, **44**:1419, 1991.

[199] Nozik, A. J.; Memming, R.: *Physical chemistry of semiconductor-liquid interfaces*. Journal of Physical Chemistry, **100**:13061, 1996.

[200] Olah, G. A.; Prakash, G. K. S.; Goeppert, A.: *Anthropogenic chemical carbon cycle for a sustainable future*. Journal of the American Chemical Society, **133**:12881, 2011.

[201] Olson, J. M.; Al-Jassim, M. M.; Kibbler, A.; Jones, K. M.: *MOCVD growth and characterization of GaP on Si*. Journal of Crystal Growth, **77**:515, 1986.

[202] Palummo, M.; Witkowski, N.; Pluchery, O.; Sole, R. del; Borensztein, Y.: *Reflectance-anisotropy spectroscopy and surface differential reflectance spectra at the Si(100) surface: Combined experimental and theoretical study*. Physical Review B, **79**:035327, 2009.

[203] Pashley, M. D.: *Electron counting model and its application to island structures on molecular-beam epitaxy grown GaAs(001) and ZnSe(001)*. Physical Review B, **40**:10481, 1989.

[204] Patterson, C. H.; Herrendörfer, D.: *Reflectance anisotropy of the Si(100)1×2-As surface: Discrete dipole calculation.* Journal of Vacuum Science & Technology A, **15**:3036, 1997.

[205] Perfetti, P.; Patella, F.; Sette, F.; Quaresima, C.; Capasso, C.; Savoia, A.; Margaritondo, G.: *Experimental study of the GaP-Si interface.* Physical Review B, **30**:4533, 1984.

[206] Pezold, J.; Bristowe, P.: *Atomic structure and electronic properties of the GaN/ZnO (0001) interface.* Journal of Materials Science, **40**:3051, 2005.

[207] Philipps, S.; Bett, A. W.; Horowitz, K.; Kurtz, S.: *Current status of concentrator photovoltaic (CPV) technology.* Fraunhofer Institute for Solar Energy Systems ISE / National Renewable Energy Laboratory NREL, 2015. Report No. TP-6A20-63196, available at http://www.nrel.gov/publications.

[208] Pollak, F. H.; Higginbo, C. W.; Cardona, M.: *Band structure of GaAs, GaP, InP and AlSb–$k \cdot p$ method.* Journal of the Physical Society of Japan, Suppl. **S21**:20, 1966. Cited after [302].

[209] Poon, T. W.; Yip, S.; Ho, P. S.; Abraham, F. F.: *Equilibrium structures of Si(100) stepped surfaces.* Physical Review Letters, **65**:2161, 1990.

[210] Powell, C.; Jablonski, A.: *NIST Electron Effective-Attenuation-Length Database (V.1.3).* National Institute of Standards and Technology, Gaithersburg, 2011.

[211] Pristovsek, M.: *In-situ monitoring towards monolayer precision for III-V semiconductor growth.* Habilitation thesis. Technische Universität Berlin (Germany), 2012.
http://www.physik.tu-berlin.de/~prissi/Habilitation-Pristovsek.pdf.

[212] Reboredo, F. A.; Zhang, S. B.; Zunger, A.: *Hydrogen-induced instability on the flat Si(001) surface via steric repulsion.* Physical Review B, **63**:125316, 2001.

[213] Reece, S. Y.; Hamel, J. A.; Sung, K.; Jarvi, T. D.; Esswein, A. J.; Pijpers, J. J. H.; Nocera, D. G.: *Wireless solar water splitting using silicon-based semiconductors and earth-abundant catalysts.* Science, **334**:645, 2011.

[214] Richard, S.; Aniel, F.; Fishman, G.: *Energy-band structure of Ge, Si, and GaAs: A thirty-band $k \cdot p$ method.* Physical Review B, **70**:235204, 2004.

[215] Rocheleau, R. E.; Miller, E. L.; Misra, A.: *High-Efficiency Photoelectrochemical Hydrogen Production Using Multijunction Amorphous Silicon Photoelectrodes.* Energy & Fuels, **12**:3, 1998.

[216] Roesener, T.; Döscher, H.; Beyer, A.; Brückner, S.; Klinger, V.; Wekkeli, A.; Kleinschmidt, P.; Jurecka, C.; Ohlmann, J.; Volz, K.; Stolz, W.; Hannappel, T.; Bett, A. W.; Dimroth, F.: *MOVPE growth of III-V solar cells on silicon in 300 mm closed coupled showerhead reactor.* Proceedings of the European Photovoltaic Solar Energy Conference and Exhibition, **25**:964, 2010.

[217] Rolland, A.; Pedesseau, L.; Even, J.; Almosni, S.; Robert, C.; Cornet, C.; Jancu, J. M.; Benhlal, J.; Durand, O.; Corre, A. L.; Rale, P.; Lombez, L.; Guillemoles, J.-F.; Tea, E.; Laribi, S.: *Design of a lattice-matched III-V-N/Si photovoltaic tandem cell monomonolithic integrated on silicon substrate.* Optical and Quantum Electronics, **46**, 2014.

[218] Romanyuk, O.; Hannappel, T.; Grosse, F.: *Atomic and electronic structure of GaP/Si(111), GaP/Si(110), and GaP/Si(113) interfaces and superlattices studied by density functional theory.* Physical Review B, **88**:115312, 2013.

[219] Rossow, U.; Dietz, N.; Bachmann, K. J.; Aspnes, D. E.: *Optical investigations of surface processes in GaP heteroepitaxy on silicon under pulsed chemical beam epitaxy conditions.* Journal of Vacuum Science & Technology B, **14**:3040, 1996.

[220] Rossow, U.; Mantese, L.; Aspnes, D.: *Lineshapes of surface induced optical anisotropy spectra measured by RDS/RAS.* Applied Surface Science, **123**:237, 1998.

[221] Sakama, H.; Kawazu, A.; Sueyoshi, T.; Sato, T.; Iwatsuki, M.: *Scanning tunneling microscopy on Ga/Si(100).* Physical Review B, **54**:8756, 1996.

[222] Sakata, I.; Kawanami, H.: *Band discontinuities in gallium phosphide/crystalline silicon heterojunctions studied by internal photoemission.* Applied Physics Express, **1**:091201.1, 2008.

[223] Schlier, R. E.; Farnsworth, H. E.: *Structure and adsorption characteristics of clean surfaces of Germanium and Silicon.* Journal of Chemical Physics, **30**:917, 1959.

[224] Schmidbauer, M.: *Röntgenstreuung: Grundlagen und Anwendungen in der Materialwissenschaft.* Script of the lecture given at Humboldt-Universität zu Berlin, 2012.

[225] Schmidt, W. G.; Bechstedt, F.; Bernholc, J.: *Terrace and step contributions to the optical anisotropy of Si(001) surfaces.* Physical Review B, **63**:045322, 2001.

[226] Schmidt, W. G.; Bernholc, J; Bechstedt, F: *(001) surfaces of GaP and InP: Structural motifs, electronic states and optical signatures.* Applied Surface Science, **166**:179, 2000.

[227] Schmidt, W. G.; Briggs, E. L.; Bernholc, J.; Bechstedt, F.: *Structural fingerprints in the reflectance anisotropy spectra of InP(001)*(2×4) *surfaces.* Physical Review B, **59**:2234, 1999.

[228] Schmidt, W. G.; Esser, N; Frisch, A. M.; Vogt, P; Bernholc, J; Bechstedt, F; Zorn, M; Hannappel, T; Visbeck, S; Willig, F; Richter, W: *Understanding reflectance anisotropy: Surface-state signatures and bulk-related features in the optical spectrum of InP(001)(2×4).* Physical Review B, **61**:16335, 2000.

[229] Schmidt, W. G.; Hahn, P. H.; Bechstedt, F.; Esser, N.; Vogt, P.; Wange, A.; Richter, W.: *InP(001)-(*2×1*) surface: A hydrogen stabilized structure.* Physical Review Letters, **90**:126101, 2003.

[230] Schmidt, W.; Bechstedt, F; Bernholc, J: *Understanding reflectance anisotropy: Surface-state signatures and bulk-related features.* Journal of Vacuum Science & Technology B, **18**:2215, 2000.

[231] Schmidtling, T.: *MOVPE growth and characterization of goup-III nitride using in situ spectroscopic ellipsometry.* Ph.D. thesis. Technische Universität Berlin (Germany), 2006.

[232] Seah, M. P.; Dench, W. A.: *Quantitative electron spectroscopy of surfaces: A standard data base for electron inelastic mean free paths in solids.* Surface and Interface Analysis, **1**:2, 1979.

[233] Seeck, O. H.: *X-ray diffraction: Modern experimental techniques.* Ed. by Seeck, O. H.; Murphy, B. M. Pan Stanford, 2015. ISBN: 978-9-81-430359-0.

[234] Shan, W.; Walukiewicz, W.; Ager, J. W.; Haller, E. E.; Geisz, J. F.; Friedman, D. J.; Olson, J. M.; Kurtz, S. R.: *Band anticrossing in GaInNAs alloys.* Physical Review Letters, **82**:1221, 1999.

[235] Shan, W.; Walukiewicz, W.; Yu, K. M.; Wu, J.; III, J. W. A.; Haller, E. E.; Xin, H. P.; Tu, C. W.: *Nature of the fundamental band gap in GaN_xP_{1-x} alloys.* Applied Physics Letters, **76**:3251, 2000.

[236] Shioda, R.; Weide, J. van der: *Observation of hydrogen adsorption on Si(001) by reflectance difference spectroscopy.* Applied Surface Science, **130–132**:266, 1998.

[237] Shockley, W.; Queisser, H. J.: *Detailed balance limit of efficiency of p-n junction solar cells.* Journal of Applied Physics, **32**:510, 1961.

[238] Sippel, P.: *Electronic structure and electron dynamics in semiconductor materials for new photovoltaic applications.* Ph.D. thesis. Technische Universität Ilmenau / Helmholtz-Zentrum Berlin (Germany), submitted, 2015.

[239] Sippel, P.; Supplie, O.; May, M. M.; Eichberger, R.; Hannappel, T.: *Electronic structures of GaP(100) surface reconstructions probed with two-photon photoemission spectroscopy.* Physical Review B, **89**:165312, 2014.

[240] Skibitzki, O.; Hatami, F.; Yamamoto, Y.; Zaumseil, P.; Trampert, A.; Schubert, M. A.; Tillack, B.; Masselink, W. T.; Schroeder, T.: *GaP collector development for SiGe heterojunction bipolar transistor performance increase: A heterostructure growth study.* Journal of Applied Physics, **111**:073515, 2012.

[241] Soga, T.; Suzuki, T.; Mori, M.; Jimbo, T.; Umeno, M.: *The effects of the growth parameters on the initial stage of epitaxial growth of GaP on Si by metalorganic chemical vapor deposition.* Journal of Crystal Growth, **132**:134, 1993.

[242] Soga, T.; Jimbo, T.; Umeno, M.: *Growth and characterization of two-dimensional GaP on Si by metalorganic chemical vapor deposition.* Journal of Crystal Growth, **146**:554, 1995.

[243] Sole, R. del; Onida, G.: *Surface versus crystal-termination effects in the optical properties of surfaces.* Physical Review B, **60**:5523, 1999.

[244] Spieß, L.; Schwarzer, R.; Behnken, H.; Teichert, G.: *Moderne Röntgenbeugung*. Vieweg+Teubner (Wiesbaden), 2005. ISBN: 978-3-35-1900522-3.

[245] Stange, H.: *Präparation und Analyse von GaPN-Schichten auf Si(001)*. Master thesis. Humboldt-Universität zu Berlin / Helmholtz-Zentrum Berlin (Germany), 2013.

[246] Steinbach, G.; Schreiber, M.; Gemming, S.: *DFT Investigation of the Heterostructure GaP(001) on Si(001)*. Nanoscience and Nanotechnology Letters, **5**:73, 2013.

[247] Stringfellow, G. B.: *Organometallic vapor-phase epitaxy: Theory and practice*. Academic Press, 1989. ISBN: 978-9-12-673840-7.

[248] Stringfellow, G. B.: *Novel precursors for organometallic vapor phase epitaxy*. Journal of Crystal Growth, **128**:503, 1993.

[249] Supplie, O.; Brückner, S.; Döscher, H.; Kleinschmidt, P.; Hannappel, T.: *III-V/Si(100) heterointerfaces studied in VPE ambient via surface dimers by in situ reflection anisotropy spectroscopy*. Proceedings of the IEEE Photovoltaics Specialists Conference, **39**:879, 2013.

[250] Supplie, O.; Brückner, S.; Romanyuk, O.; May, M. M.; Döscher, H.; Kleinschmidt, P.; Stange, H.; Dobrich, A.; Höhn, C.; Lewerenz, H.-J.; Grosse, F.; Hannappel, T.: *An experimental-theoretical atomic-scale study—In situ analysis of III-V on Si(100) growth for hybrid solar cells*. Proceedings of the IEEE Photovoltaics Specialists Conference, **40**:2707, 2014.

[251] Supplie, O.; Döscher, H.; May, M. M.; Hannappel, T.: *Heteroepitaxial III-V on Si(100) tandem absorber structures for photoelectrolysis*. AIP Conference Proceedings, **1568**:20, 2013.

[252] Supplie, O.: *In situ Reflexions-Anisotropie-Spektroskopie an MOVPE-präpariertem GaP/Si(100)*. Diploma thesis. Humboldt-Universität zu Berlin / Helmholtz-Zentrum Berlin (Germany), 2010.

[253] Supplie, O.; Brückner, S.; Romanyuk, O.; Döscher, H.; Höhn, C.; May, M. M.; Kleinschmidt, P.; Grosse, F.; Hannappel, T.: *Atomic scale analysis of the GaP/Si(100) heterointerface by in situ reflection anisotropy spectroscopy and ab initio density functional theory*. Physical Review B, **90**:235301, 2014.

[254] Supplie, O.; Hannappel, T.; Pristovsek, M.; Döscher, H.: *In situ access to the dielectric anisotropy of buried III-V/Si(100) heterointerfaces*. Physical Review B, **86**:035308, 2012.

[255] Supplie, O.; May, M. M.; Stange, H.; Höhn, C.; Lewerenz, H.-J.; Hannappel, T.: *Materials for light-induced water splitting: In situ controlled surface preparation of GaPN epilayers grown lattice-matched on Si(100)*. Journal of Applied Physics, **115**:113509, 2014.

[256] Supplie, O.; May, M. M.; Steinbach, G.; Romanyuk, O.; Grosse, F.; Nägelein, A.; Kleinschmidt, P.; Brückner, S.; Hannappel, T.: *Time-resolved in situ spectroscopy during formation of the GaP/Si(100) heterointerface*. Journal of Physical Chemistry Letters, **6**:464, 2015.

[257] Suzuki, T.; Soga, T.; Jimbo, T.; Umeno, M.: *Growth mechanism of GaP on Si substrate by MOVPE.* Journal of Crystal Growth, **115**:158, 1991.

[258] Swartzentruber, B. S.; Matzke, C. M.; Kendall, D. L.; Houston, J. E.: *STM measurements of step-flow kinetics during atom removal by low-energy-ion bombardment of Si(001).* Surface Science, **329**:83, 1995.

[259] Swartzentruber, B. S.; Mo, Y.-W.; Webb, M. B.; Lagally, M. G.: *Scanning tunneling microscopy studies of structural disorder and steps on Si surfaces.* Journal of Vacuum Science & Technology A, **7**:2901, 1989.

[260] Tachikawa, M.; Mori, H.: *Dislocation generation of GaAs on Si in the cooling stage.* Applied Physics Letters, **56**:2225, 1990.

[261] Takagi, Y; Yonezu, H; Samonji, K; Tsuji, T; Ohshima, N: *Generation and suppression process of crystalline defects in GaP layers grown on misoriented Si(100) substrates.* Journal of Crystal Growth, **187**:42, 1998.

[262] Takagi, Y.; Furukawa, Y.; Wakahara, A.; Kan, H.: *Lattice relaxation process and crystallographic tilt in GaP layers grown on misoriented Si(001) substrates by metalorganic vapor phase epitaxy.* Journal of Applied Physics, **107**:063506, 2010.

[263] Takao, Y.; Morita, A.: *Electronic structure of black phosphorus: Tight binding approach.* Physica B, **105**:93, 1981.

[264] Tanaka, H.; Colas, E.; Kamiya, I.; Aspnes, D. E.; Bhat, R.: *In situ determination of free-carrier concentration by reflectance difference spectroscopy.* Applied Physics Letters, **59**:3443, 1991.

[265] Thanh, T. N.; Robert, C.; Létoublon, A.; Cornet, C.; Quinci, T.; Giudicelli, E.; Almosni, S.; Boudet, N.; Ponchet, A.; Kuyyalil, J.; Danila, M.; Durand, O.; Bertru, N.; Corre, A. L.: *Synchrotron X-ray diffraction analysis for quantitative defect evaluation in GaP/Si nanolayers.* Thin Solid Films, **541**:36, 2013.

[266] Thieu, Q. T.; Inamoto, T.; Kuboya, S.; Onabe, K.: *Pyrolysis of dimethylhydrazine for the MOVPE growth of GaN and InN monitored by in-situ quadrupole mass spectrometry.* physica status solidi (c), **10**:405, 2013.

[267] Thompson, A.; Attwood, D.; Gullikson, E.; Howells, M.; Kim, K.-J.; Kirz, J.; Lindau, I.; Liu, Y.; Pianetta, P.; Robinson, A.; Scofield, J.; Underwood, J.; Williams, G.; Winick, H.: *X-ray data booklet.* Center for X-ray Optics and Advanced Light Source, Lawrence Berkeley National Laboratory, 2009, 3rd edition. http://xdb.lbl.gov.

[268] Ting, S. M.; Fitzgerald, E. A.: *Metal-organic chemical vapor deposition of single domain GaAs on $Ge/Ge_xSi_{1-x}/Si$ and Ge substrates.* Journal of Applied Physics, **87**:2618, 2000.

[269] Tiwari, S.; Frank, D. J.: *Empirical fit to band discontinuities and barrier heights in III–V alloy systems.* Applied Physics Letters, **60**:630, 1992.

[270] Töben, L; Hannappel, T; Möller, K; Crawack, H.; Pettenkofer, C; Willig, F: *RDS, LEED and STM of the P-rich and Ga-rich surfaces of GaP(100).* Surface Science, **494**:L755, 2001.

[271] Tok, E. S.; Hartell, A. D.; Zhang, J.: *Kinetics of Si growth from hydride precursors on As-passivated Si(001) surface.* Applied Physics Letters, **78**:919, 2001.

[272] Tromp, R. M.; Hamers, R. J.; Demuth, J. E.: *Si(001) dimer structure observed with scanning tunneling microscopy.* Physical Review Letters, **55**:1303, 1985.

[273] Troullier, N.; Martins, J. L.: *Efficient pseudopotentials for plane-wave calculations.* Physical Review B, **43**:1993, 1991.

[274] Umeno, K.; Kim, S. M.; Furukawa, Y.; Yonezu, H.; Wakahara, A.: *Band alignments of InGaPN/GaPN quantum well structures on GaP and Si.* Journal of Crystal Growth, **301–302**:539, 2007.

[275] Uppal, P. N.; Kroemer, H.: *Molecular beam epitaxial growth of GaAs on Si(211).* Journal of Applied Physics, **58**:2195, 1985.

[276] Van Vechten, J. A.; Bergstresser, T. K.: *Electronic structures of semiconductor alloys.* Physical Review B, **1**:3351, 1970.

[277] Vegard, L.: *Die Konstitution der Mischkristalle und die Raumfüllung der Atome.* Zeitschrift für Physik, **5**:17, 1921.

[278] Visbeck, S.; Hannappel, T.; Zorn, M.; Zettler, J.-T.; Willig, F.: *Temperature dependence and origin of InP(100) reflectance anisotropy down to 20 K.* Physical Review B, **63**:245303, 2001.

[279] Volz, K.; Beyer, A.; Witte, W.; Ohlmann, J.; Németh, I.; Kunert, B.; Stolz, W.: *GaP-nucleation on exact Si(001) substrates for III/V device integration.* Journal of Crystal Growth, **315**:37, 2011.

[280] Volz, K.; Gambin, V.; Ha, W.; Wistey, M. A.; Yuen, H.; Bank, S.; Harris, J. S.: *The role of Sb in the MBE growth of (GaIn)(NAsSb).* Journal of Crystal Growth, **251**:360, 2003.

[281] Vurgaftman, I.; Meyer, J. R.: *Band parameters for nitrogen-containing semiconductors.* Journal of Applied Physics, **94**:3675, 2003.

[282] Vurgaftman, I.; Meyer, J. R.; Ram-Mohan, L. R.: *Band parameters for III–V compound semiconductors and their alloys.* Journal of Applied Physics, **89**:5815, 2001.

[283] Wagner, C. D.; Davis, L. E.; Zeller, M. V.; Taylor, J. A.; Raymond, R. H.; Gale, L. H.: *Empirical atomic sensitivity factors for quantitative analysis by electron spectroscopy for chemical analysis.* Surface and Interface Analysis, **3**:211, 1981.

[284] Waldrop, J. R.; Grant, R. W.; Kowalczyk, S. P.; Kraut, E. A.: *Measurement of semiconductor heterojunction band discontinuities by X-ray photoemission spectroscopy.* Journal of Vacuum Science & Technology A, **3**:835, 1985.

[285] Wang, Y.; Chen, X.; Hamers, R. J.: *Atomic-resolution study of overlayer formation and interfacial mixing in the interaction of phosphorus with Si(001).* Phys. Rev. B, **50**:4534, 1994.

[286] Weightman, P.; Martin, D. S.; Cole, R. J.; Farrell, T.: *Reflection anisotropy spectroscopy.* Reports on Progress in Physics, **68**:1251, 2005.

[287] Weinrich, J.: *Photoluminszenzmessungen an Galliumphosphidnitrid.* Bachelor thesis. Humboldt-Universität zu Berlin / Helmholtz-Zentrum Berlin (Germany), 2014.

[288] Werner, K.; Beyer, A.; Oelerich, J.; Baranovskii, S.; Stolz, W.; Volz, K.: *Structural characteristics of gallium metal deposited on Si(001) by MOCVD.* Journal of Crystal Growth, **405**:102, 2014.

[289] Weyers, M.; Sato, M.; Ando, H.: *Red shift of photoluminescence and absorption in dilute GaAsN alloy layers.* Japanese Journal of Applied Physics, **31**:L853, 1992.

[290] Wojdyr, M.: *Fityk: A general-purpose peak fitting program.* Journal of Applied Crystallography, **43**:1126, 2010.

[291] Wolkow, R. A.: *Direct observation of an increase in buckled dimers on Si(001) at low temperature.* Physical Review Letters, **68**:2636, 1992.

[292] Wright, S. L.; Inada, M.; Kroemer, H.: *Polar-on-nonpolar epitaxy: Sublattice ordering in the nucleation and growth of GaP on Si(211) surfaces.* Journal of Vacuum Science & Technology, **21**:534, 1982.

[293] Wright, S. L.; Kroemer, H.; Inada, M.: *Molecular beam epitaxial growth of GaP on Si.* Journal of Applied Physics, **55**:2916, 1984.

[294] Wu, J.; Walukiewicz, W.; Yu, K. M.; Ager, J. W.; Haller, E. E.; Hong, Y. G.; Xin, H. P.; Tu, C. W.: *Band anticrossing in $GaP_{1-x}N_x$ alloys.* Physical Review B, **65**:241303, 2002.

[295] Xin, H. P.; Tu, C. W.; Zhang, Y.; Mascarenhas, A.: *Effects of nitrogen on the band structure of GaN_xP_{1-x} alloys.* Applied Physics Letters, **76**:1267, 2000.

[296] Yablonovitch, E.; Miller, O.; Kurtz, S.: *The opto-electronic physics that broke the efficiency limit in solar cells.* Proceedings of the IEEE Photovoltaics Specialists Conference, **38**:001556, 2012.

[297] Yang, V. K.; Groenert, M.; Leitz, C. W.; Pitera, A. J.; Currie, M. T.; Fitzgerald, E. A.: *Crack formation in GaAs heteroepitaxial films on Si and SiGe virtual substrates.* Journal of Applied Physics, **93**:3859, 2003.

[298] Yasuda, T.: *Interface, surface and bulk anisotropies of heterostructures.* Thin Solid Films, **313–314**:544, 1998.

[299] Yasuda, T.; Kuo, L. H.; Kimura, K.; Miwa, S.; Jin, C. G.; Tanaka, K.; Yao, T.: *In situ characterization of ZnSe/GaAs(100) interfaces by reflectance difference spectroscopy.* Journal of Vacuum Science and Technology B, **14**:3052, 1996.

[300] Yeh, J.; Lindau, I.: *Atomic subshell photoionization cross sections and asymmetry parameters:* $1 < Z < 103$. Atomic Data and Nuclear Data Tables, **32**:1, 1985.

[301] Yoon, S.; Seong, M. J.; Geisz, J. F.; Duda, A.; Mascarenhas, A.: *Evolution of electronic states in $GaP_{1-x}N_x$ studied by resonant Raman scattering spectroscopy.* Physical Review B, **67**:235209, 2003.

[302] Yunovich, A. E.: *Strahlende Rekombination und optische Eigenschaften von GaP.* Fortschritte der Physik, **23**:317, 1975.

[303] Zettler, J.-T.: *Characterization of epitaxial semiconductor growth by reflectance anisotropy spectroscopy and ellipsometry.* Progress in Crystal Growth and Characterization of Materials, **35**:27, 1997.

[304] Zhang, S. B.; Zunger, A.: *Surface-reconstruction-enhanced solubility of N, P, As, and Sb in III-V semiconductors.* Applied Physics Letters, **71**:677, 1997.

[305] Zhang, Y.; Fluegel, B.; Mascarenhas, A.; Xin, H. P.; Tu, C. W.: *Optical transitions in the isoelectronically doped semiconductor GaPN: An evolution from isolated centers, pairs, and clusters to an impurity band.* Physical Review B, **62**:4493, 2000.

[306] Zhang, Y.; Fluegel, B.; Hanna, M. C.; Geisz, J. F.; Wang, L.-W.; Mascarenhas, A.: *Effects of heavy nitrogen doping in III–V semiconductors—How well does the conventional wisdom hold for the dilute nitrogen "III-V-N alloys"?* physica status solidi (b), **240**:396, 2003.

[307] Zhang, Y.; Fluegel, B.; Hanna, M. C.; Mascarenhas, A.; Wang, L.-W.; Wang, Y. J.; Wei, X.: *Impurity perturbation to the host band structure and recoil of the impurity state.* Physical Review B, **68**:075210, 2003.

[308] Zhang, Z.; Chen, H.; Bolding, B. C.; Lagally, M. G.: *Vacancy diffusion on Si(100)-(2×1).* Physical Review Letters, **71**:3677, 1993.

[309] Zhou, J.; Chen, H; Li, F.; Liu, S; Mei, X.; Huang, Y: *TEM observation of GaAs on Si(100) grown by MBE.* Vacuum, **43**:1055, 1992.

[310] Zollner, S.; Garriga, M.; Kircher, J.; Humlicek, J.; Cardona, M.; Neuhold, G.: *Temperature dependence of the dielectric function and the interband critical-point parameters of GaP.* Physical Review B, **48**:7915, 1993.

[311] Zollner, S.; Garriga, M.; Kircher, J.; Humlícek, J.; Cardona, M.; Neuhold, G.: *Temperature dependence of the dielectric function and the interband critical-point parameters of GaP.* Thin Solid Films, **233**:185, 1993.

[312] Zorn, M.; Jönsson, J.; Krost, A.; Richter, W.; Zettler, J.-T.; Ploska, K.; Reinhardt, F.: *In-situ reflectance anisotropy studies of ternary III–V surfaces and growth of heterostructures.* Journal of Crystal Growth, **145**:53, 1994.

[313] Zorn, M.; Trepk, T.; Kurpas, P.; Weyers, M.; Zettler, J. T.; Richter, W.: *In situ monitoring and control of InGaP growth on GaAs in MOVPE.* Journal of Crystal Growth, **195**:223, 1998.

Acknowledgement

This work could not have been carried out without the support of numerous excellent people. In particular, it is a pleasure to thank...

... Prof. Dr. R. Manzke for your advice and support, from the basic class in solid states physics on to this work. Particularly, for continuing the supervision also as vice chancellor of Humboldt University.

... Prof. Dr. T. Hannappel for giving me the chance to contribute to this exciting field. For your guidance and trust, for many opportunities and the necessary degree of freedom.

... Prof. Dr. D. E. Aspnes for your interest in this work and, especially, for taking the effort for the external review.

... Prof. Dr. H.-J. Lewerenz for the productive collaboration and teaching a physicist the language of electrochemists.

... Prof. Dr. R. van de Krol for your generous support during the transition from HZB to TU Ilmenau and for hosting me at HZB while commuting to Thuringia.

... M. M. May for your expertise in PES and electrochemistry; for a great time in the lab and real world; for cough syrup, less meat on my menu and delicious evenings in Potsdam. Blubb ;)

... Dr. S. Brückner for efficient joint lab sessions on clean Silicon and Germanium before you transformed to, well, the best coffee-serving postdoc ever. Not to forget countless discussions about RAS and other freaky stuff.

... Dr. P. Kleinschmidt for your "tunnel vision" and pleasant teamwork.

... A. Dobrich for your support, be it personal or in the lab.

... H. Stange and J. Weinrich for the proof that supervising students pays off. And for good times off the labs as well.

... Dr. O. Romanyuk and Dr. F. Grosse for performing the DFT calculations and, together with G. Steinbach, for highly fruitful discussions.

... the Deutsche Forschungsgemeinschaft (DFG) for funding within the project "Elektronenmikroskopische Oberflächenuntersuchungen zum Verständnis der Heteroepitaxie von GaP auf Silizium" (HA3096).

... Dr. B. Borkenhagen, Dr. G. Lilienkamp and Prof. Dr. W. Daum for microscopical insights and an inspiring DFG project.

... Dr. H. Döscher for important advice and pleasant roommateship during the early stages of my scientific life.

... C. Höhn for great technical support with scientific motivation. And, together with R. Schütz, for great concerts.

... A. Müller for keeping one MOVPE alive and giving birth to a new one, including most of the requested fancy technical details. Also for reminding me that my racing bike feels badly neglected.

... S. Kubala and M. Biester for preventing pressure from building up in Berlin and Ilmenau, respectively.

... P. Sippel for proving that two photons may be exciting as well.

... E. Barrigón for a great time working on Germanium and nightlife.

... Dr. M. Pristovsek for advice, in situ SE measurements and never boring meetings.

... A. Paszuk for pushing the Si pn-junction and many helping hands; A. Nägelein and C. Koppka for reliable experimental support whenever needed; M. Steidl and W. Zhao for that new dimension along <111>.

... S. Gutsche for screening us from all that bureaucracy, perfect organization, lovely nicknames and high spirits.

... Dr. K. Schwarzburg and Dr. R. Eichberger for support at HZB.

... W. Zabka for spending many hours in front of the AFM.

... M. Guerra and K. Regelin for a lot of organizational support.

... M. Borgward for programming that lovely flow calculator.

... M. Ziwritsch for programming the recipe-to-database converter.

... Dr. A. Bronneberg for always reading acknowledgements.

... H.-J. Schroeder-Fürst for laying the foundation for my interest in physics.

... my family for magnificent support that I could always rely on.

... Jonas for keeping me open-minded.

... Britta. *Nu vill jag sjunga att sommaren är skön.*